Advances in Reservoir Geology

Geological Society
Special Publication
No 69

edited by
M. Ashton

Published by The Geological Society

Advances in Reservoir Geology

Geological Society Special Publications
Series Editor J. BROOKS

GEOLOGICAL SOCIETY SPECIAL PUBLICATION NO 69

Advances in Reservoir Geology

EDITED BY

MICHAEL ASHTON
Badley, Ashton & Associates,
Horncastle, UK.

1993

Published by

The Geological Society

London

THE GEOLOGICAL SOCIETY

The Society was founded in 1807 as the Geological Society of London and is the oldest geological society in the world. It received its Royal Charter in 1825 for the purpose of 'investigating the mineral structure of the Earth'. The Society is Britain's national learned society for geology with a Fellowship of 6965 (1991). It has countrywide coverage and approximately 1000 members reside overseas. The Society is responsible for all aspects of the geological sciences including professional matters. The Society has its own publishing house which produces the Society's international journals, books and maps, and which acts as the European distributor for publications of the American Association of Petroleum Geologists.

Fellowship is open to those holding a recognized honours degree in geology or a cognate subject and who have at least two years relevant postgraduate experience, or have not less than six years relevant experience in geology or a cognate subject. A Fellow who has not less than five years relevant postgraduate experience in the practice of geology may apply for validation and, subject to approval, may be able to use the designatory letters C. Geol (Chartered Geologist).

Further information about the Society is available from the Membership Manager, The Geological Society, Burlington House, Piccadilly, London, W1V 0JU, UK.

Published by The Geological Society from:
The Geological Society Publishing House
Unit 7
Brassmill Enterprise Centre
Brassmill Lane
Bath
Avon BA1 3JN
UK
(*Orders:* Tel. 0225 445046
Fax 0225 442836)

First published 1992

British Library Cataloguing in Publication Data

A Catalogue record for this book is available from the British Library

ISBN 0-903317-84-2

Distributors
USA
AAPG Bookstore
PO Box 979
Tulsa
Oklahoma 74101-0979
USA
(*Orders*: Tel: (918)584-2555
Fax (918)584-0469)

Australia
Australian Mineral Foundation
63 Conyngham Street
Glenside
South Australia 5065
Australia
(*Orders*: Tel: (08)379-0444
Fax (08)379-4634)

India
Affiliated East–West Press PVT Ltd
G-1/16 Ansari Road
New Delhi 110 002
India
(*Orders*: Tel: (11)327-9113
Fax (11)331-2830)

Printed and bound by The Cromwell Press, Broughton Gifford, Melksham

Contents

Introduction

With the increasing maturity of exploration in the North Sea Basin the challenge for reservoir geology has moved towards the exploitation of smaller and technically more demanding hydrocarbon accumulations, and the maximization of reserves from the established, producing fields. In both cases there is a growing need for more refined geological reservoir interpretation and modelling. This volume addresses some of the challenges reservoir geology faces in the 1990s: the improved prediction, description and modelling of hydrocarbon reservoirs through the use of new techniques and methods, the refined use of existing techniques, and the ever-increasing integration of data derived from a variety of sources, not least outcrops. The papers making up this volume address these problems from a variety of standpoints.

Improved reservoir prediction is discussed by **Gibbons *et al.*** who apply a combination of techniques, most notably sequence stratigraphy and petrography, to predict the potential impact carbonate-cemented horizons may have on the development strategy of the Troll Field reservoir (NCS), particularly the siting of horizontal wells. In similar vein **Lahann *et al.*** combine the techniques of sedimentology, petrography, inorganic geochemistry and production logging to unravel the controls on porosity and permeability in the Rotliegendes reservoir of the Vanguard Field (UKCS) and to explain the highly variable production rates from different reservoir intervals and wells. **Clelland *et al.*** describe how a relatively new technique, quantitative image analysis of pore structure, can surpass the more conventional petrographical methods in determining the controls on permeability in the variably dolomite-cemented sandstones of the Jurassic Ribble Member of the Fulmar Field (UKCS); such knowledge leads to a better appreciation of production performance and is, therefore, a potential aid to reservoir management.

The following group of papers discusses the use of outcrop-derived data in enhancing our understanding of reservoir modelling and simulation studies. Firstly **Lowry & Jacobsen** provide, from the Ferron Sandstone Member (Mancos Fm, Turonian) of Utah, valuable data on the dimensions of the component facies elements of fluvial-dominated delta-front sections. Through the use of minipermeametry they describe the permeability structure of these facies elements and demonstrate the impact these heterogeneities have on reservoir behaviour by simple simulation studies. **Hoimyr *et al.*** go a stage further by combining sedimentological (facies and geometry) outcrop analogue data from the Maroon Formation (Permo-Carboniferous) of Colorado with reservoir data from the Statfjord Formation (Jurassic) of the Snorre Field (NCS), to demonstrate the considerable impact internal sandstone heterogeneities have on recovery efficiency. **Dreyer** also uses sedimentological outcrop analogue data to tackle a subsurface reservoir description problem. This time the Ridge Route Formation (Miocene) of California is used as the analogue for the fan-delta facies of the Tilje Formation (Jurassic) of the Mid-Norwegian Shelf. Whilst Dreyer is able to demonstrate the similarity of the two delta successions he considered it necessary to apply conversion factors to the outcrop data before using it with the subsurface Tilje data. This raises questions on the application of analogues, a point expanded upon in the essay by **Alexander**.

The final two papers of the volume review the value of 'known' methodology, the

dipmeter tool, and describe a new technique, permeability imaging. In the former case **Cameron *et al.*** demonstrate how analogue dipmeter logs, carefully calibrated with sedimentological logs, can provide valuable palaeocurrent data *when* the scale of the sedimentary structures (and their nature) is used to control the dipmeter parameters. In contrast, **Bourke *et al.*** describe how probe permeameter-derived permeability images can be compared with the microresistivity images of the Formation MicroScanner (FMS) borehole logging tool, and thus provide the potential for calibrating FMS images indirectly with permeability for extrapolation into uncored well sections for more detailed reservoir analysis.

I would like to thank the many referees for their help in producing this volume, and especially Cara Tipton of Badley, Ashton & Associates Ltd for her invaluable assistance in the many administrative chores associated with editing a book. Finally my thanks to Angharad Hills at the Geological Society for her patience and guidance.

From ASHTON, M. (ed.), 1993, *Advances in Reservoir Geology*,
Geological Society Special Publication No. 69, pp. 1–31.

Sequence architecture, facies development and carbonate-cemented horizons in the Troll Field reservoir, offshore Norway

K. GIBBONS,[1] T. HELLEM,[2,4] A. KJEMPERUD,[2,5] S. D. NIO[3] & K. VEBENSTAD[1,6]

[1] *Statoil, PO Box 300, Stavanger, Norway*
[2] *Read Production Geology Services AS, PO Box 145, Sandvika, Norway*
[3] *Intergeos, Reaal 5[Q], 2353 Leiderdorp, The Netherlands*
[4] *Present address: Saga Petroleum AS, PO Box 490, 1301 Sandvika, Norway*
[5] *Present address: Petec AS, Baarsrudv. 2., PO Box 88, 3478 Naersnes, Norway*
[6] *Present address: BP Norway Ltd UA, PO Box 197, Stavanger, Norway*

Abstract: The Sognefjord Formation in the Troll Field area was deposited during a general rise in sea-level during the Late Callovian to Early Volgian. A detailed study including palynology, sedimentology, response modelling and petrography of carbonate cement has been performed on 15 wells primarily from the western part of the field. All wells have been extensively cored through the reservoir enabling detailed palynological and sedimentological study of the depositional sequences in the wells. The Sognefjord Formation is interpreted, in this study, as a shoreline-attached tidally-influenced shelf complex.

The study is based on the general consistency found between the eustatic sea-level curve published by Haq *et al.* in 1987 and the biostratigraphical zonation for the Troll Field described here. The response to sea-level fluctuations in a shallow marine environment is discussed and a response model is established. A theoretical assessment of the criteria for recognizing important events is presented. The maximum flooding surfaces (mfs) and sequence boundaries (sb) are easiest to recognize. Theoretically there is a higher probability of forming carbonate cements in connection with maximum flooding surfaces.

The stratigraphically important dinocysts on Troll are classified according to their relation to sea-level fluctuations. Most of the palynozone boundaries are related to maximum flooding surfaces, except for a few which coincide with sequence boundaries. A stratigraphical subdivision of the Troll Field reservoir is presented based on a comprehensive palynological study.

Lithofacies analysis in conjunction with palynofacies interpretation have been applied to delineate the depositional environment. As an aid to the interpretation a theoretical model was established. The predicted succession and variability of sequences and facies types outlined by the theoretical model could be recognized in all wells.

Petrographical analysis shows that early diagenetic, near-surface cementation has occurred in connection with maximum flooding surfaces and sequence boundaries on Troll.

With the help of the stratigraphical framework the presence or absence of sequence boundaries, transgressive systems tracts, maximum flooding surfaces, and highstand systems tracts in each cycle has been defined in each well. This has given the detailed geometry of the reservoir sands of the field, and also allowed correlation of carbonate cemented horizons which are associated with bounding surfaces of the systems tracts. Knowledge of the distribution and extent of these cemented horizons has considerable significance for oil production strategy, particularly the siting of horizontal wells.

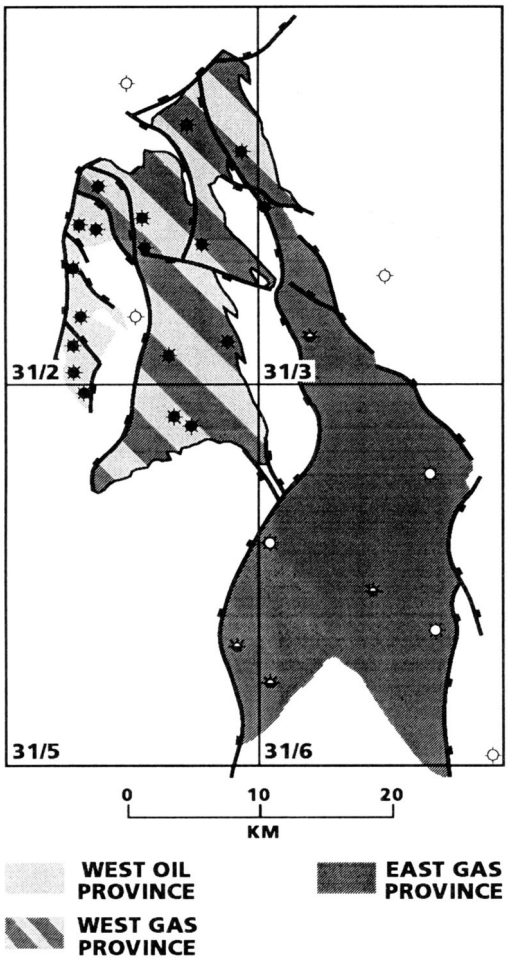

Fig. 1. Map of the Troll Field showing well locations together with the geographical locations of the eastern gas province and the western oil and gas provinces.

Troll is a giant gas field with a thin oil rim, located on the Bergen High at the northwestern edge of the Horda Platform at the eastern margin of the Viking Graben, offshore Norway. The field, which covers an area of 770 km^2, lies in Norwegian blocks 31/2, 31/3, 31/5 and 31/6. Three provinces, based on geographical position and thickness of the oil column, are recognized in the field (Fig. 1): (1) an eastern gas province with an average oil column of 3 m, (2) a western gas province with an average oil column of 12 m and (3) a western oil province with an average oil column of 22 m.

The majority of the gas reserves are contained within the Sognefjord Formation which is part of the Viking Group (Fig. 2). The Sognefjord Formation was deposited during a general rise in sea-level during the Late Callovian to early Volgian.

The thick (nearly 200 m) reservoir sands of the Sognefjord Formation are poorly consolidated with calcite-cemented horizons present in all reservoir units. These horizons vary from nodules to stratiform layers between 0.5 and 5 m thick. On average 10% of the reservoir is calcite cemented.

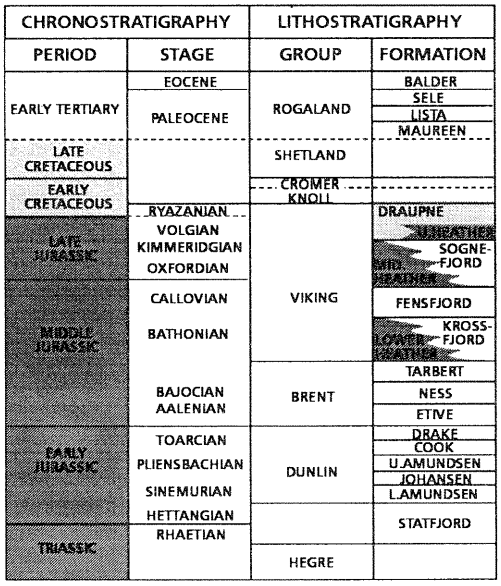

Fig. 2. Stratigraphy of the Troll Field.

An understanding of the spatial distribution and lateral extent of the cemented horizons is critical to the planning of production from the thin oil zone at Troll. Previous authors have presented key evidence regarding the controls on the origin and geometry of calcite cementation in the Troll Field (*e.g.* Irwin & Hurst 1983; Kantorowicz *et al.* 1987). These authors argue that some of the cemented horizons are potentially laterally extensive (> 1000 m); however, a predictive model which can be used to distinguish between laterally extensive and discontinuous horizons is required.

The Sognefjord Formation of the Troll Field is interpreted here as a shoreline-attached tidally-influenced shelf complex. The sediments exhibit a cyclic nature which is expressed as repeated successions of micaceous, silty, very fine- to fine-grained sandstones and mineralogically mature, clean, coarse-grained sandstones (see Grey 1987; Hellem *et al.* 1986). Beecham (pers. comm., 1985) explained this cyclic nature by fluctuations in sea-level:

> A single depositional cycle typically comprises both a progradational and a transgressive component. From the base, low-energy, frequently offshore, fine micaceous sediments coarsen upwards into nearshore, medium to coarse, clean sands which represents coastal progradation over a shallow shelf. This sequence is often overlain or partially replaced by a coarse, clean sand reworked from coastal sediments by high energy currents associated with an increase in transgressive activity.

This description is not strictly speaking within the sequence stratigraphical concept defined by Posamentier *et al.* (1988). However, the general successions anticipated by these concepts are defined and indicate that a sequence stratigraphical model should be adaptable to the Troll reservoir.

The possible link between sediment accumulation and sea-level fluctuation leads

naturally to the possibility that some of the cemented horizons at Troll are associated with maximum flooding surfaces at sea-level maxima. This link would enable the correlation and evaluation of the lateral extent of some horizons. Further, based on the premise that the eustatic sea-level curve published by Haq *et al.* (1987) is valid for the basinal complex in which the Troll field is located, the biostratigraphical zonation of the reservoir could be linked to the Haq-curve.

In the subsequent sections the theoretical aspects dealing with the relationships between sea-level fluctuations and facies development in the Troll reservoir are discussed. Further, results from the palynological, sedimentological and petrographical studies performed on 15 wells, primarily in the western gas and oil province (see Fig. 1), are presented. Due to extensive coring of the wells all stratigraphical units are well represented, enabling detailed descriptions of the reservoir. It is shown that sediments deposited during sea-level rise as well as sea-level fall are correlatable, mappable units and hence provide a framework for prediction of the lateral extent of associated cementation.

Terminology

The sequence stratigraphical terminology used in this paper is based on the work by Vail *et al.* (1977), Posamentier *et al.* (1988) and Haq *et al.* (1987, 1988). A list of terms used in this paper are summarized on Table 1.

Table 1. *Sequence stratigraphical terminology*

Systems tracts	
TR	Transgressive systems tract
HS	Highstand systems tract
LSW	Lowstand wedge systems tract
LSF	Lowstand fan systems tract
SMW	Shelf margin wedge systems tract
Surfaces	
sb	sequence boundary
mfs	maximum flooding surface
I	Type 1 sequence boundary
II	Type 2 sequence boundary

The time period during which the Sognefjord Formation was deposited correlates with the LZA-3 (lower Zuni A-3) and the LZA-4 (Lower Zuni A-4) supercycles of Haq *et al.* (1987, 1988). Each supercycle is subdivided into third-order or short-term cycles (*sensu* Haq *et al.* 1987, 1988) which are denoted as LZA 3.1, LZA 3.2 etc. The eustatic sea-level curve and corresponding third-order cycles for LZA-3 and LZA-4 supercycles are shown on Fig. 3. On this figure, a dotted line indicates the position of the maximum rate of rise in eustatic sea-level during each of the short-term cycles and corresponds to the expected position of a maximum flooding surface (mfs). A solid line indicates maximum rate of fall in eustatic sea-level and corresponds to the position of a sequence boundary (sb). Vail *et al.* (1977) defined two boundary types. A type I sequence boundary is produced as a result of rapid sea-level falls that are greater than subsidence at the shelf edge and may expose the entire shelf. A Type II

sequence boundary is produced when the rate of sea-level fall is slow and the entire shelf may not be exposed. The position of Type I and Type II sequence boundaries as given by Haq *et al.* (1987, 1988) are shown on Fig. 3. Note that the majority of boundaries for the time period in which the Troll sediments were deposited are Type II.

In this study, transgressive systems tracts (TR) and highstand systems tracts (HS; *sensu* Vail *et al.* 1977) are identified for the Troll area. The TR corresponds to the period of eustatic sea-level rise from a sb to a mfs whereas the HS corresponds to the period of eustatic sea-level fall from a mfs to a sb (indicated on Fig. 3).

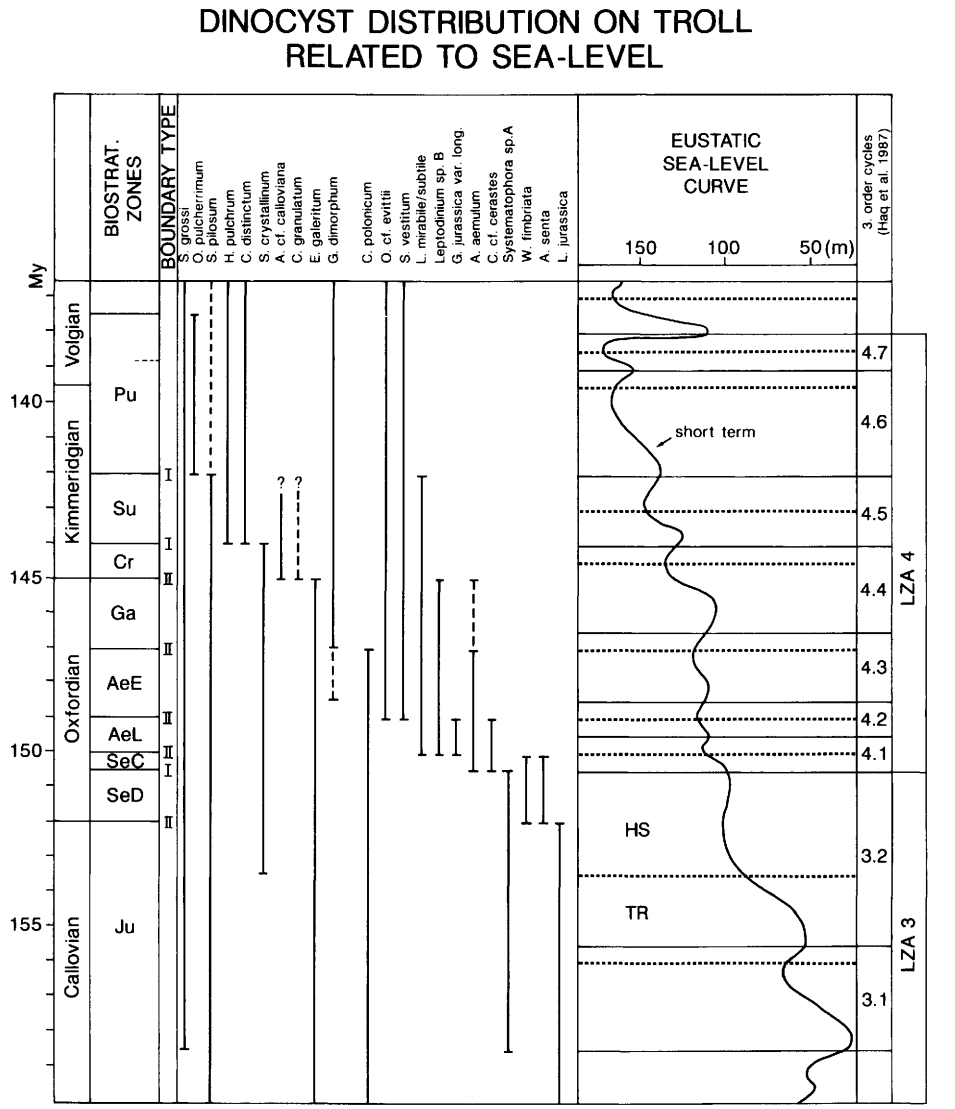

Fig. 3. Distribution of dinocysts on Troll with respect to the eustatic sea-level curve defined by Haq *et al.* (1987). HS indicates a highstand systems tract, TR indicates a transgressive systems tract, dotted lines indicate position of a maximum flooding surface and solid lines indicate position of a sequence boundary.

Fossil occurrences related to sea-level fluctuations

The fossil occurrences as found in the rock column are a result of a counterplay of biological, ecological, sedimentological and geological factors. Several of these factors seem, however, to be related to sea-level fluctuations. There is a marked correspondence between radiation and extinctions of benthic fauna and sea-level changes (Kennedy 1977). During sea-level lows the number of extinctions reach a maximum, while during the sea-level highs adaptive radiation gives an increasing number of taxa. This is thought to be true both on a broad scale e.g. the well-known periods of severe extinctions (Late Permian, Late Jurassic and Late Cretaceous) and at a finer scale, the level of short-term sea-level fluctuations. We have adopted this theory to explain the distribution of dinoflagellate cysts in the late Jurassic.

A distinction between stenotopic and eurytopic organisms can explain why some taxa can be found throughout the stratigraphy while others just can be seen for one or two cycles (Hallam 1987). Examples of long-time existing and probably eurytopic dinoflagellates from the Late Jurassic are *Pareodinia ceratophora*, *Chytroeisphaeridia chytroeides*, *Cleistosphaeridium polytrichum*, *Sirmiodinium grossii* and *Tubotuberella apatela*. Short-time existing and probably stenotypic dinoflagellates are, for example, *Wanaea fimbriata* and *Acanthaulax senta*.

Correlation: Troll stratigraphy–eustatic curve

The correlation between the eustatic sea-level curve of Haq *et al.* (1987, 1988), the Troll biostratigraphical zonation scheme based on the dinocyst occurrences shown on the Haq-curve and the occurrence of the same cysts in the Troll area is discussed in the following sections. In some cases it has been necessary to make indirect correlations by using ammonite zones and general dinocyst range charts to link the Late Jurassic taxa to the eustatic curve. The result is shown on Fig. 3. The biostratigraphical zonation is based on palynological analyses of samples from all 15 cores in addition to sidewall cores.

Lithodinia jurassica Zone (Ju). The lower boundary of the zone is based on the first appearance of *Sirmiodinium grossi* and *Systematophora* sp. A. The latter is a dinocyst much like *Adnato sphaeridium aemulum*, but it lacks trabeculae. The boundary coincides with the sequence boundary between LZA 2.4 and LZA 3.1 in the Haq-curve.

No direct correlation can be made for the top of this zone. The index fossil used on Troll, *Lithodinia jurassica* is not shown in the Haq-curve. The latest occurrence of this dinocyst is generally believed to be within the latest Callovian ammonite zone *lamberti* (Raynaud 1978). By using this as an indirect correlation, the sediments of the upper part of Zone Ju can probably be correlated with LZA 3.2 cycle sediments, except for the uppermost part of the highstand systems tract.

Acanthaulax senta Zone (Se). The base of this zone defined by the first appearance of *Wanaea fimbriata* and *Acanthaulax senta* can be correlated with the first occurrence of *W. fimbriata* in the Haq-curve at 152 Ma which is the base of the Oxfordian. This is one of the better biostratigraphically defined zonal boundaries in the Northern North Sea and regarded as a regional event. This seems to correspond to

the time of deposition of the LZA 3.2 highstand systems tract. At the present we cannot explain why this important floral event does not appear to coincide with any major eustatic event. In the following text it will be treated as caused by the LZA 3.2 maximum flooding, although this is according to Haq *et al.* (1987) 1.5 Ma older.

The top of the zone defined by the highest occurrence of *Acanthaulax senta* and *Wanaea fimbriata* is correlated with the mfs of LZA 4.1 at 150 Ma.

The boundary between the two subzones (SeC and SeD) within the *A. senta* zone (Fig. 3) is based on the first appearance of *Chytroeisphaeridia* cf. *cerastes* and the first abundant occurrences of *Adnatosphaeridium aemulum*. This seems to correlate with the sequence boundary between cycle LZA 3.2 and 4.1. A maximum occurrence of blade shaped organic particles at the zonal boundary supports this interpretation.

Adnatosphaeridium aemulum Zone (Ae). This zone can be divided in two subzones *G. jurassica* var. *longicornis* subzone (AeL) and *Occisucysta* cf. *evittii* subzone (AeE). The base of the zone is defined by the first occurrences of *Gonyaulacysta jurassica* var. *longicornis*, *Lithodinia* sp. B. and the *Leptodinium mirabile/subtile* group. There is no obvious direct correlation level for the base of this subzone since none of the index taxa used here is shown on the Haq-curve. Through indirect correlation, the base is fixed within the *cordatum* ammonite zone which makes a correlation with the mfs of LZA 4.1 at 150 Ma probable.

The top of the lower subzone can be correlated on the basis of the last occurrence of *Chytroeisphaeridia* cf. *cerastes*. The top seems to coincide with the mfs at 149 Ma of cycle LZA 4.2.

The top of the upper subzone and the zone is correlated on the basis of the last appearance of *Compositosphaeridium polonicum*. It coincides with the mfs at 147 Ma of cycle LZA 4.3.

Endoscrinium galeritum Zone (Ga). No direct correlation of the base can be made.

For the top a correlation can be made on the basis of the last occurrence of *Endoscrinium galeritum* which is observed at the top of the Oxfordian by Ioannides (pers. comm. 1987) at 145 Ma. This level does not coincide with the mfs at 144.5 Ma. It is, however, recognized within the whole area of investigation and an allocyclic mechanism is thought to control the event. We interpret this boundary to be at the mfs of cycle LZA 4.4 and believe that the discrepancies are within the uncertainties of the methods used.

Scriniodinium crystallinum Zone (Cr). The base of the zone cannot be correlated to the eustatic curve. The taxa used, *Ambonosphaera* cf. *calloviana* and *Cribroperidinium granulatum*, are not shown on the Haq-curve.

The top of the zone can be correlated by means of the last occurrence of *Scriniodinium crystallinum* seen at 144 Ma in the Haq diagram. This level coincides with the sequence boundary of cycles LZA 4.4/4.5.

Leptodinium subtile Zone (Su). The base of this zone is determined by the first appearance of *Hystrichodinium* cf *pulchrum* and *Cyclonephelium distinctum*. The exact stratigraphical occurrence of these taxa is, however, uncertain. The top of the zone is based on the last occurrence of cysts of the *Leptodinium mirabile/subtile* group. It is not possible to correlate this zone to the Haq-curve by means of

dinocysts. The absence of *S. crystallinum* and the overlying *Oligosphaeridium* sp. A. in the Haq-curve does not, however, give much choice. A correlation to cycle LZA 4.5 is the most probable and the zone is, in this study, bounded by sequence boundaries.

Oligosphaeridium pulcherrimum Zone (Pu). The top and base of this zone are correlated by means of the last occurrence and first appearance of *Oligosphaeridium* sp. A. which is the same taxon as *O. pulcherrimum* (*sensu* Ioannides *et al.* 1976; see also plate 1, fig. 8 in van der Zwaen 1989).

The base is given an age of 142 Ma which coincides with the sequence boundary LZA 4.5/4.6. The top is given an age of 137.5 Ma which falls in between the sequence boundary LZA 4.7/LZB 1.1 and the mfs of LZB 1.1.

Boundary types

The majority of zonal boundaries represent either sequence boundaries or maximum flooding surfaces. The zonal boundaries observed at sequence boundaries are: base Ju, SeD/SeC, Cr/Su and Su/Pu with the remaining zonal boundaries (SeC/AeL, AeL/AeE, AeE/Ga, Ga/Cr) at or close to maximum flooding surfaces (Fig. 3).

This implies that some of the palynozones include sediments from two sedimentary cycles. An important task has been to find other criteria for defining the sequence boundaries in these cases. This will be discussed in the subsequent sections dealing with sedimentological observations.

Effect of sea-level fluctuations on sedimentary facies development within the shoreline-attached to middle shelf zones

In order to evaluate the deposition of the Troll sediments a working model within the sequence stratigraphical time frame was established. This theoretical conceptual model and the predicted facies types associated with the depositional systems tracts are discussed below.

Sea-level fluctuations will have a major influence on the sedimentation pattern within the shallow marine environment (i.e. the inshore, shoreline-attached to outer shelf region). Depositional depths within these environments range from zero along the coast to a maximum of 200 m at the outer edge of the shelf. Slight fluctuations in sea level (up to 20 m), which were characteristic during the Late Jurassic, will have an important influence in the depositional pattern along the inshore and the inner to middle shelf area. Generally the shelf region can be subdivided into the following zones (Tillman *et al.* 1985):

shoreline-attached zone—depth range between 0 and 15 m; dominant processes are tidal currents, wave-induced currents and wave-storm processes;

inner shelf zone—depth range between 15 and 30 m; dominant processes are tidal as well as wave-induced currents and wave-storm processes; most of this zone is located within the fairweather wave base;

middle shelf zone—depth range between 30 and 100 m; dominant processes are storm activities;

outer shelf edge zone—depth range between 100 and 200 m; important processes are storm induced currents.

Variability of magnitude of relative sea-level fluctuations, sediment supply and facies development.

Deposition of the different systems tracts depends on the rate of sea-level changes and on sediment supply (see Posamentier *et al.* 1988). Our interpretation is that the Troll sediments were deposited as part of a tidally-influenced shelf complex. Nio & Yang (1991*a*) showed that different tidal sandbodies can be formed during the different stages of deposition of the systems tracts. The geometric variability of these tidal sandbodies is controlled by the sediment supply and tidal discharge of the depositional system (Fig. 4). Amongst other factors, changes in tidal discharge and sediment supply are related to relative falls and rises of sea-level. A rise in relative sea-level will enhance the effect of tidal wave propagation into the shallower parts of the basin causing an increase in tidal discharge. Conversely, a fall in relative sea-level may strongly reduce tidal action and increase fluvial discharge. Increase and decrease of tidal action depends on the propagation pattern of the tidal wave which is more or less controlled by the basin geometry (e.g. opening to the open ocean) and shelf gradient. Sea-level fluctuations are one of the parameters which may change the extent of the marine basin and shelf gradient. From studies of Holocene and ancient tidally-influenced shallow marine clastic deposits, it can be concluded that a rising sea-level generally produces tidal features in the rock record, while falling sea-level produces more fluvially-influenced sediment successions. Sand disperal into the basin will decrease with a relative rise in sea-level which will cause a flooding of the coastal plain. A large part of the sands will be trapped in the inshore depositional environments and only the fine-grained fraction will be transported basinward.

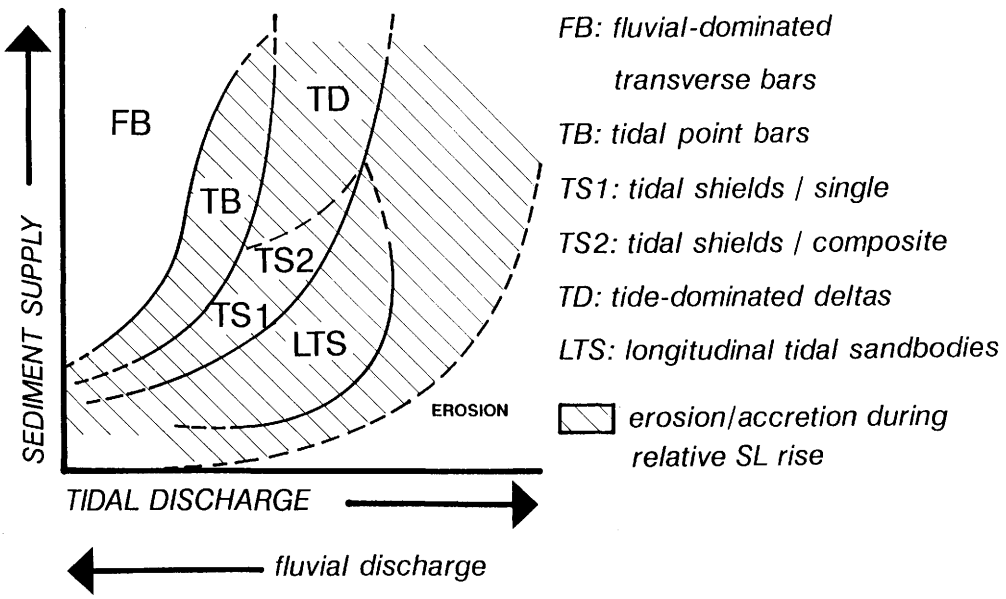

Fig. 4. The geometric variability of large-scale tidal sandbodies as related to the sediment supply and the tidal discharge of the depositional system (after Nio & Yang 1991).

The geometry of tidal sandbodies respond sensitively to the nature of the tidal wave and, therefore, may be closely related to relative sea-level changes. For example, the transition from fluvially-dominated transverse sand bars (FB in Fig. 4) into tidal point-bar complexes (TB in Fig. 4) is characterized by a change from low-sinuosity, high-gradient fluvially-dominated channels with high influxes of coarse sediments into high-sinuosity, low-gradient estuarine channels. This change is controlled by a rise of the base level which reduces the slope gradient and at the same time increases the tidal action.

From studies of modern estuarine systems (Nio & Yang 1989) it is shown that during a later stage of the transgressive systems tract (TR; *sensu* Vail *et al.* 1977) an increase in erosion within the inshore estuarine complex will occur. This results in a higher sediment influx into the offshore part of the shelf and the formation of a prograding ebb-tidal delta. A constant high sediment supply will produce an offlap pattern of the different ebb-tidal delta lobes upon the shelf. Nio & Yang (1991*a*) also showed the occurrence of the different tidal sandbodies within a sequence stratigraphical framework.

The period during which the Troll sediments were deposited was characterized by relatively mild eustatic sea-level falls, producing Type II sequence boundaries (*sensu* Vail *et al.* 1977; see Fig. 3). Figure 5 shows a cross-section across the shelf with the occurrence of various tidal sandbodies within a sequence stratigraphical framework. During the late stage of a shelf margin wedge (SMW) systems tract overlying a Type II sequence boundary (*sensu* Vail *et al.* 1977), the gradual increase in the rate of relative sea-level rise will cause an increase of the tidal discharge, resulting in increasing tidal reworking of the delta deposits belonging to the SMW or HS (highstand, *sensu* Vail *et al.* 1977) systems tract. The fluvial channels and adjacent floodplain system will be flooded and modified into an estuarine and tidal flat system (a in Fig. 5).

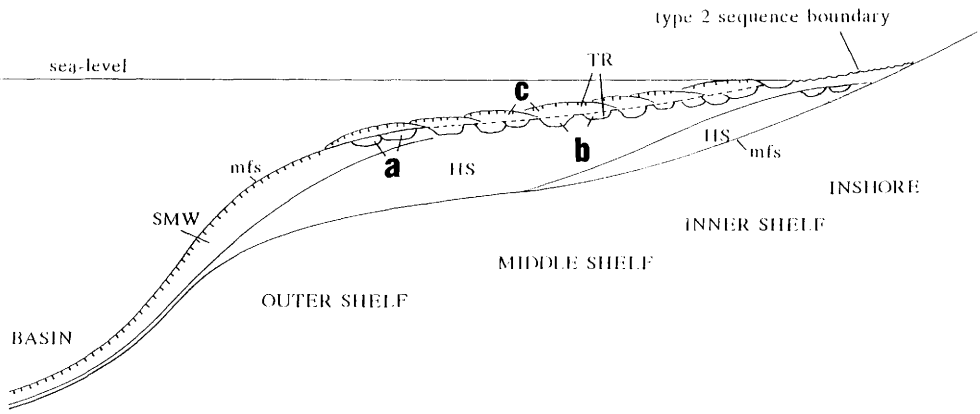

Fig. 5. A section across the shelf, showing Type II sequence boundary, lying on top of the highstand systems tract (HS), and overlain by the shelf margin wedge systems tract (SMW) and transgressive systems tract (TR). Definitions of systems tracts and type II sequence boundary follow Vail *et al.* (1977). The maximum flooding surface (mfs) is characterized by a condensed sequence. a, Estuarine and tidal flat facies during the late stage of a SMW systems tract; b, tidal point-bar facies during a TR systems tract; c, tidal delta facies or tidal sand ridge facies during a TR systems tract.

During the deposition of the TR systems tract a rapid rise in relative sea level causes a significant increase in tidal discharge. Different tidal sandbodies are formed depending on sediment supply and local palaeogeographical setting. Extensive high-sinuosity, low-gradient estuarine systems are formed (b in Fig. 5). Note the onlapping pattern of the different estuarine systems shown on Fig. 5. At a later stage of the TR systems tract an offlapping ebb-tidal delta system will be formed (c in Fig. 5). The TR systems tract is concluded with the deposition of a condensed sequence or a submarine hardground which may produce a calcium carbonate layer during the maximum flooding period (see Fig. 5).

These principles can be applied in the prediction of the different types of tidal sandbodies in a basin model. Although the rate of eustatic sea-level change can be assumed constant across the shelf, the rate of basin subsidence generally is not, and usually increases from zero at the tectonic hinge line to a maximum subsidence rate at the basin centre (Posamentier *et al.* 1988). The actual timing of the development of each systems tract and the formation of various tidal sandbodies at a specific location varies across the shelf with increasing subsidence rate, and thus with increasing rate of relative sea-level change.

Figures 6 and 7 show two synthetic sections from the inshore–shoreline attached region and the inner to middle shelf region. The inshore–shoreline attached region is the most proximal location showing a low subsidence rate. Therefore, this region is characterized by a long period of erosion during the SMW systems tract, or a long period of fluvial channel entrenchment during a LSW systems tract stage (see Fig. 6). The TR systems tract begins at a much later period in this region and is characterized by the infilling of fluvial channels (A in Fig. 6), followed by a tidal reworking and the formation of estuarine systems (C in Fig. 6). At a later stage of TR systems tract ebb-tidal deltas (D in Fig. 6) are formed followed by the maximum flooding period. The subsequent HS systems tract is characterized by fine-grained sedimentation consisting of distal shelf mud or storm layer (E in Fig. 6). At a later stage of the HS (highstand, *sensu* Vail *et al.* 1977) systems tract coarsening-upward sequences of prograding systems occur (B in Fig. 6).

In the inner–middle shelf region the synthetic section shows a higher subsidence rate which causes a significant change in the periods of deposition of the systems tract and different sedimentary facies (Fig. 7).

Depositional model, facies development and reservoir geometry on the Troll Field

Based on the theoretical conceptual model, a set of criteria to identify maximum flooding surfaces and sequence boundaries was established. These are strongly connected with the recognition of the depositional sequences and facies comprising the deposits within a cycle. Hence, the criteria used to identify maximum flooding surfaces and sequence boundaries are the main features used to identify the depositional sequences.

Three environmental provinces on Troll Field were defined by Hellem *et al.* (1986): a northwestern, a central and an east-southeastern province, all of which maintained distinct characteristics during most of the time of deposition. The central province represents the most proximal offshore part characterized by prograding ebb-tidal lobes. It separates the open marine shelf areas of the northwestern province from the

sheltered, enclosed, partly inshore, tidally dominated province to the east and southeast.

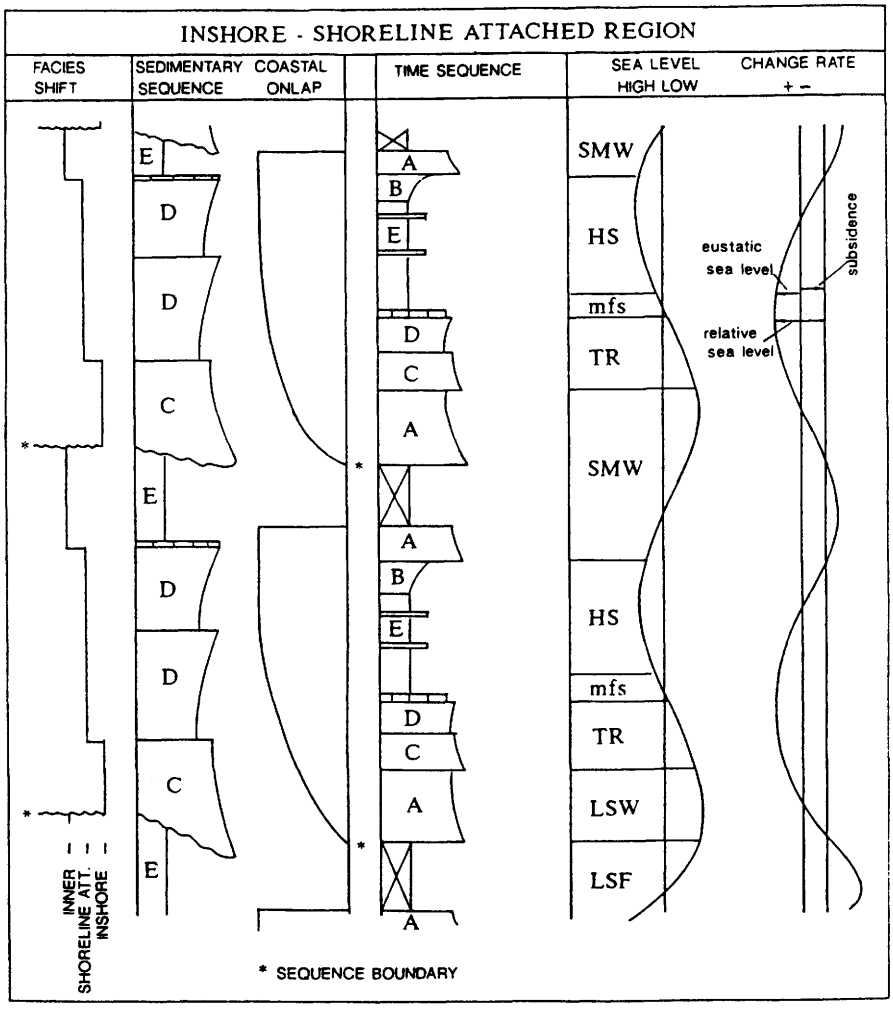

Fig. 6. Synthetic stratigraphical section from the inshore–shoreline-attached region. Right side of the figure shows systems tracts in relation to relative sea-level. Time sequence refers to 'ideal' facies successions relative to sea-level, whereas sedimentary sequence shows the facies successions which should be preserved in the sedimentary record according to the theoretical model. Facies types are: A, alluvial–fluvial facies; B, coarsening-upward sequence of prograding delta systems; C, estuarine facies; D, ebb-tidal delta systems; E, distal shelf muds with storm layers.

Hellem *et al.* (1986) showed that the Troll Field reservoir consists of several genetically related lithofacies which could be combined into five major facies successions, represented by the following main depositional environments:

(1) low-energy marine
(2) moderate-energy marine

(3) high-energy marine
(4) tide-influenced marine
(5) storm deposits.

These five facies successions can be organized into facies types resembling the facies types B, C, D, E, and F as outlined in Figs 6 and 7. Table 2 illustrates the relationship between these facies successions, the facies types and the depositional systems tracts.

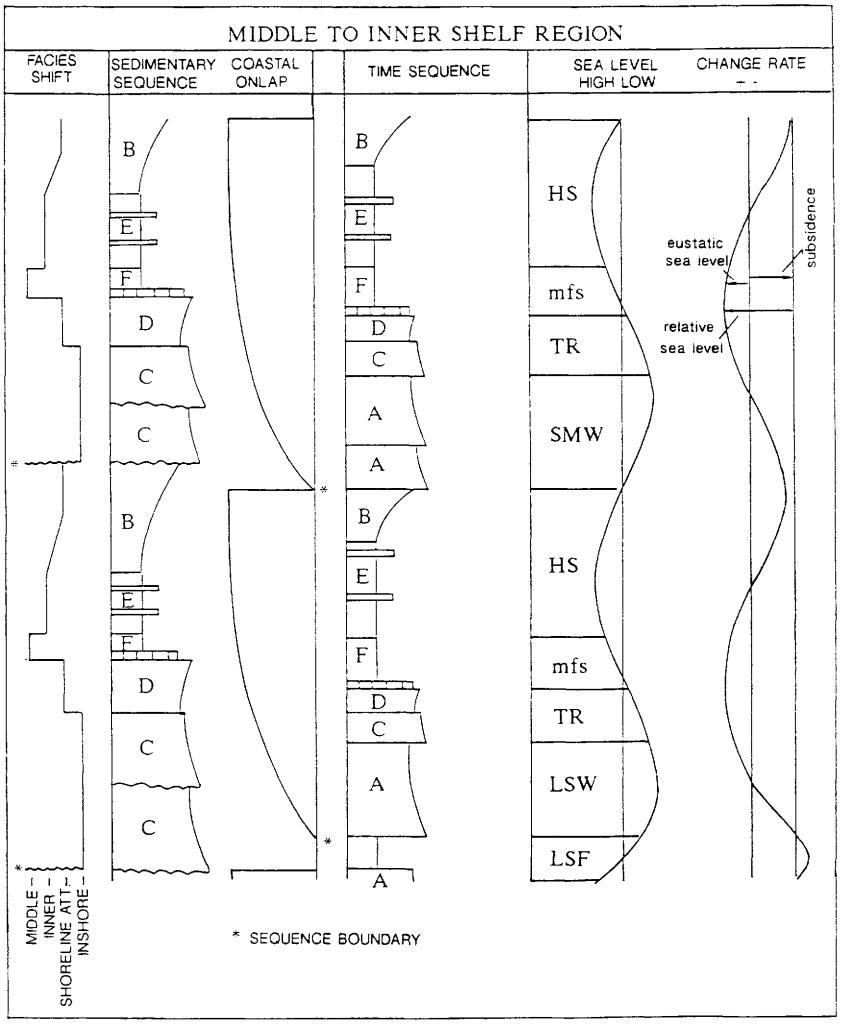

Fig. 7. Synthetic stratigraphical cross-section from the inner to middle shelf region (see Fig. 6 for explanation).

Criteria used in identifying the facies types

Facies type A should, as defined, include typical fluvial deposits; however, such deposits have not been observed within the cored sections of the Troll Field reservoir.

This indicates that subsidence at the time was not sufficient for fluvial deposits to escape transgressive erosion.

Facies type B should show a coarsening-upwards trend from lower to upper shoreface deposits, and on Troll this occurs as a succession of types 2 to 3 with intercalations of 5 (as defined above). The lack of tidally-dominated, channellized units within the succession is the major criterion used to discriminate it from ebb-tidal delta deposits (facies type D in Figs 6 and 7).

Table 2. *Relationship between facies types, facies successions and depositional systems tracts*

Deposition systems tracts	Facies types	Facies successions
HS	B	2, 3 and 5
TR	C	3 and 4
TR	D	2, 3 and 4
HS	E	5
HS	F	1

A, fluvial deposits; B, coarsening-upwards sequence of prograding delta systems; C, estuarine deposits; D, ebb-tidal deltas; E, distal shelf mud with storm layers; F, very fine-grained sediment, deposited below storm wave base.
1, low-energy marine; 2, moderate-energy marine; 3, high-energy marine; 4, tide-influenced marine; 5, storm deposits.

The preservation potential of these facies associations depends mainly on the interaction between subsidence and net sea-level rise during a cycle. Generally the upper shoreface deposits are less likely to be preserved due both to the falling sea level and the tidal erosion during the early phase of the subsequent sea-level rise. In micro-tidal areas a more complete upper shoreface deposit should be preserved and capped by a thin reworked and condensed unit as a result of shoreface retreat during sea-level rise. In this situation F or E facies types (very fine grained sandstones/distal shelf muds) would then directly overlie facies type B.

Facies type C, estuarine channel deposits (Fig. 8a), is mainly identified by the single criterion of bundle sequences and double mud drapes (Nio *et al.* 1981; Nio & Yang 1991*b*). Complete sequences should show fining-upward trends with fine-grained restricted marine sediments on top. In the Troll Field reservoir this appears as type 4 in association with type 3. The preservation potential of the upper units of this facies type is as expected very low and not seen in the Troll West cores. Also the estuarine channel deposits may have a low preservation potential offshore to the final shoreline during a sea level rise. B and E facies types are therefore observed to be erosively overlain by D sequences in the offshore areas, as seen in well 31/2-3 (Fig. 9).

On logs alone, the coarsening-upward sequences of an ebb-tidal delta complex, *facies type D*, is impossible to discriminate from facies type B. In cores, these sequences show intercalations of tidally-dominated channel deposits (type 4) together with wave-reworked shoals—tidal shields or ebb-tidal bars—(types 2 and 3). One example from this facies type is shown in Fig. 8b which is a wave dominated interval with storm laminations. Sedimentologically, the finer-grained lower part is not expected to be different from the lower shoreface deposits of the B sequences.

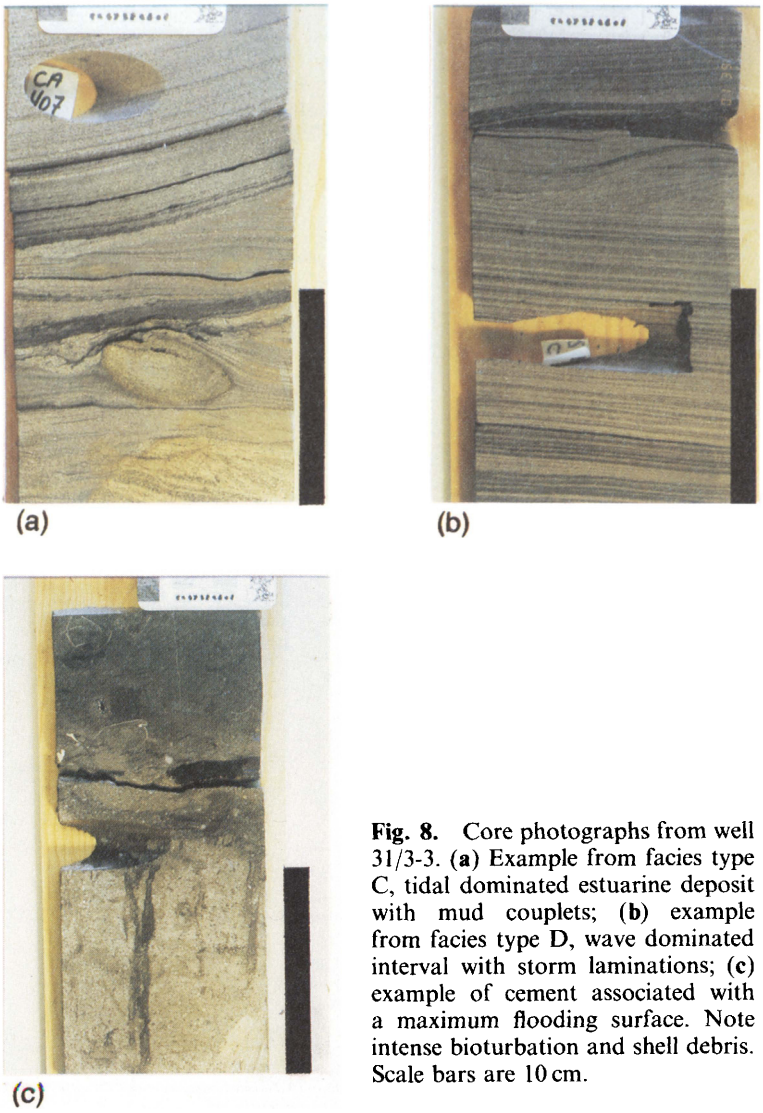

Fig. 8. Core photographs from well 31/3-3. (**a**) Example from facies type C, tidal dominated estuarine deposit with mud couplets; (**b**) example from facies type D, wave dominated interval with storm laminations; (**c**) example of cement associated with a maximum flooding surface. Note intense bioturbation and shell debris. Scale bars are 10 cm.

Facies type E represents the transition between middle to inner shelf or lower shoreface and consists of distal storm layers (type 5) indicating the initiation of shoreline progradation as the sea level starts to fall. The storm deposits might be suspension fall-out showing no indications of direct wave or current transport. The transition from F to E facies can be difficult to identify in cores.

Ideally *facies type F* consists of very fine-grained sediments (type 1) deposited below storm wave base during maximum flooding. The duration of low or 'zero' sedimentation increases basinwards and hence the character of the F sediments should vary laterally. The deposition of fines could be balanced by wave or current interaction and, therefore, non-depositional conditions are likely to prevail in areas above storm wave base. Hence, dependent on the duration, carbonate cementation of

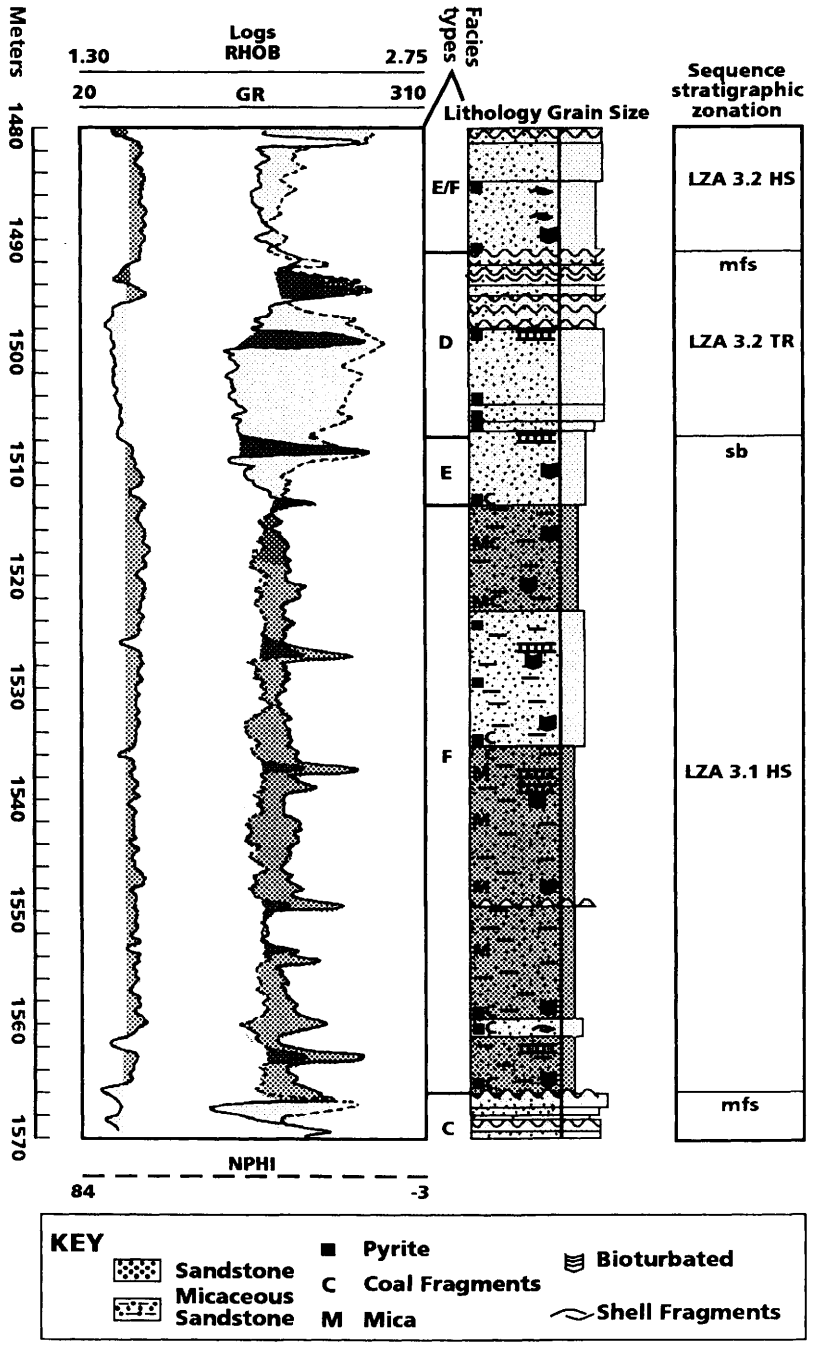

Fig. 9. Example of inner shelf sequence architecture as observed in well 31/2-3, Troll Field.

the top of an ebb-tidal delta lobe (D facies) or shoreface deposits (B facies) would represent the F equivalent in these areas. Thicker, but condensed, fine grained deposits would be expected basinwards or in more protected nearshore areas. At

least in the more distal areas facies type F could contain more than one carbonate cemented horizon (Fig. 8c) correlatable to one single horizon in the proximal areas due to autocyclic variations within the distributary system landwards.

Sequence boundaries

A sequence boundary should be identified by an abrupt change from facies types F, E (very fine-grained sediments/distal shelf muds) and/or B (prograding delta systems) to facies types C or D (estuarine/ebb-tidal delta deposits; see also Figs 6 and 7). Ideal successions following the theoretical patterns are exceptions rather than the rule, but examples of patterns close to the ideal can be demonstrated in well 31/2-6 (Fig. 10). Here the LZA 4.1 transgressive tract follows the predicted succession of C and D facies types, except that the D is rather thin. The maximum flooding surface lacks cementation which could also be expected in a proximal shoreline attached position. The following coarsening-upward sequence (not shown on Fig. 10) is seen as a typical B facies type, while the sequence boundary which is the base of a D sequence, belongs to the LZA 4.3 cycle indicating that the LZA 4.2 cycle is missing. This sequence boundary is carbonate cemented, a feature which is not a surprise considering the hiatus represented by the missing deposits of the LZA 4.2 cycle. In fact, more than 60% of the sequence boundaries recognized within the studied wells are carbonate cemented, and where petrographically analysed, they often indicate near-surface cementation (see following discussion on petrographical observations).

In most wells the sequence boundaries identified in this study lack facies type C. This is in contrast to the predicted successions on Figs 6 and 7. This is due to the dominant offshore position of Troll during time of deposition and thus the low preservation potential of the facies type C as discussed above.

In more distal positions severe erosion can be identified which at first might be mistaken for storm layers, and which seems to be overlain by similar sediments as those below. This is the case for the LZA 4.1 sequence boundary in wells in the westernmost part of the Troll Field, where the proof of sequence boundary is based on palynology, the appearance of fossils characteristic for palynozone SeC (see Fig. 3) or a major inertinite peak as indicated from palynological studies. The fine-grained sediments above are therefore the distal parts of an ebb-tidal delta and not the lower shoreface of a prograding coastline or fluvial delta. As mentioned previously, the lower parts of facies type B (prograding delta systems) and facies type D (ebb-tidal delta deposits) can only be discriminated from each other on purely sedimentological evidence.

Further basinwards, sequence boundaries can be very hard to identify. The reason for this is that sequence boundaries and maximum flooding surfaces are likely to amalgamate. This can be seen in most wells within the LZA 3 supercycle and oldest parts of the LZA 4 supercycle. The amalgamation of sequence boundaries and maximum flooding surfaces is caused by the entrapment of clastic sediments in the coastal plains during a rise of sea-level. Consequently, this will initiate a long period of low or non-deposition giving optimum conditions for condensation and carbonate cementation. Therefore it is highly probable that in distal areas, where amalgamation of maximum flooding surfaces and sequence boundaries is likely, carbonate cementation will develop. Consequently, in cases where only sidewall cores and logs are available the mfs/sbs are defined at the closest carbonate cemented horizon.

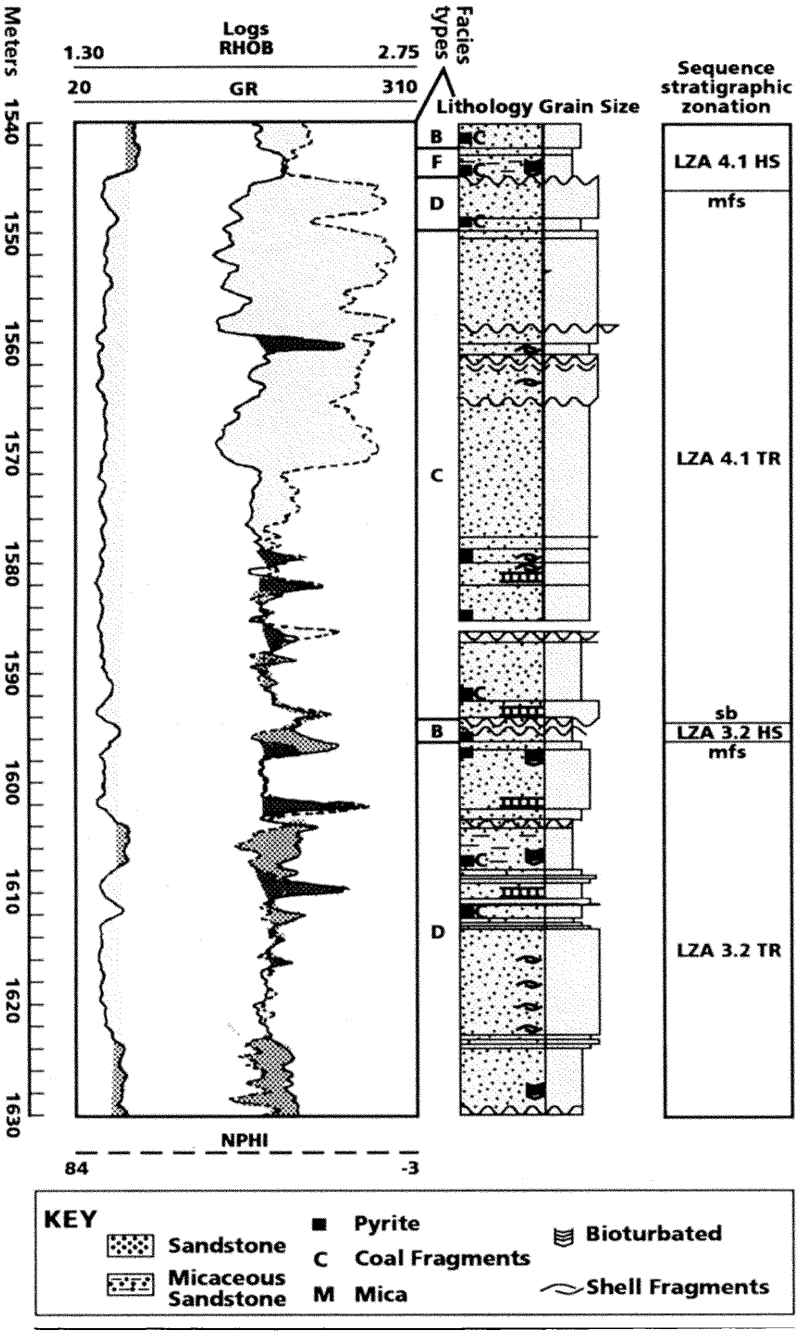

Fig. 10. Example of inner shelf sequence architecture as observed in well 31/2-6, Troll Field.

Maximum flooding surfaces

An example of cementation at a maximum flooding surfaces is shown in Fig. 8c. Maximum flooding surfaces are mainly identified by the combination of sedimento-

logical and palynological evidence. Fine-grained sediments similar to F sequences are ubiquitous and the actual F facies type are distinguished by palynological evidence. However, in the absence of palynological data, sedimentological indications and/or log interpretations have been used to establish or reject the presence of maximum flooding surfaces.

Sequence stratigraphical framework and carbonate cementation

The predicted succession and variability of sequences and facies types outlined by the theoretical model can be recognized in all wells. With the help of the stratigraphical framework the presence or absence of sequence boundaries, transgressive systems tracts, maximum flooding surfaces, and highstand systems tracts in each cycle has been defined in each well. A single depositional cycle typically comprises the transgressional and progradational components described by Beecham (pers. comm.). Here the start of a cycle is defined at a sequence boundary with the transgressional component of clean, coarse-grained sandstones reworked from coastal sediments by high-energy currents associated with an increase in transgressive activity. These sandstones comprise the transgressional systems tract. The progradational component includes the low-energy, frequently offshore, fine-grained micaceous sediments which comprise the highstand systems tracts.

All carbonate cemented horizons in the 15 wells have been detected and their thickness measured either directly from cores or indirectly by logs, mainly the microresistivity log or the density/neutron porosity logs. A simple calculation shows that 70–75% of the observed maximum flooding surfaces and 60–65% of the sequence boundaries are carbonate cemented. The lack of carbonate cement of 25–30% of the maximum flooding surfaces can be ascribed to several factors:

the mfs is erroneously detected;

the time or conditions for development of early cementation have been unfavourable;

later dissolution of carbonate has taken place

The occurrence of carbonate cement at sequence boundaries is no surprise, but the frequency of such cementation should initiate further study of this feature.

The maximum flooding surfaces and sequence boundaries have been correlated along several profiles across the field. Several of the carbonate cemented mfs and sb can be correlated between neighbouring wells, and some of them can even be traced into the eastern gas province around well 31/3-3 giving them possible fieldwide significance. As shown on Fig 11a and b carbonate cementation of both mfs and sb occurs in several wells which together delineate a distinct area and therefore their possible lateral extent.

A statistical analysis of carbonate cemented horizons in the reservoir units, other than those associated with mfs or sb sediments, shows trends that cannot be ascribed to any single factor. Generally, cemented horizons are more frequent in transgressive systems tracts than in the highstand systems tracts.

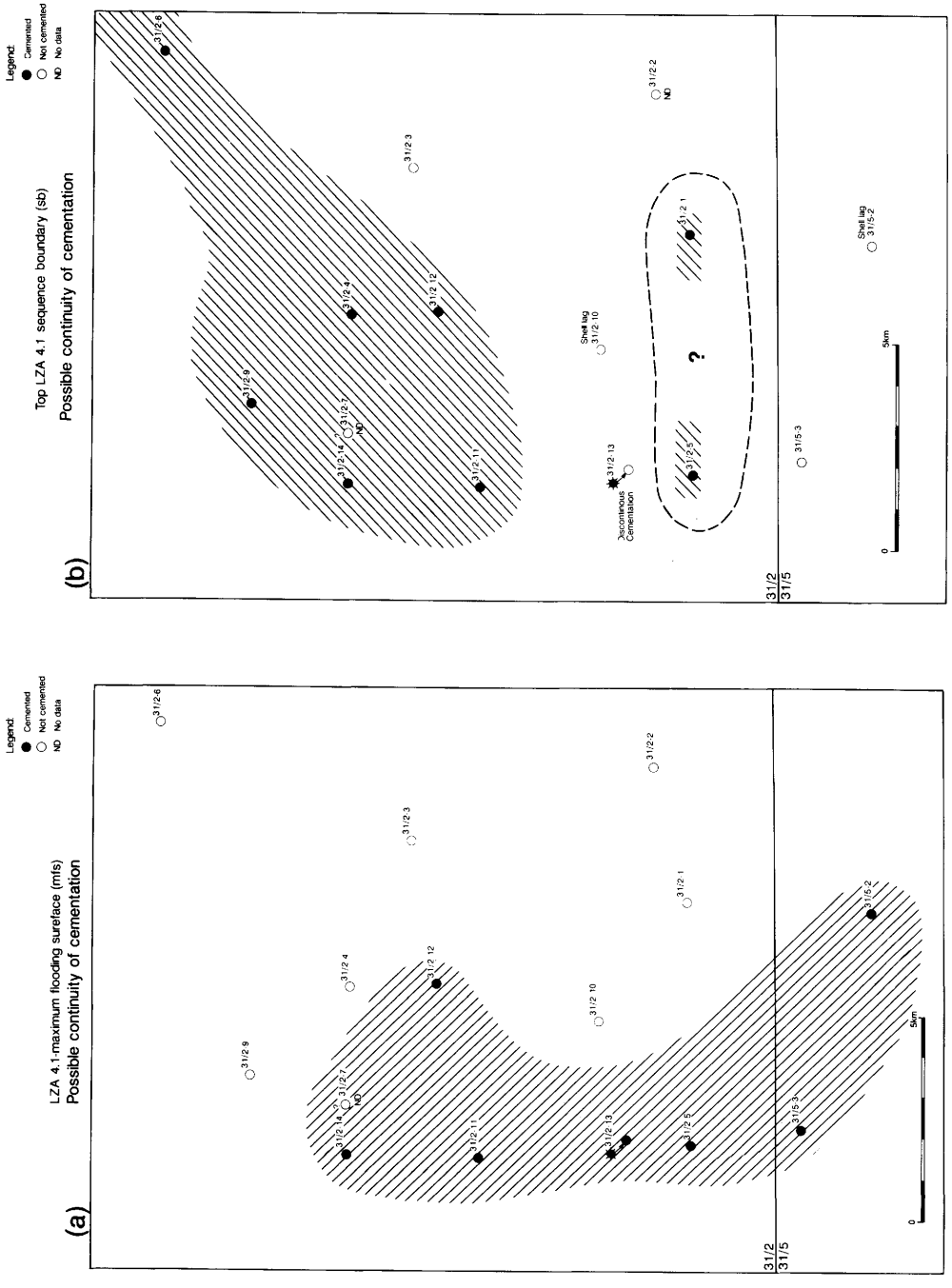

Fig. 11. Distribution and possible continuity of cementation (**a**) at a maximum flooding surface (LZA 4.1) and (**b**) at a sequence boundary (top of LZA 4.1).

The thickness distribution and relative proportion of thickness of the cycles demonstrate that sea-level fluctuations controlled the facies development through most of the Troll reservoir. However, minor synsedimentary tectonics, mostly as differential subsidence, did influence, to some degree, thickness distribution during deposition. This is discussed in the next section.

Sequence stratigraphical cross-sections through the Central Troll Field

A synthetic sequence stratigraphical cross-section through the Central Troll Field is shown in Fig. 12. The basinal location of the Central Troll Field is at A in this figure. The datum line for this cross-section is set at the top of the Fensfjord Formation which represents the minimum sea-level of the LZA 3.1 cycle. This is also the boundary between the supercycles LZA 3 and LZA 2, which according to Haq *et al.* (1987, 1988) represents a major event of building out low-stand fans, leaving no coastal onlap. Hence, this was a situation where large shelf areas were eroded and sediments were brought into deeper parts of the basin. The top of the Fensfjord Formation therefore occurs as an erosional surface directly overlain by a condensed maximum flooding sequence followed by a highstand systems tract belonging to the LZA 3.1 cycle. Logs and core description of this section are shown on Fig. 9. The LZA 3.1 highstand systems tract comprises the informal lithostratigraphical unit, the Heather Formation unit B (Mid. Heather Formation on Fig. 2). As seen in Fig. 3, the period during which the Troll sediments were deposited was characterized by a general eustatic sea-level rise of more than 100 m. The third-order eustatic sea-level fluctuations during this period (see Fig. 3), however, were less than 50 m and in most cases only about 20 m with the exception of the dramatic sea-level fall at the end of the LZA 4.7 cycle. Figure 12 was constructed by digitizing the eustatic sea-level curve and then calculating the relative rates of eustatic sea-level changes. The calculated rates of eustatic sea-level fall are rather minor, usually less than 15 m/Ma. The major exception is the boundary between LZA 4.7 and the overlying LZB 1.1 cycle which is characterized by a very high rate of eustatic sea-level fall.

The subsidence rate at Troll has been estimated from the thickness of the depositional sequences using well data. The effects of palaeo-water depth, eustatic sea-level changes and hydroisostasy have been corrected. The average minimum subsidence rate in the Troll western provinces is 4 m/Ma. A higher subsidence rate is assumed for the shelf margin.

The cross-section in Fig. 13 is a detail of position A in Fig 12. The section cuts through the western provinces of Troll and shows the thickness variations in the TR and HS systems tracts as seen in the wells. The datum line for this cross-section is the same as for Fig. 12.

Together these cross-sections show several interesting features.

(1) In Fig. 12 most sequence boundaries are Type IIs, as defined by Vail *et al.* (1977), and result from small rates of eustatic sea-level fall, which were less than the subsidence rates at the shelf margin. The rapid eustatic sea-level fall at the end of the LZA 4.7 cycle, however, produced a Type I sequence boundary, which is characterized by a severe truncation of the LZA 4.7 and LZA 4.6 sequences and the development of the LZA 1.1 lowstand systems tract. Comparison of Figs 12 and 13 shows that this predicted truncation is recognized in the wells.

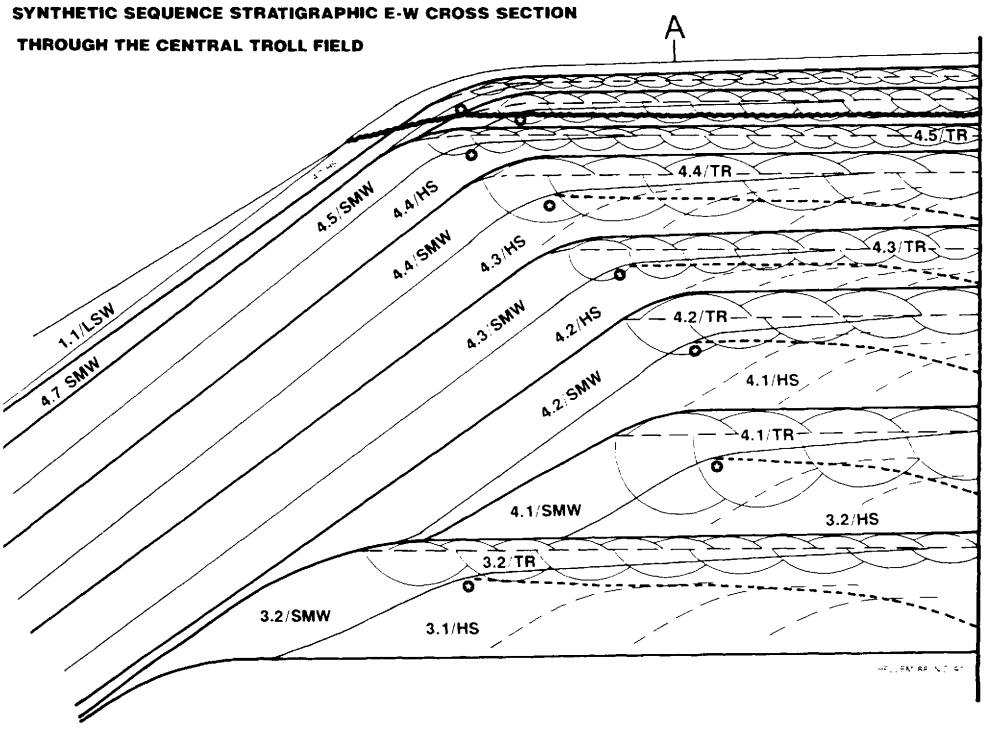

Fig. 12. Synthetic sequence stratigraphical E–W cross-section. 'A' marks position of the Central Troll Field. See text for explanation.

(2) The position of the Troll Field (inner to middle shelf region) dictates that the sequences observed only consist of highstand and transgressive systems tracts. No shelf margin wedge systems tract can be observed at the Troll Field. The position of the equilibrium point (*sensu* Posamentier *et al.* 1988) at the sequence boundaries (asterisks in Fig. 12) shows a consistent basinward migration in time. This indicates a basinward progradation of the systems tracts.

(3) The preservation of the Troll reservoir was controlled by the development of accommodation space which depended on the eustatic sea-level rise and the basin subsidence. The net eustatic sea-level rise during the LZA-3 and LZA-4 supercycles was more than 100 m and the subsidence was about 80 m during the same period. Both factors contributed to the relative sea-level rise and the accommodation development. This also accounts for the thicknesses of the individual TR and HS systems tracts seen in the synthetic cross-section (Fig. 12) as well as the cross-section based on well data (Fig. 13).

For example, cycles LZA 3.1 and 3.2 together induced a large net sea-level rise within the LZA 3 supercycle which left a large accommodation potential on the shelf, and thick sequences could develop. In addition, during cycles LZA 4.1 to 4.3 no net rise in eustatic sea-level is achieved (see Fig. 3). This left very thin or no sequences in the areas where the accommodation potential of the former cycles had already been filled up, and a major basinward progradation of the system took place.

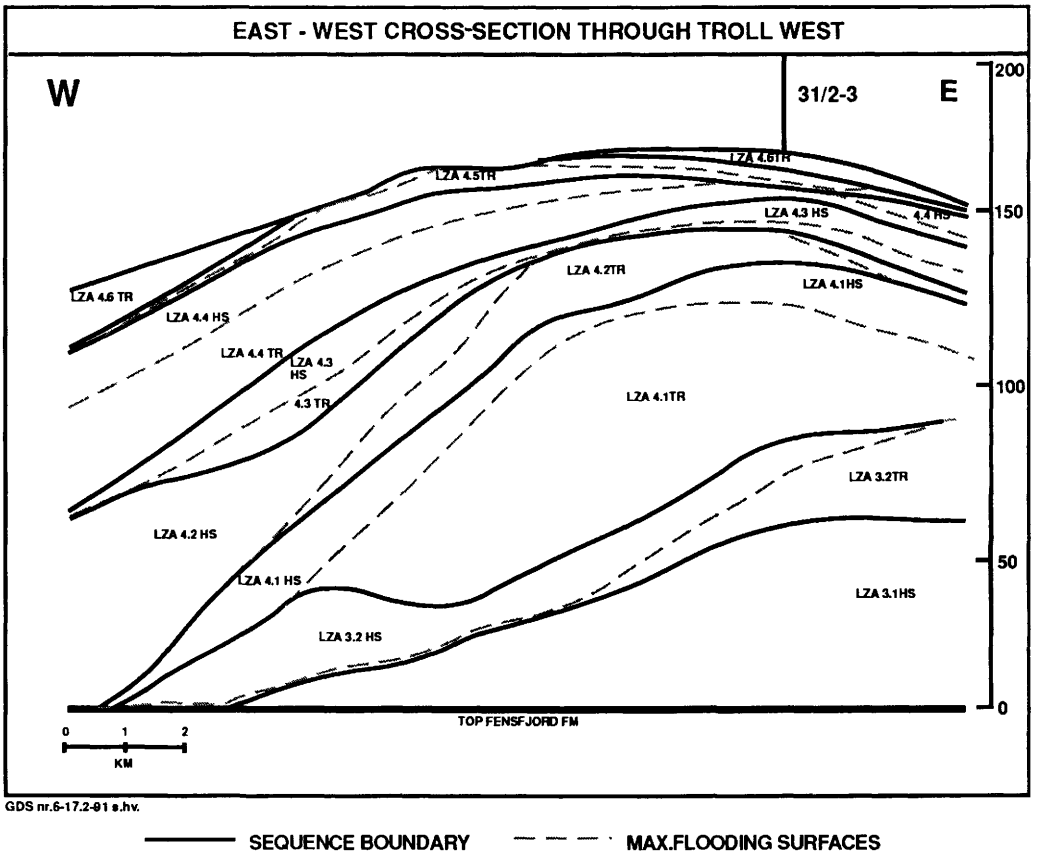

Fig. 13. E–W cross-section through the western oil and gas provinces in Troll showing depositional sequences. See text for explanation.

(4) The cross-section in Fig. 13 also indicates the preservation potential of the maximum flooding surfaces (mfs). In the distal basinward position, less erosion of the HS systems tracts has occurred due to the available accommodation space and the mfs is preserved. However, in proximal positions the HS is thin or eroded and there is a higher potential for erosion of cements. Mapping of the cementation at sb and mfs concurs with this observation.

Petrography of carbonate cements

This section discusses the petrographical observations that suggest cementation of some of the Troll calcite-cemented horizons took place under near-surface conditions (within 1 m of the sediment–sea water interface). These observations show that near-surface cementation is, as predicted by the theoretical model, associated with maximum flooding surfaces. However, some textural similarities exist between cemented horizons associated with sediments other than mfs (e.g. sequence boundaries). Consequently, unlike the palynological and sedimentological models, defini-

tive criteria for identification of a maximum flooding surface using petrography alone could not be established.

The sandstones of the Sognefjord Formation in the Troll Field are generally unconsolidated, texturally immature, subarkosic to lithic arenites. Petrographical classification of the sandstones reflects the sedimentological variation in the reservoir i.e. fine-grained micaceous sandstones (lithic arenites) to mineralogically mature, coarse-grained sandstones (subarkosic arenites). Previous petrographical studies of the calcite cemented horizons in the Troll Field by Irwin & Hurst (1983) and Kantorowicz *et al.* (1987) describe a relatively complex cement stratigraphy.

Calcite-cemented horizons observed in the cored intervals were subdivided into four 'macro-types' dependent upon their sedimentological context (Table 3). Each cemented horizon was thus classified according to its relationship to the overall stratigraphical and facies association. The sampling strategy for petrographical study of the cements was based on these four 'macro-types'. A total of 180 polished thin-sections from selected horizons in all wells included in the present study have been described qualitatively. All four macro-types are represented in the sample set.

Cathodoluminescence observations indicate that the cements composed of pure calcite (identified by its characteristic pink stain with potassium ferricyanide), exhibit brown, orange, and yellow–orange luminescence, whereas the subordinate, slightly ferroan to ferroan calcite (blue–purple stained) luminesce dull orange to red. A general luminescence stratigraphy for the samples, starting with the earliest cements, is: brown, yellow and yellow–orange, orange, dull orange to red. This cement stratigraphy concurs with observations of Kantorowicz *et. al.* (1987).

A single cemented horizon can contain several generations of cement. Earlier cement generations, which are 'pure' calcite, are frequently observed within the central portion of a horizon and later generations, slightly ferroan to ferroan cements, towards the outer edges. This is interpreted as reflecting the growth of a horizon outwards as successive cements nucleate. Horizons classified as macro-types I to III (see discussion below) show this feature in particular, whereas for horizons classified as macro-type IV slightly ferroan to ferroan cements dominate throughout.

Isotopic analyses ($\delta^{18}O$, $\delta^{13}C$) have been carried out on some selected samples. It is also possible, in some cases to relate isotopic compositions reported in previous studies (Irwin & Hurst 1983; Kantorowicz *et al.* 1987) to samples examined in this study.

Relationships between macro-types, sequence stratigraphy and cement textures

The petrographical characteristics for each 'macro-type' are summarized on Table 3.

Macro-type I. Examples of textures exhibited in this group are shown in Fig. 14a and b. By definition, cemented horizons falling into this category are associated with maximum flooding surfaces. However, petrographical textures associated with macro-type I are not exclusively associated with cements at maximum flooding surfaces. Some of the textural features described below for macro-type I are also observed in cements from sequence boundaries as well as in macro-types II and III.

Textural features given for macro-type I in Table 3 are interpreted as indicative of cementation at or near the sediment–water interface. Descriptions of cement textures associated with near-surface cementation in so-called 'clastic hardgrounds' presented

for the Roda sandstone (Molenaar *et al.* 1988) and the Bridport sands (Bryant *et al.* 1988) indicate additional criteria such as the introduction of a carbonate matrix into sediments through burrowing and/or matrix infiltration and boring/micritization of bioclasts as a result of algal colonization. Neither of these criteria is dominant in the cements at Troll; however, the microsparry pore filling calcite could have formed by recrystallization of an earlier micrite or carbonate matrix.

Table 3. *Carbonate horizons: classification and petrographical description*

		Micro-scale	
Type	Macro-scale	Clastic composition	Cement textures
I	Occur at mfs: ideally situated on top of facies Type D or within facies Type F Generally intensively bioturbated Fractures with infill of overlying sediments	Very fine to fine/medium grain size Very well to moderately sorted Mica (>10%); bioclastic fragments (5–10%); organic material (5–10%); matrix-clay/silt/carbonate (1–5%) Glauconite or chamosite occasionally observed	Rim and fringe calcite Microsparry to mosaic pore filling calcite Floating grain textures (minus cement porosity up to 40%) Displacive prismatic calcite in micas Brecciated textures Fracturing of clastic grains Absence of feldspar overgrowths
II	Associated with autocyclic abandonment surfaces (i.e. channel abandonment) Macroscopically identical to type I	As for type I except for glauconite/chamosite	As for type I but lack brecciated cement textures and fracturing of clastic grains
III	Variegated layers or nodules containing shells or shell fragments (Coquinas); Typically associated with storm deposits	High content bioclastic fragments and shells (>50%) Poorly sorted	Mosaic to blocky calcite Fringe cements occurring as polygonal calcite around bioclastic fragment Blocky calcite replaces disolved bioclastic components Can exhibit textures given for Type I
IV	Variegated layers or nodules with no apparent association to particular facies Generally formed during later stage of cementation following significant burial	Full spectrum of sandstone compositions seen at Troll i.e. subarkosic to lithic arenites	Well developed feldspar overgrowths Vermicular kaolinite enclosed by cement Tangential grain contacts Blocky to poikilotopic slightly ferroan to ferroan calcite

The absence of feldspar overgrowths in the macro-type I cements is significant. Although overgrowths on feldspar can occur at any time during the diagenetic history of a sediment, the absence of feldspar overgrowths in macro-type I cements indicates that diagenetic alteration of the clastic grains on Troll has been minimal prior to cementation. Thus, cementation must have occurred very early in the diagenetic history.

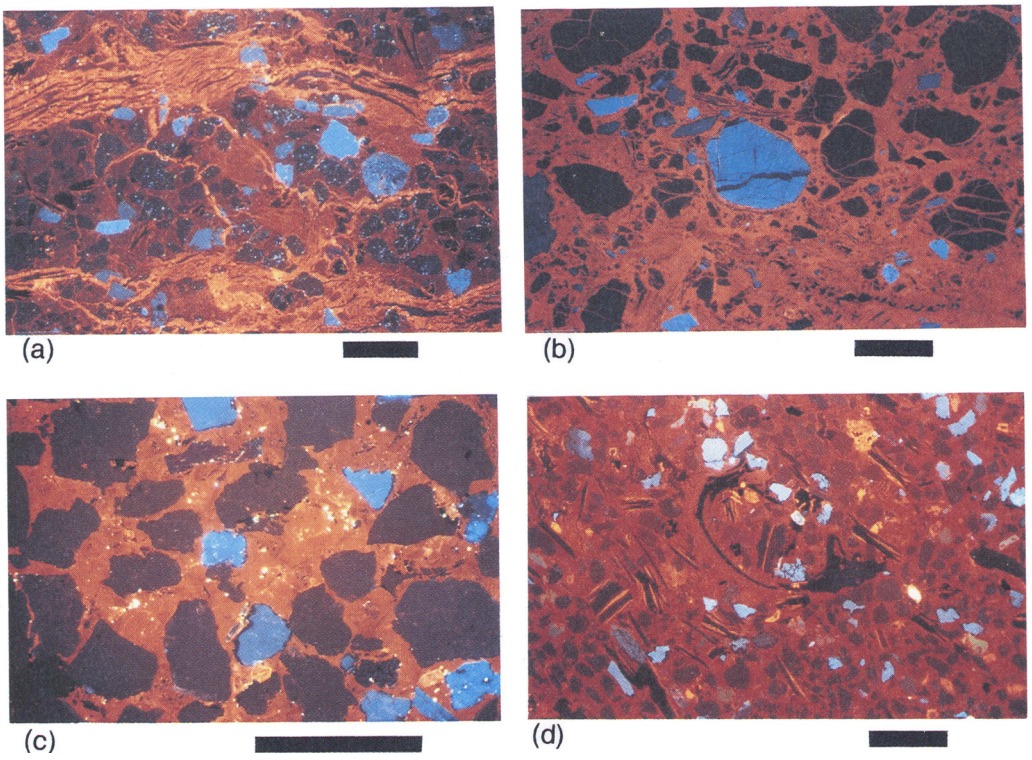

Fig. 14. (**a**) and (**b**) Cathodoluminescence photomicrographs of cement textures typically associated with mfs and sb sediments (macro-type I). (**a**) Sample from mfs 4.3 in well 31/2-4 is an example of 'brecciated' texture. Brown luminescent clasts of microsparry and 'exploded' mica are enclosed by yellow/orange luminescent fracture fill. Displacive prismatic calcite cement is forming between mica flakes in the fractured area. Note floating grain texture. (**b**) Sample from mfs 4.4 in well 31/2-11 shows rim cement around feldspar (centre of photo) and extensive fracturing of the clastic grains. (**c**) and (**d**) Cathodoluminescence photomicrographs of cement textures associated with macro-type IV cementation. (**c**) Sample from a clean, high permeable type sandstone and (**d**) sample from a micaceous sandstone. Both (c) and (d) show well-developed feldspar overgrowths seen as non-luminescent rims around blue luminescent feldspar grains which are post-dated by the blocky to poikilotopic ferroan calcite cements. Scale bars are 0.5 mm.

Displacive prismatic or 'exploded' mica textures are commonly observed, particularly in horizons associated with either mfs or sb sediments (Fig. 14a) 'Exploded' textures are frequently associated with biotite mica, whereas prismatic textures are associated with muscovite mica. 'Exploded' textures usually exhibit brown luminescence, whereas displacive prismatic textures luminesce yellow–orange and are often

associated with fractures parallel to bedding and/or brecciated textures. These textures are indicative of near-surface cementation because growth of carbonate between mica flakes may occur only if the mica grains are unrestricted and consequently near the sediment–water interface.

Brecciated textures and fracturing of clastic grains (see Fig. 14a,b) are frequently well developed in macro-type I horizons, particularly in cases where an mfs and sb are coincident or within metres of each other. Brecciated textures could have formed as a result of decompaction. After initial cementation (seen as brown luminescing cement) the sediments were covered during deposition of the overlying highstand system tract and then subsequently re-exposed as the overburden was removed as a result of erosion of the highstand system tract. Under decompaction the initial cemented portion of the sandstone is fractured and subsequently cemented. Alternatively, these textures could have formed after shallow burial where the laterally extensive mfs horizon would create a 'seal' or pressure barrier which is broken due to overburden pressure and subsequently recemented.

Isotopic analyses of the samples from which the photomicrographs shown in Fig 14 (a and b) were taken, show $\delta^{18}O$ values of -0.7 to -3.8‰ PDB and $\delta^{13}C$ values of -14.0 to -40.0‰ PDB. These isotopic compositions are indicative of carbonate sourced from oxidation of biogenic methane and are consistent with cementation at or near the sediment–water interface.

Displacive prismatic cements within mica grains and fractured/brecciated textures have been reported from calcrete profiles (e.g. Braithwaite 1989). However, this is not compatible with the sedimentological model. Nevertheless, these textures are extremely interesting and warrant further investigation.

Fractures parallel to bedding are usually pure calcite, but a second generation of fractures (at some angle to bedding) filled with ferroan calcite is also observed. In some cases, vertical fractures are infilled with sediments. This is also described macroscopically. This clearly indicates that some fracturing of the cements has occurred prior to subsequent sedimentation and therefore dates cementation as indeed occurring at a very early stage.

Macro-type II. Petrographical textures observed in macro-type II horizons are similar to those described for macro-type I with the notable exception that brecciated textures and fracturing of clastic grains do not occur.

Macro-type III. Early fringe cements occurring as polygonal calcite around bioclastic fragments together with mosaic to blocky calcite cement are characteristic of macro-type III. In general, a higher proportion of the total rock volume consists of bioclastic debris than observed in macro-types I and II. As for macro-types I and II, feldspar overgrowths are absent.

Macro-type IV. Primary sand compositions seen in macro-type IV include the full spectrum of sandstone types observed on Troll. Examples of this type are shown in Fig. 14 (c and d). Textural features exhibited by this group (Table 3) are characteristic of cementation following significant burial of the sediments. Isotopic compositions for these samples, $\delta^{18}O$ -10 to -12‰ PDB and $\delta^{13}C$ from -10 to $+10$‰ PDB, indicate that the carbonate was sourced by biogenic fermentation (methanogenesis) and/or thermal decarboxylation (see also Kantorowicz *et al.* 1987).

In summary, some very distinct textural features typical of early cementation can be delineated for cements associated with maximum flooding surfaces and sequence boundaries, particularly the fractured/brecciated textures. However, since these features are not exclusive to cements from mfs sediments it is not possible to use petrographical data as an independent tool for the identification of these surfaces.

Possible implications of mfs and carbonate-cemented horizons as permeability barriers

In order to predict well performance and find an optimal location for production wells, mapping of any permeability barriers is vital. The lateral continuity and extension of calcite-cemented horizons has important consequences for oil production from vertical wells as suggested by Kantorowicz *et al.* (1987).

For horizontal wells these consequences may be even more important. Joshi (1987) has demonstrated that for horizontal wells i.e. where the flow is linear to the well bore, the ratio of vertical to horizontal permeability is crucial to the total productivity.

From a reservoir point of view the calcite cemented horizons recognized in the Troll Field can be divided into two groups:

(1) laterally extensive (>1000 m);
(2) discontinuous (tens to hundreds of metres).

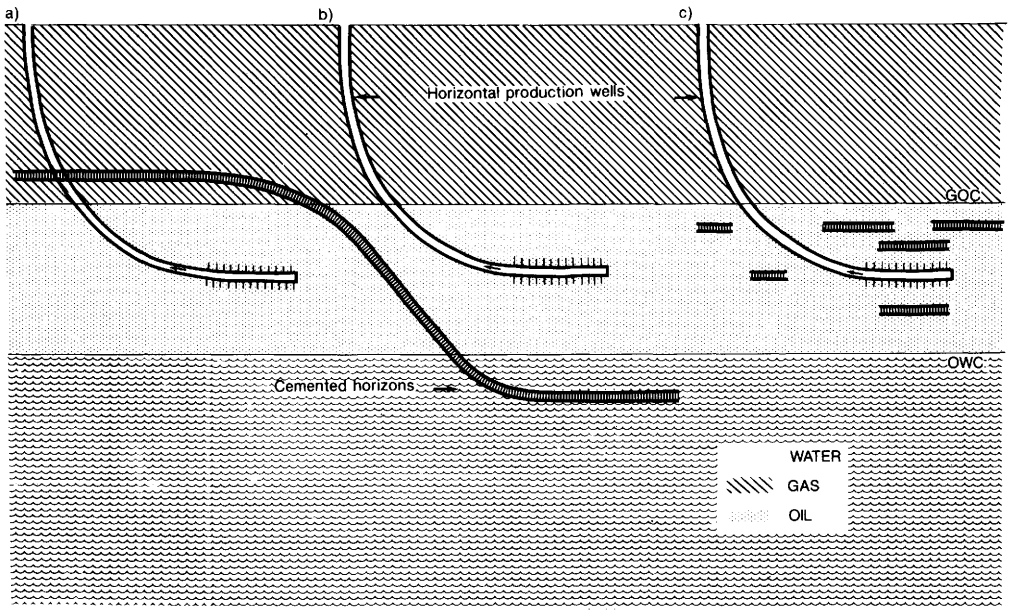

Fig. 15. Conceptual relationship between cemented horizons and oil production from horizontal wells: a, reduced gas coning due to a laterally continuous cemented layer above GOC; b, reduced water influx due to cemented layer below the OWC; c, discontinuous cemented layers reduce vertical permeability and thus reduce productivity from the oil zone.

For thin oil zones as in the Troll Field, one obvious complication presented by laterally extensive cemented layers is that of dip, in which case cemented layers will subdivide the oil zone and thereby reduce the oil volume available for the well.

Laterally extensive permeability barriers can also have a great impact both on gas coning and water influx. In Fig. 15 two possible well locations with respect to calcite-cemented horizons are shown. In position (a) gas coning could be delayed and hence total oil production increased. For position (b), the horizontal well will not be protected from gas breakthrough, but water influx will be reduced.

The sensitivity to the ratio of vertical to horizontal permeability implies that even discontinuous cemented layers will affect the oil production from a horizontal well as indicated by well position (c) (Fig. 15). Here, the vertical flow of oil to the horizontal well will be hindered by the barriers. Gas, because its viscosity is orders of magnitude lower than oil, will flow around flux barriers and advance to the well making it less receptive to oil. Since the water cut may be reduced by some of the barriers, the total effect on the oil production is a delicate balance between: (a) the lateral extension and placement of the barriers, (b) the rate at which oil is produced and (c) where the horizontal well is perforated.

A laterally extensive boundary layer such as a mfs or sb does not necessarily have to be completely calcite cemented in order to influence fluid flow in the reservoir. The exact reduction of transmissibility is of course indeterminable but the mappability of these horizons represents important improvements on the reservoir simulation model.

Conclusions

Results from this study allow the following conclusions to be drawn.

(1) The extinction and radiation of benthic fauna on Troll is to a large degree consistent with the eustatic sea-level curve defined by Haq *et al.* (1987, 1988).
(2) Based on palynology and sedimentology a model for identifying stratigraphical sequences and facies associations in a sea-level controlled system has been developed. The model is shown to be valid for the reservoir units within the Sognefjord Formation of the Troll Field.
(3) The model makes correlation of carbonate cemented horizons possible and thus provides a framework for the prediction of the lateral extent of the cemented horizons.
(4) Roughly 70 to 75% of all identified maximum flooding surfaces and 60 to 65% of identified sequence boundaries are found to be calcite cemented.
(5) Petrographical analysis alone cannot be used for correlating carbonate-cemented horizons but it has shown that near-surface (early) cementation is prevalent in the cemented horizons at maximum flooding surfaces and sequence boundaries.
(6) Oil production by horizontal wells from thin oil zones requires as much information as possible on laterally extensive barriers to flow. Results for sequence stratigraphical studies, at the reservoir level, are relevant to the prediction of potentially extensive barriers.

The partners of the Troll licence group: Statoil, Norsk Hydro Produksjon as, Saga Petroleum as, A/S Norske Shell, Norske CONOCO A/S, Elf Aquitaine Norge A/S and Total Marine Norsk A/S, are thanked for allowing release of this paper. We thank R. Steel, M. Ashton and an anonymous reviewer for providing valuable criticisms and suggestions during the preparation of this manuscript. Special thanks to A. Henriquez for his contributions to this paper.

References

BRAITHWAITE, C. J. R. 1989. Displacive calcite and grain breakage in sandstones. *Journal of Sedimentary Petrology*, **59**, 258–266.

BRYANT, I. D., KANTOROWICZ, J. D. & LOVE, C. F. 1988. The origin and recognition of laterally continuous carbonate-cemented horizons in the Upper Lias Sands of southern England. *Marine and Petroleum Geology*, **5**, 108–133.

GREY, D. I. 1987. Troll. *In*: SPENCER, A. M. (ed.) *Geology of Norwegian Oil and Gas Fields*. Norwegian Petroleum Society, Oslo, 389–401.

HALLAM, A. 1987. Eustatic cycles in the Jurassic. *Palaeogeography, Palaeoclimatology, Palaeoecology*, **23**, 1–32.

HAQ, B. V., HARDENBOL, J. & VAIL P. R. 1987. The chronology of fluctuating sea-level since the Triassic. *Science*, **235**, 1156–1167.

——, —— & —— 1988. Mesozoic and Cenozoic chronostratigraphy and eustatic cycles. *In*: WILGUS, C. K. *et al.* (eds) *Sea-level changes: An integrated approach*. Society of Economic Paleontologists and Mineralogists Special Publication **42**, 71–108.

HELLEM, T., KJEMPERUD, A. & ØVREBØ, O. K. 1986. The Troll Field: a geological/geophysical model established by the PL085 Group. *In*: SPENCER, A. M. (ed.) *Habitat of Hydrocarbons on the Norwegian Continental Shelf*. Norwegian Petroleum Society, Graham & Trotman, London, 217–236.

IOANNIDES, N. S., STAVRINOS, G. N. & DOWNIE, C. 1976. Kimmeridgian microplankton from Clavell's Hard, Dorset, England. *Micropalaeontology*, **22**, 443–478.

IRWIN, H. & HURST, A. 1983. Applications of geochemistry to sandstone reservoir studies. *In*: BROOKS, J. (ed.) *Petroleum Geochemistry and Exploration of Europe*. Geological Society, London, Special Publication, **12**, 127–145.

JOSHI, S. D. 1987. Review of horizontal well and drain hole technology. *Society of Petroleum Engineers 16868, 62nd Annual Technical Conference and Exhibition, Dallas, Texas, Sept.*, 27–30.

KANTOROWICZ, J. D., BRYANT, I. D. & DAWANS, J. M. 1987. Controls on the geometry and distribution of carbonate cements in Jurassic sandstones: Bridport Sands, southern England and Viking Group, Troll Field, Norway. *In*: MARSHALL, J. D. (ed.), *Diagenesis of Sedimentary Sequences*. Geological Society, London, Special Publication, **36**, 103–118.

KENNEDY, W. J. 1977. Ammonite evolution. *In*: HALLAM, A. (ed.) *Patterns of Evolution*. Elsevier, Amsterdam, 251–304.

MOLENAAR, N., VAN DER BILT, G. P., VAN DER HOEK OSTENDE, E. R. & NIO, S. D. 1988. Early diagenetic alteration of shallow-marine mixed sandstones: An example from the Lower Eocene Roda sandstone member, Tremp-Graus basin, Spain. *Sedimentary Geology*, **55**, 295–318.

NIO, S. D., SCHUTTENHELM, R. T. E. & VAN WEERING, TJ. C. E. (eds) 1981. *Holocene Marine Sedimentation in the North Sea Basin. International Association of Sedimentologists, Special Publication*, **5**, Blackwells, Oxford.

NIO, S. D. & YANG, C. S. 1989. *Recognition of tidally-influenced facies and environments*, Short course notes series No. 1, International Geoservices BV.

—— & —— 1991*a*. Sea level fluctuations and the geometric variability of tide-dominated sand bodies. *Sedimentary Geology*, **70**, 161–193.

—— & —— 1991*b*. Diagnostic attributes of clastic tidal deposits—a review. *In*: SMITH, D. G. *et al.* (eds) *Clastic tidal sedimentology*. Canadian Society of Petroleum Geology, Memoir **16**, 3–28.

POSAMENTIER, H. W., JERVEY, M. T. & VAIL, P. R. 1988. Eustatic controls on clastic deposition I—Conceptual framework. *In*: WILGUS *et al.* (eds) *Sea level changes: an integrated approach*. Society of Economic Paleonotologists and Mineralogists Special Publication **42**, 109–124.

RAYNAUD, J. F. 1978. Principaux dinoflagelles characteristiques du Jurassique superieur d'Europe du Nord. *Palinologia*, **1**, 387–405.

TILLMAN, R. W., SWIFT, D. J. T. & WALKER, R. G. 1985. *Shelf sands and sandstone reservoirs*. Society of Economic Paleontologists and Mineralogists Short Course notes **13**.

VAIL, P. R., MITCHUM, R. M. & THOMPSON III, S. 1977. Seismic stratigraphy and global changes of sea level, part 3: relative changes of sea level from coastal onlap. *In*: PAYTON, C. E. (ed.) *Seismic stratigraphy applications to hydrocarbon exploration*. American Association of Petroleum Geologists Memoir **26**, 63–97.

VAN DER ZWAEN, C. J. 1989. Palynostratigraphical principles as applied in the Jurassic of the Troll and Draugen Fields, offshore Norway. *In*: COLLINSON, J. D. (ed.) *Correlation in hydrocarbon exploration*. Norwegian Petroleum Society, Graham & Trotman, London, 357–365.

From ASHTON, M. (ed.), 1993, *Advances in Reservoir Geology*,
Geological Society Special Publication No. 69, pp. 33–56.

Reservoir heterogeneity in the Vanguard Field, UKCS

RICHARD W. LAHANN,[1] JON A. FERRIER[2] & SUSAN CORRIGAN[3]

[1] *Conoco Exploration Research and Services, 1000 South Pine, Ponca City Oklahoma 74603, USA*
[2] *Conoco United Kingdom Limited, currently at Conoco Norway Inc., Finnestadveien 28, P. O. Box 488, 4001 Stavanger, Norway*
[3] *Corrigan Associates, 2 The Drove, Ditchling, Sussex BN6 8TR, UK*

Abstract: The Rotliegendes Group in the Vanguard Field, UKCS, consists of a series of aeolian, fluvial, and reworked aeolian sediments, organized into four broadly correlatable lithostratigraphical units. Within these units, reservoir properties are strongly linked to lithofacies, with aeolian dune sandstones possessing the best porosity and permeability.

A comparison of production log spinner profiles (PLT) with detailed sedimentological logs from three development wells shows that gas production is intimately associated with specific lithofacies and their spatial organization. Although dune sandstones in the upper section of the Rotliegendes have good petrophysical characteristics, they do not contribute significantly to production because they are contained within laterally extensive and relatively impermeable interdune sandstones. Most production comes from 15–30 feet thick and highly permeable (100–1000 mD) dune foreset intervals deposited near the bases of large aeolian dunes.

Significant interwell variation in production rates and in porosity exists for all lithofacies due to the variable extent of diagensis. Petrographical studies, combined with whole-rock geochemical analysis, have outlined a diagenetic sequence for the field. Two end-member mineralogical assemblages are identified which are closely linked to reservoir quality. High porosity wells contain a chlorite–K-feldspar–quartz–dolomite assemblage while low porosity wells contain an illite–quartz–ankerite assemblage. Empirical evidence shows that porosity loss is associated with conversion of K-feldspar, chlorite and dolomite to illite and ankerite, and is due to compaction rather than cementation. Post-depositional faults acted as conduits for fluid which altered mineralogy, removed soluble components and, in one case, introduced anhydrite cement.

The Vanguard Field is located in Block 49/16, approximately 45 miles east of Mablethorpe near the centre of the Sole Pit Basin, United Kingdom Continental Shelf (UKCS Fig. 1). The field was discovered in 1982 and brought into gas production as part of the Conoco-operated V-Fields development programme in October 1988. The field produces from the Leman Sandstone Member of the early Permian, Rotliegendes Group. The Leman Sandstone varies from 620 to 750 feet in thickness in the Vanguard Field. The paleogeography and structural history of the Rotliegendes Group are adequately discussed in the literature (Glennie *et al.* 1978) and are not dealt with here.

The field is located on a NW–SE-elongate, faulted anticline with steeply dipping flanks (Fig. 2). It is partially overlain by a Triassic collapse zone (Walker & Cooper 1987) and Zechstein salt swell which create problems with seismic depth conversion and imaging, rendering seismic delineation and detailed mapping of the structure

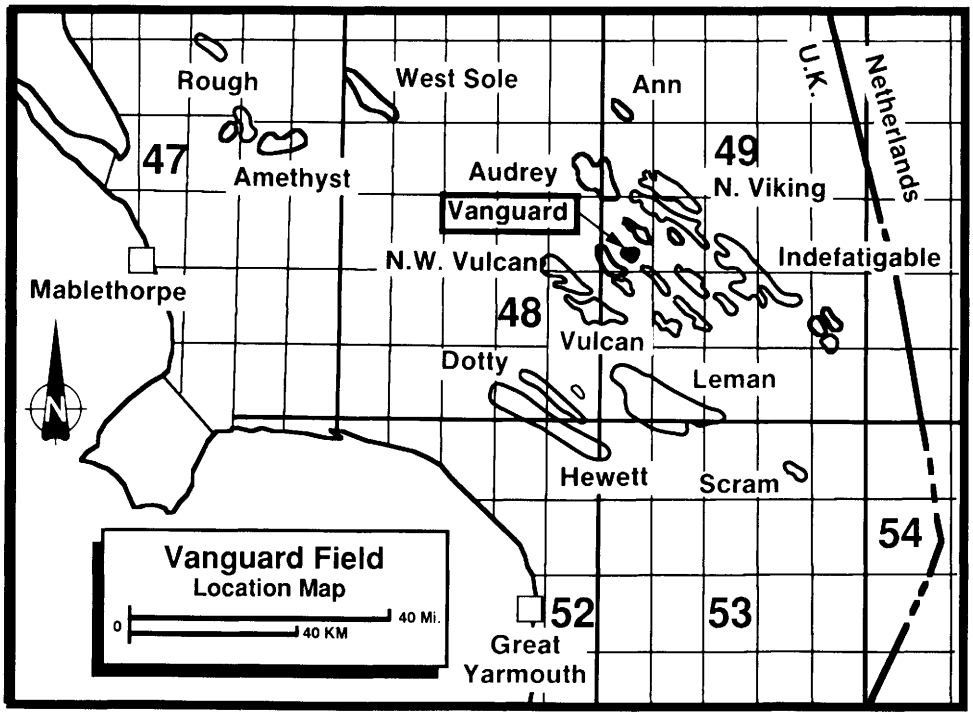

Fig. 1. Location map for the Vanguard Field, UKCS.

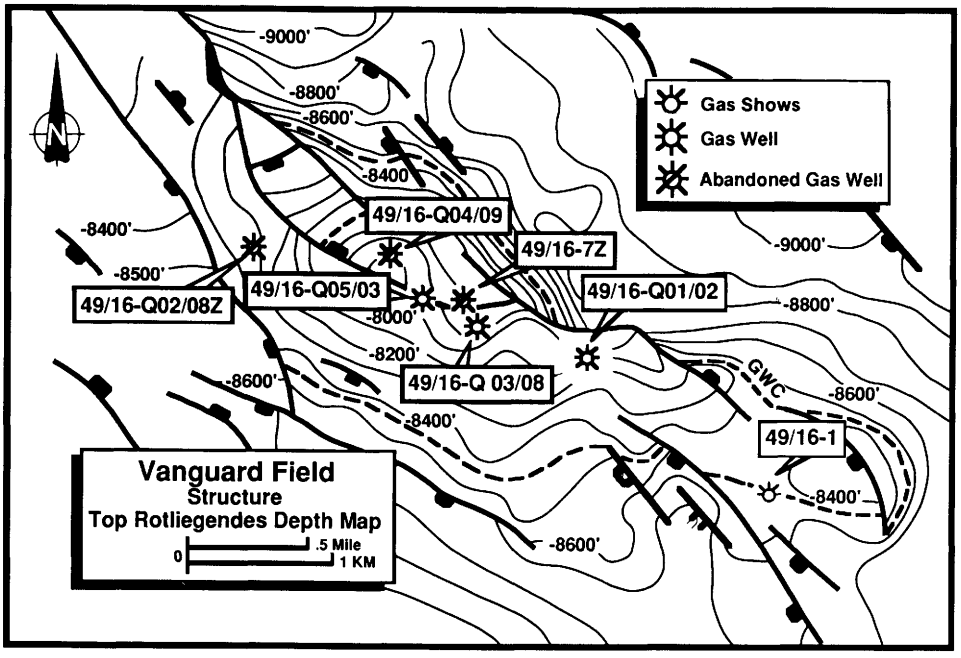

Fig. 2. Structure map at top Rotliegendes for the Vanguard Field. GWC refers to gas–water contact. Only major (seismically resolvable) faults are shown.

extremely difficult. Seismically resolvable faults are dominantly oriented NW–SE, following the pronounced Charnoid/Variscan trend. A NW–SE strike section outlines the basic structure and shows the position of the gas/water contact in the wells (Fig. 3).

Initial core examination showed the Vanguard wells to be highly heterogeneous in terms of colour, facies, fracturing, porosity, and permeability. Heterogeneity in aeolian reservoirs has been described by Lindquist (1988) and Heward (1990). The extent of the variability between wells in the Vanguard Field is far greater than had been encountered in other Rotliegendes gas fields developed by Conoco.

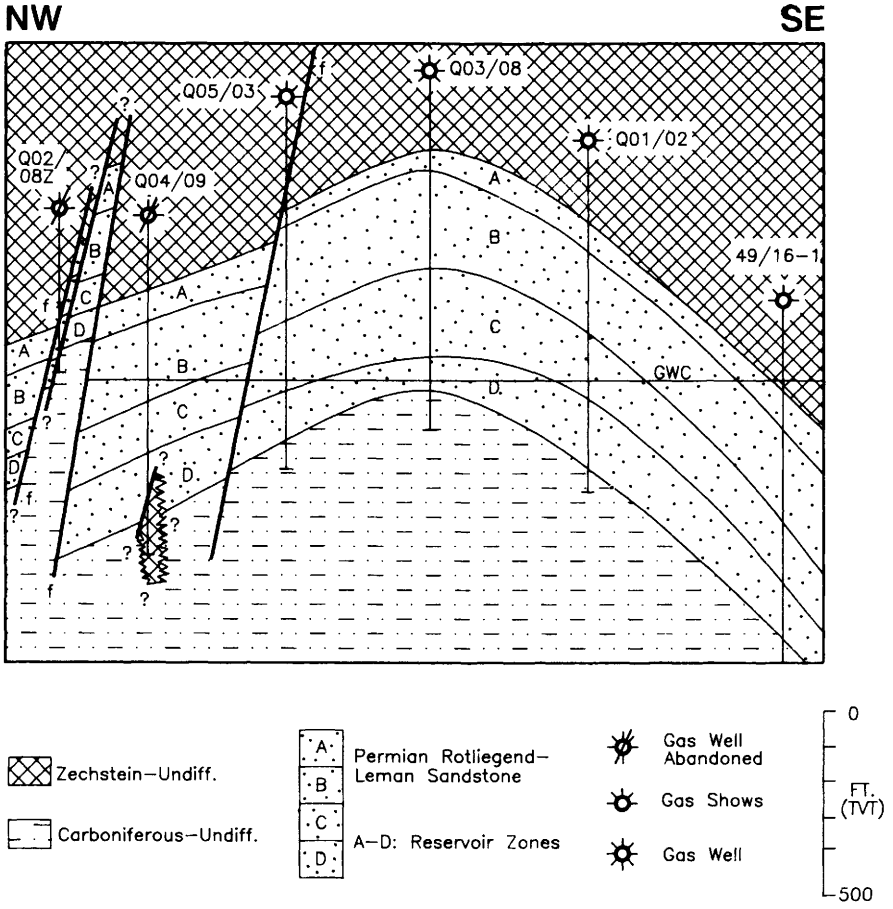

Fig. 3. NW–SE cross-section through the Vanguard Field demonstrating the structure and the location of the gas–water contact (GWC).

The purpose of this paper is to document intrawell and interwell heterogeneity in the Vanguard Field and to examine the causes for that heterogeneity and the associated variable productivity. Knowledge of the variable productivity of the lithofacies present in a well can help to optimize production and avoid a variety of production problems (e.g., early water production). An understanding of the causes for interwell productivity variations can contribute to the design of field-scale

production strategies (e.g., future well locations) and engineering decisions on existing wells. Finally, a thorough understanding of the sedimentological and diagenetic controls on well productivity can contribute to the efficient development of other Rotliegendes reservoirs.

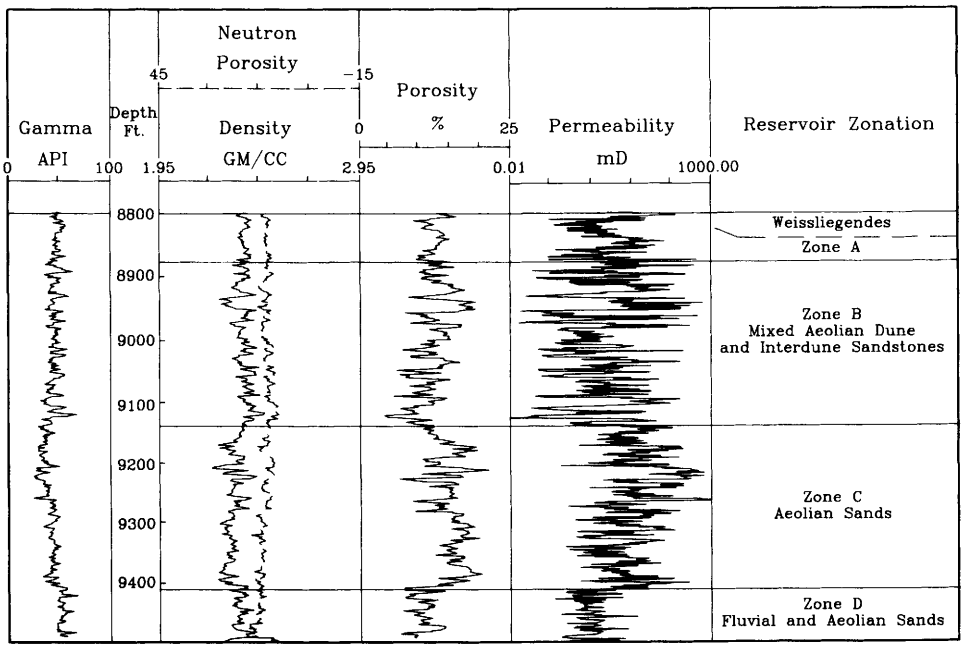

Fig. 4. Type section for the Leman Sandstone, Rotliegendes Group, in the Vanguard Field. The section is taken from well Q03/08. Porosity and permeability data are from core analysis.

Table 1. *Reservoir property characteristics of the reservoir zones in well Q03/08*

Zone	Porosity range %	Permeability range, mD	Sorting
A	7–17	0.15–550	Good (25) Mod (11)
B	5–20	0.02–800	Good (44) Mod (32) Poor (2)
C	8–20	2–1500	Good (30) Mod (15)
D	8–20	0.1–180	Good (31) Mod (58) Poor (14)

The numbers in parentheses in the sorting column are number of occurrences.

Sedimentology

The Vanguard Field reservoir is divided into four zones illustrated by the type log from development well 49/16-Q03/08 (henceforth Q03; Fig. 4). The basal Leman Sandstone, zone D, contains fluvial/wadi facies with minor aeolian dune sandstones. The fluvial sandstones are generally massive with rare pebble beds and rip-up clasts whereas the aeolian sandstones are laminated and frequently contain adhesion ripples (Fig. 5). Fluid level fluctuations following deposition introduced grain-coating pellicle clays. Reservoir properties are generally poor due to poor sorting and the high pellicle clay content (Table 1). Zone D is usually either below or too close to the gas/water contact to be completed as a producing reservoir.

Zone C, stratigraphically above zone D, constitutes the primary producing reservoir in the Vanguard Field. It consists of stacked deposits of compound aeolian dunes and draas (Fig. 6). Cores contain a series of subhorizontal, texturally bimodal bottom-set beds which grade upward into moderately- to well-sorted foreset beds up to 20 feet thick (Table 1). Orientation of the foreset laminae is highly uniform, suggesting that these laminae represent the lee slope of transverse dunes. Dune foreset sandstones contain primarily grainflow structures, with minor grainfall and wind-ripple structures. Porosity and permeability of the bimodal bottom-set wind-ripple-laminated sandstones are less than that of the moderately- to well-sorted overlying foreset beds.

Zone B consists of dune, adhesion-rippled sheet (thin, ripple-laminated interdune aeolian sandstones), and rare thin (less than 2 ft) fluvial sandstones (Fig. 7). The combination of these lithologies indicates more frequent deposition in damp interdune depositional environments, relative to zone C.

The end of Leman Sandstone deposition is marked by the development of fine grained aeolian dunes in zone A (Fig. 8). The uppermost dunes are locally reworked by and during the Zechstein transgression producing (in all Vanguard Field wells) a lithostratigraphical unit commonly called the Weissliegendes. It represents a distinct genetic unit, although its reservoir properties are similar to zone B.

Both zones B and A contain highly variable reservoir properties because of the large number of lithologies present (Table 1). The best porosities and permeabilities, present in aeolian dune foreset sandstones, can rival the properties of zone C. The adhesion-rippled damp interdune and fluvial sandstones have substantially poorer reservoir properties than do the aeolian dune sandstones (Fig. 4).

Sedimentology/production data integration

Porosity and permeability profiles for well Q05/03 (Q05) are shown in Fig. 9. Although the best reservoir properties occur in zone C, many individual sandstones in zone B approach 1000 mD permeability. The right-hand column on Fig. 9 (PLT) is a plot of gas flow rate within the well bore scaled from 0 to 100%. The variation in flow rate indicates the vertical distribution of production within well Q05. Zone B contributes only about 10% of the well production despite a thicker perforated interval than zone C. A single 35 ft interval in zone C (near depth 9790 ft) contributes 67% of the flow entering the well. The interval from about depth 9680 ft to 9700 ft (Zone B) contributes virtually no flow despite permeability from 1–100 mD, the same permeability as the interval from 9760–9780 ft (Zone C) which contributes substantially to the flow.

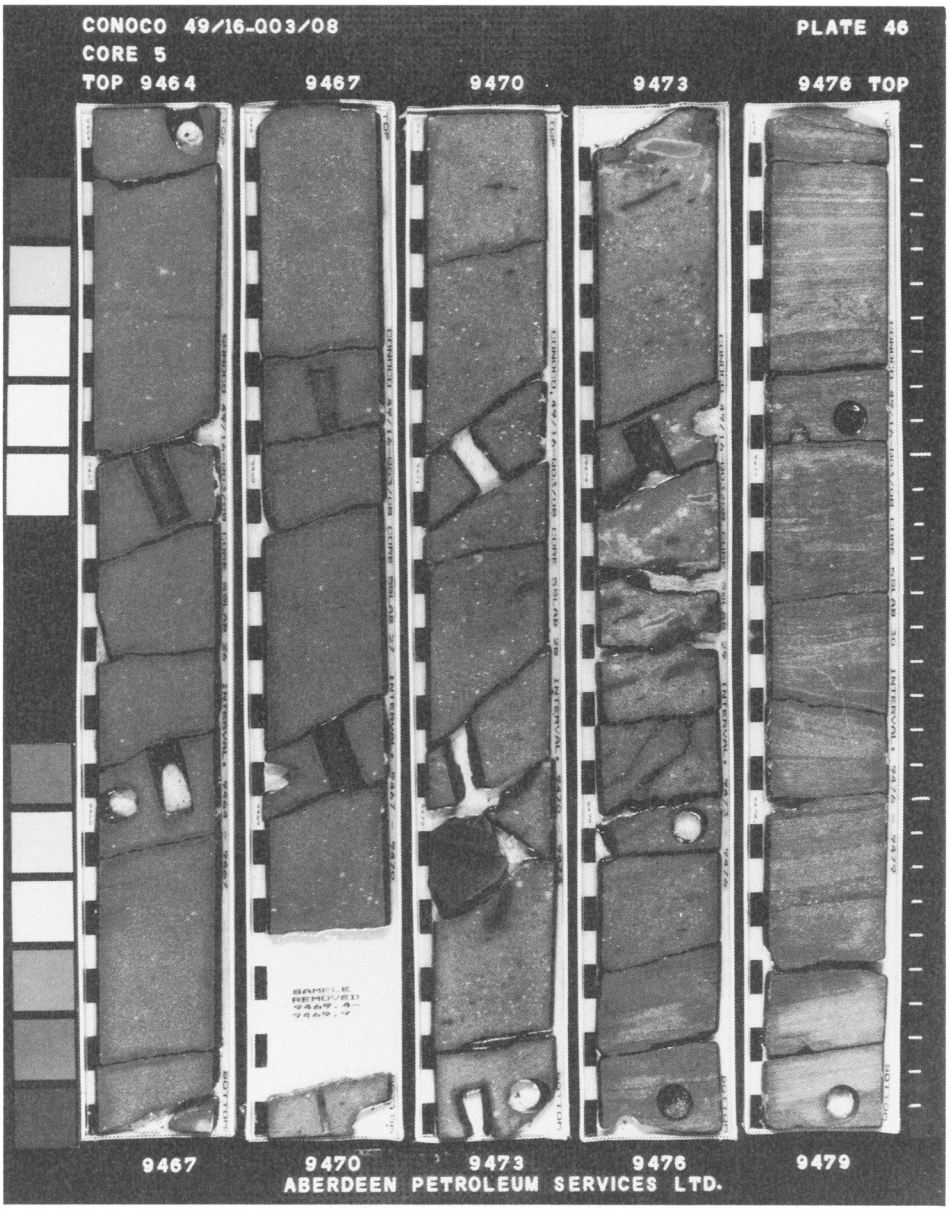

Fig. 5. Photograph of Leman Sandstone core from depth 9464 to 9479 ft, zone D in well Q03/08. The section from 9464 to 9470 ft is largely structureless. Note the occurrence of pebbles from 9470–9473 ft and rip-up clasts from 9473–9475 ft. The interval from 9476 to 9479 ft is finer grained and wind-ripple laminated with local adhesion ripples.

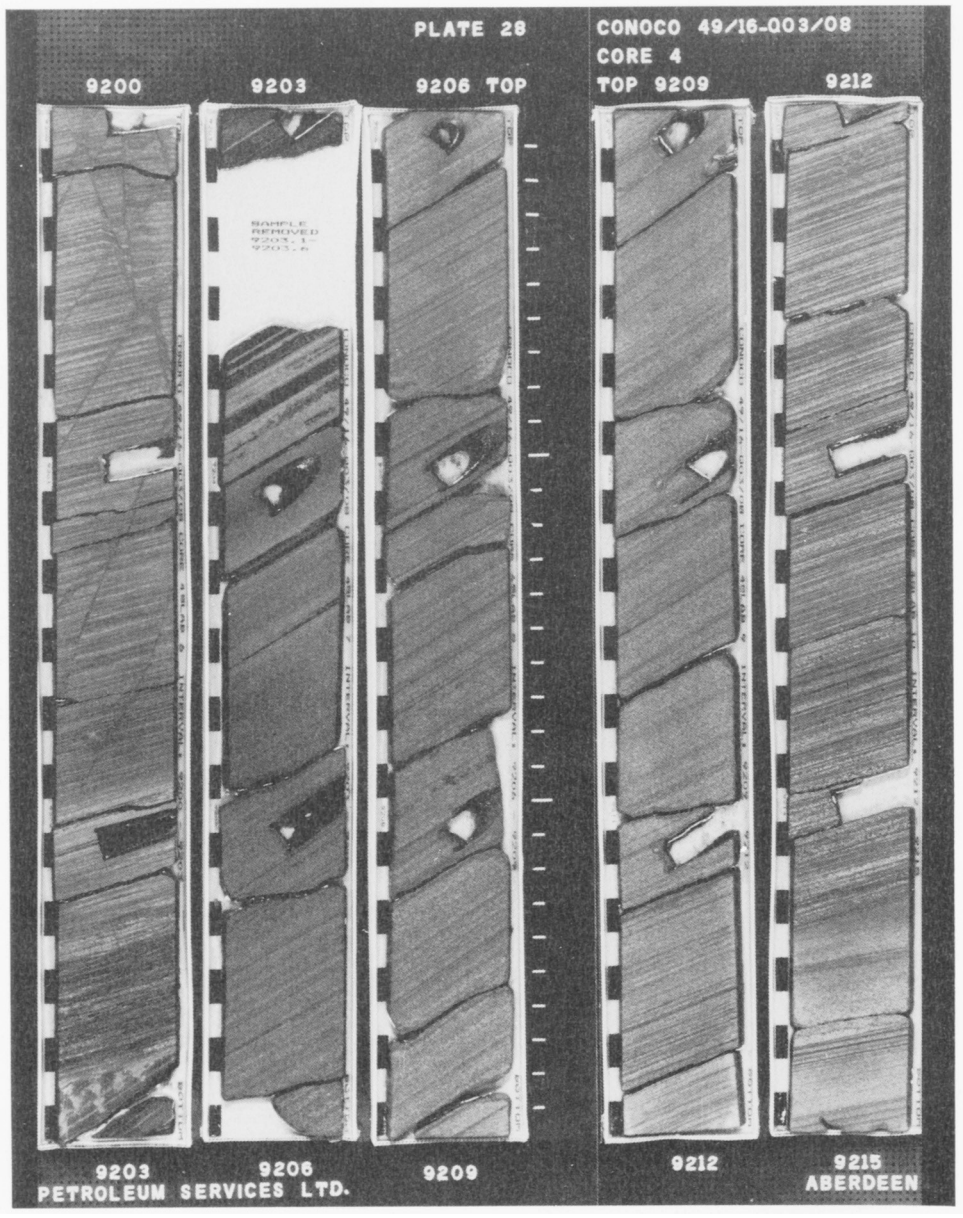

Fig. 6. Photograph of Leman Sandstone core from depth 9200 to 9215 ft, zone C (aeolian dune) in well Q03/08. The section from 9200 to 9202 ft is fractured. Virtually the entire interval is composed of moderately- to well-sorted aeolian dune foreset beds. The interval from 9202.8–9204 ft has hydrocarbon stains along coarse-grained laminae.

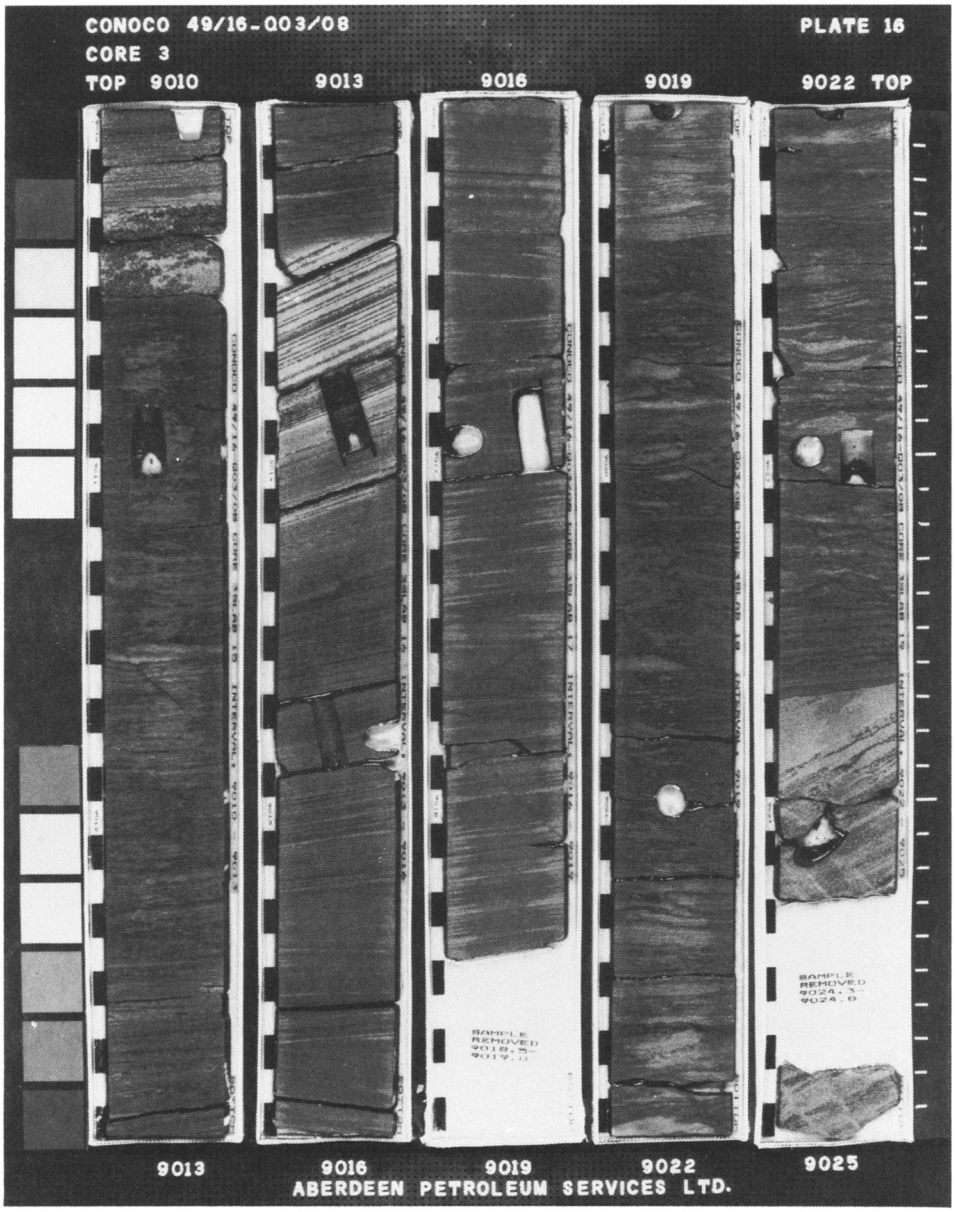

Fig. 7. Photograph of Leman Sandstone core from depth 9019 to 9025 ft, zone B (aeolian dune and wet interdune) in well Q03/08. The base of the photographed interval contains dune foreset sandstones. From 9013.2 to 9023.7 ft is an upward-coarsening cycle from adhesion rippled damp interdune sandstones to well-sorted, fine-grained foreset sandstones. This cycle is then overlain by adhesion rippled, damp interdune sandstones. Hydrocarbon stains occur at depth 9013.5 ft.

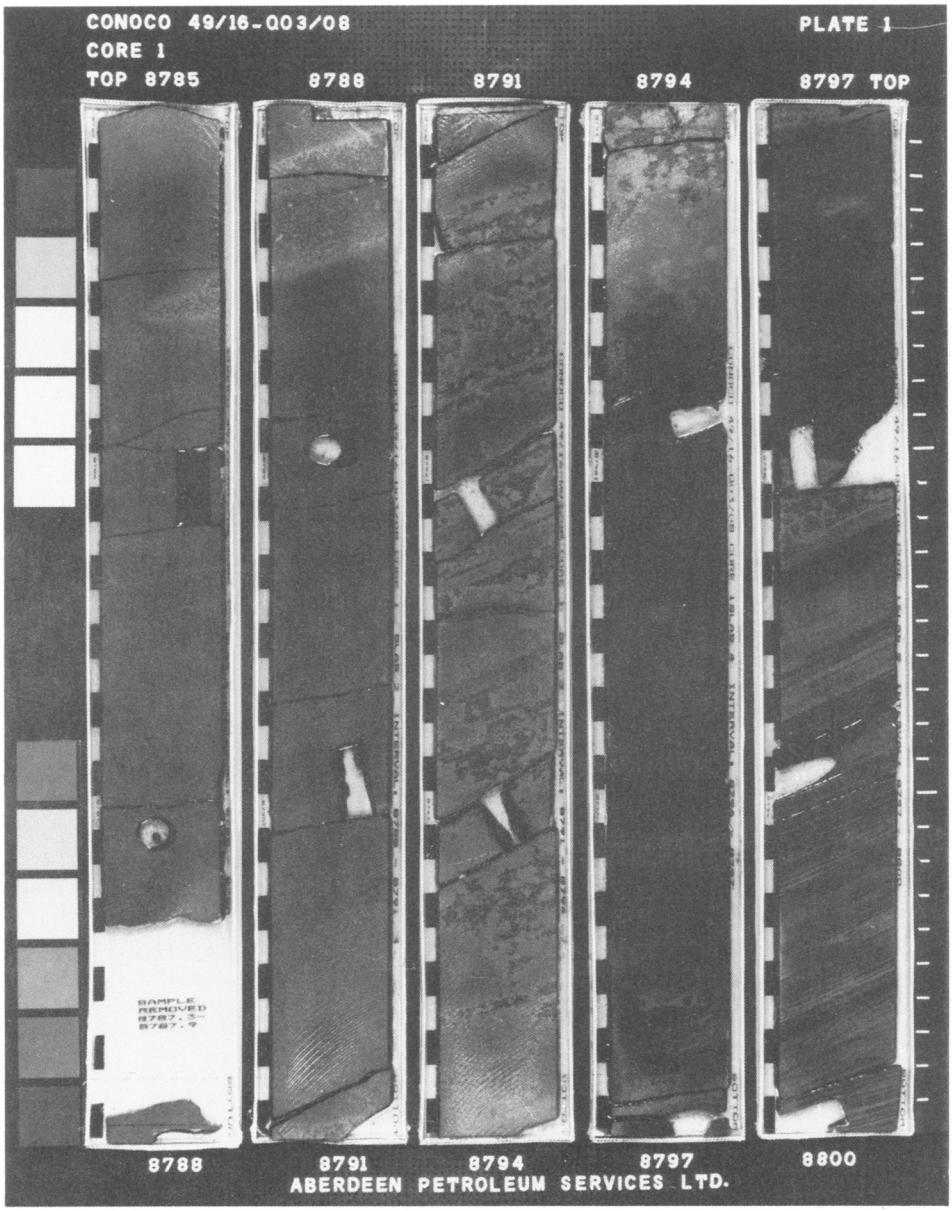

Fig. 8. Photograph of Leman Sandstone core from depth 8785 to 8800 ft, zone A (Weissliegendes) in well Q03/08. Note the structureless and massive character from 8785 to 8798 ft, overlying aeolian dune foreset beds.

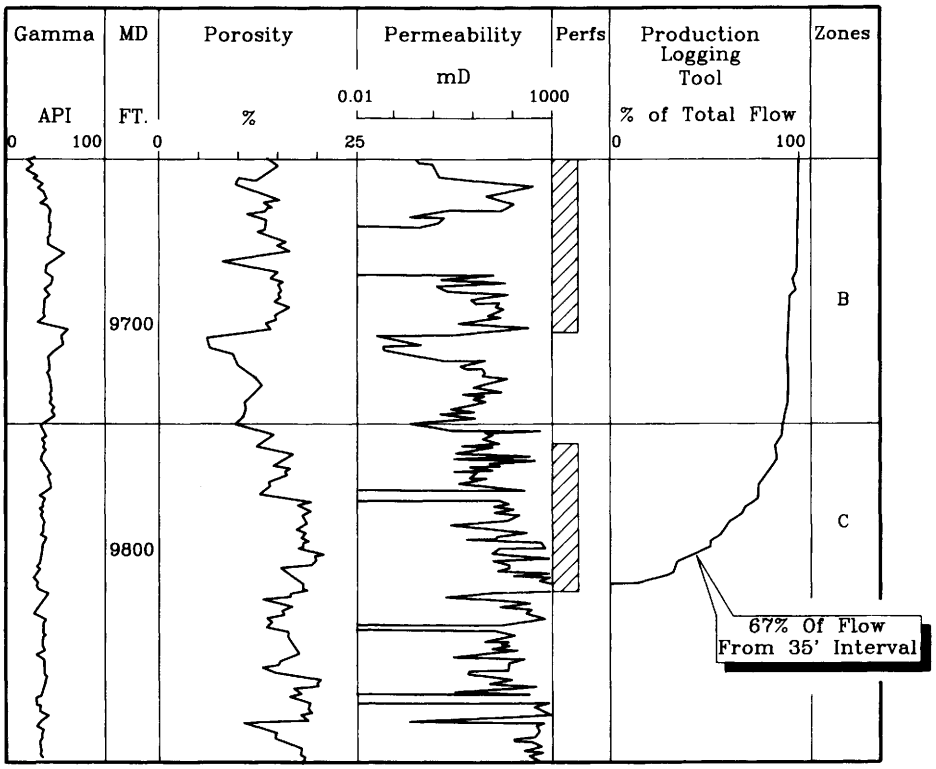

Fig. 9. Well Q05/03 integrated petrophysical log. MD refers to measured depth.

The vertical distribution of porosity, permeability and production in well Q03 is similar to well Q05 (Fig. 10). Virtually all the production is from zone C. Two distinct steps in flow are present on the PLT log for well Q03. At about depth 9280 ft a 5 ft interval contributes 15% of the total well production and at about depth 9230 ft a 10 ft interval contributes 30% of the well production.

Clearly factors in addition to the core-measured rock properties (porosity and permeability) strongly influence productivity. The primary difference between the highly productive zone C dune foresets and the nonproductive zone B foresets is the three dimensional interconnectivity of the producing facies. We conclude that the damp interdune facies in zone B effectively isolate individual dunes of good reservoir quality, thereby greatly reducing the production achievable by perforating the well within those dunes.

Although the thickness and facies content (e.g., percent of wet interdune in zone B) of the reservoir units vary little between wells, two of five production wells (Q02 and Q04) could not be completed economically (Table 2; Fig. 11). Further, dramatic differences in production rate exist among the three producing wells. Well Q05 produces 46% of the field production, well Q03 produces 33%, and well Q01 produces 21%. These differences exist despite similar perforated intervals in terms of reservoir zonation.

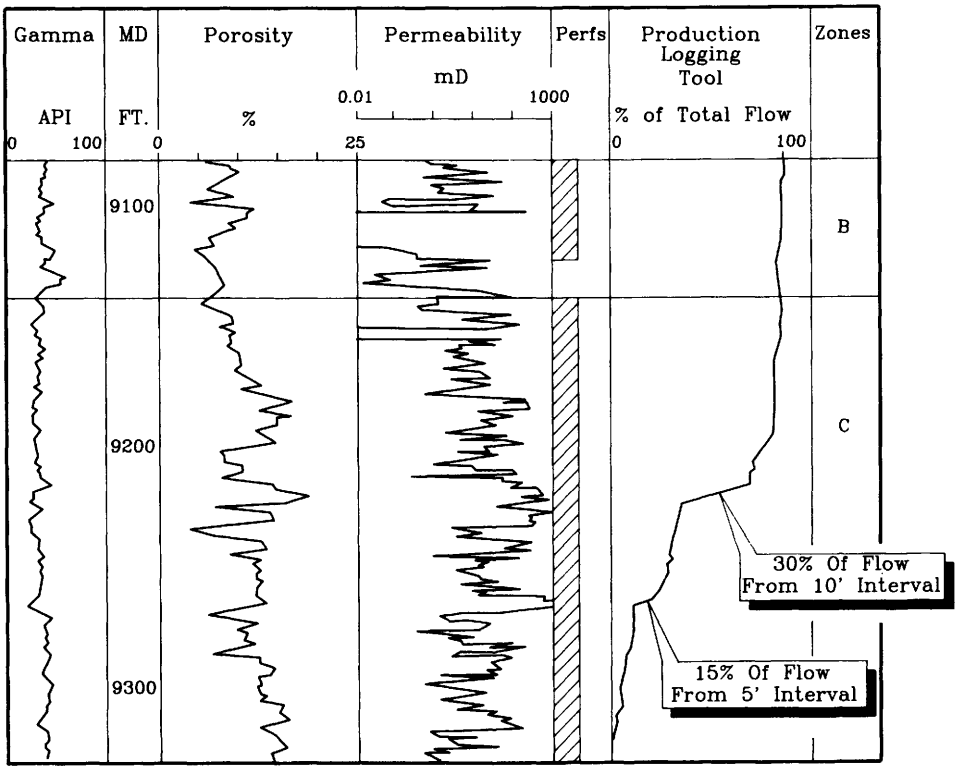

Fig. 10. Well Q03/08 integrated petrophysical log. MD refers to measured depth.

Table 2. *Abundance of aeolian dune facies in zones B and C in wells Q01/02, Q03/08, and Q05/03 in the Vanguard Field*

Well	Zone	%Aeolian dune	%Medium and coarse sand
Q01/02	B	81	39
	C	100	42
Q03/08	B	74	30
	C	100	54
Q05/03	B	84	27
	C	98	49

Petrophysical characteristics

Core porosities from the aeolian dune sandstone in wells Q01, Q03, and Q05 generally correlate well with core-measured permeability (Fig. 12). Although the data fields for the wells overlap to a considerable degree, the Q05 well contains the highest

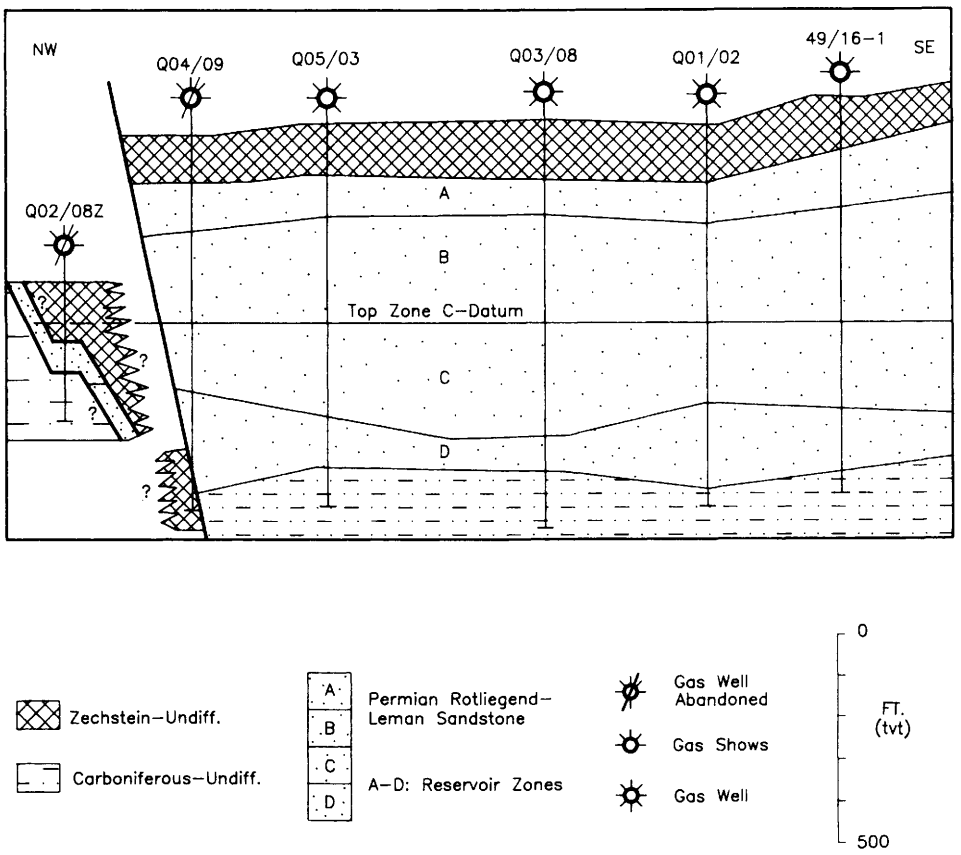

Fig. 11. Schematic cross-section across the Vanguard Field. Reference datum is the top of reservoir zone C. Note that only minor differences exist in zone thicknesses between wells.

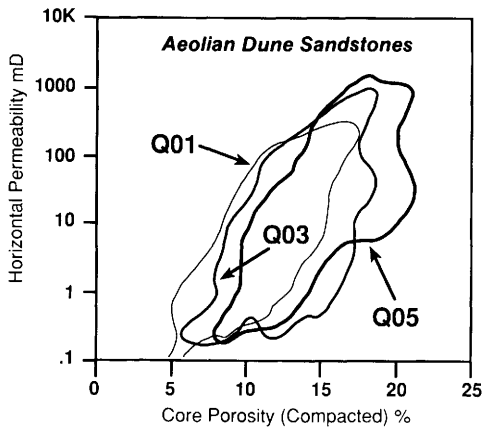

Fig. 12. Compacted (laboratory-measured porosity values adjusted to reflect stress at reservoir depth) porosity versus logarithm of core permeability cross-plot for aeolian dune facies sandstones from wells Q01/02, Q03/08, and Q05/03. Data displayed are from all aeolian dune lithofacies and are taken from all reservoir zones.

porosities and permeabilities (maximum values of 22% and 2000 mD respectively) and Q01 the poorest reservoir properties (maximum porosity of 17% and maximum permeability 300 mD). Data displayed represent all aeolian dune lithofacies from all reservoir zones. The Q03 and Q01 data fields are progressively shifted toward lower permeability and porosity, relative to the Q05 data.

Damp interdune facies from well Q05 also possess better reservoir properties than the same facies from wells Q03 or Q01 (Fig. 13). Data displayed represent all damp interdune lithofacies from all reservoir zones. As with the aeolian dune facies, the data fields overlap with the Q03 and Q01 data fields offset to lower porosity. Figures 12 and 13 demonstrate that the aeolian dune sandstones possess better porosity and permeability than the damp interdune sandstones. Lindquist (1988) also established strong linkages between reservoir properties and lithofacies. The distinction between Q05 and Q01, in terms of reservoir properties, is more distinct in the generally more porous aeolian dune facies.

Sandstones from the same facies and with similar textural characteristics, but from different wells, have different porosity-permeability characteristics. Well-sorted, medium-grained aeolian dune sandstones from well Q05 average 15.9% porosity and 219 mD permeability. Well-sorted, medium-grained aeolian dune sandstones from wells Q03 and Q01 average 13.9 and 12.6% porosity and 42 and 6 mD permeability, respectively. Diagenesis must, therefore, account for the differences between wells Q01, Q03, and Q05.

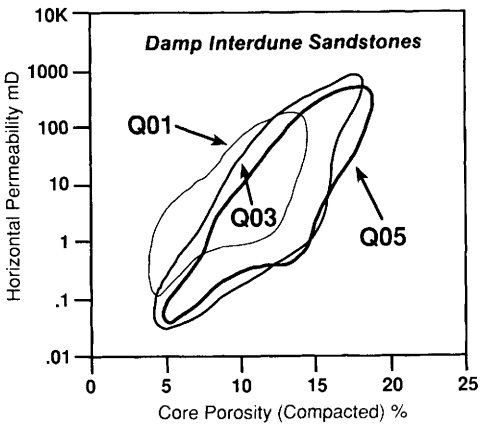

Fig. 13. Compacted porosity (laboratory-measured porosity adjusted to reflect stress at reservoir depth) versus logarithm of core permeability cross-plot for damp interdune facies sandstones from wells Q01/02, Q03/08 and Q05/03. Data displayed are from all damp interdune lithofacies and are taken from all reservoir zones.

Petrology

Petrological study of productive (Q05, Q03, and Q01) and noneconomic (Q02 and Q04) wells shows substantial differences in mineralogy and texture. The discussion and figures that follow concentrate on aeolian dune foreset sandstones, the facies that

contributes most of the production. Figure 14 is a thin-section photomicrograph of porous and permeable aeolian dune foreset sandstone from Q05. The aeolian dune sandstones in well Q05 are generally red with local 'bleached' zones associated with coarse-grained laminae which contain hydrocarbon residues. The sandstone is quartz-rich, with 10–30% lithic fragments. Although several of the lithic fragments are partially dissolved, most still retain readily recognizable primary grain shapes (Fig. 14). Sandstones from this well contain about 2.5–3.0% K-feldspar and about 2.5% dolomite cement (Table 3).

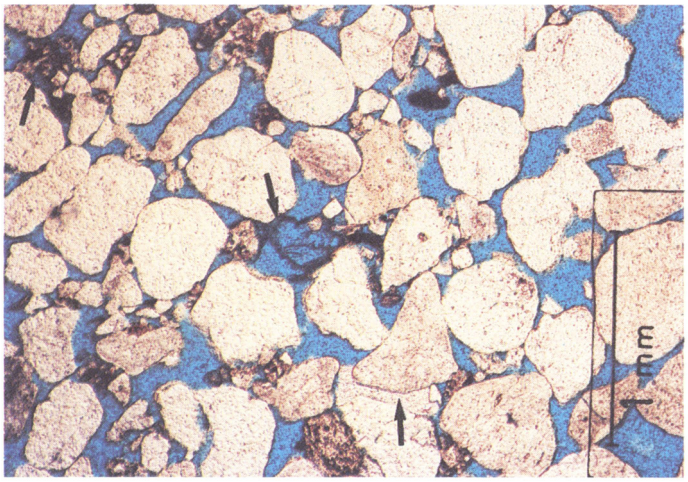

Fig. 14. Thin-section photomicrograph of porous, coarse-grained aeolian dune foreset sandstone in well Q05/03. Porosity is 22.5%, and permeability is 961 mD. Thin, brown rims on grains are chlorite grain coats (see Fig. 15). Note the etched lithic grains at upper left (arrow) and large, well-defined dissolution pore near centre (arrow), defined by residual clay coat. The primary shape of the dissolved grain is unaltered. Most grain contacts are tangential, and considerable primary porosity is preserved. Anhydrite cement is present at centre bottom of photograph (arrow).

Table 3. *Petrographical characteristics of wells Q05/03, Q03/08, Q49/16-7, Q01/02, Q04/09, and Q02/08Z in the Vanguard Field*

Well	Chl/I ratio (by XRD)	K-feldspar (percent) Pt. count	K-feldspar (percent) XRD	Dolomite + ankerite (percent by XRD)	Anhydrite (percent by geochem)	Quartz cement (percent by Pt. count)	Average porosity (percent by core analysis)
Q05	1.4(22)	2.5(20)	3.1(22)	2.5(22)	0.4(22)	1.5(20)	18(500)
Q03	0.35(16)	2.0(25)	2.6(26)	1.6(26)	0.20(26)	2.0(25)	15(700)
49/16-7	0.25(7)	2.0(8)	2.0(7)	1.1(7)	–	1.5(8)	15(400)
Q01	0.20(9)	1.5(11)	2.1(9)	2.7(9)	2.0(32)	1.5(11)	10(700)
Q04	0.11(11)	0.5(11)	0.3(11)	4.2(11)	0.8(11)	1.0(11)	9(550)
Q02	0.05(13)	0.5(13)	2.0(13)	2.0(13)	7.0(13)	1.5(13)	8(70)

The numbers in parentheses are numbers of samples; the values are means.

The nature of the clay coats in well Q05 is shown in Figure 15, a scanning electron microscope (SEM) photograph of an aeolian dune foreset sandstone (22.5% porosity, 961 mD permeability). The primary pore system is relatively clay-free in this sandstone. The grain coats are mostly chlorite, with minor pore-bridging, fibrous illite. The relative abundance of chlorite and illite varies systematically with the abundance of the clay coats; thick clay coats are primarily chloritic, whereas thin clay coats (as in Fig. 15) show some illite development. The chlorite/illite ratio in well Q05 and other Vanguard Field wells is shown in Table 3.

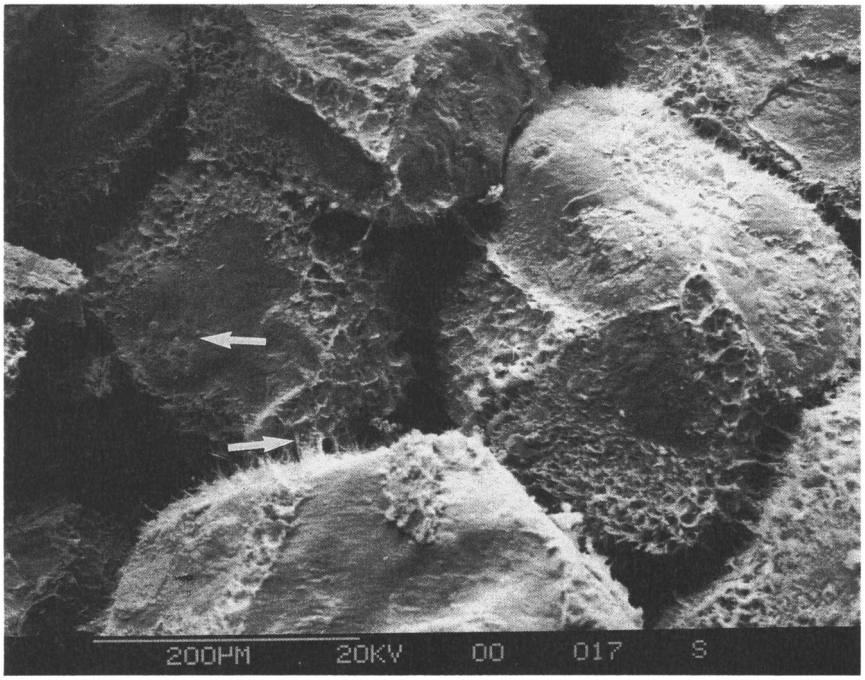

Fig. 15. Scanning electron micrograph of coarse-grained aeolian dune foreset sandstone in well Q05/03. Note the absence of clay in the area of grain contacts (arrow). Grain coating clay is mostly chlorite with some pore-bridging illite (arrow). Large primary pores are not bridged by clay.

The petrography of dune sandstones in well Q03 differs slightly from that in the more productive Q05 well. The core from well Q03 is grey to pink and lacks the red colour and prominent bleached zones of well Q05. Dissolution porosity is present (Fig. 16) but is often more difficult to recognize than in well Q05. Some secondary pores show signs of crushing. Linear grain contacts and other relatively minor compaction features are present. Petrography and XRD (Table 3) indicate slightly less K-feldspar and increased illite relative to chlorite in comparison to the more porous Q05 well. Ankerite (ferroan dolomite) occurs as ferroan rims on dolomite cements.

A compacted dissolution pore is shown in Fig. 17. The clay-coat outlining the dissolved grain was broken and displaced by compaction following dissolution. The

remaining clay-coat outlines an irregular and elongate dissolution pore. Aeolian deposition of a grain with this shape is highly unlikely (cf. Figs 14 and 16).

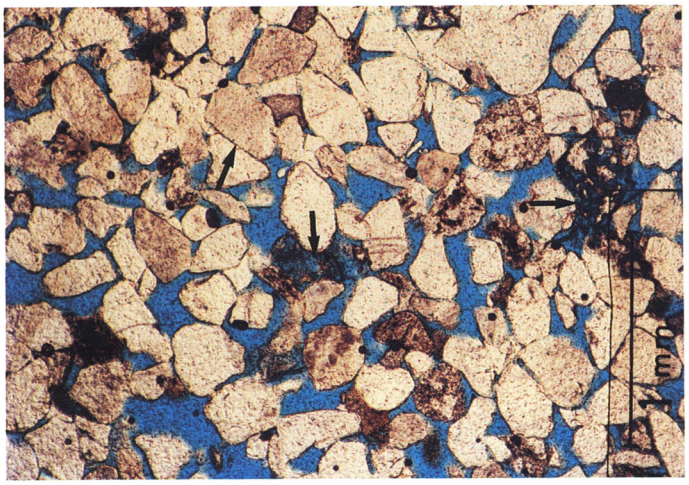

Fig. 16. Thin-section photomicrograph of medium- to coarse-grained aeolian dune foreset sandstone in well Q03/08. Porosity is 20%, and permeability is 750 mD. Note the etched feldspar/lithic grains near centre and at far right (arrows). The partially dissolved grain near the centre was partially crushed after the etching event. Many linear grain contacts (arrow) are present.

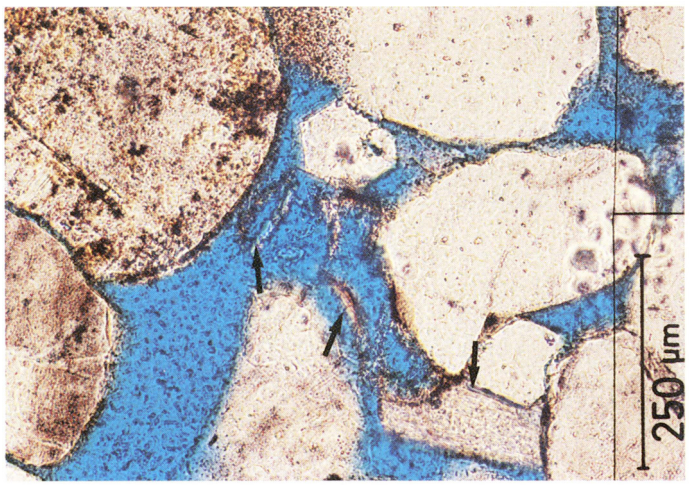

Fig. 17. Higher magnification (relative to Fig. 16) thin-section photomicrograph of medium- to coarse-grained aeolian dune foreset sandstone in well Q03/08. Note the clay-coat outline of a dissolved grain near centre (arrows). The clay-coat has been broken and displaced by compaction yielding a very irregular and elongate dissolution pore. The clay-coat development preceded formation of carbonate cement (arrow). Grain dissolution occurred after formation of the carbonate cement.

The sandstone in well Q01 is generally red in zones B and C and lacks the prominent bleached zones of well Q05 and grey intervals of well Q03. Petrography and XRD indicate decreased abundance of K-feldspar and chlorite relative to well Q03 (Table 3). Ankerite cements are present as are minor compaction features. Texturally, the thin-sections appear intermediate between well Q03 (Figs 16 and 17) and wells Q02 and Q04, discussed below.

Well Q02 was not completed due to poor reservoir properties and a fault-truncated section. The core from this well contains abundant fractures and the sandstone is generally grey in colour. Thin-section photomicrographs of a aeolian dune foreset sandstone from well Q02 (6% porosity, 0.1 mD permeability) are shown in Fig. 18. The sandstone is highly compacted, including crushed lithic fragments, and contains substantially more anhydrite than is typical for the Vanguard Field (Table 3). Authigenic illite appears more abundant (Fig. 19) than in well Q05. The data in Table 3 indicate that well Q02 contains less K-feldspar and has a lower chlorite/illite ratio than wells Q03 and Q05. The data in Table 1 and the textures in Figs 17 and 18 suggest introduction of anhydrite, as a diagenetically late (post-compaction) pore-filling cement in well Q02. The most probable source of anhydrite is via Zechstein-sourced fluids which entered the Rotliegendes through the faults which cut the Rotliegendes in this well. This cement addition contributes to the poor reservoir quality in this well.

Well Q04, like well Q02, could not be economically completed. The core from this well was highly indurated and grey/white throughout and is probably truncated by a fault near the base of zone C. A thin-section photomicrograph from an aeolian dune foreset sandstone (13% porosity, 0.22 mD permeability) in well Q04 is shown in Fig. 20. The sandstone is highly compacted and contains little porosity. The data in Table 3 indicate that K-feldspar is practically absent from this well.

The diagenesis of the Vanguard Field sandstones, both aeolian dune foreset sandstones and other facies, is summarized in Fig. 21. The Vanguard Field sandstones did not experience the extensive formation of kaolinite from feldspar which characterizes the early diagenesis of many Rotliegendes reservoirs (Glennie *et al.* 1978; Lee *et al.* 1989). This conclusion is consistent with the observations of Rossel (1982) that Rotliegendes reservoirs in the Sole Pit Basin contain drusy illite/chlorite and feldspar rather than kaolinite. The textural features present in Figs 14 and 15 suggest that the grain coating chlorite formed from pellicle clays and iron oxide cements. The development of illite is associated with the diagenetically later dissolution of K-feldspar.

Discussion

Several patterns are apparent from Table 3 and the preceding discussion. The progression from well Q05 to Q03, Q01 and Q04 corresponds to rapidly declining productivity directly related to diagenesis. Average porosity declines from 18% (Q05) to 9% in well Q04 (Table 3). The reservoir property decline is paralleled by decreases in K-feldspar content and chlorite–illite ratio. The associated losses of porosity and feldspar (Table 3) appear contradictory since much of the secondary porosity observed in wells Q05 and Q03 is developed in K-feldspar grains or in K-feldspar bearing lithic grains. The small distance between the wells (about 2 km maximum) and the similarity in grain size and facies make differences in primary sand composition highly unlikely.

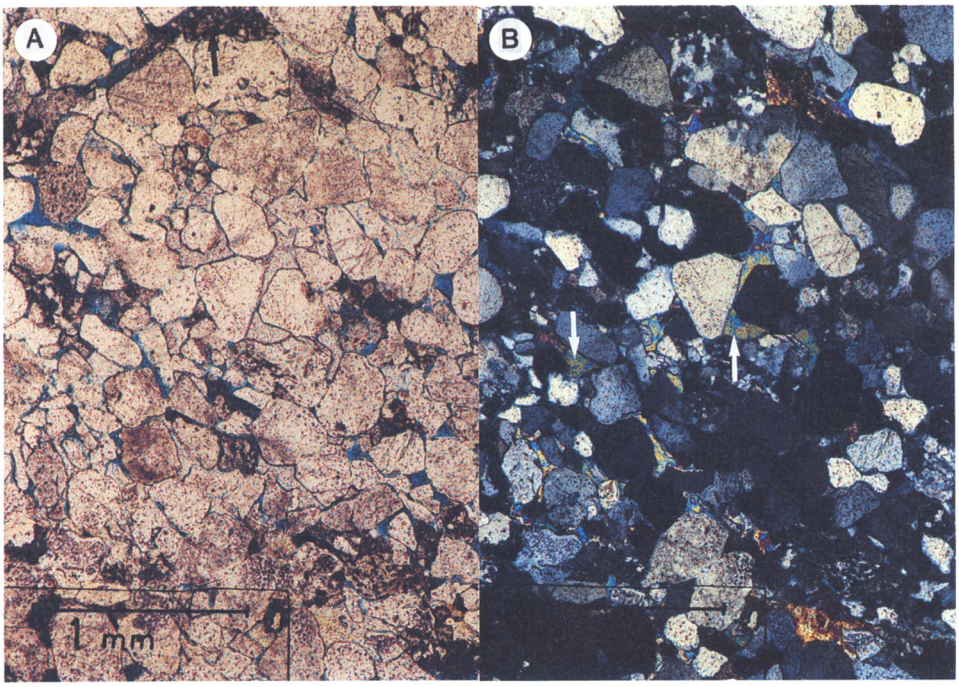

Fig. 18. (**A**) Thin-section photomicrograph of medium- to coarse-grained aeolian dune foreset sandstone in well Q02/08Z. Note the crushed lithic grain at top of photograph (arrow) and the general absence of porosity. Core measured porosity is 6%, and permeability is 0.1 mD. (**B**) Same field of view as in (**A**), with crossed polarizers. Note the many small areas of pore-filling birefringent anhydrite cement (arrows).

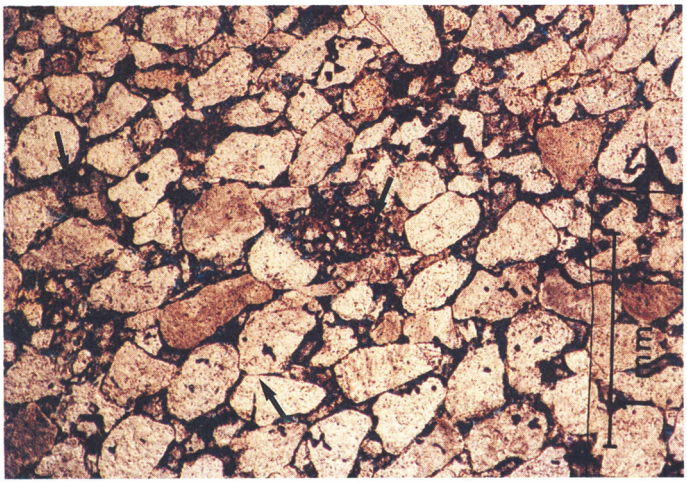

Fig. 20. Thin-section photomicrograph of medium- to coarse-grained aeolian dune foreset sandstone in well Q04/09. Porosity is 13%, and permeability is 0.22 mD. Note the compacted texture, the absence of porosity, and the long grain contacts at the lower left (arrow). Near centre (arrow) is a crushed lithic fragment. Pseudo-matrix clay from crushed lithic fragements is dispersed throughout the field of view, especially at the upper left (arrow).

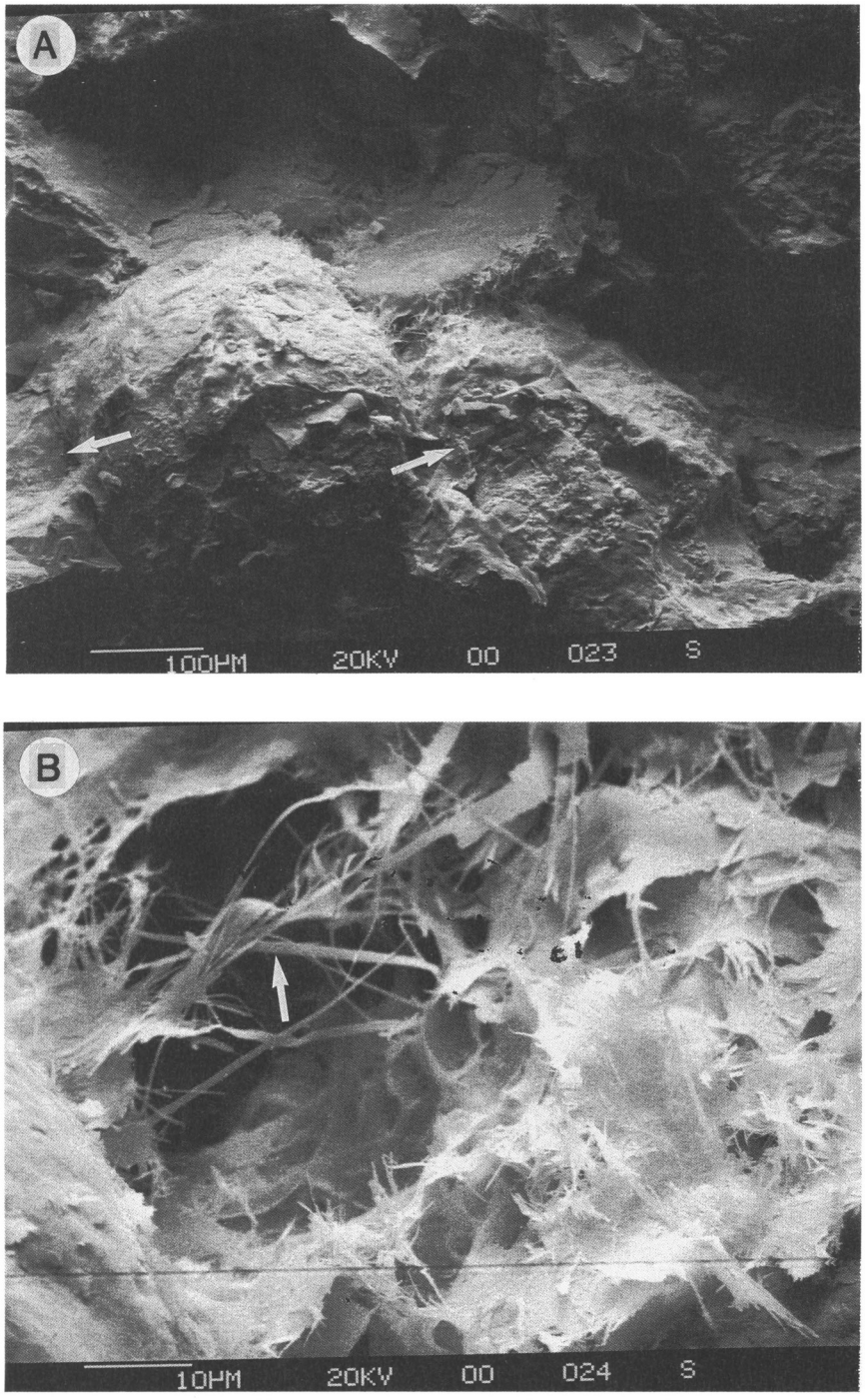

Fig. 19. (**A**) SEM photograph of medium- to coarse-grained aeolian dune foreset sandstone in well Q02. Note the linear grain contact at lower left (arrow) and minor anhydrite cement near centre (arrow). (**B**) High magnification view of centre of (**A**). Note extensive development of pore-bridging authigenic illite (arrow).

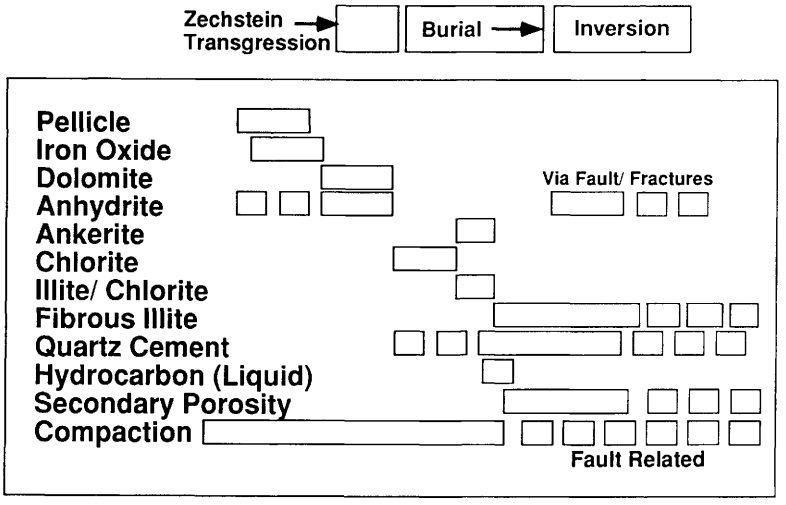

Fig. 21. Diagenetic summary for the Leman Sandstone of the Vanguard Field.

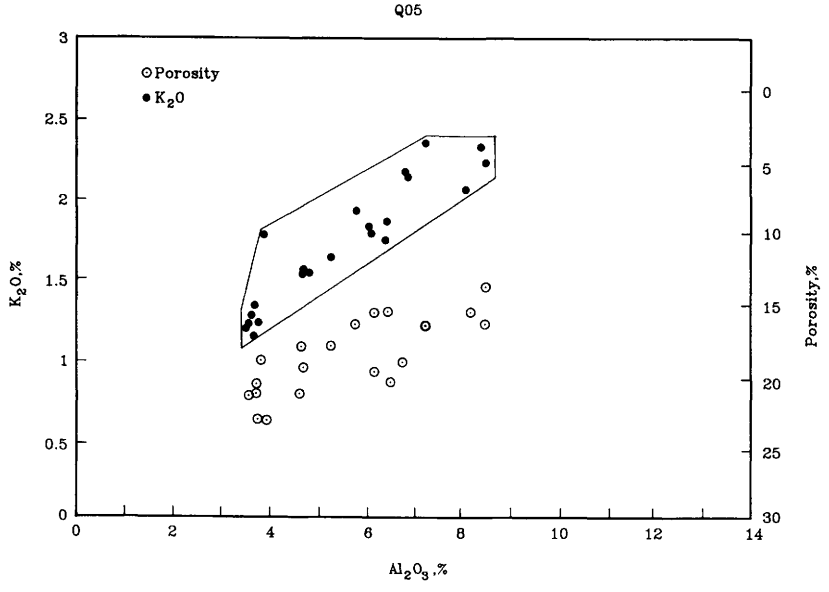

Fig. 22. Cross-plot of K_2O and porosity versus Al_2O_3 content for well Q05/03.

The assumption of uniform sand population, for a given facies, suggests that the current K-feldspar content of well Q05 is a minimum value for primary K-feldspar content for all the wells. Although secondary porosity is most prominent (visible) in well Q05, wells Q03, Q01, Q02 and Q04 experienced more feldspar dissolution. Recent work by Harris (1989) and McBride (1987) suggests that sandstones become

more quartzose during diagenesis because of feldspar dissolution. The data in Table 3 indicate that such a relationship exists among the Vanguard Field wells. Progressive loss of K-feldspar might lead to removal of K_2O from the sandstone as well. Figure 22 presents cross-plots of K_2O and porosity against Al_2O_3 content for aeolian dune and damp interdune sandstones from well Q05. Highly porous, quartz-dominated sandstones have compositions at the low Al_2O_3 end of the data field, whereas low porosity sandstones have compositions at the Al_2O_3 enriched end of the data field. Low K_2O content is associated with low Al_2O_3 and high porosity; high K_2O is associated with high Al_2O_3 and low porosity. K_2O and Al_2O_3 correlate inversely with reservoir properties because K_2O and Al_2O_3 are associated with K-feldspar and clay, which are both enriched in the finer-grained and less well-sorted facies. The samples with least amounts of K_2O and Al_2O_3 are consistently the aeolian dune foreset sandstones from unit C.

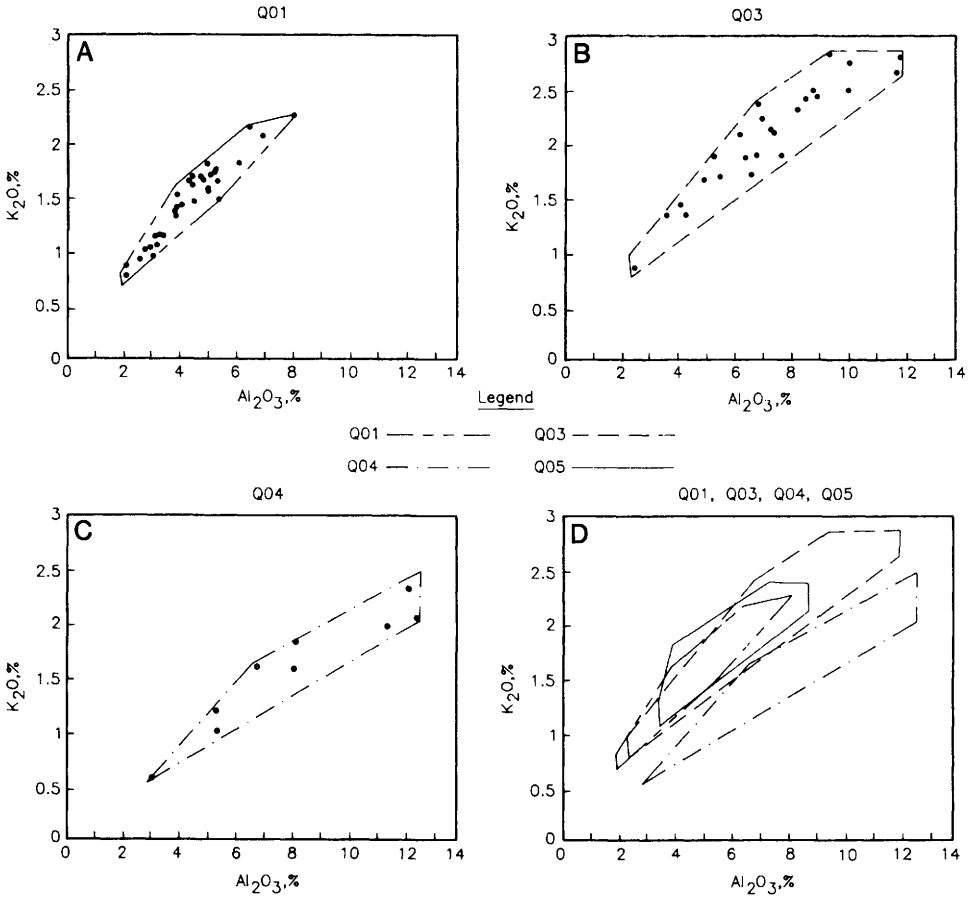

Fig. 23. Cross-plots of K_2O and Al_2O_3 for wells Q03/08 (**A**), Q01/02 (**B**), and Q04/09 (**C**). (**D**) overlays the data fields for wells Q05/03, Q03/08, Q01, and Q04/09.

Several interesting patterns exist in the data on Fig. 23, which shows cross-plots of K_2O against Al_2O_3 from all facies in wells Q05, Q03, Q01, and Q04. The range in maximum Al_2O_3 content is quite large, reflecting the sampling of some clay-rich

sandstones. The minimum Al_2O_3 varies to a far smaller degree among the wells. The minimum K_2O content observed for well Q05 was 1.15%. Minimum values of 0.9, 0.75, and 0.6% K_2O were recorded for wells Q03, Q01, and Q04, corresponding to the decreased K-feldspar content of these wells (Table 3). Unrepresentative sampling is an unlikely cause for this offset since the most porous and permeable sands were sampled in each well. The geochemical data indicate that some of the K_2O present in the K-feldspar was removed from the system, especially from the most porous intervals, leaving those intervals depleted in K_2O, relative to well Q05.

Although K_2O was removed from wells Q03, Q01, and Q04, these wells are less porous than Q05; the volume of dissolved K-feldspar was not preserved as dissolution porosity. Wells Q03 and Q04 often contain fine-grained silicic material in the pore system (Figs 16 and 20). This material can sometimes be identified as deformed lithic fragments (pseudomatrix). We propose that wells Q05–Q03–Q01–Q04 represent a continuum of progressive K-feldspar dissolution. As feldspar was removed, many of the lithic fragments were crushed. This process led to a net reduction in primary porosity and deterioration of reservoir properties. The early chlorite grain coats (Fig. 16), which inhibited quartz cementation, helped preserve a friable and compactible rock fabric. Although average porosity declines from 18 to 9% from well Q05 and Q04, the volume of quartz cement is constant at about 1–2% (Table 3), supporting the conclusion that compaction, not cementation, is the primary cause of porosity loss. Carbonate, anhydrite, and clay cements show a similar lack of increase between Q05 and Q04.

The data in Table 3 indicate a decrease in the chlorite/illite ratio, as determined by peak area ratios, associated with the loss of K-feldspar. Some of the K_2O (and Al_2O_3) released by K-feldspar dissolution was probably incorporated in conversion of chlorite in illite, thereby lowering the chlorite/illite ratio and providing iron for formation of ankerite. XRD peak locations indicated that substantial amounts of mixed-layer chlorite/illite were not formed.

Figures 15 and 19 indicate increased development of authigenic illite in well Q02 relative to Q05. This reaction probably occurred after conversion of most of the available chlorite to illite. Formation of authigenic illite cannot accommodate all the K_2O released by K-feldspar dissolution, leading to a net loss of K_2O from the system (reaction 1).

$$KAlSi_3O_8 + 2/3\ H_2CO_3 = 1/3KAl_2(Si_3AlO_{10})(OH)_2 + 2SiO_2 + 2/3K^+ + 2/3HCO_3^- \quad (1)$$

The progressive loss of K_2O from the system, the low K-feldspar content, and the very low chlorite/illite ratio suggest that much of the K-feldspar originally present in wells Q02 and Q04 was converted to authigenic illite.

We have no evidence in the form of interval velocity differences, shale density differences, or missing/expanded portions of the section to suggest that burial history differences can account for the dramatically different reservoir properties and mineralogies between wells Q04 and Q02. A deeper burial history for well Q04, to account for the lower porosity, is further constrained by the virtually identical burial depth for the wells today.

Reaction 1 requires input of acidity from the solution in some form. We have chosen to balance the equations using a H_2CO_3 acid source. This acid requirement

suggests that the extent of K-feldspar removal or alteration may be related to the amount and/or corrosive strength of the pore fluids which have passed through the sandstone.

The least porous/least feldspathic well examined, Q04, is cut by a fault which could have acted as a conduit for both acidic fluids and gas to be trapped in the Vanguard structure. Similarly, well Q02 is cut by faults and is highly illitic and feldspar depleted. We propose that the great variability in reservoir quality in Vanguard Field is due to spatial variations in fluid migration paths. Low-porosity wells were altered relative to the high porosity wells by passage of more corrosive or greater amounts of corrosive fluids. The source of the fluids was most likely faults which cut the wells and introduced acidic fluids from the underlying Carboniferous units. The effect of this fluid was to dissolve K-feldspar, thereby facilitating compaction of the rock framework, illitization of chlorite, and ankerite formation.

Wells Q04 and Q02 could have been located beneath a paleo-gas–water contact during this migration/alteration event, but we have no direct evidence for such an interpretation. The sandstones beneath the gas–water contact in wells Q01, Q03, and Q05 are petrographically similar to gas-saturated sandstones in the wells and do not resemble wells Q02 and Q04. The absence of extensive illite formation in the water-bearing portion of wells Q03 and Q05 suggests that the water associated with the illitization event was more chemically reactive than the current pore-water.

The reaction of K-feldspar with kaolinite to produce illite does not require an acid source (Bjørlykke 1984). Thus, illitization of kaolinite/feldspar-bearing Rotliegendes reservoirs may proceed as a relatively closed chemical system, leading to widespread illite development as reported by Lee *et al.* (1989) and Rossel (1982). The requirement of an external acid source for illitization of chlorite (reaction 1) probably contributes to the localized nature of the altered reservoirs in the Vanguard Field. The relative absence of illitization in wells Q03 and Q05 can be attributed to the lack of early kaolinite development combined with minimal introduction of fault-associated fluids.

Conclusions

(1) Zone C is the principal producing zone in the Vanguard Field. The high productivity of this zone is due to a good porosity and permeability in aeolian dune foreset sandstones and good interconnectivity of the dune sandstones.

(2) Aeolian dune sandstones in zones A and B are generally unproductive because the individual dunes with good reservoir characteristics are isolated by impermeable damp interdune sandstones.

(3) Productivity differences between sedimentologically similar zones in wells are related to the extent of diagenetic alteration. The most porous and productive well, Q05, was least chemically altered by migrating pore fluids. The least productive wells, Q04 and Q02, were highly altered by migrating fluids. Well Q04 experienced almost complete alteration of K-feldspar to illite and extensive physical compaction; well Q02 was chemically altered, mechanically compacted, and cemented by the introduction of anhydrite.

(4) Understanding the controls on gas production in the Vanguard Field requires integration of a variety of information types, including sedimentology, petro-

graphy and production logging. Explanation of the highly variable production rates would not have been possible without extensive core control.

References

BJØRLYKKE, K. 1984. Formation of secondary porosity: How important is it? *In:* MACDONALD, D.A. &: SURDAM, R.C. (eds) *Clastic Diagenesis*. American Association of Petroleum Geologists Memoir, **37**, 277–286.

GLENNIE, K.W., MUDD, G.C. & NAGTEGAAL, P.J.C. 1978. Depositional environment and diagenesis of Permian Rotliegendes sandstones in Leman Bank and Sole Pit areas of the U.K. southern North Sea. *Journal of the Geological Society, London*, **135**, 25–34.

HARRIS, N.B. 1989. Diagenetic quartzarenite and destruction of secondary porosity. An example from the Middle Jurassic Brent sandstone of northwest Europe. *Geology*, **17**, 361–364.

HEWARD, A.P. 1990. Inside Auk—The Anatomy of an Eolian Oil Reservoir. *In*: MIALL, A.D. & TYLER, N. (eds) *The Three-Dimensional Facies Architecture of Terrigenous Clastic Sediments, and its Implications for Hydrocarbon Discovery and Recovery*. SEPM Concepts and Models in Sedimentology and Palaeontology Series, **583**, 44–56.

LEE, M., ARONSON, J.L. & SAVIN, S.M. 1989. Timing and conditions of Permian Rotliegend sandstone diagenesis, southern North Sea: K/Ar and oxygen isotopic data. *American Association of Petroleum Geologists Bulletin*, **73**, 195–215.

LINDQUIST, S.J. 1988. Practical characterisation of eolian reservoirs for development: Nugget Sandstone, Utah–Wyoming thrust belt. *Sedimentary Geology*, **56**, 315–339.

MCBRIDE, E.F. 1987. Diagenesis of the Maxon sandstone (Early Cretaceous), Marathon region, Texas: a diagenetic quartzarenite. *Journal of Sedimentary Petrology*, **57**, 98–107.

ROSSEL, N.C. 1982. Clay mineral diagenesis in Rotliegend aeolian sandstones of the southern North Sea. *Clay Minerals*, **17**, 69–78.

WALKER, I.M. & COOPER, W.G. 1987. The structural and stratigraphic evolution of the north-east margin of the Sole Pit Basin. *In*: BROOKS, J. & GLENNIE, K. (eds) *Petroleum Geology of North West Europe*. Graham & Trotman, London, 263–276.

From ASHTON, M. (ed.), 1993, *Advances in Reservoir Geology*,
Geological Society Special Publication No. 69, pp. 57–79.

Quantitative analysis of pore structure and its effect on reservoir behaviour: Upper Jurassic Ribble Member sandstones, Fulmar Field, UK North Sea

W. D. CLELLAND,[1] J. D. KANTOROWICZ[2] & T. W. FENS[3]

[1] *Present address: Shell Expro, 1 Altens Farm Road, Nigg, Aberdeen, UK*
[2] *Present address: Conoco (UK) Ltd, Park House, 116/129 Park Street, London W1Y 4NN, UK*
[3] *Koninklijke/Shell Exploratie en Produktie Laboratorium, Postbus 60, 2280 AB Rijswjik ZH, Netherlands*

Abstract: Image analysis has been used to quantify the pore structure of dolomite-cemented sandstones in the Ribble Member of the Fulmar Field, UK North Sea. This technique was used because the data obtained from conventional petrography did not enable quantification of the controls on permeability. Three-quarters of the sandstones in the Ribble Member have high measured porosity and permeability (ϕ17–29%, K_h40–1800 mD). In these poorly cemented sandstones, intergranular porosity predominates and permeability reflects (depositional) sediment texture. One quarter of the sandstones contain >20% dolomite. The dolomite (mean δ^{13}C PDB +0.8‰, mean δ^{18}O PDB −2.3‰) formed from sea water trapped and buried within the sediments and occurs as patches or nodules that should not form reservoir scale barriers to fluid flow. These cemented sandstones are less permeable (ϕ15–25%, K_h0.4–600 mD). They contain grain-dissolution pores created by the dissolution of sponge spicules and intercrystalline pores between the dolomite rhombs.

Backscattered electron imaging and automated image analysis have enabled quantification of the differences in pore structure between the poorly cemented and cemented sandstones. Permeability is not only related to the amount of porosity present, but also to the amount of dolomite cementation. The degree of cementation influences average pore area and pore connectivity, which in turn controls permeability. Permeability is lower in the cemented sandstones because the dolomite rhombs have occluded the intergranular pores, creating restricted flow paths through small intercrystalline pores. As a result of these differences in pore structure, hydrocarbon production from the cemented sandstones will be slower than from the poorly cemented sandstones.

The permeability of the cemented sandstones cannot be predicted from porosity logs alone but also requires knowledge of the amount of dolomite cement present. In uncored wells this information should be obtainable using modern wireline log evaluation techniques. This study demonstrates the importance of combining a detailed understanding of the rock's pore structure with a sound geological model in order to predict reservoir behaviour.

Thin-section description has been at the core of most petrographical studies during the last century. Recent developments such as cathodoluminescence and scanning electron microscopy have greatly enhanced such studies (Burley *et al.* 1985) but the thin-section usually remains the fundamental source of data. The percentages of the minerals and different types of porosity present are quantified using modal analysis, although this is inherently inaccurate for less abundant components (van der Plas & Tobi 1965). However, most of the other data that could be derived from a thin-section are obtained qualitatively rather than quantitatively. Sometimes they are not

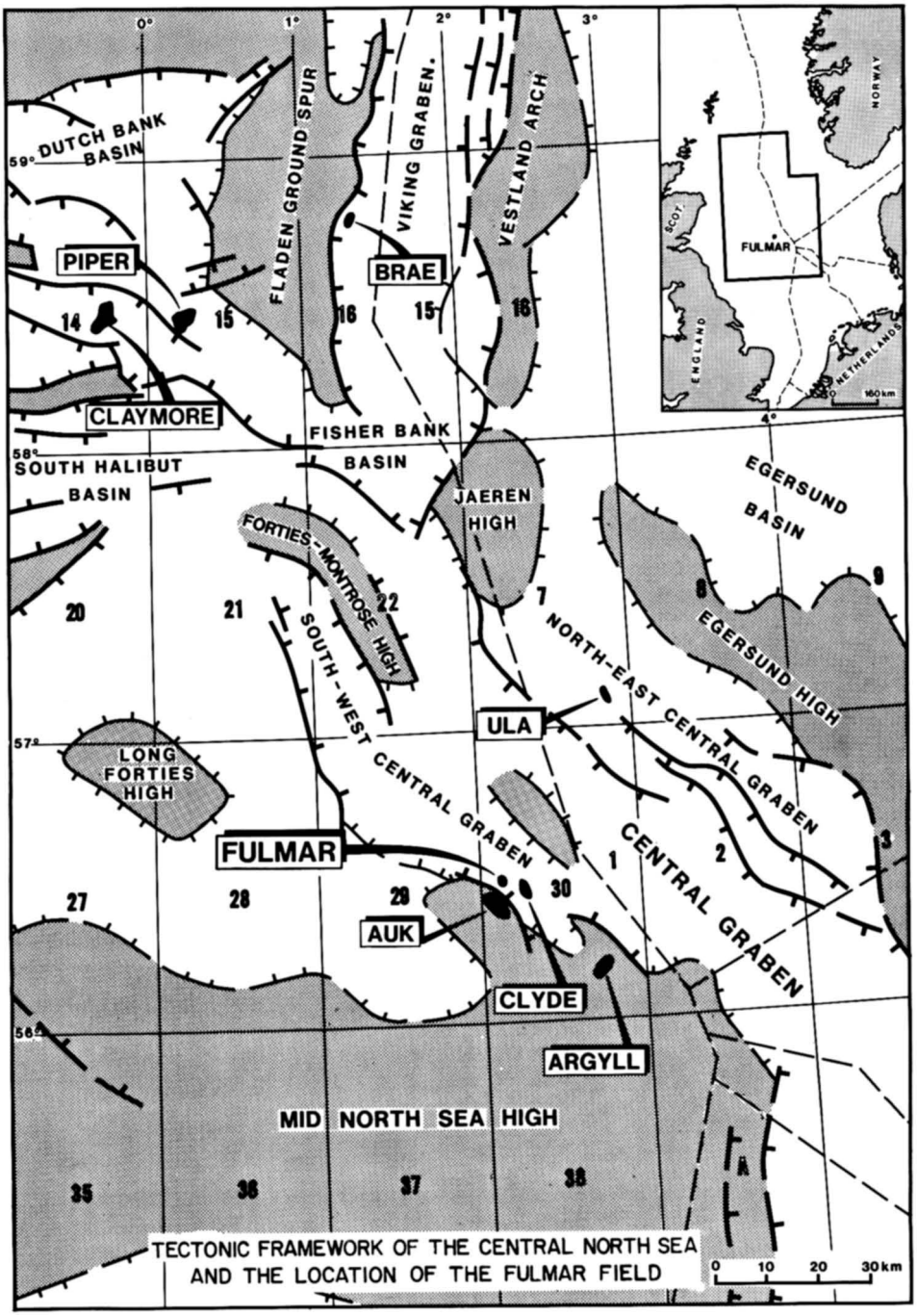

Fig. 1. Tectonic framework of the central North Sea and the location of the Fulmar Field

collected at all. Detailed textural information such as grain shape or grain size, or information regarding pore structure is collected rarely. This is because attempts to obtain such data during visual examination of a thin-section are liable to be subjective, inaccurate, difficult to repeat and extremely labour intensive. Image analytical techniques offer an alternative means of generating such data (Ehrlich *et al.* 1984; Rink & Schopper 1977). Using an automated system offers a number of advantages over conventional thin-section description. First, the procedures are applied consistently. This removes operator bias, subjectivity and errors. The analysis also is repeatable. Secondly, the data are more accurate, being collected with a system with a two micron resolution. Thirdly, as the procedures are automated, a significant time saving can be made.

This paper describes how image analytical techniques were employed to provide quantitative porosity data during a petrographical analysis of Upper Jurassic sandstones from the Ribble Member in the Fulmar Field. The study was undertaken to establish the controls on porosity and permeability in the sandstones. The purpose of this type of study is to establish if a relationship exists between porosity and permeability which will enable the estimation of permeability in uncored wells where porosity has been measured using wireline logs. Image analytical techniques were employed during this investigation because the data obtained from more conventional techniques did not enable rigorous quantification of the controls on permeability. Image analysis was used to quantify aspects of the porosity such as the size and degree of connectivity of the pores, and the length of the pore throats. Using image analytical techniques these data were collected automatically and so they are both consistent and repeatable. Data collection and data processing takes a few minutes per sample. During conventional thin-section petrography, measurement of pore area is likely to be inaccurate, the identification of pore throats will be subjective, and connectivity would have to be calculated manually. All these measurements are extremely time consuming and therefore labour intensive during conventional thin-section description and are unlikely to be repeatable accurately.

This study of the Ribble Member was undertaken to enable prediction of likely reservoir behaviour prior to oil production. The history of Fulmar Field development has been described by van der Helm *et al.* (1990) and will not be discussed further in this paper. The Ribble Member forms the shallower of two reservoirs in the Fulmar Field (Figs 1 & 2). The sandstones in the Ribble Member are interpreted as mass flow and turbidite deposits that probably were derived from the erosion of the Auk Horst and, as a result, form discrete lobes or lenses within the Kimmeridge Clay Formation that are restricted to the western side of the field (Johnson *et al.* 1986; van der Helm *et al.* 1990).

Petrography and diagenesis

Petrographical description

Sixteen core plug samples were selected from the Ribble Member sandstones in Well 30/16-FA31 (Fig. 2). The samples were selected to encompass the range of porosity and permeability measured on plugs from the core (Fig. 3). Macroscopically, the

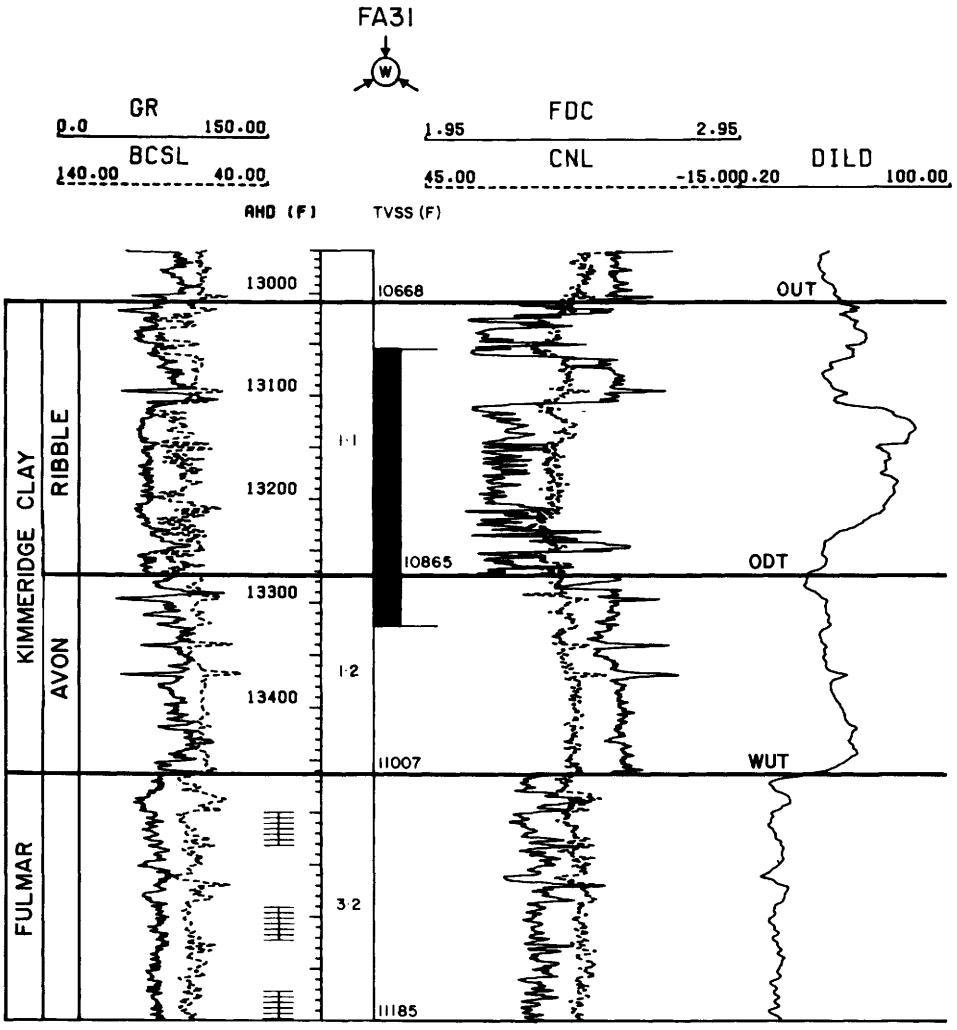

Fig. 2. Wireline log display, Ribble Member, Well 30/16-FA31. The Gamma Ray (GR), Borehole Compensated Sonic (BCSL), Formation Density (FDC), Compensated Neutron (CNL) and Dual Induction Log-Deep (DILD) are shown. The well was drilled during 1982 to inject water into the Fulmar sandstones through the perforated interval shown. The logs are displayed in along-hole depth and true vertical depth subsea, in feet. No oil–water contact is present in the well, the top of the Ribble corresponding to an 'oil-up-to', and the bottom to an 'oil-down-to'. The Fulmar Fomation contains water. The cored interval is indicated in black and is shown at logger's depth. Throughout the paper, core samples are referred to in driller's depths. Logger's depths are approximately 17 ft deeper than driller's depths.

cored interval comprises (from the base) 20 ft of 4–5 ft thick massive sandstone beds interbedded with thin shales, 20 ft of shales with thin sandstone beds up to a foot thick, 120 ft of fine to medium grained massive or locally cross-bedded sandstone and 50 ft of shales, siltstones and 1–2 ft thick sandstones. Most of the sandstones are heavily oil stained, the remainder are patchily oil stained or light grey due to the presence of dolomite cement. The cemented intervals are not restricted to any

particular grain size or lithofacies, nor are they restricted to bed boundaries, sandstone–shale contacts, or beds of a certain thickness. Cementation occurs in dispersed patches and over intervals several feet thick. None of the classic features of early septarian nodule growth such as deformation of the surrounding laminae are observed (cf. Raiswell 1971).

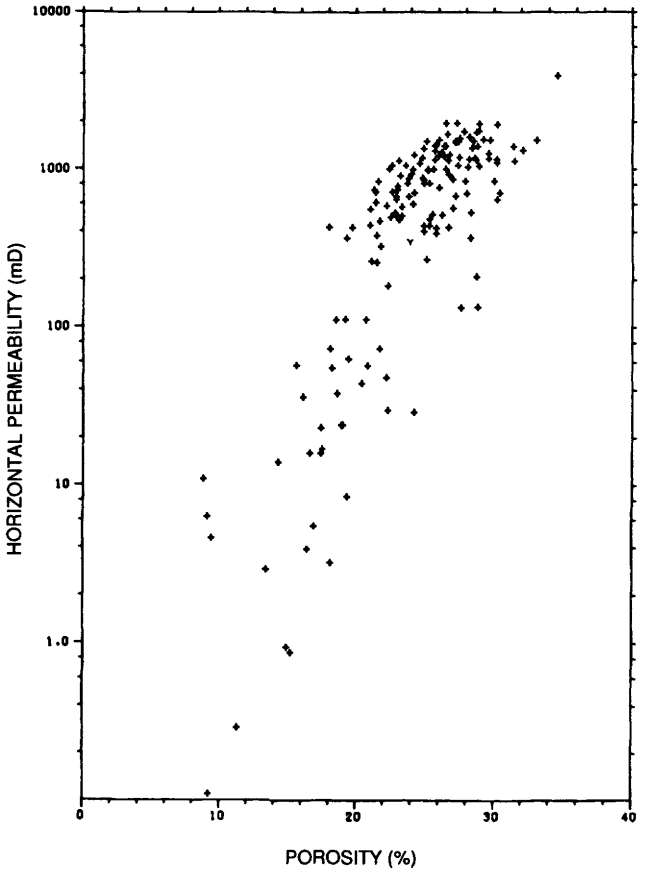

Fig. 3. Cross-plot of horizontal permeability versus plug porosity, Ribble Member sandstones, Well 30/16-FA31, Fulmar Field.

Thin-sections were made for all the samples, and examined using transmitted light and cathodoluminescence microscopy. Representative samples were examined using the scanning electron microscope (SEM), and the clays and carbonates present were identified using X-Ray diffraction (XRD). Texturally, most of the sandstones are mature. Grain size varies from very fine to coarse sand but is usually fine or medium (Table 1). In the majority of the sandstones the grains are rounded to subrounded and form a well sorted, grain-supported fabric (Fig. 4a & b). In some sandstones abundant dolomite cement creates a floating grain texture (Fig. 4c & d). Mineralogically, the sands are arkosic or subarkosic and quite similar in composition to the sandstones in the marine Members of the Fulmar Formation below (Fig. 5; cf. Stewart 1986).

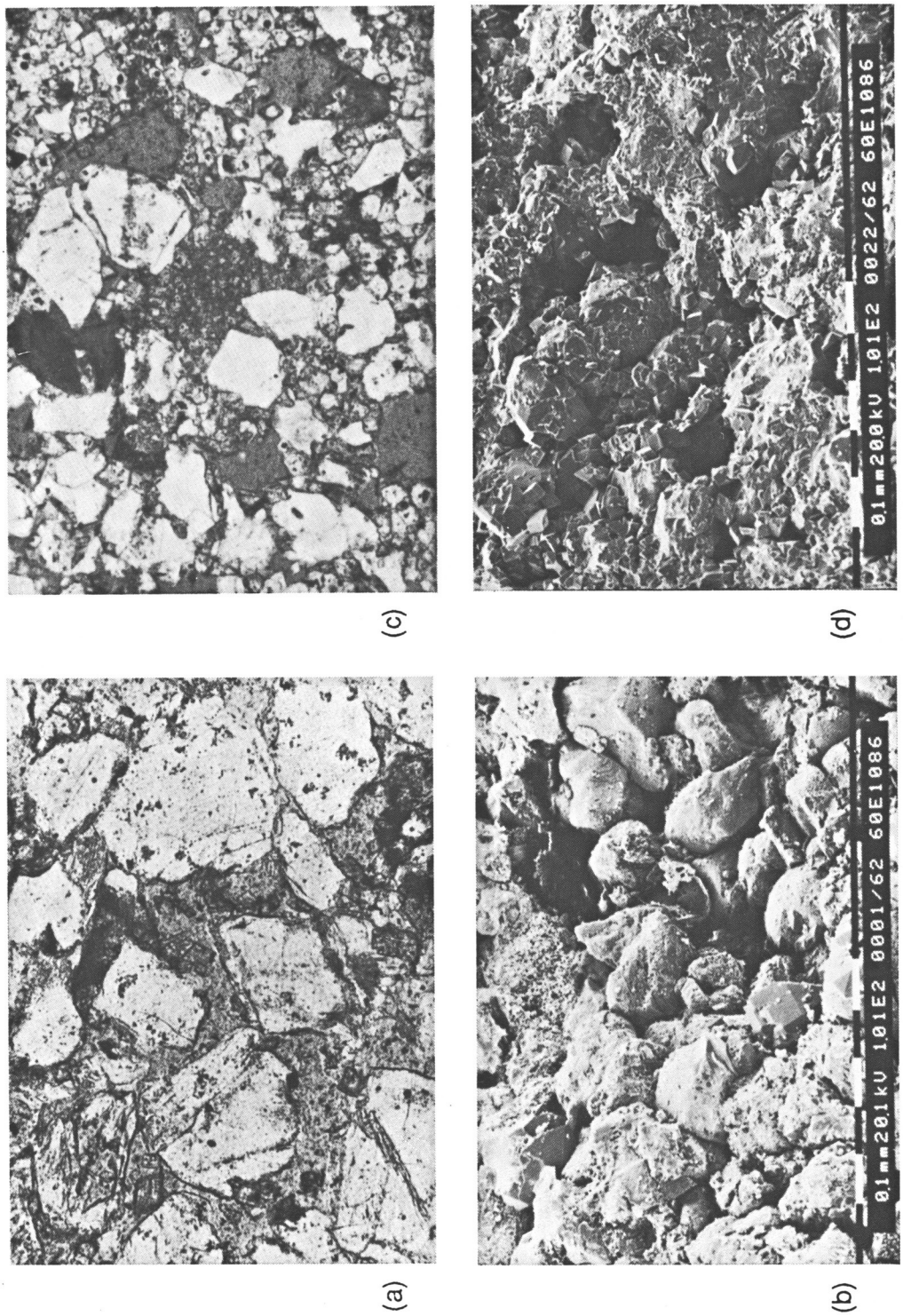

The most volumetrically significant authigenic minerals in these sandstones are dolomite, feldspar, quartz and chalcedony. Pyrite, illite, kaolinite, and barite also occur in places (Table 1). Dolomite occurs as microcrystalline nodules up to 500 μm in diameter and as pore-filling rhombs. The microcrystalline dolomite is non-ferroan and luminesces bright orange and red. The rhombs have non-ferroan cores and rims with a ferroan band. The cores and rims luminesce red, the thin ferroan rim is non-luminescent. The microcrystalline nodules (0–3%, mean 0.4%) enclose authigenic pyrite and are frequently associated with traces of plant debris. Feldspar overgrowths (1–7%, mean 3.7%) occur ubiquitously as a thin veneer on both fresh and subsequently corroded feldspar grains. The rhombic dolomite (0–39%, mean 18.5%) encloses authigenic feldspar overgrowths and micronodular dolomite, and corrodes and replaces detrital quartz and feldspar grains. Spherical pores often occur within the dolomite cemented areas of thin-sections. Dolomite does not enclose authigenic quartz. Chalcedony (0–9%, mean 0.6%) occurs throughout the sandstones as a thin veneer on detrital grains and on feldspar overgrowths. Chalcedony was observed during SEM examination of all the samples but was only locally abundant enough to be quantified during modal analysis. The relationship between the rhombic dolomite and chalcedony could not be established from the petrographical observations. Quartz overgrowths (0–3%, mean 1.3%) occur as a thin veneer on detrital quartz grains in more porous samples but are absent from areas that are tightly cemented by rhombic dolomite. Quartz overgrowths appear to enclose or engulf the chalcedony coatings that exist on the same grains. Illite occurs replacing detrital feldspar grains. Pore-filling types of illite were not observed.

Porosity in these sandstones occurs as intergranular, intragranular, grain dissolution and intercrystalline pores. Observed (modal) porosities (11–32%, mean 19%) generally are lower than measured (plug) porosities (16–29%, mean 22%). This may result from the thin-sections being cut from plugs adjacent to those used for petrophysical analysis, or because thin intercrystalline pores within the dolomite-cemented areas are difficult to observe in thin-section (Fig. 4c & d). Intergranular porosity predominates in the samples with less dolomite cement. As the degree of cementation increases the proportion of remarkably well-rounded grain-shaped (inferred grain-dissolution) porosity increases. SEM examination of dolomite-cemented samples reveals a significant amount of intercrystalline porosity between the dolomite rhombs. This porosity is difficult to quantify in thin-section as these pores are very small (Fig. 4d), and most pores cut the section obliquely.

Fig. 4. (**a**) and (**b**) General views of porous sandstones with thin chalcedony grain coatings, rare quartz overgrowths and feldspar grain dissolution. (**a**) 30/16-FA31, 13 153 ft, porosity 26.7%, permeability 924 mD. Thin-section photomicrograph, plane-polarized light, photomicrograph width 720 μm. (**b**) 30/16-FA31, 13 039 ft, porosity 28.9%, permeability 1765 mD. Scanning electron photomicrograph, scale bar 100 microns.

(**c**) and (**d**) General views of a cemented sandstone. Dolomite occurs as micronodules and distinct rhombs filling porosity between quartz grains. Intercrystalline porosity occurs between the rhombs. Grain-dissolution porosity formed after sponge spicule dissolution. (**c**) 30/16-FA31, 13 193 ft, porosity 16.6%, permeability 16 mD. Thin-section photomicrograph, plane-polarized light, photomicrograph width 1000 μm. (**d**) 30/16-FA31, 13 193 ft, scanning electron photomicrograph, scale bar 100 μm.

Table 1. *Modal and textural analysis, Ribble Member sandstones, Well 30/16-FA31*

Driller's depth (feet)	13 039.0	13 054.5	13 101.5	13 110.2	13 119.8	13 129.0	13 145.0	13 153.0	13 175.0	13 193.0	13 199.5	13 218.0	13 247.0	13 253.0	13 258.0	13 268.0
Rock type*	P	C	P	C	P	C	C	P	P	C	C	P	P	P	P	C
Detrital minerals																
Quartz: simple	44.0	33.3	40.7	20.0	45.3	19.3	30.0	40.7	36.7	21.3	30.0	40.0	44.7	43.4	45.0	26.7
polycrystalline	3.0	2.7	2.7	5.3	1.7	1.0	4.0	3.0	2.7	2.0	5.0	10.3	6.7	7.7	4.0	2.3
K-feldspar	14.7	10.7	13.0	6.3	8.7	11.3	6.7	10.0	9.7	9.0	10.0	4.7	10.0	9.7	11.7	10.0
Microcline		0.7	0.7			0.7	0.7			0.3						
Plagioclase		0.3	0.7				1.0			2.0						
Altered feldspar	6.0	3.3	5.0	4.0	3.3	2.3	4.7	5.0	7.7	6.7	2.3	4.3	5.0	8.3	6.0	4.0
Altered rock fragments							2.0						0.3			
Clay clasts	0.3															
Muscovite		0.3				0.3		1.3	0.3		0.3	0.6				1.0
Heavy minerals		0.3							0.3							
Matrix clay		2.3														1.0
Total	68.0	53.9	62.8	35.6	59.0	34.9	49.1	60.0	57.4	41.3	47.6	59.9	66.7	69.0	66.7	45.0
Authigenic minerals																
Quartz overgrowths	0.7	2.3	2.7	1.7	2.0	1.3	2.7	1.0	1.3	2.7	1.7	0.3			0.3	
Chalcedony									0.3	0.3			9.0	0.3		
Feldspar overgrowths	2.7	2.7	5.0	5.0	4.7	2.3	2.7	3.7	3.0	3.0	1.3	4.0	5.7	6.7	3.0	3.3
Illite	1.0	1.0						0.3		0.3	0.6	1.0				0.3
Microcrystalline dolomite			3.3			2.0				1.7						
Rhombic dolomite		23.0	3.3	36.3	17.0	38.7	31.7	10.3	18.3	36.0	28.0	2.0	1.3	2.7	9.0	39.0
Pyrite		2.3	0.3	2.7		1.0	0.7			1.3	0.3	1.0				1.3
Kaolinite				0.3												
Barite				0.3												
Total	4.4	31.3	14.6	46.3	23.7	45.3	37.8	16.3	22.9	45.3	31.9	8.3	16.0	9.3	12.3	43.9
Porosity																
Intergranular	27.3	8.3	22.0	16.0	15.3	11.7	5.3	22.7	19.3	3.7	13.3	30.3	16.7	20.3	10.7	2.0
Intragranular			1.0						0.3							
Grain dissolution	0.3	6.3		2.0	2.0	8.0	8.0	2.0		9.7	7.0	1.3	0.7	1.0	10.3	9.0
Total	27.6	14.6	23.0	18.0	17.3	19.7	13.3	24.7	19.6	13.4	20.3	31.6	17.4	21.3	21.0	11.0
Core porosity	28.9	19.3	26.4	23.3	19.7	21.1	15.6	26.7	22.8	16.6	25.3	18.0	21.6	26.4	20.4	16.4
Core permeability	1765	8.46	1410	575	426	52	57	924	529	16	436	427	833	1204	43	0.99
Grain size	Fine	Very fine	Fine	Medium	Fine	Fine	Fine	Fine	F–M	Fine	Fine	Medium	Medium	Fine	Fine	Fine
Sorting	Good	Moderate	Good	Moderate	Moderate	Moderate	Good	Good	Moderate	Moderate	Good	Moderate	Good	Good	Good	Good

Cemented (C) and poorly cemented (P) samples are distinguished by a 20% dolomite cut-off.
Modal analysis data are given as percentages.
Modal analyses are based on 300 points per thin-section.
Permeabilities quoted are in millidarcies.

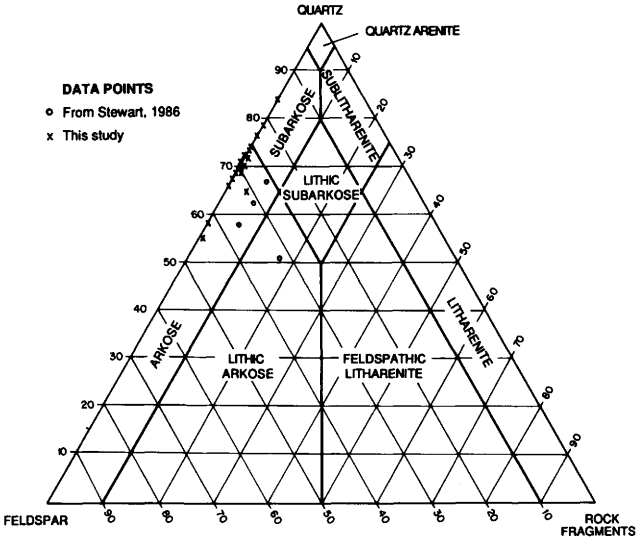

Fig. 5. Detrital mineralogical classification of the Ribble Member sandstones.

Reservoir quality

Reservoir quality in these sandstones reflects both detrital sediment texture and the dolomite content. Analysis of the data indicates that in the samples with less than 20% dolomite cement permeability can be related directly to sediment texture (Table 1). Specifically, for any given average grain size, permeability is highest in the better sorted samples and lower where the original sediment was more poorly sorted. The only exception is 13258 ft which has only 9% dolomite. However, half the porosity is grain-dissolution porosity, whereas in most of the poorly-cemented sandstones, virtually all the pore space is intergranular. In the samples with over 20% dolomite cement, the floating grain textures and evidence of corrosion and grain replacement negate any direct textural comparisons. In these samples permeabilities are one or two orders of magnitudes lower than in the poorly cemented ones. The two cemented samples that do not conform to this trend (13110.2 ft & 13199.5 ft) have relatively high permeabilities. Both have lower proportions of grain dissolution porosity than the other cemented samples. The importance of quantifying the impact of the development of isolated grain-dissolution and intercrystalline pores rather than intergranular porosity led to the application of image analysis described later in this paper.

Stable-isotope analysis

Carbon and oxygen stable-isotope analysis was undertaken to elucidate the origin of the dolomite. Although two dolomite morphologies are present, rhombic dolomite is most abundant in these samples (Table 1) and so it is assumed that the analysis reflects the composition of this cement. The results are presented in Table 2 and Fig. 6 where they are compared with interpretations from Hudson (1977). The carbon

isotopic composition (mean $\delta^{13}C$ PDB +0.81‰) is indicative of a predominantly marine source of carbon when compared to ideal Jurassic sea water compositions of +2‰ (Hudson 1977), with a minor component of more negative bacteriogenic bicarbonate. The oxygen isotopic composition ($\delta^{18}O$ PDB −2.23‰) is approximately 3‰ lighter than would be expected following precipitation from ideal Jurassic sea water ($\delta^{18}O$ PDB + 1‰, Hudson 1977). This suggests dolomite formed at temperatures approaching 40°C (Land 1980).

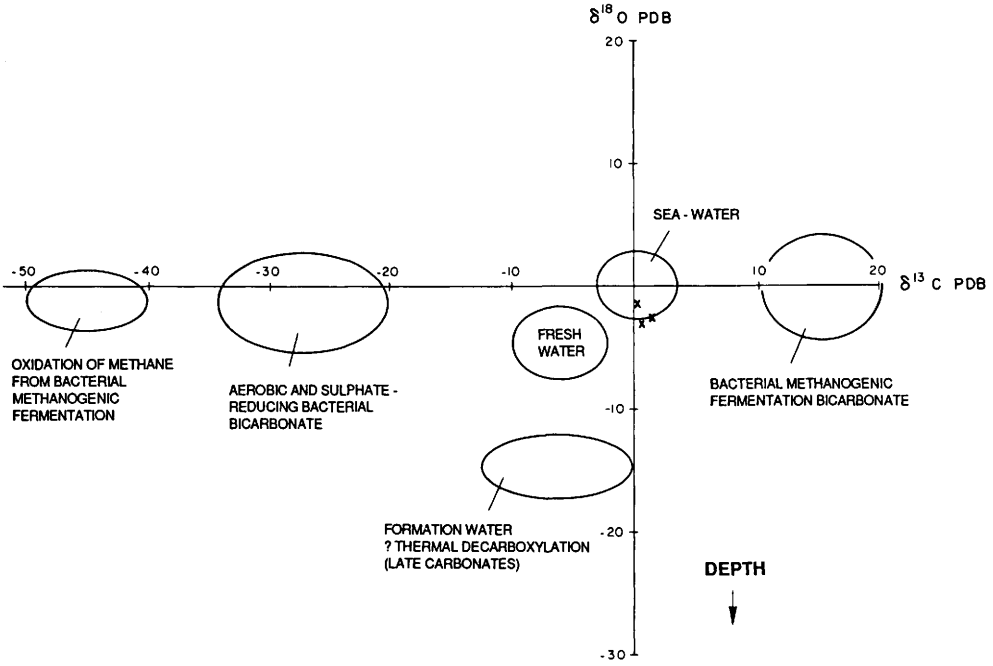

Fig. 6. Comparison of the carbon and oxygen stable isotopes values from the dolomites of the Ribble Member sandstones (x), with common sources of authigenic carbonates in clastic sediments.

Table 2. *Stable isotopic analysis of authigenic dolomites, Ribble Member, Well 30/16-FA31, Fulmar Field*

Driller's depth	$\delta^{13}C$	$\delta^{18}O$
13 119.8 ft	+0.49	−2.91
13 129.0 ft	+1.61	−2.50
13 193.0 ft	+0.33	−1.49
Average	+0.81	−2.23

Dolomite identification was confirmed by XRD

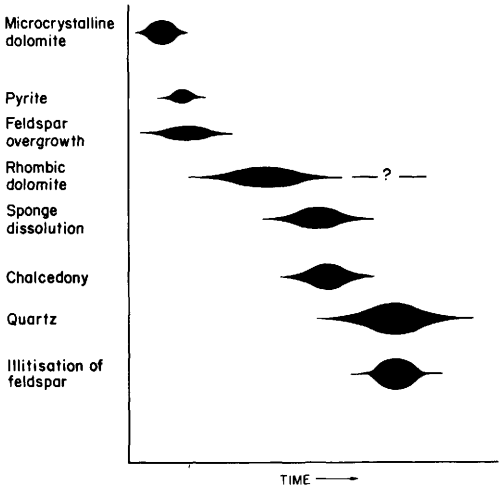

Fig. 7. Generalized diagenetic sequence, Ribble Member sandstones.

Diagenetic model

The interpreted sequence of diagenetic modifications of the Ribble Member sandstones is summarized in Fig. 7. Diagenesis began with the formation of microcrystalline dolomite nodules containing pyrite. The presence of authigenic dolomite cements in these marine sandstones rather than the more normal carbonate cements, calcite or aragonite, is anomalous and requires explanation. Aragonite usually forms rather than calcite for kinetic reasons, whilst both calcium carbonate minerals usually form before dolomite because the sulphate in sea water inhibits dolomite precipitation (Baker & Kastner 1981). However, in organic-rich sediments sulphate reducing bacterial activity removes sulphate from the pore waters and allows dolomite to form (e.g. Hein *et al.* 1979; Baker & Burns 1985). The process is accelerated in areas with high heat flow as would be expected on the margin of the central graben during the late Jurassic (Barton & Wood 1984). Sulphate reduction would also lead to the formation of the associated pyrite. However, the carbon isotopic composition of the dolomites suggests that bacterial activity was not great enough to mask the marine carbonate signature of the original depositional pore waters.

Feldspar overgrowths are enclosed by the dolomite and so are also interpreted to have precipitated from the sea water trapped and buried within the pores during deposition (Kastner & Siever 1979). Subsequently the fabric of the sandstones was modified by two processes: rhombic dolomite cementation, and dissolution of sponge spicules. The dolomite's isotopic composition is indicative of continuing precipitation from the sea water tapped within the sediments. In view of the relatively heavy oxygen isotopic composition, dolomite precipitation may have occurred at a temperature as low as 40°C. Assuming a geothermal gradient of greater than 30°C/km this suggests formation during the first kilometre of burial. Where dolomite cementation was concentrated locally, subsequent spicule dissolution created mouldic or grain-dissolution porosity. This has affected approximately one quarter of the samples studied. On the edges of cemented patches, partially cemented grain-

dissolution moulds occur, suggesting that grain-dissolution porosity is preserved only where there is sufficient dolomite cement to maintain an open fabric after dissolution. In three-quarters of the samples dolomite cementation was less extensive, and a chalcedony lining on most quartz grains is the only evidence that sponge spicules were present originally. No data were collected to elucidate whether this silica is truely amorphous or whether it is a form of opal. In these rocks, the pore system is predominantly intergranular. No textural evidence of the former presence of spicules remains. Quartz overgrowths formed relatively late during diagenesis. The silica may have been supplied in part from the alteration of feldspars (Bjørkum & Gjelsvik 1988) but is most likely to have formed from silica originally present as spicules (Kastner *et al.* 1977; Murata *et al.* 1977). The alteration of potassium feldspars to illite also is inferred to have occurred relatively late during burial diagenesis, as this requires more elevated temperatures.

Discussion and implications for mineral distributions

The diagenetic modifications to the Ribble Member sandstones in the Fulmar Field are interpreted to have operated within an essentially closed system. All the diagenetic processes appear to require only the presence of the original sediments or sea water. No externally-derived solutes are involved. Feldspar overgrowths and dolomite formed from sea water that was either trapped within the sands or was forced into them from the surrounding mudrocks. Illite and chalcedony (later altered to quartz) precipitated following the alteration of feldspars and dissolution of sponge spicules.

The volume of material that can precipitate from sea water trapped or expelled into a sand is limited (Bjørlykke 1979). Texturally, the dolomite cemented intervals showed no distinct zonation from cores to margins, suggesting that they grew from a compositionally similar source of pore water, rather than the variable sources one might expect from continued growth during burial (cf. Hudson 1977). In view of this and the isotopic data, the cemented intervals are interpreted to be patchily distributed or possibly nodular rather than laterally extensive, and lacking obvious nuclei such as clays or organic matter, are probably randomly distributed throughout the sands. This petrographical observation is consistent with the distribution of dolomite cementation observed macroscopically. Although no sponge spicule remains were observed in any of the samples, it is worth considering whether they might have provided a nucleus for dolomite precipitation and so localized dolomite development. The most obvious contrary indicator is that evidence of spicule dissolution also exists outside the cemented intervals. The former presence of sponge spicules does not appear to have been restricted to any particular horizon. This may reflect their originating on the Auk Horst, from where they were reworked during turbidite deposition. It may be concluded that the dolomite cement is patchily distributed and occurs in irregularly coalescing areas that are unlikely to cause compartmentalisation or form barriers to fluid flow at a macroscopic or reservoir scale (cf. Kantorowicz *et al.* 1987). Nonetheless, the cemented sandstones are significantly less permeable than the poorly-cemented ones and so, as they represent approximately a quarter of the cored interval, their pore structure and its likely impact on reservoir behaviour was investigated further.

Quantification of pore structure

The petrographical examination of the Ribble Member sandstones highlighted a number of features of the pore structure that warranted further investigation. The sandstones which are tightly cemented with dolomite often contain a significant amount of grain-dissolution porosity resulting from sponge spicule dissolution. From thin-section and SEM observations this porosity appears to be isolated or poorly connected through thin sheet-like intercrystalline pores between the dolomite rhombs. As a result permeabilities can be very low although plug porosities are high (e.g. 13054.5 ft; porosity: 19.3%, permeability: 8.46 mD; see Table 1). This effect is greater in samples where grain-dissolution porosity makes up a significant proportion of the total modal porosity (Fig. 8). The suggestion that the grain-dissolution pores do not increase permeability because they are poorly connected is consistent with all the observations but is not supported by any quantitative data on the pore system itself. Six samples were therefore chosen for further analysis with a scanning electron microscope/image analysis system (Fig. 8). Although only a limited data set was used, the samples chosen were representative of the complete data set.

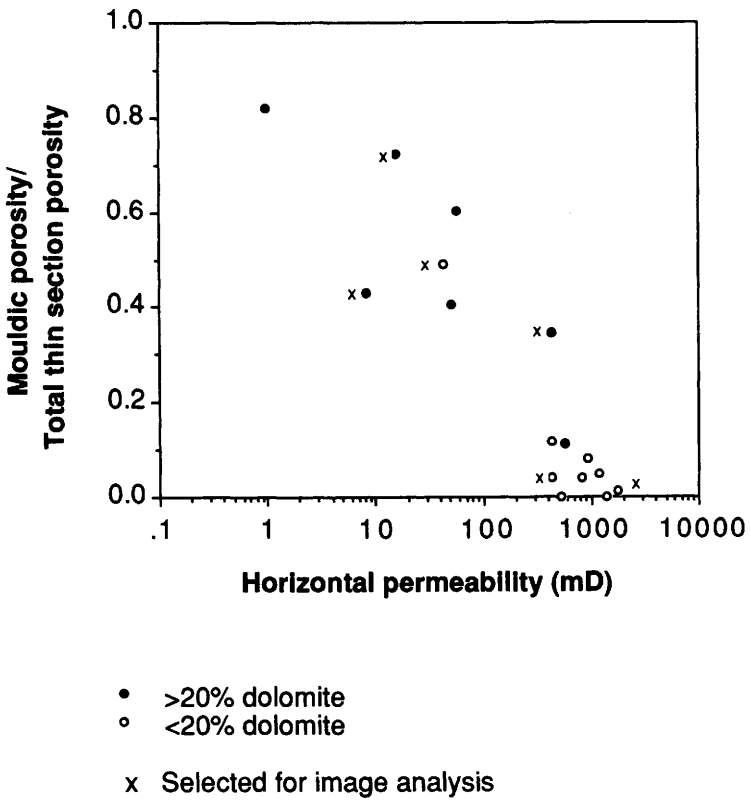

Fig. 8. Correlation between permeability and abundance of grain-dissolution porosity, Ribble Member sandstones, Well 30/16-FA31.

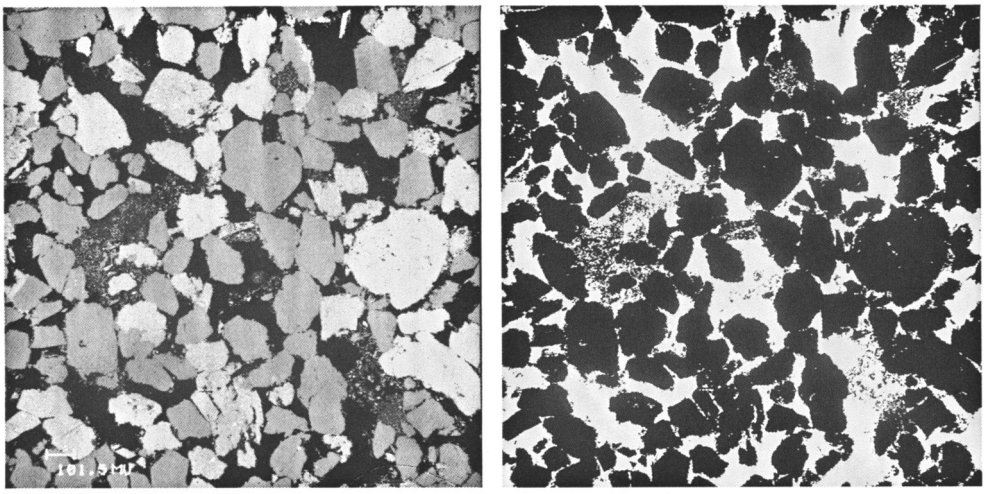

(a) (b)

Fig. 9. Backscattered electron image (**a**) of a sample analysed and binary image (**b**) showing discriminated pore structure in white. In the BSE image porosity is black and minerals are varying shades of grey. In the binary image the minerals are all black and the porosity white.

Image analytical method

Resin-impregnated, polished blocks were made from the samples (core plugs) and examined using the backscattered electron (BSE) detector of the SEM. This technique can be used to obtain information regarding mineralogy because the brightness of a mineral on a BSE image (Fig. 9a) is directly related to the density of that mineral (Dilks & Graham 1985; Hall & Lloyd 1981). This effect also allows the pores to be seen easily as they are filled with a low-density epoxy resin and hence appear very dark in the image. Careful selection of the resin will also enable pores to be distinguished from sedimentary carbonaceous material.

BSE imaging was preferred to the use of transmitted light images from thin-sections because it enables better pore definition. In thin-section analysis a 30 μm slice of rock is examined and it is therefore difficult to determine the exact position of a sloping grain-to-pore boundary. Small pores are also difficult to resolve. Although these problems also exist in BSE imaging, they are much reduced as only a one micron section of the sample surface is examined.

Eight fields of view were collected for each sample. The images were initially digitized and stored on the image analysis system as a 512 by 512 array of pixels (picture elements). Each pixel can have one of 256 possible grey values ranging from 0 (black) to 255 (white). The magnification was chosen so that each pixel was approximately 2 by 2 μm in size, allowng the smaller pores to be resolved. Typically, between 300 and 400 pores were included in each field of view. Discrimination of the complete two-dimensional pore structure from these images is carried out using a technique called segmentation, where only those pixels whose grey level falls within a certain range are detected and displayed as white. The other, non-detected, pixels are

displayed as black. Therefore, in order to segment the resin-filled pores only those pixels with the lowest grey levels should be detected resulting in a binary (or black and white) image where the pores appear white and the minerals black (Fig. 9b).

The next step was to identify the individual pores and pore throats present in the binary images. In this study a pore throat was defined as a constriction in the two-dimensional network separating two pores. In three dimensions, the pore throats are therefore planes between, or separating individual pores. The pore throats themselves have no volume. Mathematical morphology techniques (Serra 1982) were then applied to discriminate between pores and pore throats. The basic operations used are described below and are illustrated in Fig. 10, which shows a number of pores connected in the two-dimensional image plane.

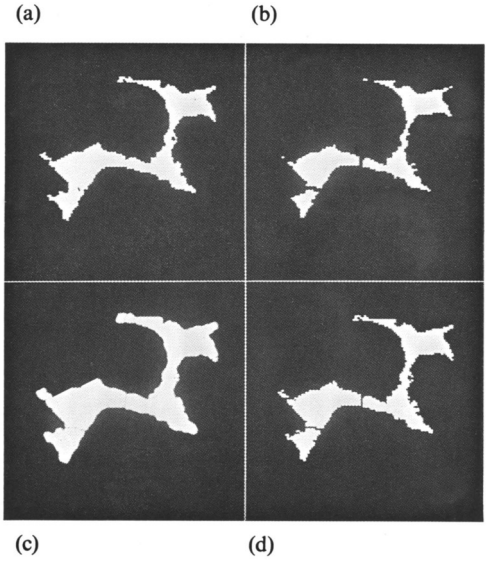

Fig. 10. Operations performed on a binary image (minerals black, pores white) to discriminate between pores and pore throats: (**a**) original image; (**b**) eroded image; (**c**) thickened image; (**d**) final image.

Step 1. The first operation is called an erosion. This consists of removing (i.e. changing from white to black) layers of pixels from the edges of the pores. After a certain number of layers have been removed the connection between the pores 'breaks' (Fig. 10a–b).

Step 2. A binary thickening of the pores is then performed. Here layers of pixels are added (i.e. changed from black to white) to the pores but only if this can be done without making the pores connect again. The result of performing this operation a number of times is shown in Fig. 10c and it can be seen that the pores are now oversized.

Step 3. In order to restore the pores to their original shape and size (but without the connection) a Boolean AND operation is performed between the original image (Fig. 10a) and the thickening image (Fig. 10c). This operation involves

detecting only those white pixels which are present in both the original and the thickened image. These are the white pixels in Fig. 10d. The pore throats that separate individual pores are displayed in grey.

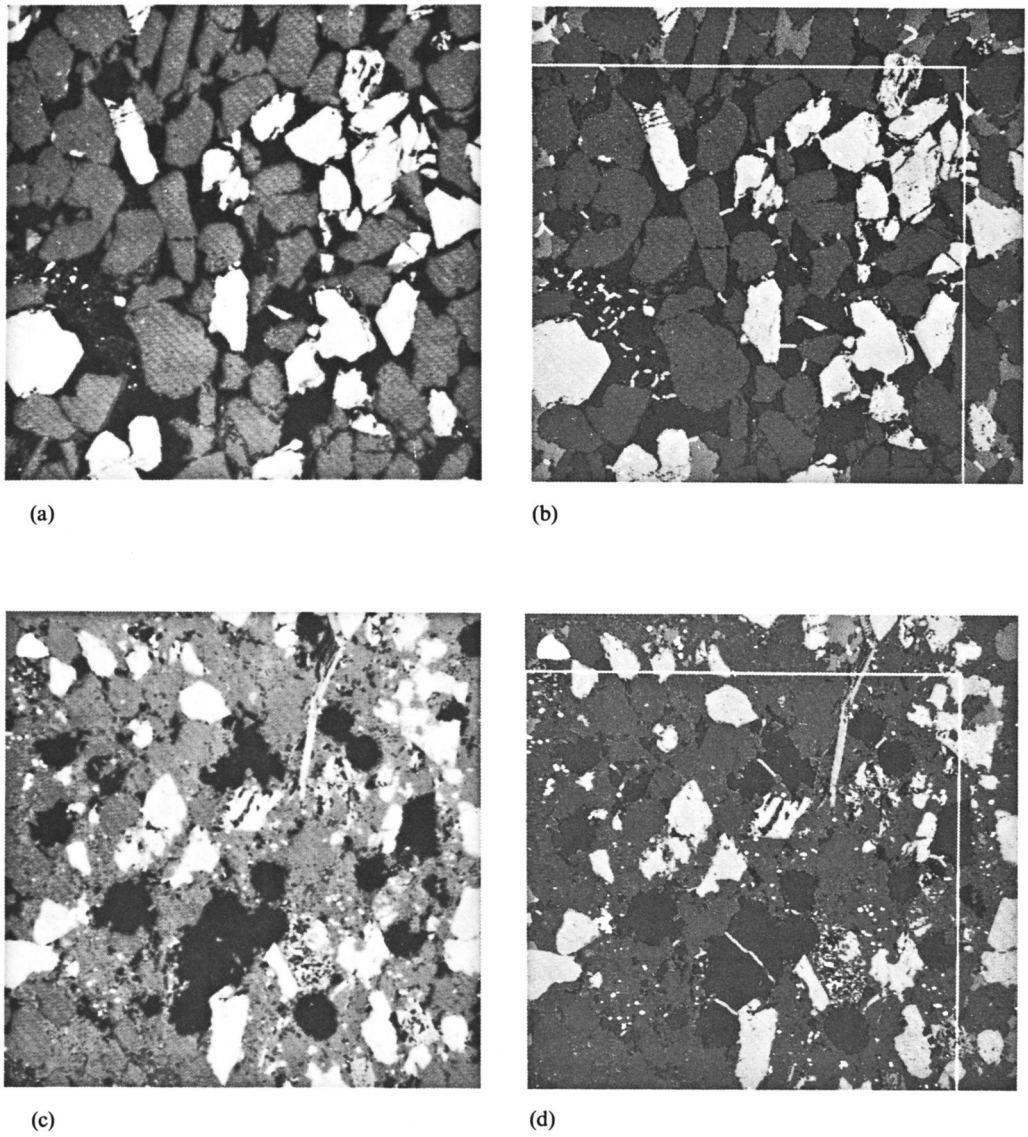

Fig. 11. Backscattered electron and processed images of two samples analysed: (**a**) and (**b**) non-cemented sample with mainly intergranular porosity; (**c**) and (**d**) cemented sample containing grain-dissolution pores. BSE images show porosity black, and minerals in varying shades of grey and white. Processed images show matrix in black, pores in grey and pore throats in white. Note the number of small pores within the matrix. These pores are smaller than they appear on the photomicrographs because of the light dispersing during photography.

These are the basic operations involved. The actual procedure is somewhat more complicated in order to deal with throats of varying sizes which can occur within the same image and also with irregularly shaped pores. The images obtained after applying this procedure to two of the samples analysed are shown in Fig. 11 where the individual pores are displayed in grey and the pore throats in white.

Once the image has been processed it is very easy to programme the computer image analysis system to measure various geometrical parameters of the pore structure. In this study three, two-dimensional parameters were considered: mean pore size (area), mean throat size (length) and pore connectivity (a measure of the average number of throats connecting pores). In order to convert these two-dimensional parameters to the appropriate three-dimensional values, stereological techniques must be used (Weibel 1980). However, this would involve making simplifying assumptions about pore shape and pore structure that were not regarded to be realistic. Therefore, two-dimensional parameters were used in the work described below. A problem occurs with those pores which touch the outer edge of the image as their geometrical characteristics cannot be determined. It was therefore necessary to exclude them from the analysis. However, excluding only these pores will lead to a biased size distribution as the larger pores tend to be rejected. In order to overcome this, a measuring frame (shown in Fig. 11) was used and any pore which lay entirely outside the frame was rejected, as well as those pores that touched the edge of the image. Considering Fig. 11, larger pores are preferentially rejected in the bottom and left-hand sides where the measuring frame coincides with the edge of the image. However, in the top and right-hand part, where the measuring frame lies inside the image, smaller pores are preferentially rejected. Such a configuration between the measuring frame and the image leads to an unbiased distribution of pores. Eight fields of view were analysed for each sample. As the image analyser is fully interfaced with the SEM the whole data set could be obtained in one continuous automatic procedure.

Results

Plots of plug permeability against the three measured pore parameters are shown in Fig. 12. Pore area and connectivity show good to moderate correlations with permeability respectively, but the relationship between permeability and pore throat length is poor. These results are explained below. During this discussion, the samples are referred to as poorly cemented or cemented depending upon whether their dolomite content is $<20\%$ or $>20\%$ respectively. This is the dolomite content below which sandstone permeability appears to reflect detrital sediment texture and above which it does not.

As the average pore area (that is, pore size) increases, the permeability increases (Fig. 12a). Such a relationship is expected for granular porous media where the pores are well connected, such as the poorly-cemented sandstones analysed here (Fig. 11a, b). However, the cemented samples are characterized by the development of grain-dissolution porosity (Figs 4c, d & 11c, d). Although these grain-dissolution pores are larger than the intergranular pores, they appear to be poorly connected in thin-section. Hence it was expected that the cemented sandstones would have low permeabilities in spite of larger pore areas, and would not show the same relationship

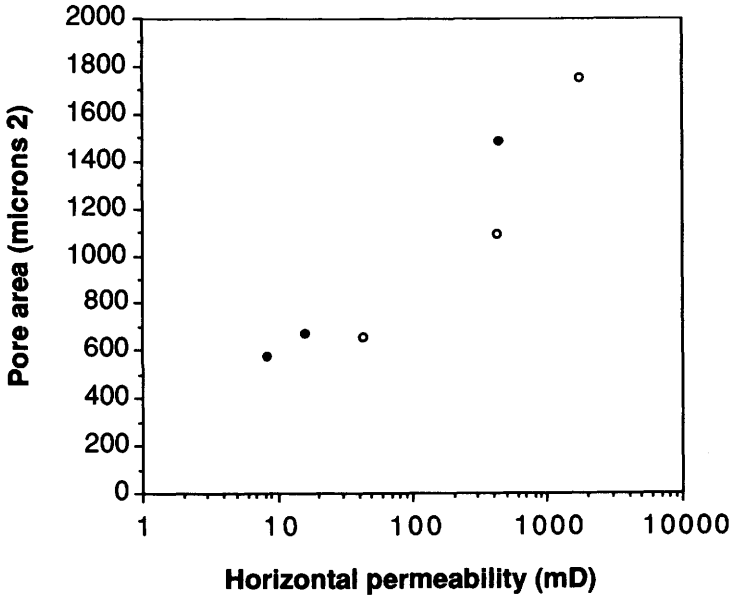

(a)

• >20% dolomite
○ <20% dolomite

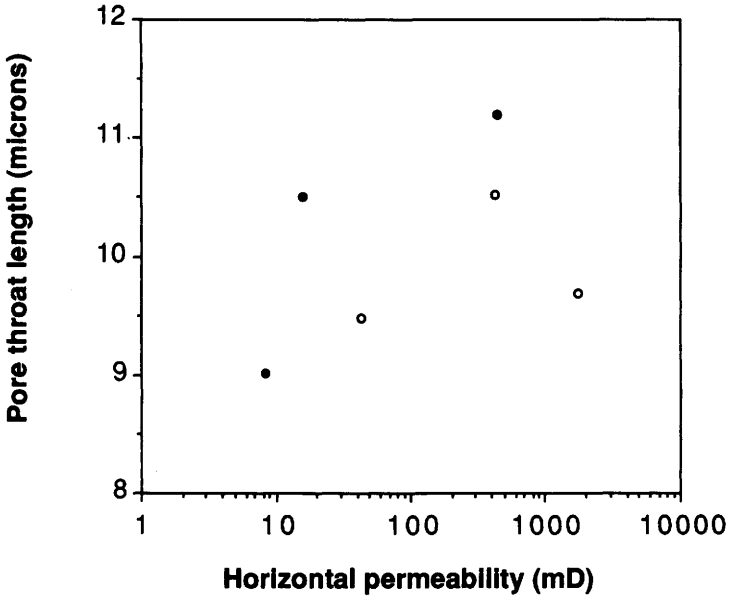

(b)

• >20% dolomite
○ <20% dolomite

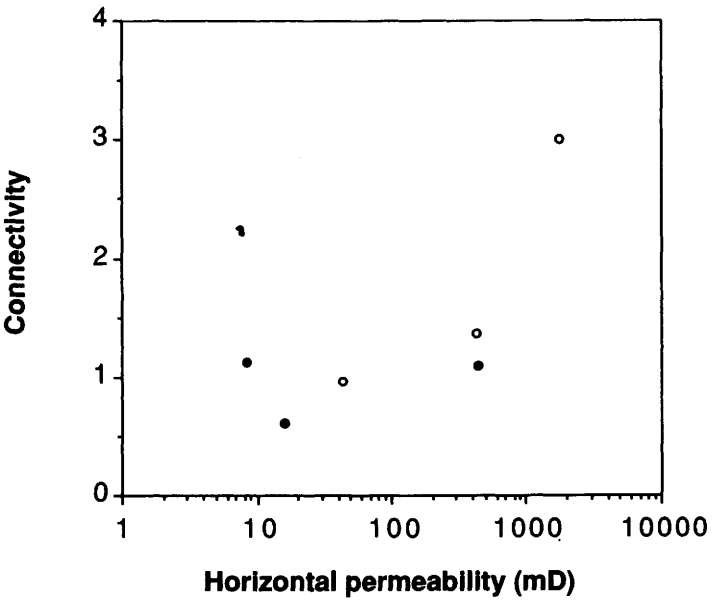

(c)

Fig. 12. Plot of horizontal plug permeability versus the image analysis derived pore parameters: pore area (**a**), pore throat length (**b**), and connectivity (**c**).

as the more porous ones. However, Fig. 12a shows that all six samples exhibit the same relationship. This is probably because rather than being increased by the creation of grain-dissolution pores, the average pore area is reduced by the numerous small intercrystalline pores that are created during cementation (Fig. 11c & d). The greater proportion of small pores in the better-cemented samples results in a corresponding decrease in permeability.

The poor relationship between pore throat length (that is, pore throat size) and permeability (Fig. 12b) may be because the image processing technique does not detect the very small throats and so the results are biased towards the larger sizes, particularly in the cemented sandstones. Carrying out the analyses at a higher magnification may lead to some improvement in the detection of very small throats, although this would be limited to the one micron resolution of BSE imaging. The use of mercury intrusion porosimetry may give a better description of the pore throat size distribution (Dullien 1979).

Figure 12c shows that a good relationship exists between two-dimensional connectivity and permeability. Figure 11b shows clearly the pore throats through which large intergranular pores are connected. As the pore connectivity decreases, due to increased blocking of pore throats by dolomite rhombs (Fig. 11b), the tortuosity of flow paths through the rock increases, resulting in lower permeability.

Comparison with conventional petrography

A comparison of Figs 3 and 12a illustrates the benefits of the image analytical techniques over conventional petrography. The porosity and permeability data in Fig. 3 reveal a range of permeabilities for any given porosity. However, this is the samples total porosity. Cross-plots against modal porosity are similar but less reliable as shown by a comparison of plug and modal porosities from Table 1. Microporosity is not generally observed during point counting. Figure 12a by contrast shows that a relationship can be established between average pore area and permeability. Having identified individual pores as being isolated or separated by pore throats the relationship between permeability and connectivity in Fig. 12c can be calculated. This would be prohibitively time-consuming during conventional thin-section description. As the data in Fig. 12 have been constructed from measurement of over 2000 pores per thin-section, many of which are too small to quantify manually, the benefits of obtaining and using image analytical data should be obvious.

Implications for reservoir behaviour

Prediction of permeability from porosity logs will not be straightforward for the Ribble Member sandstones. In the poorly cemented sandstones there will be a 'normal' porosity/permeability relationship which is governed by the sediment texture. However, for the cemented sandstones, a high porosity can exist while the permeability is low (Fig. 13).

It is likely that hydrocarbon recovery from the cemented intervals will be slower than from adjacent sandstones. Given the difference in permeabilities between the cemented and poorly cemented sandstones (0.4–600 mD and 40–1800 mD respectively), the grain-dissolution porosity in the cemented sandstones is unlikely to contribute significantly to production during initial drawdown. Oil production may occur slowly as reservoir pressure drops. If the cemented sandstones are water-wet, oil may be displaced into the porous sandstones by imbibition. This will take place after either natural aquifer encroachment or the passage of a waterflood front, and so the liberated oil will only reach the producing wells after the onset of water breakthrough. If the cemented sandstones are oil-wet, oil may drain into the poorly cemented sandstones and be produced as long as this occurs before the aquifer/floodfront passes (Salathiel 1973).

Conclusions

Automated-image analytical techniques have been used to quantify pore structure during a petrographical analysis of sandstones from the Ribble Member in the Fulmar Field. The application of these techniques has led to the geometrical properties of over 2000 individual pores being measured on each sample. If manual methods had been employed, the collection of such a wealth of data would have been significantly more time consuming. The data obtained have enabled the influence of diagenesis on certain reservoir properties to be understood and quantified.

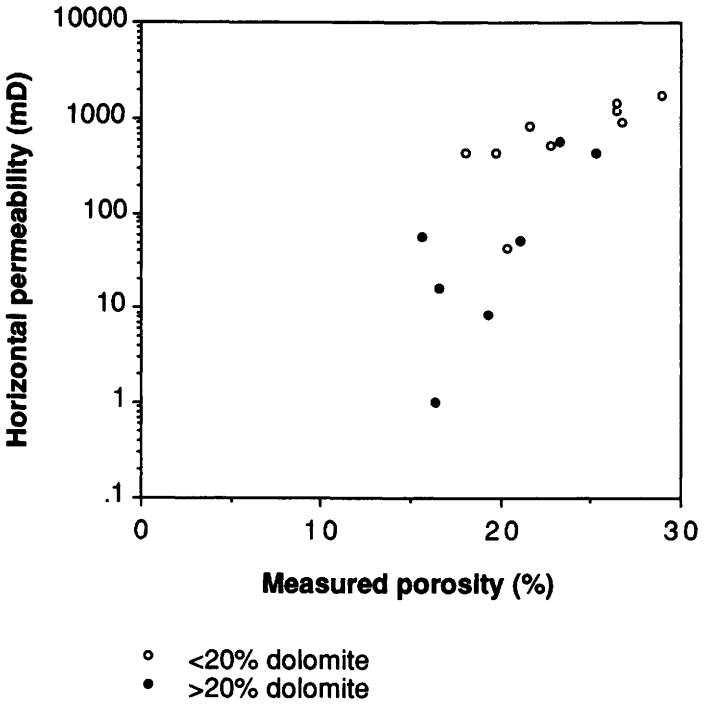

Fig. 13. Cross-plot of horizontal permeability versus plug porosity, Ribble Member sandstones, Well 30/16-FA31, Fulmar Field. Differring porosity/permeability relationships are shown for (**a**) poorly cemented samples and (**b**) cemented samples.

The sandstones in the Ribble Member are texturally mature, fine- to medium-grained subarkoses. During diagenesis, sponge spicules present in the sediment have dissolved, liberating quartz that has precipitated as chalcedonic grain coatings and quartz overgrowths. Where abundant (>20%) rhombic dolomite cementation occurs, spicule dissolution is recorded by the presence of grain-dissolution porosity. Irrespective of the amount of cementation, pore area and two-dimensional connectivity are identified as the main controls on permeability. In the poorly cemented sandstones higher permeabilities exist as these sandstones contain relatively large interconnected pores. As the degree of cementation increases, an increasingly significant number of small intercrystalline pores are found between the authigenic dolomite rhombs. In spite of the large size of individual grain-dissolution pores, the number of small intercrystalline pores reduces average pore size. These pores are poorly connected and permeability is correspondingly lower.

Establishing a single porosity/permeability relationship from cores in order to aid permeability prediction in uncored wells will not adequately characterize these sandstones. The poorly cemented and cemented sandstones appear to have different porosity/permeability relationships (Fig. 13). However, distinction between the two cannot be achieved on the basis of their porosity alone, as it requires reference to their dolomite content. Therefore, quantification of the amount of dolomite cement will be important for recovery predictions and when trying to derive permeabilities

from porosity logs. It may be possible that a log evaluation package could be used to do this but it must be emphasized that any evaluation of dolomite abundance from logs needs to be calibrated with mineralogical data from a cored well.

Quantification of the pore structure in sandstones from the Ribble Member has improved the understanding of the influence of diagenesis on permeability. The diagenetic model suggests that all the cements present in the reservoir are likely to have formed from either the original depositional pore waters, or the detrital sediments themselves. No large-scale influx of fluids is invoked during, for example, Cimmerian exposure or Tertiary burial. This closed-system diagenesis has resulted in patchy or locally concentrated dolomite cements which are not likely to cause reservoir-scale compartmentalisation or to form significant barriers to fluid flow through the uncemented sands. The effect of rhombic dolomite cementation has been to change the pore structure in a quarter of the reservoir and reduce the permeability of these sandstones significantly. Oil recovery from these sandstones will be slower than from the surrounding poorly cemented sandstones.

This paper is published with the permission of Shell International Research Maatschappij, Shell International Petroleum Maatschappij, Shell UK Exploration and Production, Esso Exploration and Production UK and the Fulmar Partners (Amoco (UK) Exploration Co, Enterprise Oil PLC, Mobil North Sea Ltd, and Amerada Hess (UK) Ltd).

The authors thank their colleagues at KSEPL for their help and encouragement with various aspects of this work. J. D. Marshall (Liverpool University) is thanked for the stable isotope analysis. J. Marshall (no relation) and R. Garden are thanked for comments on the manuscript.

References

BAKER, P. A. & BURNS, S. J. 1985. Occurrence and formation of dolomite in organic-rich continental marine sediments. *Bulletin of the American Association of Petroleum Geologists*, **69**, 1917–30.

BAKER, P. A. & KASTNER, M. 1981. Constraints on the formation of sedimentary dolomite. *Science*, **213**, 214–216.

BARTON, P. & WOOD, R. 1984. Tectonic evolution of the North Sea Basin: crustal stretching and subsidence. *Geophysical Journal of the Royal Astronomical Society*, **79**, 987–1022.

BJØRKUM, P. A. & GJELSVIK, N. 1988. An isochemical model for formation of authigenic kaolinite, K-feldspar and illite in sediments. *Journal of Sedimentary Petrology*, **58**, 506–511.

BJØRLYKKE, K. 1979. Cementation of sandstones—Discussion. *Journal of Sedimentary Petrology*, **49**, 1358–1359.

BURLEY, S. D., KANTOROWICZ, J. D. & WAUGH, B. 1985. Clastic diagenesis. *In*: BRENCHLEY, P. J. & WILLIAMS, B. P. J. (eds) *Sedimentology: Recent developments and applied aspects*. Geological Society, London, Special Publication, **18**, 189–226.

DILKS, A. & GRAHAM, S. C. 1985. Quantitative mineralogical characterization of sandstones by backscattered electron image analysis. *Journal of Sedimentary Petrology*, **55**, 347–55.

DULLIEN, F. A. L. 1979. *Porous media: fluid transport and pore structure*. Academic Press, London.

EHRLICH, R., CRABTREE, S. J., KENNEDY, S. K. & CANNON, R. L. 1984. Petrographic image analysis, I. Analysis of reservoir pore complexes. *Journal of Sedimentary Petrology*, **54**, 1365–78.

HALL, M. G. & LLOYD, G. E. 1981. The SEM examination of geological samples with a semiconductor backscattered electron detector. *American Mineralogist*, **66**, 362–68.

HEIN, J. R. O'NEIL, J. R. & JONES, M. G. 1979. Origin of authigenic carbonates in sediments from the deep Bering Sea. *Sedimentology*, **26**, 681–705.

HELM, VAN DER A. A., GRAY, D. I., COOK, M. A. & SCHULTE, A. M. 1990. Fulmar: The development of a large North Sea Field. *In*: BULLER, A. T., BERG, E., HJELMELAND, O., KLEPPE, J., TORSAETER, O. & AASEN, J. O. (eds) *North Sea oil and gas reservoirs—II*. Graham and Trotman, London. 25–45.

HUDSON, J. D. 1977. Stable isotopes and limestone lithification. *Journal of the Geological Society, London*, **133**, 637–60.

JOHNSON, H. D., MACKAY, T. A. & STEWART, D. J. 1986. The Fulmar Oil Field (Central North Sea): geological aspects of its discovery, appraisal and development. *Marine and Petroleum Geology*, **3**, 99–125.

KANTOROWICZ, I. D., BRYANT, I. D. & DAWANS, J. M. 1987. Controls on the geometry and distribution of carbonate cements in Jurassic sandstones: Bridport Sands, southern England and Viking Group, Troll Field, Norway. *In*: MARSHALL, J. D. (ed.) *Diagenesis of Sedimentary sequences*. Geological Society, London, Special Publication, **36**, 103–18.

KASTNER, M. & SIEVER, R. 1979. Low temperature feldspars in sedimentary rocks. *American Journal of Science*, **279**, 435–79.

——, KEENE, J. B. & GIESKES, J. M. 1977. Diagenesis of siliceous oozes—I. Chemical controls on the rate of opal-A to opal-CT transformation—an experimental study. *Geochimica et Cosmochimica Acta*, **41**, 1041–1059.

LAND, L. S. 1980. The isotopic and trace element geochemistry of dolomite: the state of the art. *In*: ZENGER, D. H., DUNHAM, J. G. & ETHERGINTON, R. L. (eds) *Concepts and models of dolomitisation*. Society of Economic Paleontologists and Mineralogists Special Publication, **28**, 87–110.

MURATA, K. J., FRIEDMAN, I. & GLEASON, J. D. 1977. Oxygen isotope relations between diagenetic silica minerals in Monterey Shale, Tremblor Range, California. *American Journal of Science*, **277**, 259–272.

PLAS, VAN DER L. & TOBI, A. C. 1965. A chart for judging the reliability of point counting results. *American Journal of Science*, **263**, 87–90.

RAISWELL, R. 1971. The growth of Cambrian and Liassic concretions. *Sedimentology*, **12**, 147–171.

RINK, M. & SCHOPPER, J. R. 1977. On the application of image analysis to formation evaluation. *Transactions of the Fifth European Logging Symposium*, **17**, 1–22.

SALATHIEL, R. A. 1973. Oil recovery by surface film drainage in mixed-wettability rocks. *Journal of Petroleum Technology (October)*, **25**, 1216–1224.

SERRA, J. 1982. *Image analysis and mathematical morphology*. Academic Press, London.

STEWART, D. J. 1986. Diagenesis of the shallow marine Fulmar Formation in the Central North Sea. *Clay Minerals*, **21**, 537–64.

WEIBEL, E. R. 1980. *Stereological methods. Volume 2. Theoretical foundations*. Academic Press, London.

From ASHTON, M. (ed.), 1993, *Advances in Reservoir Geology*,
Geological Society Special Publication No. 69, pp. 81–103.

Sedimentological and reservoir characteristics of a fluvial-dominated delta-front sequence: Ferron Sandstone Member (Turonian), East-central Utah, USA

PHILIP LOWRY[1,2] & TORGRIM JACOBSEN[3]

[1] *IFE, PO Box 40, N-2007 Kjeller, Norway*
[2] *Present address: ARCO Oil and Gas Company, 2300 West Plano Parkway, Plano, Texas 75075, USA*
[3] *IKU, N-7034 Trondheim, Norway*

Abstract: Exposures of the Ferron Sandstone Member (Turonian) of the Mancos Shale Formation in east-central Utah offer an opportunity to examine the dimensions of delta-front reservoir elements and their associated heterogeneities. Field mapping within the Ferron Sandstone has demonstrated that distributary mouth-bar facies have maximum lengths of 8–9 km and maximum widths of 4–6 km. Distributary channel width-to-thickness ratios commonly have values between 10:1 and 20:1. Distal bar sandstone thicknesses and shale lengths are dependent upon their location within the mouth-bar. Distal bar shales are shortest within the proximal region of the mouth-bar, where amalgamation of distal bar sandstones is greatest.

850 field minipermeameter measurements were obtained from the various facies elements of a distributary mouth-bar sandbody. The data display significant correlation between facies elements and permeability structure. Trough cross-bedded upper mouth-bar facies exhibit the highest means and lowest coefficient of variation. Muddy and bioturbated distal bar facies exhibit the lowest means and highest coefficient of variation. The permeability distributions appear to be related to the degree of heterogeneity, and show increasing left-skewness with increasing heterogeneity.

Fluid flow simulations of two geological models of a distributary mouth-bar were conducted to assess the effect of permeability contrasts on predicted reservoir behaviour. One of the models depicts a lithologically homogeneous mouth-bar, while the other depicts a mouth-bar that is composed of two internal facies elements (lower and upper mouth-bar). Results of the simulations show that up to 30–45% difference in predicted water breakthrough can occur between the two models.

Prediction of interwell lithological heterogeneity is a major concern in the exploitation of oil and gas reservoirs (Weber 1986; Finley & Tyler 1986; Weber & van Geuns 1990). This is especially so offshore, where well costs are high and simple offset drilling is not a viable option. Although the structure of the reservoir will often determine the strategy for siting production and injection wells, the distribution of internal heterogeneities has a significant influence on the reservoir behaviour and choice of development strategy.

In the recent years stochastic modelling has been employed as an approach which allows the realistic simulation of interwell heterogeneity. The approach is heavily dependent on the use of reliable data concerning facies dimensions, spatial inter-relationships and petrophysical characteristics. The present scarcity of such data,

however, limits the applicability of stochastic modelling. The work described herein has been carried out to address this topic within a delta-front subenvironment.

Exposures of the Ferron Sandstone Member (Turonian) of the Mancos Shale Formation in east-Central Utah (Fig. 1) afford an excellent opportunity to examine at outcrop, the facies architecture of a deltaic unit. In this work, outcrop data were collected on the dimensions, architecture and absolute permeability structure of the following delta-front elements: distributary mouth-bars (lower and upper); distal bars; and distributary channels. The sampled data and a geological model of one mouth-bar are used as input to a series of fluid-flow simulation experiments. These experiments were designed to determine the effect minor permeability variations within the mouth-bar would have on predicted fluid flow.

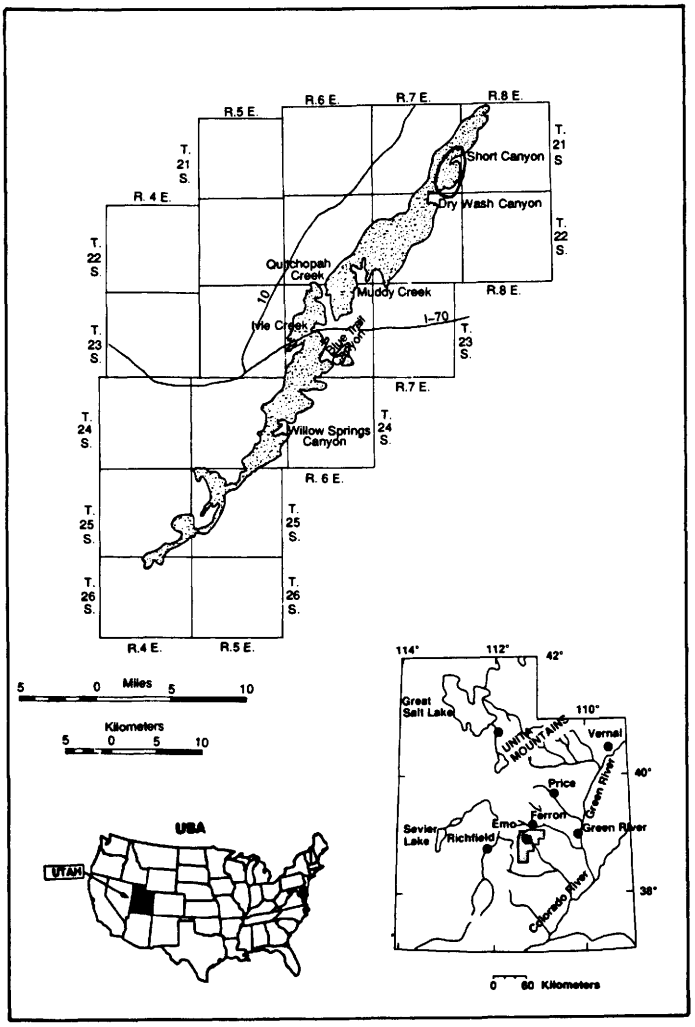

Fig. 1. Location map of the study area within the state of Utah and the general orientation of the outcrop belt (stippled). Note the location of the sandbody shown in Fig. 2, in the Short Canyon area in Township 21 south, Range 7 east. Basinward is to the east.

Ferron sandstone stratigraphical framework

Located in east-central Utah (Fig. 1), exposures of the Ferron Sandstone (Turonian) of the Mancos Shale afford an excellent opportunity to examine at outcrop, the facies architecture of a coastal-deltaic sequence. The Ferron deposits represent an early phase of late Cretaceous progradation in the Western Interior Seaway and have been extensively studied over the last century. Building on early work by Gilbert (1877), Lupton (1916) named the Ferron Sandstone and documented in great detail the coal seam stratigraphy. Successive geologists have refined the stratigraphical framework, (Hunt 1946; Spieker 1949; Hunt *et al.* 1953; Doelling 1972; Ryer 1982); detailed the biostratigraphy (Cobban & Reeside 1952; Sarmiento-Soto, 1957; May 1962; Gray *et al.* 1966) and presented palaeogeographical representations (Cotter 1975*a,b*, 1976; Ursek 1979; Ryer 1981; Ryer & McPhillips 1983; Thompson *et al.* 1986; Balsley 1988; Tripp 1989). Recently, the Ferron Sandstone has been the site of renewed studies. These studies have focused on the three-dimensional facies architecture of fluvial and coastal-deltaic deposits particularly at a reservoir scale (Leverson & Gardner 1987; Gardner *et al.* 1987; Stapor & Adams 1988). The Ferron Sandstone has been interpreted to represent a fluvial-dominated, lobate delta system with progradation from southwest to northeast (Ryer 1981). Ryer (1982) recognized at least five progradational events within the Ferron Sandstone. Utilizing the existing framework, the intention of this project was to delineate individual delta-front sandbodies, document their dimensions, and characterize the lithological heterogeneity.

Methods

The first phase of the fieldwork involved mapping within the second progradational interval of Ryer (1982) to ascertain the dimensions of facies elements.

The second phase focused on the variation of permeability within a distributary mouth-bar sandbody. Permeability data were collected using a field-minipermeameter (Jacobsen & Rendall 1990). Numerous canyons dissect the outcrop belt and provide three-dimensional access to the areas of interest. Access to vertical cliffs 15–50 m in height required the use of rock climbing techniques to sample permeability at the outcrop. Each geologist working on the vertical wall was able to ascend or descend on a rope using rock climbing equipment. Sitting in a harness, both hands are free to allow face preparation (removal of the weathered surface) and permeability measurements. Because the minipermeameter is calibrated with a 6 m long hose, allowing only a 12 m coverage, it was also necessary in some cases to move the device up and down the cliff face.

A total of about 850 permeability measurements were obtained at four different stations along the outcrop (Fig. 2). The measurements were performed with a sample density of 0.25 m along vertical transects at each station. At station 2 in the central part of the deposit, however, data were sampled on a more comprehensive grid (Fig. 3).

Dimensions and architecture of delta-front facies elements

The problem of providing quantitative geological data for reservoir simulations has been approached by examining the dimensions of some facies elements within the

Ferron Sandstone delta-front deposit. These facies elements include distributary mouth-bars, distributary channels (isolated cut-and-fill and laterally accreting), and distal bar sandstones and shales.

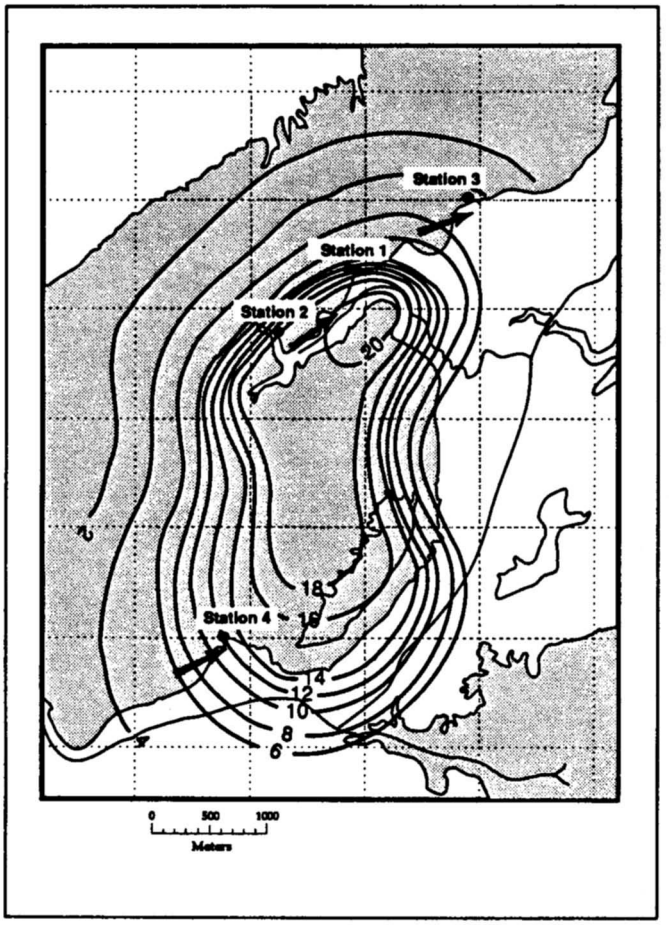

Fig. 2. Isopach map of the distributary mouth-bar sandbody complex at Short Canyon (T21S,R7E). The contour interval is 2 m. The arrows indicate palaeocurrent directions (indicating flow from southwest to northeast), which means that the distal part of the mouth-bar is towards the upper right corner of the map. Notice the four sampling stations for permeability data. Measured sections for these localities are shown on Fig. 9.

Distributary mouth-bar sandbodies in the Ferron Sandstone can be traced up to 9 km along strike and up to 6 km in dip direction. These distances are large when compared to similar data published in earlier papers (Fig. 4). Isolated channels that incise the mouth-bars are quite rare, but where they occur, they commonly have width to thickness ratios between 10:1 and 20:1 (Fig. 5). The channel width/thickness data also give an empirical relationship in the form $w = 12.7t^{1.2}$ (Fig. 6).

Shales within the distributary mouth-bar facies are relatively rare and laterally discontinuous. Shales within the underlying distal bar facies can be traced up to

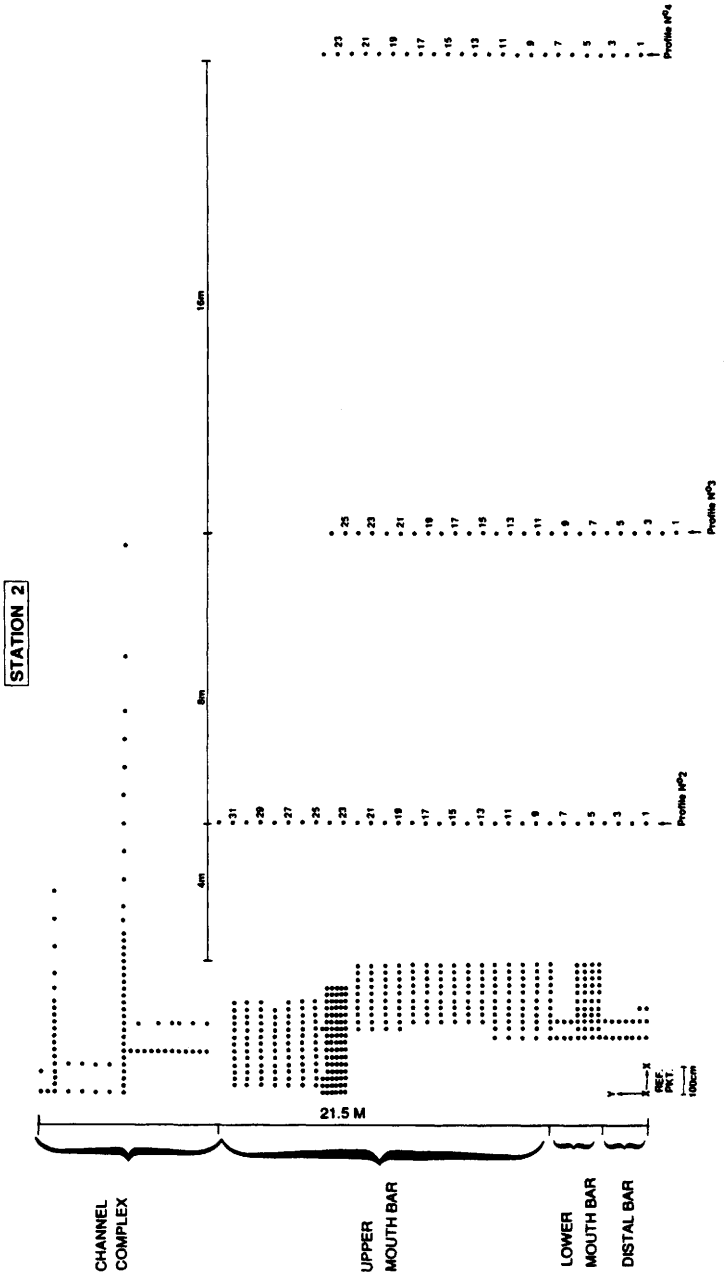

Fig. 3. Sampling grid for permeability data at station 2 (in the central part of the distributary mouth-bar). The measured section at station 2 shown in Fig. 9 corresponds to the location of profile 1 (the leftmost profile).

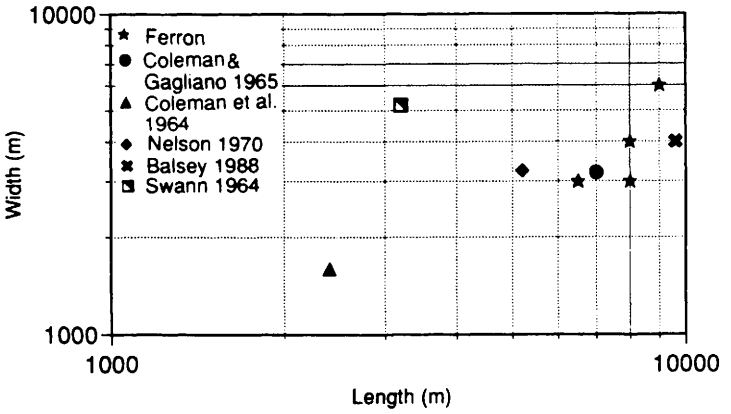

Fig. 4. Scatter diagram showing width-to-length relationship of some distributary mouth-bars.

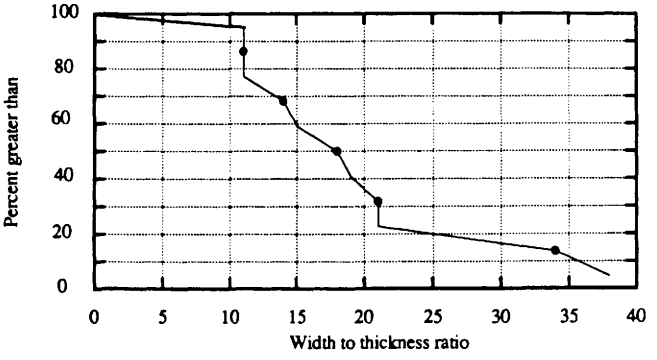

Fig. 5. Cumulative frequency diagram showing distribution of width-to-thickness ratios of isolated distributary channels.

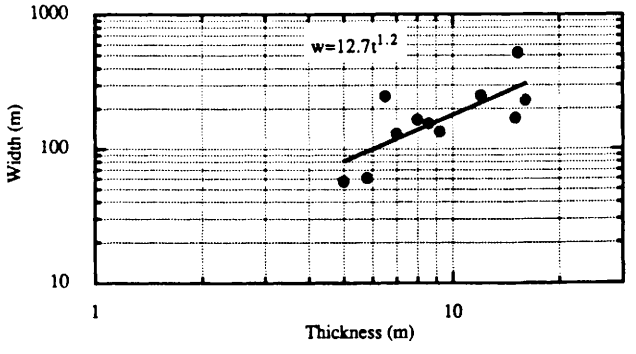

Fig. 6. Scatter diagram showing the empirical relationship between width (w) and thickness (t) of isolated distributary channels.

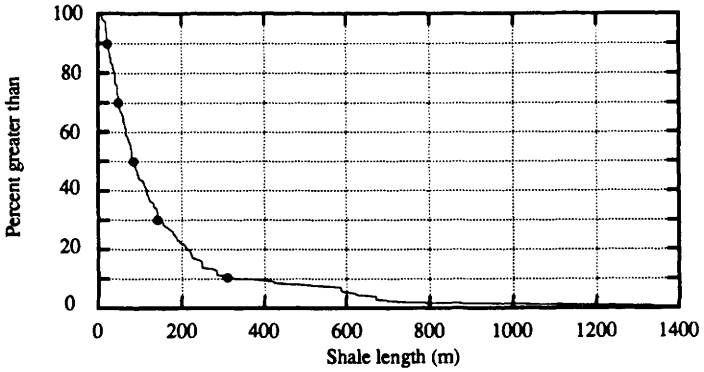

Fig. 7. Cumulative frequency diagram showing distribution of shale lengths in distal bar facies.

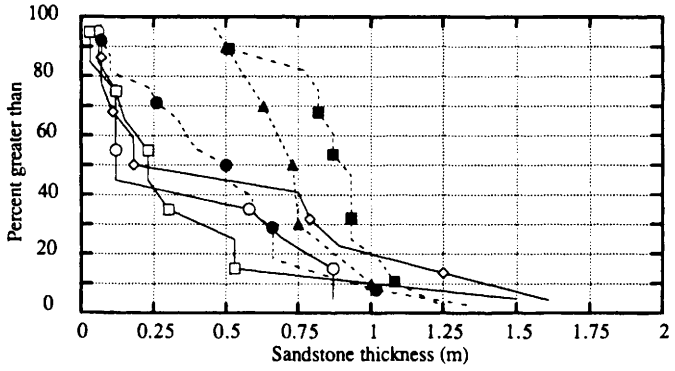

Fig. 8. Cumulative frequency diagram showing the distribution of sandstone thickness in the distal bar facies of a single lobe complex. The stippled lines indicate sites located in the central part of the lobe complex, and the solid lines indicate sites located in the distal part.

0.6 km (Fig. 7). Such a diagram, however, can be quite misleading because this implies that there are no spatial variations in shale length within the distal bar facies. Examination of the distal bar facies associated with the sandbody shown in Fig. 2 reveals that shale length and distal bar sandstone thickness is dependent on the relative location to the proximal portion of the sandbody. This question of spatial variability is further illustrated in the cumulative frequency diagram (Fig. 8) for distal bar sandstone thickness from six localities within a single mouth-bar sandbody. The dashed lines indicate sites located in the central part of this complex, and the solid lines depict measurements from more distal locations. On average, distal bar sandstone beds tend to be thicker in the central region of the sandbody than in the distal regions. In effect this reflects a greater degree of amalgamation of sandstone beds, and laterally discontinuous shales. These observations suggest potentially better vertical conformance in the proximal regions of the highly stratified distal bar facies.

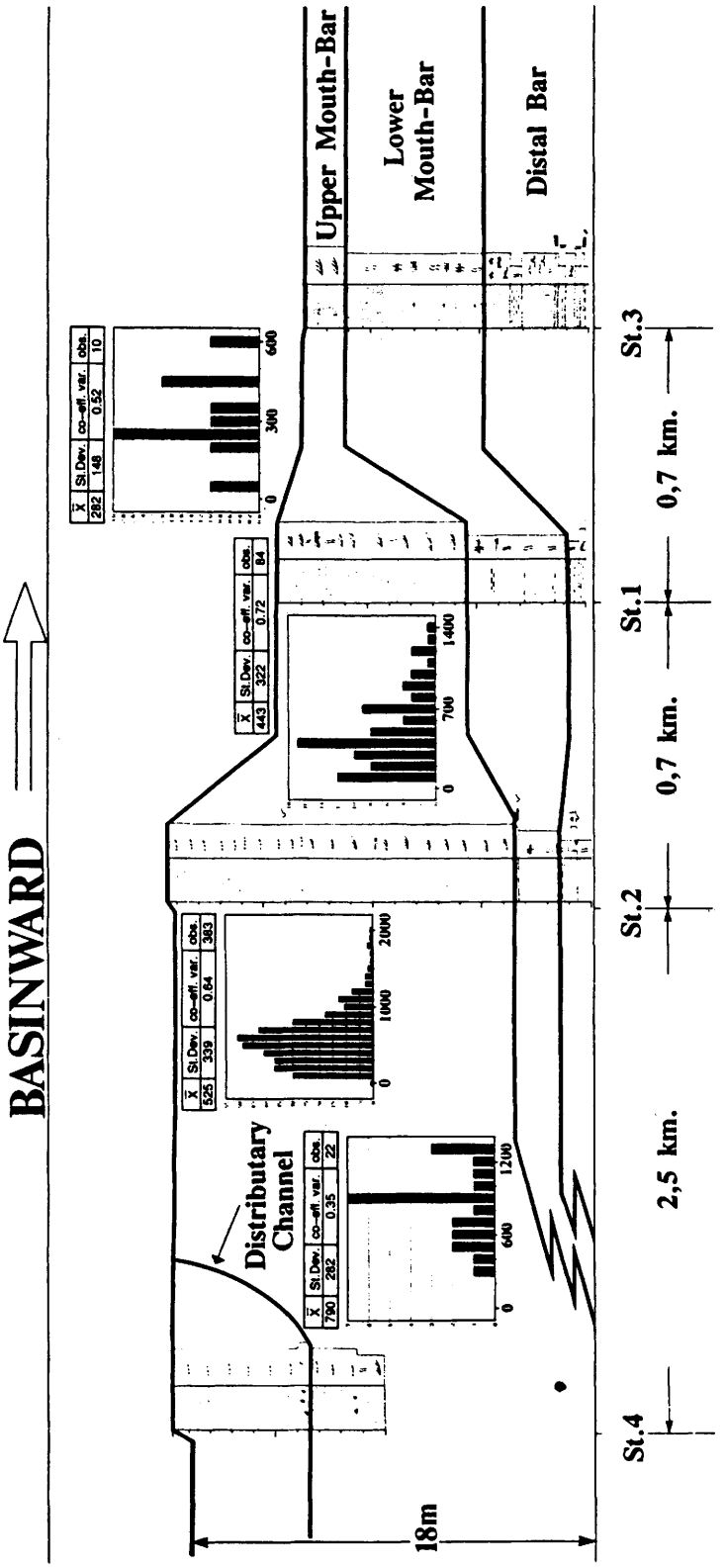

Prograding delta-front system (Ferron Member)

Fig. 9. Cross-section through the mouth-bar complex in the Short Canyon Spring area (Fig. 2). In addition to statistical parameters, frequency distributions (histograms) of permeability in the upper mouth-bar are displayed at each sampling station. Notice the gradual decrease in average (arithmetic) permeability in a distal direction.

While such data can provide important input to a stochastic modelling program, they reveal no information about the internal complexity of these facies elements. At least two distinct types of mouth-bars occur in the Ferron Sandstone. One type is relatively heterogeneous and characterized by steeply dipping foresets (up to 15°; see Cotter 1975*c*) with abundant discontinuous shales along bedding planes. The other type of mouth-bar is sheet-like with relatively limited degrees of lithological heterogeneity. Sheet-like mouth-bars appear to be the predominant along the outcrop belt. Figure 2 is an isopach map of one such mouth-bar in the Short Canyon Spring region of the outcrop belt. This mouth-bar extends 9 km along strike and 4 km along dip. Palaeocurrent orientations from megaripple foresets near the top of the mouth-bar indicate a bipolar current direction, but with a dominant flow to the northeast. This direction is oblique to the longest axis of the mouth-bar. Westward, the mouth-bar begins to interfinger with thin coal beds (30–40 cm thick) and mudstone-rich deposits. The sandbody is cut by numerous discrete channels in this region. Figure 9 is a cross-section through the entire lobe complex in the same area. The mouth-bar is composed of two internal lithofacies elements: (a) a mixed burrowed and horizontally laminated fine-grained lowermost sandstone, and (b) an uppermost cross-bedded (set thickness approximately 30–80 cm) medium-grained sandstone. These are referred to hereafter as the lower and upper mouth-bar, respectively. There is a progressive basinward increase in the relative proportion of the lower mouth-bar to the entire distributary mouth-bar. Upper mouth-bar sandstones are well sorted and there is little evidence of significant shale intercalation. The contact between these two lithofacies elements is sharp, but becomes less pronounced basinward.

Permeability structure of delta-front facies elements

It is obvious that the individual mouth-bars described here can be volumetrically significant enough to occur as individual reservoirs in the subsurface. The question here is whether such a mouth-bar should be represented as a homogeneous feature and simulated as such in a reservoir model. Since the mouth-bar may be further subdivided into upper and lower zones, the question we pose here is to what extent the inclusion of this level of geological detail will affect the results of the fluid-flow simulations. The permeability data sampled at outcrop were all related to the individual delta-front elements, grain size, and sedimentary structures so that such sensitivity tests could be carried out.

Arithmetic, geometric and harmonic means, standard deviation, and coefficient of variation were calculated for the delta-front facies elements at: (a) each station and (b) the overall outcrop (Table 1). Trough cross-bedded upper mouth-bar facies exhibit the highest means and lowest coefficient of variation. Muddy and bioturbated distal bar facies exhibit the lowest means and highest coefficient of variation.

There is a distinctive relationship between permeability structure, sedimentary structures and grain size. Trough cross-bedded facies have the highest permeability, and hummocky cross-bedded facies have the lowest permeability (Table 2).

Permeability distributions were determined by frequency histogram analysis and supplemented by Kolmogorov–Smirnov tests for the goodness of fit to model permeability populations (Davis 1986). A *P*-transformation (Box & Cox 1964) with *P*-values of 1, 0.5 and 0 has been applied to test for the null hypothesis that the population approximates respectively a normal, square-root normal or log normal

Table 1. *Permeability structure of the individual delta-front elements at (a) each sampling station, and (b) all sampling stations*

	Channel	Channel complex	Upper mouth-bar	Lower mouth-bar	Upper+ Lower mouth-bar	Distal bar
Station 1						
Harmonic mean			103	17		18
Geometric mean			296	105		44
Arithmetic mean			443	197		90
Standard deviation			322	150		102
Coefficient of varation			0.72	0.76		1.14
Observations			84	54		3
Station 2						
Harmonic mean		27	81	22		53
Geometric mean		171	379	95		86
Arithmetic mean		313	525	177		159
Standard deviation		272	339	190		209
Coefficient of variation		0.87	0.64	1.08		1.31
Observations		83	383	75		6
Station 3						
Harmonic mean			104	5		2
Geometric mean			217	29		3
Arithmetic mean			282	125		7
Standard deviation			148	204		10
Coefficient of variation			1.52	1.64		1.47
Observations			10	32		24
Station 4						
Harmonic mean	128		648			
Geometric mean	178		710			
Arithmetic mean	283		790			
Standard deviation	429		282			
Coefficient of variation	1.51		0.35			
Observations	59		22			
All stations						
Harmonic mean	128	27	88	12	35	3
Geometric mean	178	171	370	134	253	7
Arithmetic mean	283	313	518	173	434	42
Standard deviation	429	272	339	182	342	106
Coefficient of variation	1.51	0.87	0.66	1.05	0.79	2.52
Observations	59	83	499	161	660	33

distribution. The results have to satisfy Kolmogorov–Smirnov statistics (dependent on the number of observations) for a significance level of $a = 0.20$ (Davis 1986, table 2.26). The test was run on all three distributions to identify the lowest (most significant) Kolmogorov–Smirnov value.

Table 2. *Permeability structure of areas with different sedimentary structures within a single distributary mouth-bar.*

	X-Bedding	Hor. Lam	Bioturb.	Hummocky
Arithmetic mean	518	156	164	70
Min.	0	0	0	0
Max.	1985	927	787	588
St. Dev.	339	186	165	135
Co. Var.	0.66	1.19	1.01	1.91
Obs.	499	50	125	19

The permeability distributions for the different delta-front elements appear to be related to the degree of heterogeneity, and show increasing left-skewness with increasing heterogeneity. This is reflected by the approximately square-root normal distribution for the upper mouth-bar, and best fit (but not very good) to log-normal distribution for the distal bar (Fig. 10).

Ideally variogram analysis should be based on a large number of measurements (at least several hundred), where the measurement points are arranged in a regular grid. Due to time constraints, however, it was impossible to collect such an ideal data set from each station. The most comprehensive data set was collected at station 2 (Fig. 3). Horizontal and vertical variograms of minipermeameter data from the upper mouth-bar of this station are displayed in Figure 11. They reflect the overall horizontal layering and permeability anisotropy of the mouth-bar (Fig. 12). Applying a spherical variogram model (Clark 1979; Davis 1986), the vertical variogram has a sill value considerably above the total variance and a range of influence of about 3.25–4.25 m. It is difficult to apply the spherical model and detect any sill and range of influence for the horizontal variogram. This variogram seems to have a horizontal form indicating a long range of influence with a semivariance considerably below the total variance. Due to large dispersion and limited data points it is impossible to extract reliable ranges and sills from the other sampling stations.

Frequency histograms and a few statistical parameters for permeability in the upper mouth-bar at the four sampling stations are illustrated in Fig. 9. Note the gradual distal-ward decrease (trend) in permeability giving a non-stationary dataset. Ideally this has to be adjusted for when carrying out statistical analysis of all the data sampled in this facies element. Such trends within single facies can easily be included in stochastic heterogeneity models (MacDonald *et al.* in press).

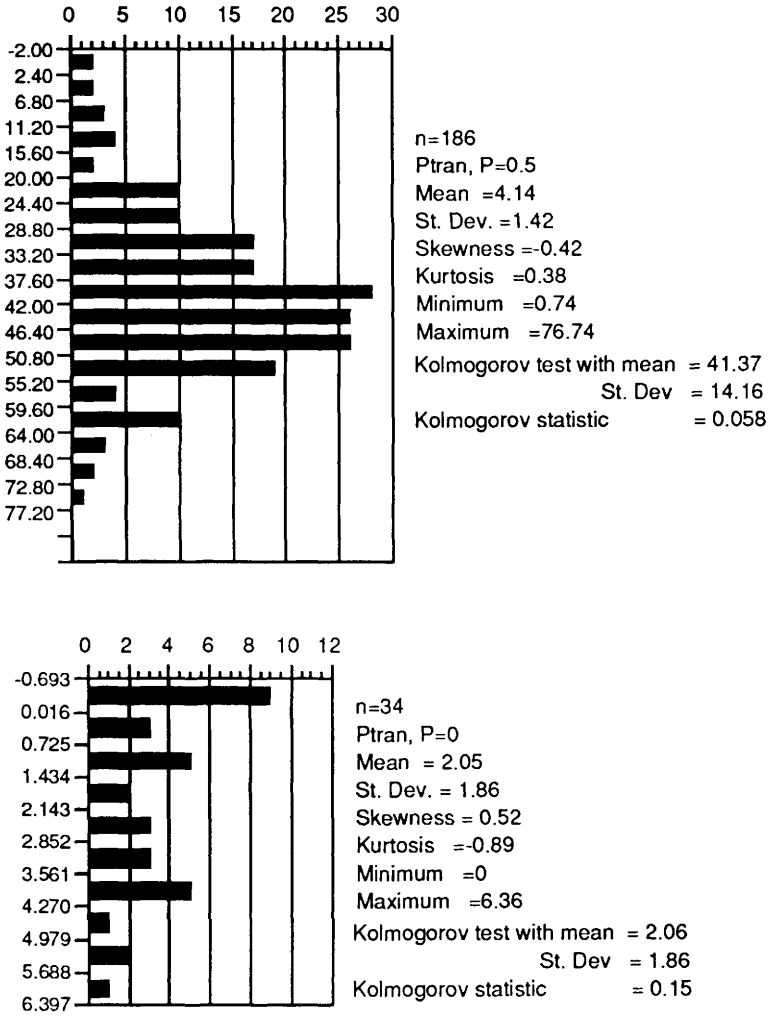

Fig. 10. Histograms showing transformed permeability distributions for upper mouth-bar facies (top) and distal bar facies (bottom). Upper mouth-bar data give best fit to a square-root normal distribution ($P = 0.5$), while distal bar facies data give a best fit to a log-normal distribution.

Effects of permeability contrasts on predicted fluid-flow

Polasek & Hutchinson (1967) recognized four common deviations from the idealistic homogeneous and continuous reservoir that can affect the fluid flow performance of a particular reservoir. These reservoir conditions are:

(a) restrictive faults;
(b) discontinuous sedimentary deposits;
(c) permeability variation in the clean sand portion of the deposit;
(d) complex sand, shaly-sand arrangements within a continuous deposit.

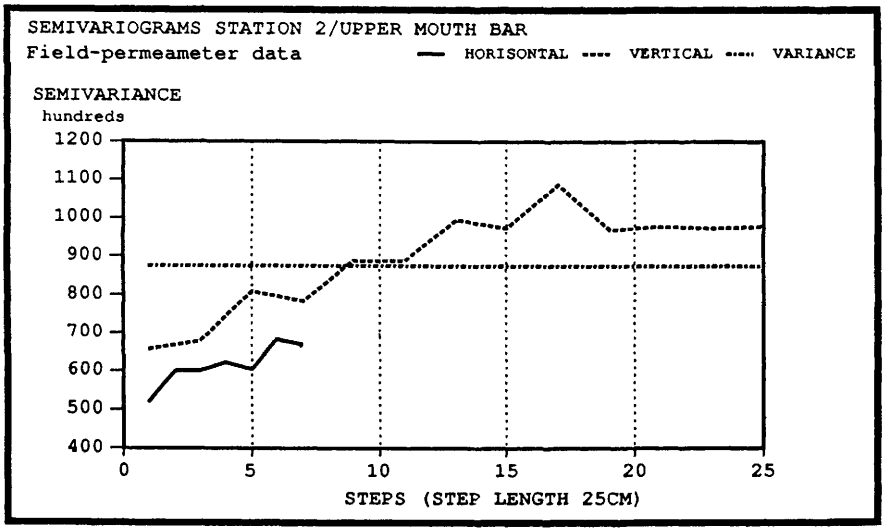

Fig. 11. Empirical semivariograms (horizontal and vertical) constructed from minipermeameter data from the upper mouth-bar at sampling station 2.

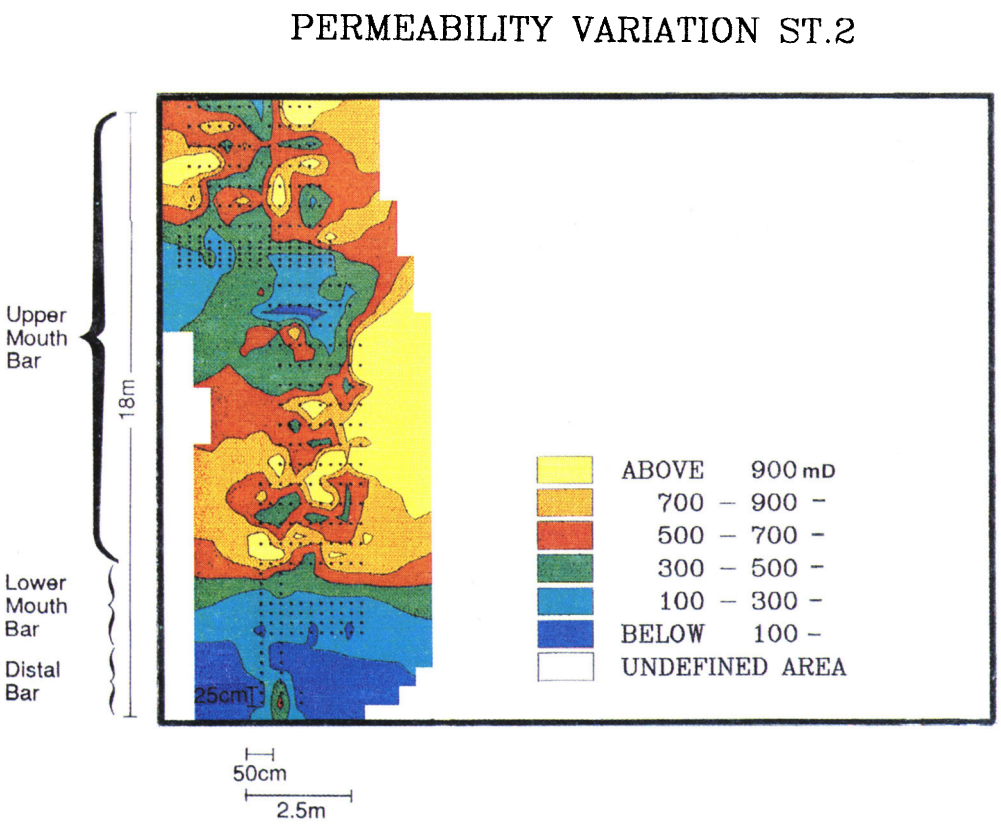

Fig. 12. Contour plot of permeability variations in the mouth-bar and distal bar facies at sampling station 2.

They stated that items (a) and (b) are the most influential and can be addressed through recourse to well pressure testing and improved reliability of correlations in areas of discontinuous reservoirs (e.g., channel sands and heterolithic layered intervals such as distal bar or turbidite sequences). Of the other heterogeneities the arrangement of the shales within a sandbody, and not the permeability variations within the sand were thought to be of critical first order importance.

In the type of deposits described herein, there are few shales distributed throughout the interval, and potential reservoir heterogeneities are associated with relatively minor differences in absolute permeability. The question, therefore, is whether a deposit such as the one described in the previous section can be treated as a homogeneous unit in a fluid flow simulator.

Hypothetical delta-front reservoir

A series of hypothetical reservoir simulation experiments were conducted to assess the relative influence of minor permeability contrasts of delta-front elements on predicted flow conditions. The objective of this experiment was to determine if the predictions of a simplistic homogeneous reservoir model differed significantly from the predictions of the two lithofacies element model. The simulator used for these experiments was a three-dimensional, three-phase, black-oil, reservoir simulation program. The experiments deal simply with two-phase flow in two-dimensional space.

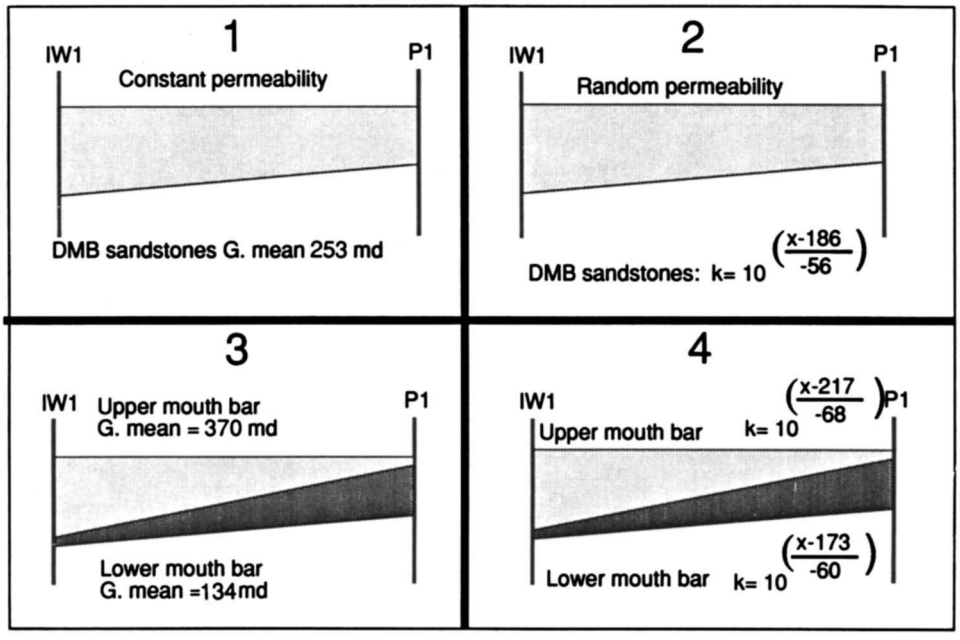

Fig. 13. Set-up of the four simulation experiments. (1) and (2) demonstrate the one element models with constant and random permeability respectively. (3) and (4) demonstrate the two element models with element internal constant and random permeability. (G. mean, geometric mean; DMB, distributary mouth-bar).

The experiment assumes the Short Canyon Spring distributary mouth-bar is buried at 2000 m in the subsurface, tilted at 5°, is 80% oil filled, and has no gas present. Two measured sections are treated as wells that have been drilled through the mouth-bar. Well I W1 (the injector) is located downdip in the central part of the deposit and well P1 (the producer) is located in the distal part of the deposit (Fig. 13). The entire mouth-bar interval is assumed to have been perforated, and it is represented by a 32 by 4 simulation grid where each grid cell is 50 × 50 m in the *xy*-plane. The height of each cell is variable in accordance with the geometry of the mouth-bar. Initial reservoir pressure was set at 300 bars, with a bubble point pressure of 256 bars. A constant porosity of 20% was assumed for all grid blocks, and vertical permeability was initialized at 10% of the horizontal permeability. Realistic relative permeability data were used and held constant for the entire reservoir.

Permeability models

Absolute permeability values for the reservoir simulation were derived from the field minipermeameter data (Table 1). In addition cumulative permeability probability functions were calculated for three subsets of the data (Fig. 14). The first subset was chosen to represent the cumulative permeability distribution in the entire distributary mouth-bar where it is assumed that no available information on the character and distribution of internal lithofacies elements existed. The two other subsets reflect the cumulative permeability distribution of the lower and upper mouth-bar respectively.

Four basic experiments were conducted (Fig. 13). In the first experiment the reservoir interval is depicted as a homogeneous continuous sandstone. The thickness of the reservoir interval is 14 m at the injection well (I W1) and 9 m at the producing well (P1). The distance between the wells is 1600 m. In this experiment constant absolute permeability (geometric mean) is assigned to each of the grid blocks. In the second experiment the mouth-bar is still considered as a one element model. In this case, however, the permeability of each grid cell was assigned by random sampling of the permeability probability function for the entire mouth-bar (Fig. 14). Experiments 3 and 4 consider the mouth-bar to comprise two lithofacies elements. In experiment 3, the lithofacies elements are considered to have constant permeability values (geometric means). Finally in experiment 4 the permeability of each grid cell is calculated from random sampling of the cumulative permeability probability functions for the lower and upper mouth-bar, respectively (Fig. 14).

In these experiments we are assuming that the permeability model of the mouth-bar can be described in terms of a random model with no spatial correlation.

Simulation results

There were two series of experiments. The first involved a constant injection and production rate and unrestricted bottom hole pressures. A pressure ceiling was set in the second series leading to variation in rates. The first series modelled a situation where the injection rate (100 m^3 per day) and the production rate (100 m^3 day) were held constant throughout the duration of the simulation. Figure 15 shows the plots of oil recovery and water cut throughout the duration of the simulation for each experiment.

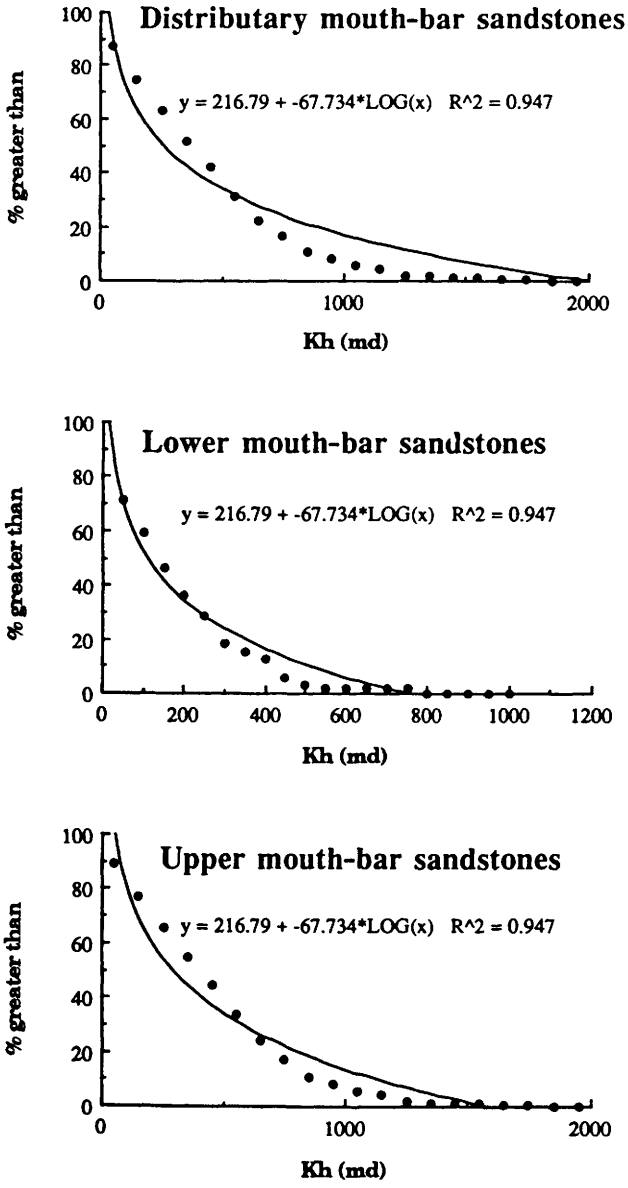

Fig. 14. Cumulative permeability probability functions for the distributary mouth-bar facies, and its internal lower and upper mouth-bar facies.

In this first series there was no appreciable difference in the breakthrough time in each of the experiments. Each simulation begins on 1 January 1990, and all four of the experiments have experienced water cut of more than 60% by 2.1 to 2.2 years. These results, however, are extremely misleading. They imply that the inclusion of both a randomly distributed permeability model and a two lithofacies element model does not affect the predicted breakthrough times.

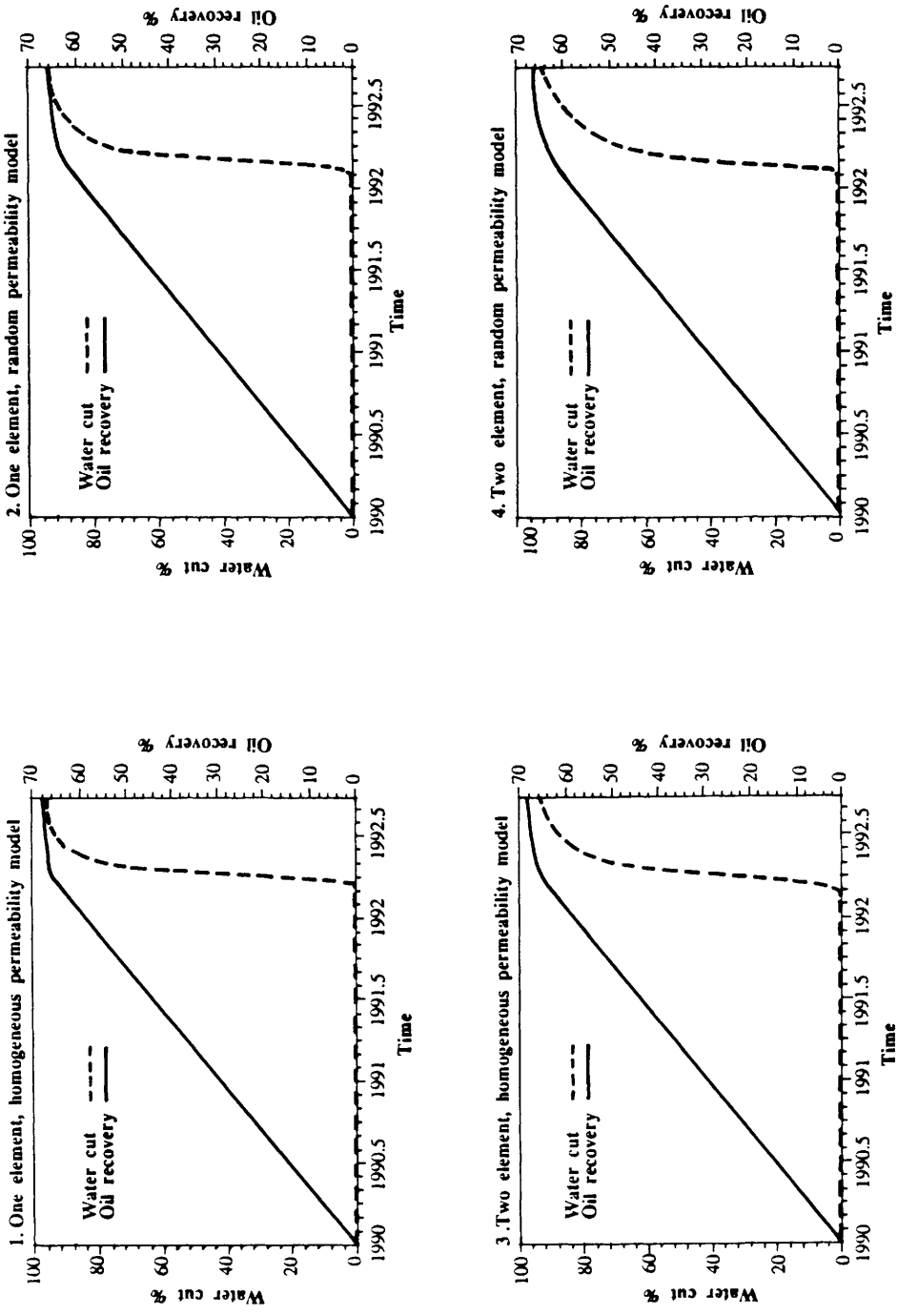

Fig. 15. Oil recovery and water cut for the first set of experiments. Injection and production rates were held constant. All four models give water breakthrough after 2.1 to 2.2 years.

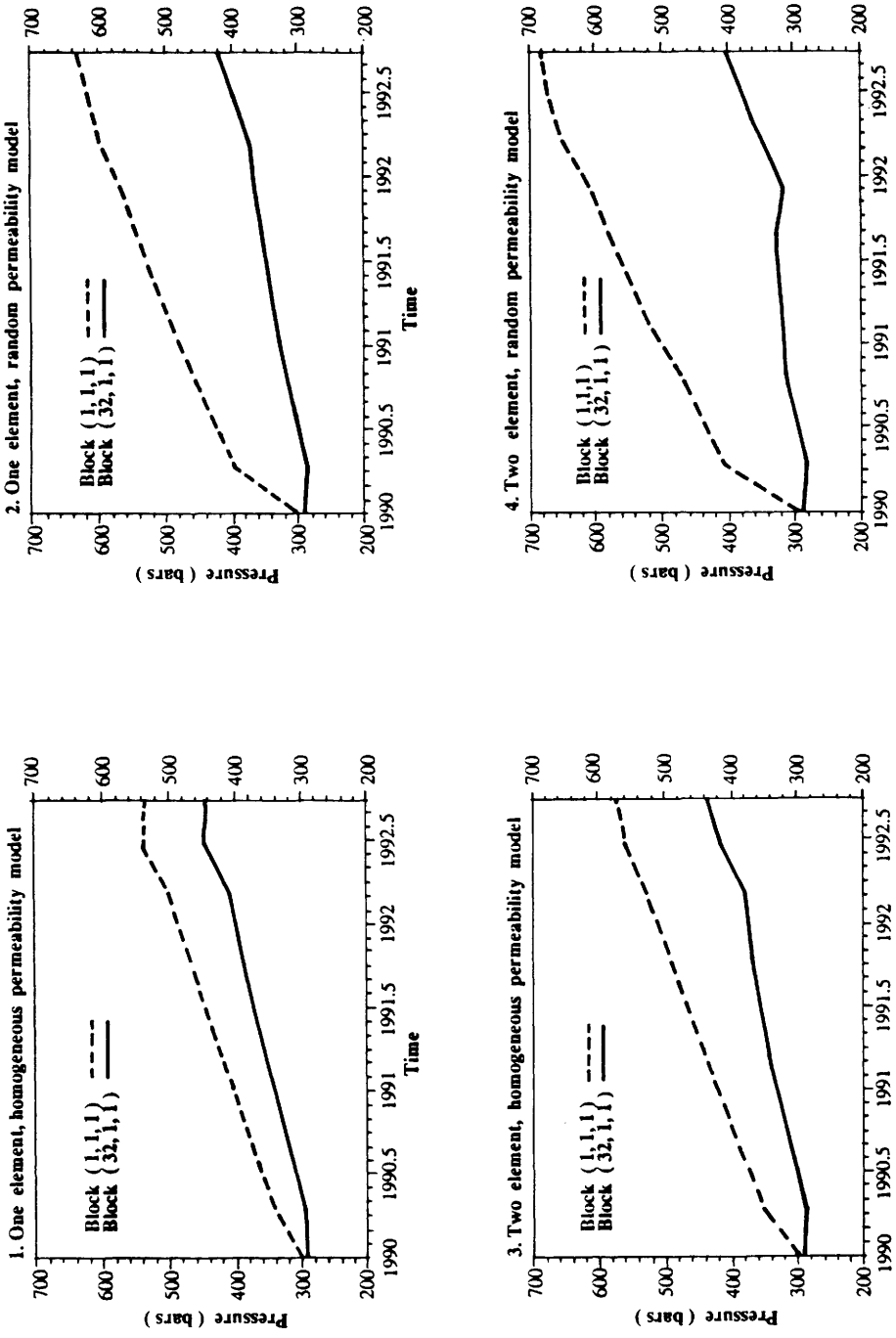

Fig. 16. Pressure changes with time in the lowermost grid block of the injecting well (stippled line) and producing well (solid line) throughout the duration of the simulations.

Examination of the reservoir pressure in the lowermost cell of the injector and the producing well reveals a different pressure build-up for the different set-ups (Fig. 16). The upper stippled line shows the change in pressure in the lowermost grid block of the injecting well throughout the duration of the experiments. The lower solid line depicts the change in pressure in the lowermost grid block of the producing well.

Notice the initial pressure difference between these two cells. This pressure difference reflects the fact that the reservoir is tilted (5°).

In this first series of experiments no constraints were placed on the upper limits of reservoir pressure. Consequently, reservoir pressure built-up from an initial value of 300 bars to unrealistically high pressures (greater than 700 bars) by the end of the simulation. A pressure difference of 100 bars developed between the injector and the producing well in the homogeneous, one element model. The pressure difference exceeded 210 bars when the one element model had randomly varying permeability. In the constant permeability two element model, the pressure difference at the end of the simulation is not as pronounced as the random permeability single layer model. The random permeability, two element model exhibits the greatest pressure difference between wells. The pressure difference in this model is almost three times that of the homogeneous, one element model and just over 40% greater than the one element, random permeability model.

The second series of experiments was conducted to examine the simulated flow conditions without permitting such unrealistic pressure build-ups to occur. In these experiments the reservoir pressure was not permitted to exceed 300 bars (i.e., the original reservoir pressure). This was accomplished by varying the water injection rate. Comparison of the breakthrough times for the various permeability models should focus on the differences between the predicted breakthrough times of experiments one and three and two and four respectively (Fig. 17). Breakthrough occurs in the homogeneous, one element model after 2.2 years and in the homogeneous, two-element model after 3.2 years. That means the two element model predicts a 45% longer breakthrough time than the one element model. For the random permeability model the one element situation gave breakthrough after 5 years while the two-element situation gave breakthrough after approximately 7 years, which means a 40% longer breakthrough time. The difference in predicted breakthrough times is even greater when one compares the homogeneous and random permeability models for the one and two element models respectively. The difference is close to 145% for one element models, and about 135% for the two element models.

These results indicate that significant differences in reservoir performance can occur when one refines the architecture of an apparently homogeneous reservoir. Even though the contrast in absolute permeability of the different elements is relatively minor, in the simple scenario presented here, it may have significant impact on the modelling of flow behaviour.

Summary and conclusions

The data collected here are specific to fluvial-dominated delta-front deposits, and the general implications of these results may be quite limited. However, in addition to presenting some information on facies dimensions, facies architecture and permeability structures in this particular subenvironment, the study also illustrates

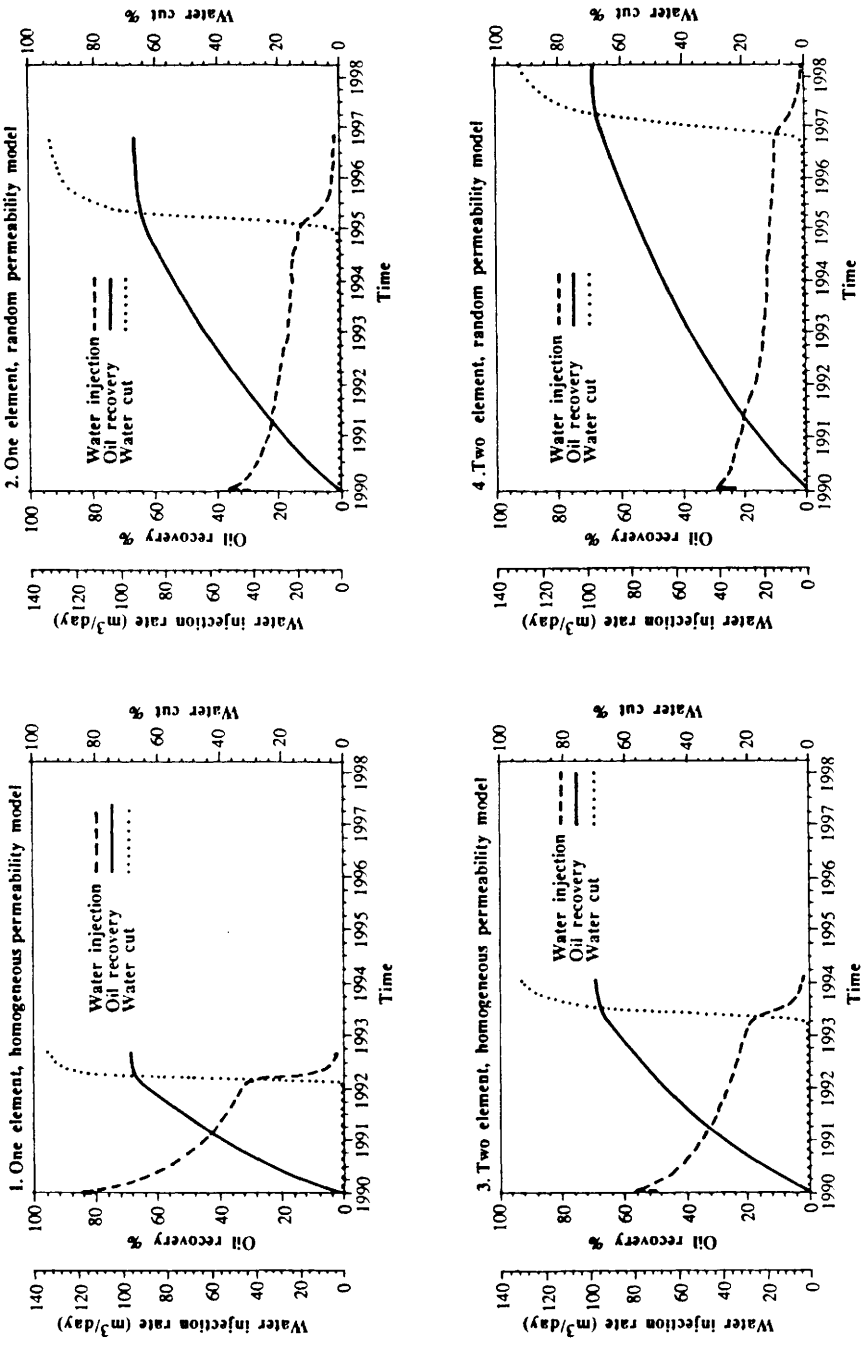

Fig. 17. Oil recovery, water cut and water injection for the second set of experiments. In these experiments a pressure ceiling was set at 300 bars. The results indicate significant differences in reservoir performance for the different models under these changed conditions.

several key considerations that need to be taken into account when developing a quantitative model of a reservoir.

(a) The quantitative data on dimensions showed that distributary mouth-bars may range up to 9 km in length and 6 km in width. Distributary channel width to thickness ratios range from 10 : 1 to 20 : 1.
(b) A random approximation of shale occurrence can grossly misrepresent the spatial variation of transmissibility within a reservoir interval. As we have seen here, the distal bar facies can vary significantly. There are regions where the degree of interconnectedness of the individual sandstones is much greater, and therefore, the communication within the reservoir significantly improved. The equation that represents the cumulative shale distribution is not sufficient to characterize adequately this type of heterogeneity.
(c) Although there are many potential problems with the applicability of outcrop derived absolute permeability data, our results indicate significant correlation between permeability structure and genetic sedimentary elements. The data also demonstrate that similar descriptive sedimentary facies in different genetic elements might have significantly different permeability structures. For example the trough cross-bedded, medium-grained, upper mouth-bar facies has significantly higher permeability than the trough cross-bedded, medium-grained, distributary channel facies.
(d) Consideration of internal permeability contrasts may be extremely important in the development of a reservoir model. A series of simple, hypothetical experiments has shown that the inclusion of seemingly small differences in permeability between two internal lithofacies elements can lead to quite large differences in predicted reservoir behaviour. The final observation warrants the continued study of facies dimensions, facies architecture, and absolute permeability structures if we are to incorporate the necessary geological detail into a petrophysical model of the reservoir.

This work was funded by the Norwegian Petroleum Directorate SPOR programme. H. Brændshøi, H. Rendall and A. Råheim assisted in the field, and A. MacDonald checked the manuscript. Norsk Hydro a.s. provided the field minipermeameter, and T. Dreyer and Å. Scheie instructed us in its use. To all these individuals and organizations we express our sincere thanks. We also would like to thank M. Ashton, J. Marshall and A. Pulham for their helpful comments on the manuscript.

References

BALSLEY, J.K. 1988. *Wave dominated deltas, shelf sands and submarine fans: Clastic depositional models for hydrocarbon exploration.* Field trip notes.

BOX, G.E.P. & COX, D.R. 1964. An analysis of transformations. *Journal of the Royal Statistical Society*, **B26**, 211–252.

CLARK, I. 1979. *Practical Geostatistics.* Applied Science Publishers, London, 129p.

COBBAN, W.A. and REESIDE, J.B., Jr. 1952. Correlation of the Cretaceous formations of the western interior of the United States. *Geological Society of America Bulletin*, **63**, 1011–1047.

COLEMAN, J.M. & GAGLIANO, S.M. 1965. Sedimentary structures: Mississippi River deltaic plain. *In*: MIDDLETON, G.V. (ed.) *Primary sedimentary structures and their hydrodynamic interpretation.* Society of Economic Paleontologists and Mineralogists, Special Publication, **12**, 133–148.

——, ——. & WEBB, J.E. 1964. Minor sedimentary structures in a prograding distributary. *Marine Geology*, **1**, 240–258.

COTTER, E. 1975*a*. Late Cretaceous sedimentation in a low energy coastal zone: the Ferron Sandstone of Utah. *Journal of Sedimentary Petrology*, **45**, 669–685.

—— 1975*b*. The role of deltas in the evolution of the Ferron Sandstone and its coals, Castle Valley, Utah. *Geological Society of America Abstracts with Programs*, **7**, 1039–1040.

—— 1975*c*. Deltaic deposits in the Upper Cretaceous Ferron Sandstone of Utah. *In*: BROUSSARD, M.L. (ed.) *Deltas, Models for Exploration*. Houston Geological Society, Houston, Texas, 471–484.

—— 1976. The role of deltas in the evolution of the Ferron Sandstone and its coals, Castle Valley, Utah. *Brigham Young University Geology Studies*, **22**, 15–42.

DAVIS, J.C. 1986. *Statistics and Data Analysis in Geology*. John Wiley & Sons.

DOELLING, H. H. 1972. *Central Utah coal fields: Sevier, Sanpete, Wasatch Plateau, Book Cliffs, and Emery*. Utah Geological and Mineralogical Survey, Monograph Series, **3**.

FINLEY, R.M. & TYLER, N. 1986. Geological characterization of sandstone reservoirs. *In*: LAKE, L.W. & CARROLL, H.B. Jr. (eds) *Reservoir Characterization*. Academic Press, 1–38.

GARDNER, M.H., LEVERSON, M.K. & CROSS, T.A. 1987. Volumetric analysis of Facies Partitioning in Shallow Marine to Coastal-Plain Strata, Ferron Sandstone, Utah. *Geological Society of America Abstracts with Programs*, **19**, 672–672.

GILBERT, G.K. 1877. *Report on the geology of the Henry Moutains (Utah)*. U.S. Geographical and Geological Survey, Rocky Mountain Region (Powell).

GRAY, R.J., PATALSKI, R.M. & SHAPIRO, N. 1966. Correlation of coal deposits from central Utah. *In*: Central Utah coals: A guidebook prepared for the Geological Society of America and associated societies. *Utah Geological and Mineralogical Survey Bulletin*, **80**, 81–86.

HUNT, C.B. 1946. *Guidebook to the geology and geography of the Henry Mountain region*. Utah Geological Society Guidebook, **1**.

——, AVERITT, P. and MILLER, R.L. 1953. *Geology and geography of the Henry Mountains region, Utah*. U.S. Geological Survey Professional Paper 228, 234p.

JACOBSEN, T. & RENDALL, H. 1990. Permeability Patterns in Some Fluvial Sandstones. An Outcrop Study from Yorkshire, North East England. *2nd Int. Reservoir Characterization Tech. Conf., June 25–28, 1989, Dallas.*

LEVERSON, M.K. & GARDNER, M.H. 1987. Changes in Geometries of Facies Tracts related to Time-Space Variations in Accommodation Potential, Ferron Sandstone, Utah. *Geological Society of America Abstracts with Programs*, **19**, 672–672.

LUPTON, C.T. 1916. *Geology and coal resources of Castle Valley in Carbon, Emery, and Sevier countries, Utah*. U.S. Geological Survey Bulletin, **628**.

MACDONALD, A.C., HØYE, T., JACOBSEN, T., AASEN, J.O., GRINDHEIM, A.O. & LOWRY, P. in press. Stochastic Flow Unit Modelling of a North Sea Coastal-Deltaic Reservoir. *6th European Symposium on Improved Oil Recovery, 21–23 May 1991, Stavanger, Norway.*

MAY, F.F. 1962. A survey of palynomorphs from several coal-bearing horizons of Utah. *Utah Geological and Mineralogical Survey Monograph Series*, **3**, 497–542.

NELSON, B.W. 1970. Hydrography, sediment dispersal and recent historical development of the Po River delta, Italy. *In*: MORGAN, J.P. & SHAVER, R.H. (eds) *Deltaic Sedimentation Modern and Ancient*. Society of Economic Paleontologists and Mineralogists, Special Publication, **15**, 152–184.

POLASEK, T.L. & HUTCHINSON, C.A. Jr. 1967. Characterization of Non-Uniformities within a Sandstone Reservoir from a Fluid Mechanics Standpoint. *In: Proceedings, Seventh World Petroleum Congress, Mexico*, 397–407.

RYER, T.A. 1981. Deltaic Coals of Ferron Sandstone Member of Mancos Shale; Predictive Model for Cretaceous Coal-Bearing Strata of Western Interior. *American Association of Petroleum Geology Bulletin*, **65**, 2323–2340.

—— 1982. *Cross-section of the Ferron Sandstone Member of the Mancos Shale in the Emery Coal field, Emery and Sevier Counties*. U.S. Geol. Survey Map, MF-1357.

—— & MCPHILLIPS, M. 1983. Early Late Cretaceous paleogeography of east Central Utah. *In*: M.W. REYNOLDS and E.D. DOLLY (eds) *Mesozoic Paleogeography of the West-Central United States, Rocky Mountain Section*. Society of Economic Paleontologists and Mineralogists, 253–272.

SARMIENTO-SOTO, R. 1957. Microfossil zonation of Mancos Group, Utah. *American Association of Petroleum Geologists Bulletin*, **41**, 1683–1693.

SPIEKER, E. M. 1949. Sedimentary facies and associated diastrophism in the Upper Cretaceous of central and eastern Utah. *In*: LONGWELL, C.P. (chairman) *Sedimentary facies in geologic history*. Geological Society of America Memoir **39**, 55–82.

STAPOR, F. W. & ADAMS, R. D. 1988. Delta morphologies and progradational styles: Ferron Member of the Mancos Shales, East Central Utah. *American Association of Petroleum Geologists Bulletin*, **72**, 250–251.

SWANN, D. H. 1964. Late Mississippian rhythmic sediments of Mississippi Valley. *American Association of Petroleum Geologists Bulletin*, **48**, 637–658.

THOMPSON, S.L., OSSIAN, C.R. & SCOTT, A.J. 1986. Lithofacies, inferred processes, and log response characteristics of shelf and shoreface sequences, Ferron Sandstone, central Utah. *In*: MOSLOW, T.F. & RHODES, E. G. (eds) *Modern and Ancient Shelf Clastics: A Core Workshop*. Society of Economic Paleontologists and Mineralogists Core Workshop No. **9**, 325–361.

TRIPP, C.N. 1989. *A hydrocarbon exploration model for the Cretaceous Ferron Sandstone Member of the Mancos Shale, and the Dakota Group in the Wasatch Plateau and Castle Valley of east-central Utah, with emphasis on post-1980 subsurface data*. Utah Geological and Mineral Survey Open File Report 160.

URSEK, J. 1979. Sedimentary environment of the Cretaceous Ferron Sandstone near Caineville, Utah. *Brigham Young University Geology Studies*, **26**, 81–100.

WEBER, K.J. 1986. How heterogeneity affects oil recovery. *In*: LAKE, L.W. & CARROLL, H.B. (eds) *Reservoir Characterization*. Academic Press, 487–544.

—— & VAN GEUNS, L.C. 1990. Framework for constructing clastic reservoir simulation models. *Journal of Petroleum Technology*, **42**, 1248–1297.

From ASHTON, M. (ed.), 1993, *Advances in Reservoir Geology*,
Geological Society Special Publication No. 69, pp. 105–134.

Effects of heterogeneities in a braided stream channel sandbody on the simulation of oil recovery: a case study from the Lower Jurassic Statfjord Formation, Snorre Field, North Sea

ØISTEIN HØIMYR, AMUND KLEPPE & JOHAN P. NYSTUEN

Saga Petroleum, PO Box 490, N-1301 Sandrika, Norway

Abstract: Three heterogeneous models of a channel sandbody of braided stream origin were constructed by combining reservoir data from the middle reservoir unit of the Lower Jurassic Statfjord Formation in the Snorre Field in the Norwegian Sector of the North Sea, with facies and geometry data from an exposed analogue channel sandbody in the Pennsylvanian–Permian Maroon Formation, Colorado. Permeability classes corresponding to those in the Statfjord Formation were distributed according to facies variation in the analogue sandbody and to the recorded vertical distribution in the Middle Statfjord sandbodies. Relative permeability and capillary pressure curves were made for individual permeability classes. Two-dimensional (*yz*-plane) reservoir simulation of waterflooding was carried out with injection at the down-dip end and production at the up-dip end of the models, which measured 104 m × 8.75 m and had a structural dip of 8°.

The results were compared with simulations on two reference models, one of a homogeneous sandbody and one with the permeability zonation organized in parallel layers with decreasing permeability from base to top. All models had the same volume-weighted arithmetic mean permeability. The 104 m long basic models were also compared with scaled-up versions measuring 312 m and 936 m, respectively.

The simulations show that variation in internal heterogeneity has considerable impact on recovery efficiency. Compared with the homogeneous reference model, the heterogeneous models had reduced recovery efficiencies at water breakthrough of 11% to 33%, depending on the type and degree of heterogeneity, and a corresponding reduction in mean effective permeability of 9% to 42%. This study also demonstrated the importance of using capillary pressure data in simulations of this type.

Capillary pressure allows imbibition into the low permeability rocks during waterflooding and explains the higher recovery efficiency on simulation runs on the scaled-up models compared to the short basic models. The effect of capillary pressure also results in higher recovery efficiency in runs with low flow rate than in runs with high rate. Similar simulation studies, also in 3-D, should be performed on various types of internal heterogeneities in complex fluvial reservoirs.

Fluvial reservoirs are generally highly heterogeneous, and the simulation of fluid flow in two- and three-dimensional models of specific heterogeneity properties has become an important tool in the prediction of recovery efficiency and for production planning in oil fields. Here the term 'modelling' is used to describe the static geometrical and physical properties of the reservoir, and the term 'simulation' implies testing, by theoretical flow mechanics, the dynamic behaviour of fluid flow in the reservoir.

Geological modelling of fluvial reservoirs includes the treatment of heterogeneities varying in dimensions from field to microscopic scale (e.g. Weber 1986; Miall 1988; Van de Graaff & Ealey 1989). At the 'field-to-reservoir scale', corresponding to the overall *fluvial architecture* of Allen (1983) and Miall (1985), the critical modelling criteria are sandstone interconnectedness and lateral and vertical fluid continuity. Genetic modelling of sandstone interconnectedness has been attempted by Allen (1978), Bridge & Leeder (1979) and Alexander & Leeder (1987). In North Sea reservoirs, stochastic geological modelling has been applied to the fluvial Upper Triassic Lunde Formation and the Lower Jurassic Statfjord Formation (Augedal *et al.* 1986; Stanley *et al.* 1990; Clemetsen *et al.* 1990) and to the Middle Jurassic Ness Formation (Gundesø & Egeland 1990). Deterministic modelling has been carried out on the Statfjord Formation by Johnson & Krol (1984) and Martin *et al.* (1988).

Geological modelling and field experience have shown that thick, extensive floodplain deposits of mudrocks restrict the possibilities of vertical connectivity between sandbodies. In such reservoirs, individual sandbodies should be treated as separate reservoir units. At this genetic sandbody scale, internal heterogeneities such as bedding structures, shale drapes, cementation and grain size variation are, together with pore-textural properties, of great importance to fluid flow behaviour during oil production (e.g. Weber 1986; Van de Graaff & Ealey 1989).

However, there are great variations in the dimensions, geometries, internal structures, and textures of fluvial channel sandbodies (e.g. Weber 1986; Miall 1988; Van de Graaff & Ealey 1989). Although general fluid flow behaviour can be deduced from vertical and lateral grain size and facies variations, and the spatial distribution of internal permeability barriers in fluvial channel sandstones, quantitative knowledge of the effects of heterogeneities at this scale on reservoir simulation is restricted.

The aim of the present study is to simulate the effect of heterogeneities, within a single fluvial sandbody deposited in a braided stream environment, on recovery efficiency and flow capacity during waterflooding. The main emphasis is placed on the effect of discontinuous shale drapes, internal permeability variations and a basal high permeability zone. It should be noted that the recovery efficiency in this study is restricted to the performance of 2-D presentations of small elements of the reservoir and is not a measure of field recovery efficiency. The recovery efficiency is calculated as the ratio between simulated produced oil volume and oil volume initially in place. This ratio is seen in relation to the corresponding water content in the produced liquid, the 'water cut', when comparing results from different sandbody models.

The case study involves a channel sandbody having properties (thickness, internal geometry of facies distribution, bounding surfaces, shale drapes and grain size variation) characteristic of reservoir sandbodies in the Lower Jurassic Statfjord Formation of the Snorre Field in the North Sea (Fig. 1). The heterogeneous models were constructed by combining external geometry and internal heterogeneity from a channel sandbody recorded in the Pennsylvanian–Permian Maroon Formation in western Colorado with petrophysical and field reservoir data from sandbodies in the middle part of the Statfjord Formation, here called the MSF sandbodies. We do not suggest that the Maroon Formation as a whole is an analogous formation to the Statfjord Formation, neither that the chosen heterogeneous channel sandbody from this formation is the only representative one for the MSF sandbodies. However, the selected sandbody from the Maroon Formation is an analogue unit to MSF sandbodies in the sense of similarities with respect to depositional environment,

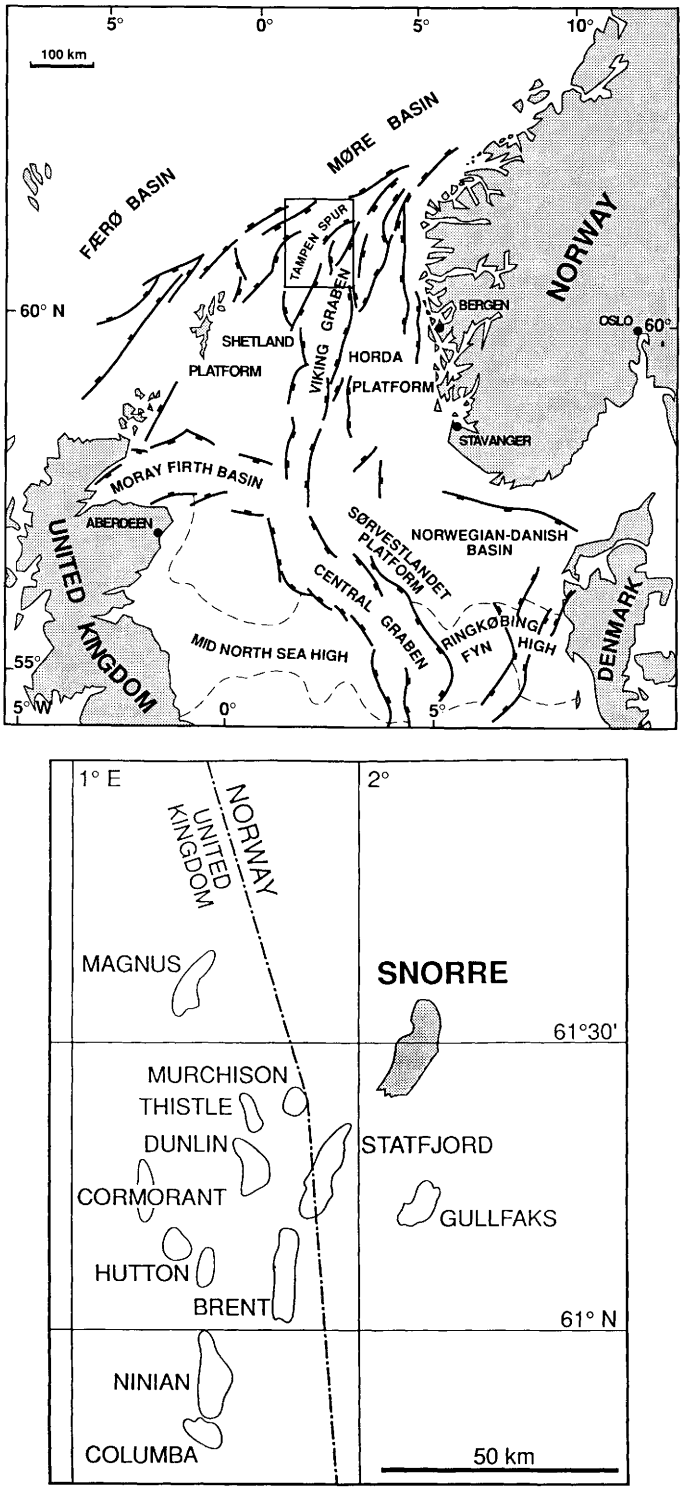

Fig. 1. Location of the Snorre Field and the Tampen Spur in the northern North Sea.

thickness, and internal organization of sedimentary structures, grain size and bounding surfaces.

Reservoir simulation has previously been performed on the Statfjord Formation using a 3-D element model on stochastically modelled representations of the overall reservoir scale heterogeneity (Nybråten *et al.* 1990). The aim of the present study is to supply additional information on the effect of one type of heterogeneity on recovery efficiency within one individual sandbody.

The simulation was performed in two dimensions by using the ECLIPSE reservoir simulator. Although three-dimensional simulation at this genetic scale is highly desirable, the necessary additional input of time and money is usually high relative to a 2-D simulation (e.g. Ravenne & Beucher 1988). The 2-D simulation at this scale is, however, a practical first-step tool for testing, quantitatively, sensitivities on oil recovery of various types of heterogeneities. During the last five years the interest for mapping heterogeneity patterns of fluvial and deltaic sandstones has been steadily increasing. As most of this material is recorded in two dimensions, 2-D simulation of fluid flow through genetic sandbody units is considered a valid application of these field databases. The present study also demonstrates how results obtained from investigations on analogous sandstone units, exposed onshore, can be integrated into the reservoir evaluation of offshore and other unexposed reservoir rocks.

Model data derived from the Statfjord Formation, Snorre Field

Geological data

The Lower Jurassic Statfjord Formation is a major reservoir unit in the northern North Sea area and contributes significantly to the hydrocarbon production in fields such as the Brent, Statfjord and Gullfaks, and to the expected future production from Snorre. All of these fields are located within the Tampen Spur, a structural high consisting of a series of rotated fault blocks west of the northern Viking Graben (Fig. 1). In the Tampen area the Statfjord Formation succeeds the Triassic redbed sequence within the thick (up to about 2000 m) Hegre Group, and is overlain by marine mudstones, marls and sandstones of the Dunlin Group (Deegan & Scull 1977; Vollset & Doré 1984; Fig. 2). The Statfjord Formation attains a maximum thickness of about 320 m and is, in its type well in the Statfjord Field, subdivided into three members, in ascending order, the Raude, Eiriksson and Nansen. The formation generally forms an upward-coarsening sequence with the two lower members of fluvial origin and the uppermost member of shallow marine origin (Vollset & Doré 1984; Steel & Ryseth 1990).

The Statfjord Formation in the Snorre Field is 85–105 m thick and forms an overall upward-coarsening and thickening sequence (Fig. 3). The upper marine member of the type area has not been identifed and the formation has been informally subdivided into two members and three reservoir units (Figs 3 & 4). The middle and upper reservoir units host 103×10^6 Sm^3 oil-in-place (Hollander 1987). The formation rests conformably above the Upper Triassic Lunde Formation, which is also an alluvial sequence, and a major component to the reservoir of the Snorre Field. The Statfjord Formation is penetrated by 10 exploration wells on the Snorre Field and in immediately adjacent areas. The formation is nearly completely cored in

five of these wells (Nystuen *et al.* 1989) and data from these cored intervals are included in the present study.

Deegan & Scull (1977) suggested that the main part of the Statfjord Formation was of braided stream origin, deposited on an alluvial plain. Moiola (*in* Chauvin & Valachi 1980; and *in* Kirk 1980) also suggested a fluvial, mainly braided stream origin for the Raude and Eiriksson Members. Johnson & Krol (1984) interpreted the fluvial sandstones of the Statfjord Formation as coarse-grained, moderate to low sinuosity meandering stream deposits, but braided streams were also suggested to be represented by sand-dominated, multistorey intervals. Røe & Steel (1985) concluded that the Raude Member represents distal fan and coastal flood-basin environments and the overlying Eiriksson Member depositional settings of alluvial fans, coastal flood basin and lagoonal bay.

<table>
<tr><th colspan="3">Chronostratigraphy</th><th colspan="3">Lithostratigraphy</th></tr>
<tr><th>System</th><th>Series</th><th>Stage</th><th>Group</th><th>Formation</th><th>Member</th></tr>
<tr><td rowspan="3">Jurassic</td><td rowspan="3">Lower</td><td>Pliens-bachian</td><td>Dunlin</td><td>Amundsen</td><td>Calcareous</td></tr>
<tr><td>Sinemurian</td><td rowspan="3"></td><td rowspan="3">Statfjord</td><td rowspan="2">Upper</td></tr>
<tr><td>Hettangian</td></tr>
<tr><td rowspan="8">Triassic</td><td rowspan="3">Upper</td><td>Rhaetian</td><td>Lower</td></tr>
<tr><td>Norian</td><td rowspan="6">Hegre Group</td><td rowspan="3">Lunde</td><td>Upper</td></tr>
<tr><td>Carnian</td><td>Middle</td></tr>
<tr><td rowspan="2">Middle</td><td>Ladinian</td><td>Lower</td></tr>
<tr><td>Anisian</td><td>Lomvi</td><td></td></tr>
<tr><td rowspan="2">Lower</td><td rowspan="2">Scythian</td><td rowspan="2">Teist</td><td>Upper</td></tr>
<tr><td>Lower</td></tr>
</table>

Fig. 2. Chrono- and lithostratigraphical position of the Statfjord Formation, Snorre Field, northern North Sea. The subdivision of the Statfjord Formation into lower and upper members is informally applied in the Snorre Field.

Our observations from the Snorre Field support the interpretations of a braided stream origin for the Statfjord Formation on the Tampen Spur. The sand-rich upper member of the Statfjord Formation in the Snorre Field consists of up to 22 m thick sandbodies intercalated with mudstone units ranging in thickness from about 0.5 m to about 10–12 m. These mudstones are reddish-brown to grey and are characterized by stacked palaeosols. The sandstones have erosional lower contacts and are dominated by trough cross-bedded medium to very coarse-grained and gravelly, moderately to poorly sorted sandstone, facies St in the terminology of Miall (1978). Planar cross-beds (facies Sp), horizontal bedding (facies Sh) and current ripple cross-lamination (facies Sr) occur in minor amounts. Most sandbodies can be subdivided into several smaller sequences bounded below by an erosional surface (scour) and

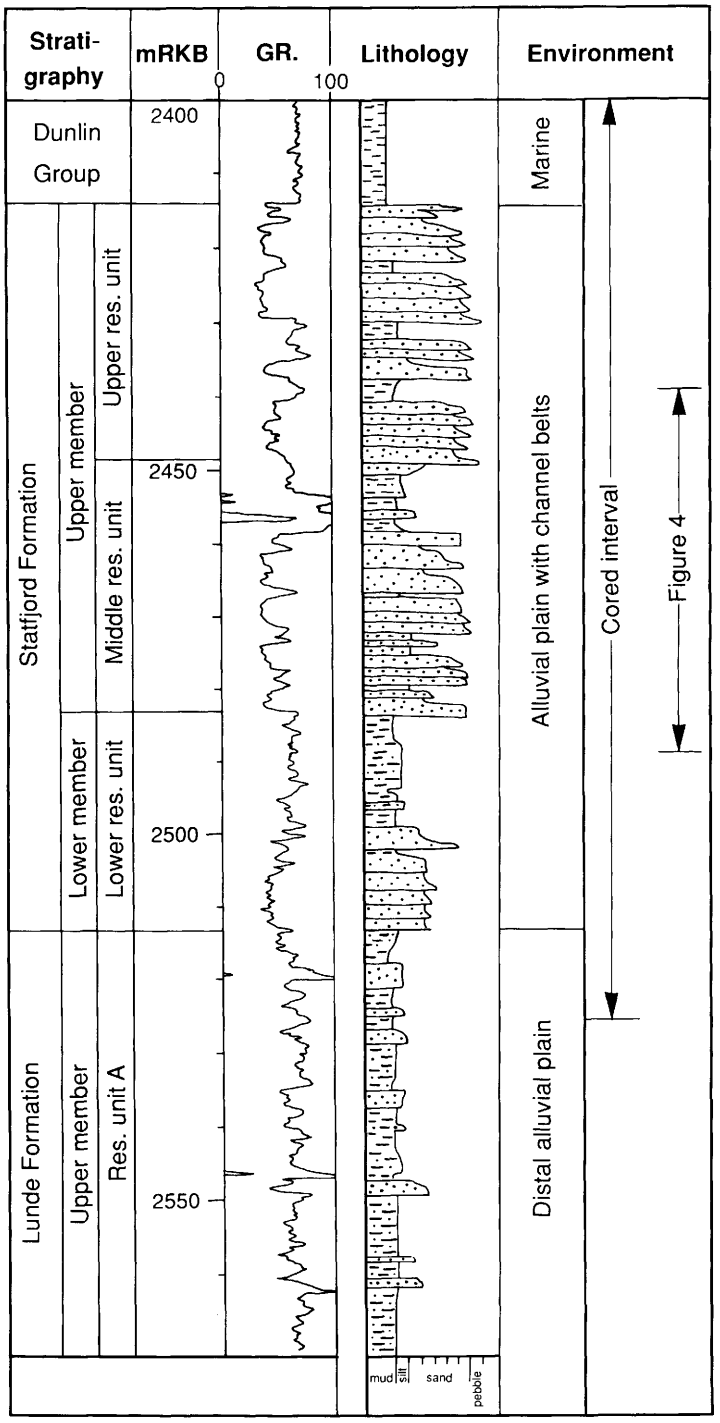

Fig. 3. Gamma ray curve and lithology trend through the uppermost part of the upper member of the Lunde Formation and the Statfjord Formation, well 34/7-3, Snorre Field, northern North Sea. Stratigraphical position of Fig. 4 is shown.

having a slight internal upward-fining grain-size trend (Fig. 4). These subunits can be capped by thin beds of very fine-grained sandstone or mudstone. These trough cross-bedded bedsets are thought to represent minor channel-fill deposits of sandy bedforms or units of channel bars. Very pronounced upward-fining units having thick low-angle, cross-bedded bedsets in association with small-scale cross-bedding and current-ripple lamination, that could indicate the presence of laterally accretionary large bar forms, have not been identified in the MSF sandbodies (but these are very abundant in the upper part of the underlying Lunde Formation).

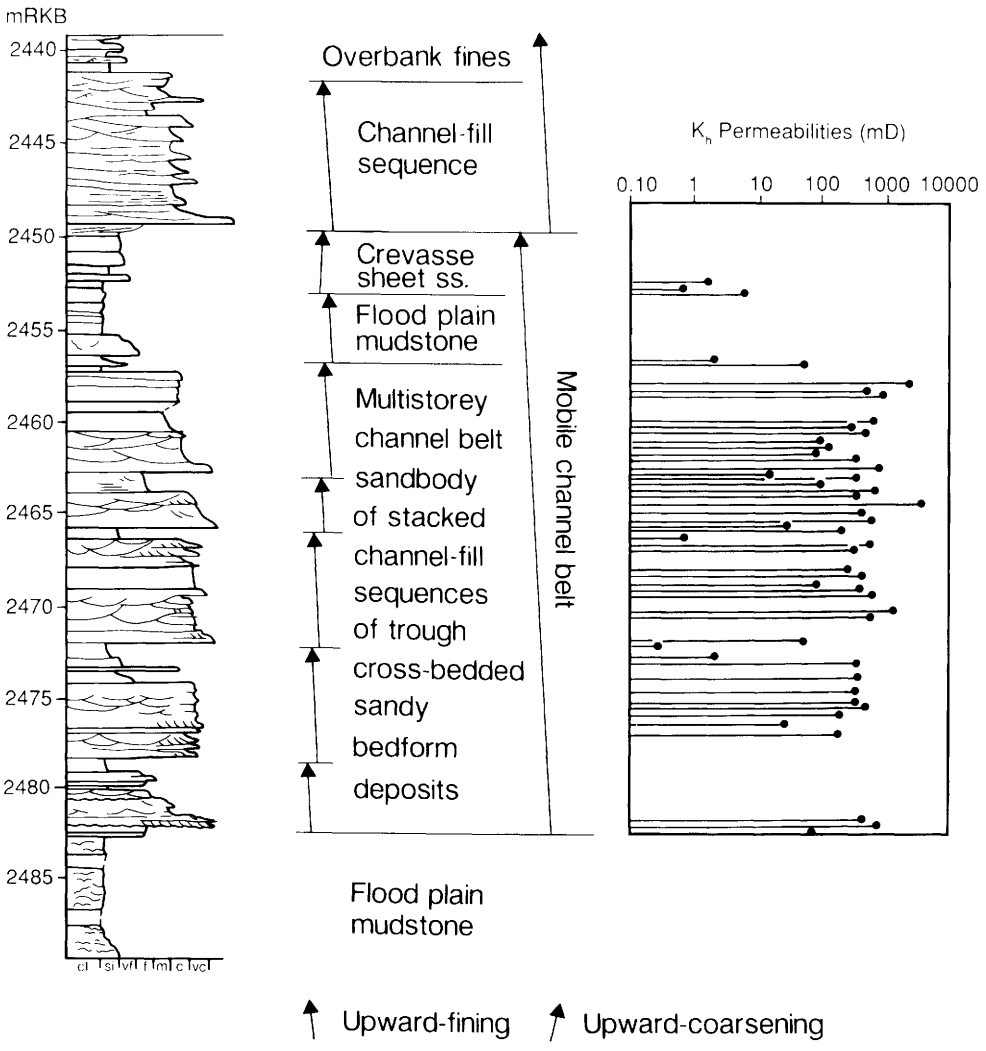

Fig. 4. Detail of lithology column of Fig. 3 showing the vertical stacking of individual upward-fining channel-fill sequences and bar units in mobile channel belt sandstones of a braided stream origin. Horizontal permeability measurements from core plug analyses are presented to the right.

Though we are aware of the uncertainties in interpreting ancient fluvial channel types from borehole data (e.g. Miall 1985; Bridge 1985), we think that the dominance of trough cross-bedded sandstone facies, moderate to poor sorting, coarse sand grain size (although grain size varies considerably over short vertical distances), and the stacked multistorey character of the sandbodies are characteristic elements of sandy braided stream deposits (e.g. Miall 1977, 1985; Cant 1978; Rust 1978). The composite, thick sandbodies are interpreted to represent mobile channel belt deposits lain down during ephemeral flooding and subsequently enclosed by flood-plain mudstones (Nystuen *et al.* 1989).

Correlation suggests that the sandbodies of the middle reservoir units of the Statfjord Formtion have a more restricted lateral extent than the thicker and coarser grained sandbodies in the upper reservoir unit. Also the sandbodies in the middle unit are more heterogeneous than in the upper unit with greater grain-size variation and more interstratified thin shale beds. The sandbodies of the middle Statfjord Formation (MSF) thus represent reservoir units in which internal heterogeneity distribution is typically expected to affect recovery efficiency. In order to test the sensitivities of recovery efficiency on internal heterogeneity within MSF types of sandbodies, petrophysical and reservoir field data from the middle reservoir unit of the Statfjord Formation in the Snorre Field have been incorporated in the models.

Field data

The Snorre Oilfield is located on a structural high consisting of several rotated fault blocks. The oil-bearing sandstones have an average dip of 8° to the westnorthwest. The Statfjord Formation reservoir is located in the southwestern part of the field. The oil will be produced from wells located updip near the top of the structure, whereas water injection wells will be positioned downdip at a distance of about 900 m from the nearest producer (production started August 1992). The fluvial channel sandbodies are interpreted to be orientated approximately northeast–southwest with a regional palaeoflow approximately towards the northeast (Nystuen *et al.* 1989). The waterflooding is thus planned to be mainly transverse to the palaeoflow direction. Static reservoir parameters used in the reservoir simulations are shown in Table 1.

Petrophysical properties used in the study

Permeability. Horizontal air (helium) permeabilities obtained from conventional core analyses of the MSF sandstones from four wells from the Snorre Field range from less than 1 mD to over 4000 mD. 1 mD is taken as the cut-off value in the calculation of the net/gross ratio of the reservoir rocks. In the present study, permeability data are used from 118 core plugs obtained from two wells, 34/7-3 and 34/7-6 (Table 2). The permeability range has been subdivided into 9 permeability classes, which have been applied to the heterogeneous models used in the present simulation study, and in a pattern which resulted in a frequency distribution (Fig. 5) approximating to that recorded in the MSF sandbodies (Table 2). The frequency distribution of Fig. 5 represents the horizontal permeability frequency in the heterogeneous model 2 calculated after gridding, and this frequency distribution is also used in models 1, 3 and 4.

Table 1. *Static reservoir parameters used in simulation. Data derived from the fluvial reservoir sandstones in the middle reservoir unit of the Statfjord Formation, Snorre Field, North Sea*

Reference depth* (mSS)	2475
Depth of OWC (mSS)	2595
Datum pressure (bar)	383
Reservoir oil gradient (bar/m)	0.07
Oil viscosity (cP)	0.77
Mean log porosity (fraction)	0.24
Pore compressibility (bar $^{-1}$)	70×10^{-6}
Mean air permeability (mD)	460
Initial water saturation (fraction)	0.08
Residual oil saturation after water flooding	0.17

* Reference depth is chosen to approximate midway between the oil–water-contact (OWC) and the crest of the structure in the Snorre Field.

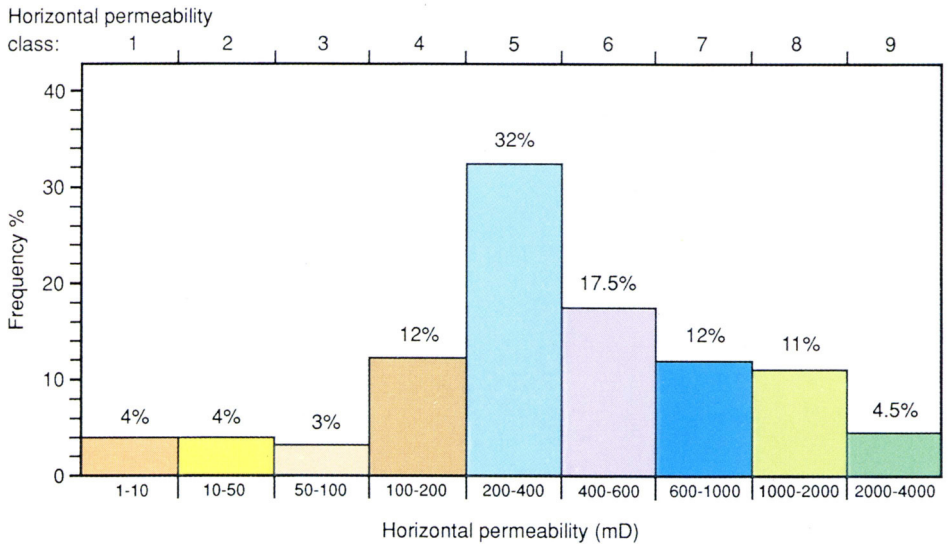

Fig. 5. Frequency distribution of horizontal permeability classes applied in the reservoir simulations on the heterogeneous models 2–4 and reference model 1. The colours of permeability classes are the same as used in Figs 9 and 10.

The pore volume weighted arithmetic mean permeability was 420 mD and the geometric mean was 304 mD, calculated from the permeability distribution in model 2. These model values correspond to the mean horizontal permeabilities of 386 and 174, respectively, obtained from the MSF sandbodies (Table 2). Thus, our heterogeneous models have been simulated with slightly higher permeabilities than recorded in the MSF sandbodies. The vertical to horizontal permeability ratio (K_v/K_h) was set to 0.7 which is the mean ratio determined from conventional core analyses. A constant mean permeability was applied for each permeability class, and these permeability values were multiplied by a factor of 0.54 to account for the effect

Table 2. *Permeability distribution in sandbodies in the middle reservoir unit of the Statfjord Formation, wells 34/7-3 and 34/7-6, Snorre Field, North Sea. Basic data used in the building of simulated heterogeneous models*

Permeability class	Horizontal permeability (K_h) mD	Number of samples	Frequency %	Arithmetic mean K_h mD	Geometric meanK_h mD	Mean helium porosity	Frequency %				
							Siltstone	Very fine–fine sandstone	Medium sandstone	Coarse sandstone	Very coarse sandstone
1	1–10	8	7	4	4	18	13	75	12		
2	10–50	12	10	24	22	23		58	34	8	
3	50–100	13	11	68	67	24		46	31	15	8
4	100–200	15	13	144	141	25		20	40	33	7
5	200–400	32	27	297	292	28		6	34	19	41
6	400–600	18	15	494	491	28		6	44	17	33
7	600–1000	11	9	764	757	28			18	64	18
8	1000–2000	7	6	1346	1312	26			14	71	15
9	2000–4000	2	2	2967	2900	28					100
Sum		118	100								
Mean of all samples				386	174	26					

of connate water and overburden pressure corresponding to the reservoir depth of the MSF reservoir (Table 1).

The core permeabilities obtained from the MSF sandbodies have a positive correlation with porosity and grain size (Table 2 and Fig. 6). The vertical trend of the horizontal permeability within individual sandbodies is stepwise but generally decreases from base to top (Fig. 4). This permeability trend reflects grain size variation and the stacked units of upward-fining channel-fill sequences or bar units. Vertical and lateral variations in the horizontal permeability within individual beds or bedsets are thought to be related to grain size variation between internal laminae and beds.

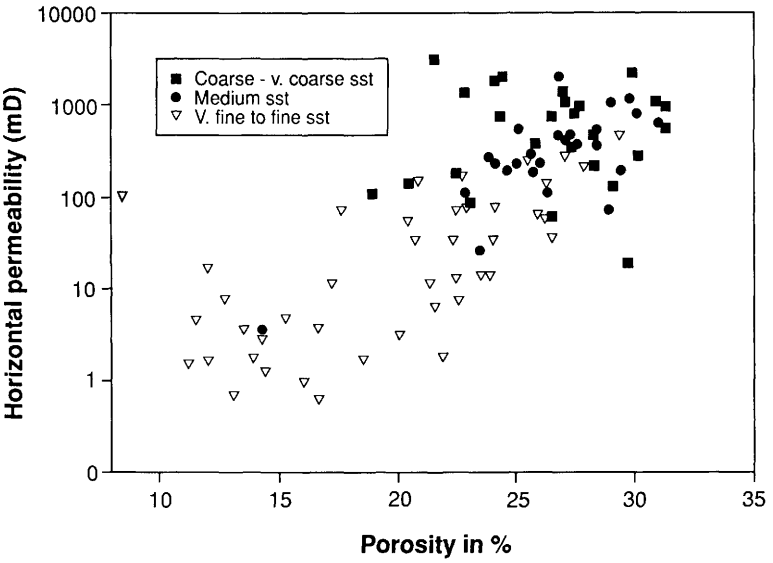

Fig. 6. Variations of porosity and horizontal permeability obtained from 130 core plug analyses from sandbodies in the middle reservoir unit of the Statfjord Formation, wells 34/7-3 and 34/7-6, Snorre Field. Values less than the cut-off values of 1 mD and 12% porosity for the MSF sandbodies have not been included in the study.

Cementation and diagenetic clay minerals are known to destroy or strongly modify the original depositional relationship between grain size and permeability (e.g. Mazzullo & Mazzullo 1985; Walton *et al.* 1986; Evans 1987). Modification of this relationship has also taken place in the MSF reservoir rocks due to patchy carbonate cementation and authigenic kaolinite, but still the general trend and internal variation of permeability (Figs 4 & 6) are considered to be a feature mainly inherited from the depositional grain size variation. Similar relationships between grain size and permeability as recorded from the MSF sandbodies (Table 2 and Fig. 4) are also reported from other braided stream reservoir rocks (Qiu *et al.* 1987; Gardiner *et al.* 1990). Thus, in the simulations, horizontal permeability has only been modelled as a function of sedimentary lithofacies and grain size and not as a feature reflecting diagenetic alteration.

Porosity and rock compressibility. The helium-measured porosity of the reference sandstones in the middle Statfjord Formation varies, according to measurements on 118 dry core plugs from wells 34/7-3 and 34/7-6, from about 8 to 32%, with a mean of 26%. A cut-off value of 12%, corresponding to 1 mD, is used in the calculation of net/gross ratio. The range in porosity, as seen from the core plug data obtained from the wells 34/7-3 and 34/7-6, is greatest for the assemblage of very fine and fine-grained sandstones (Fig. 6). For all sandstone samples grouped together there is a positive correlation between porosity and permeability, but no significant correlation is found between porosity and permeability for each of the assemblages medium- and coarse-grained sandstones (Fig. 6). However, the mean porosity values for the three grain size assemblages of sandstones are very close to the overall mean for the sandstones of 26%. This core plug mean value corresponds to 24% porosity measured from density and sonic logs and this mean log-porosity value of 24% was used as a constant for all grain sizes in all of the heterogeneous models used in the present study. Pore compressibility was fixed at 70×10^{-6} bar^{-1}.

Capillary pressure, irreducible water saturation and relative permeability. Capillary pressure curves were developed for each of the permeability classes on the basis of a total of 101 core plug capillary pressure tests. The highest permeability classes 9, 8, 7 and 6 are represented by one curve (Fig. 7). These curves, which are based on drainage capillary measurements (Lien & Nysetvold 1988), were used both for initialization of the models and simulation. In the simulation models, irreducible water saturation was set equal to the water saturation at a level 200 m above the OWC. The irreducible water saturation was calculated for each permeability class (Table 3).

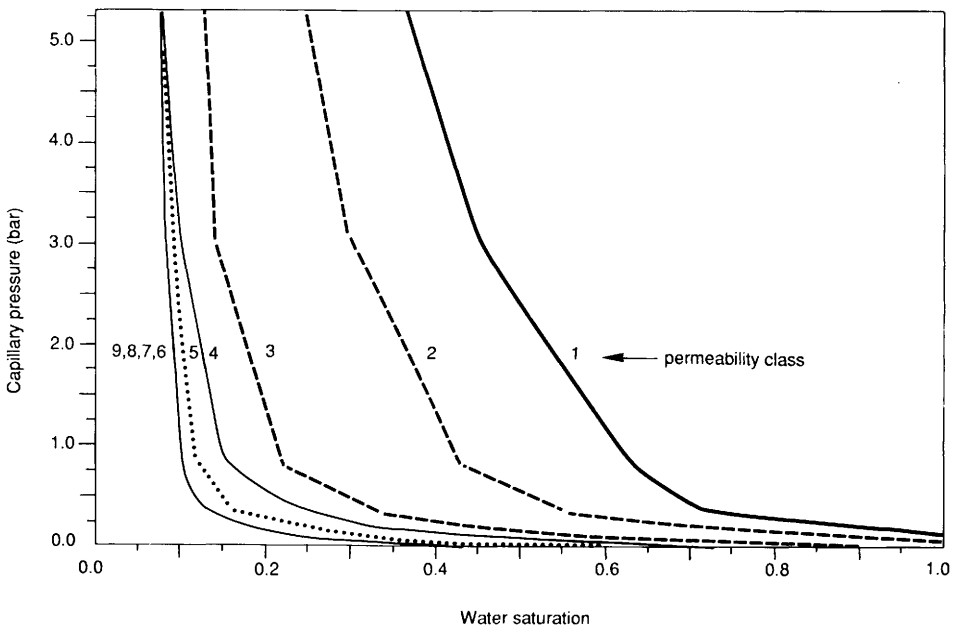

Fig. 7. Capillary pressure curves calculated for horizontal permeability classes 1 to 9 used in the reservoir simulations. Based on 46 core plug analyses.

Table 3. *Relationship between horizontal permeability and irreducible water saturation applied to the simulation study. Data obtained from sandbodies in the middle reservoir unit of the Statfjord Formation, wells 34/7-3 and 34/7-6, Snorre Field, North Sea*

Horizontal permeability (mD)	Irreducible water saturation
400	0.08
300	0.082
150	0.11
75	0.145
30	0.19
5	0.29

Relative permeability was obtained from measurements on 46 fresh and cleaned cores (Lien & Nysetvold 1988). Relative permeability curves were made for each of the permeability classes by using the exponential Corey equation with constant oil and water exponents of 5.2 and 3.1, respectively, and with constant residual oil saturation of 0.17, but with varying irreducible/initial water saturation for each class. Relative water permeability at residual oil saturation was set equal to 0.64. Fluid properties corresponding to those measured and calculated for the MSF sandbodies were applied in the simulation models (Table 1).

Heterogeneity models derived from the Maroon Formation, western Colorado

The Middle Pennsylvanian to Lower Permian Maroon Formation in western Colorado is in its upper part a continental redbed sequence, deposited in the cratonic Eagle Basin. Deposition in the Eagle Basin was strongly controlled by local tectonics, relative sea-level changes, and arid climate (Bartleson 1972; Mallory 1972; Walker 1972; Johnson 1989). The redbed sequence of the Maroon Formation consists of braided stream channel sandstones intercalated with thick, floodplain mudrocks (Johnson 1987). The sandbodies represent individual channel-fills, channel belt complexes and sheetflood deposits. In most of the formation exposed along the Colorado and White Rivers, the sand/shale ratio and sand grain-size distribution are very similar to the corresponding parameters encountered in the Upper Triassic–Lower Jurassic reservoir succession in the Snorre Field. Irrespective of the fact that the Maroon Formation has been deposited in a basin of different structural and climatic framework than the Early Jurassic basin of the Statfjord Formation, some of the individual channel-fill sandbodies in the Maroon Formation have internal geometry and heterogeneity patterns similar to the channel sandbodies in the Statfjord Formation.

External geometry and internal heterogeneity were recorded in a vertical road section of an individual channel sandbody at Warner Point along the White River southeast of Meeker (107° 43′ 30″W, 39° 56′ 30″N; Fig. 8). The sandstone thickness of 8–9 m corresponds to that of a typical MSF reservoir sandstone unit. There are also thought to be close similarities as regards grain size, vertical grain size trend and internal bounding surfaces. The 104 m long road section, which is oriented approximately normal to the regional palaeoflow direction and is thus analogous to a section

in the *yz*-plane of the Snorre Field, is shown in Figs 8–10. The internal units of lensoid sandstones are bounded by erosional surfaces along which there are discontinuous shale drapes. The measured sandbody at Warner Point corresponds to the 'Sandbody Type 3' of Johnson (1987) as regards internal architectural elements. This type of Maroon Formation sandbody was interpreted by Johnson (1987, pp. 9–10) to have been deposited in a mobile channel, bedload-dominated, ephemeral, braided fluvial system resembling models 2 or 3 of Miall (1985).

The shale drapes vary from less than 1 cm up to 10–20 cm in thickness and tend to increase in frequency upwards. Shale beds are considered to be effective permeability barriers to fluid flow vertical to the bounding surfaces, and discontinuous shale barriers are known to create tortuous fluid pathways, greatly decreasing overall vertical permeability of a reservoir sandbody (Richardson *et al.* 1978; Haldorsen & Chang 1986).

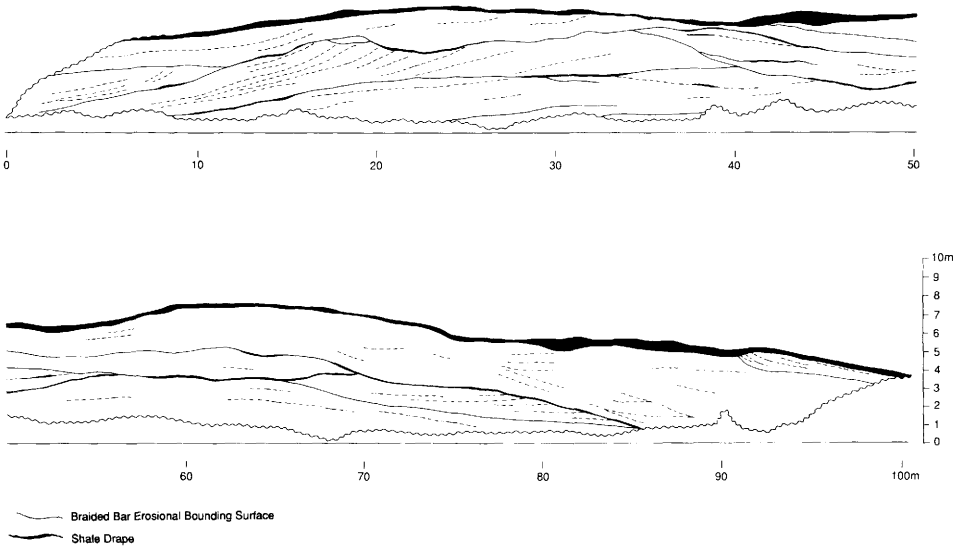

Fig. 8. Heterogeneity of braided stream channel sandstone in the Upper Pennsylvanian to Lower Permian Maroon Formation. Road section at Warner Point (107°43′30″W, 39°56′30″N), White River, northwestern Colorado, USA. Basis for heterogeneous models 2, 3 and 4.

The individual sandstone units are trough cross-bedded or tabular cross-bedded of facies St and Sp in the terminology of Miall (1978, 1988). They are architectural elements which represent small sub-channel infills (storeys in the terminology of Friend *et al.* 1979) and braid-bar deposits (Johnson 1987). The thickest units display a slight upward decrease in grain size, and there are also variations in grain size between adjacent laminae in the cross-bed sets. The channel sandbody, as a whole, also reveals a general decrease in grain size from base to top. The basal beds of the sandstone are not exposed in the measured road section and are inferred from an adjacent outrop. The channel sandstone unit is sandwiched between flood-plain mudstones of several metres thickness above, and a 5 m thick fine-grained flood-plain section below.

The measured section of the Maroon Formation represents just one of a series of fluvial heterogeneity types that may be present in the MSF sandbodies. It has been chosen as a framework for our heterogeneous models because it shares a number of features with a typical MSF sandbody: (1) overall architectural make-up of repeated channel sandbodies and flood-plain mudrocks, (2) braided stream origin on a wide alluvial plain, (3) thickness, (4) grain size and vertical grain size trend, (5) dominance of large-scale cross-bedded bedsets bounded by scour surfaces, and (6) discontinuous mud drapes. Within the constraints of these similarities, the Maroon channel sandbody is considered an analogue to the MSF sandbodies of the Snorre Field.

Heterogeneous models used in simulation

Model 0

Model 0 is a reference model which has the external geometry of the channel sandbody recorded from the Maroon Formation (Fig. 9A). This model is a homogeneous sandstone having the arithmetic mean horizontal permeability of 420 mD. This value corresponds to the mean of the horizontal permeability distribution applied to the reference model 1 and the heterogeneous models 1, 2 and 3 (see below).

Model 1

Model 1 is the second reference model. Within the geometrical outline of the Maroon analogue channel sandbody model, the permeability classes are arranged in layers with the highest horizontal permeability at the base and the lowest at the top (Fig. 9B). The permeability classes 8 and 9 are combined at the bottom of the sandstone. The permeability classes are represented volumetrically according to their frequency distribution in Fig. 5. This pattern of permeability distribution is in accordance with the general decrease of horizontal permeability from base to top in the MSF sandbodies and the observed positive correlation between grain size and permeability (see above).

Model 2

In model 2, the internal two-dimensional geometry of lensoid sandstone units within the Maroon analogue channel sandbody model is used as the basis for the heterogeneous model. The shale drapes are treated as permeability barriers of zero transmissibility (Fig. 10A). The nine permeability classes derived from the MSF sandbodies (Fig. 5) were distributed in accordance with their vertical occurrence in a typical MSF sandbody, with a general upward decrease in permeability and a stepwise arrangement of permeability variation according to the vertical grain size trend (Fig. 4). The actual vertical permeability distribution within the individual subunits is made, however, to reflect variations in sedimentary structures and grain size within bedsets, following the measured variations in the MSF sandbody well cores (Fig. 4).

Minipermeameter studies on channel sandbodies reveal great vertical and lateral variation of permeability with the vertical variations depending on the type of fluvial

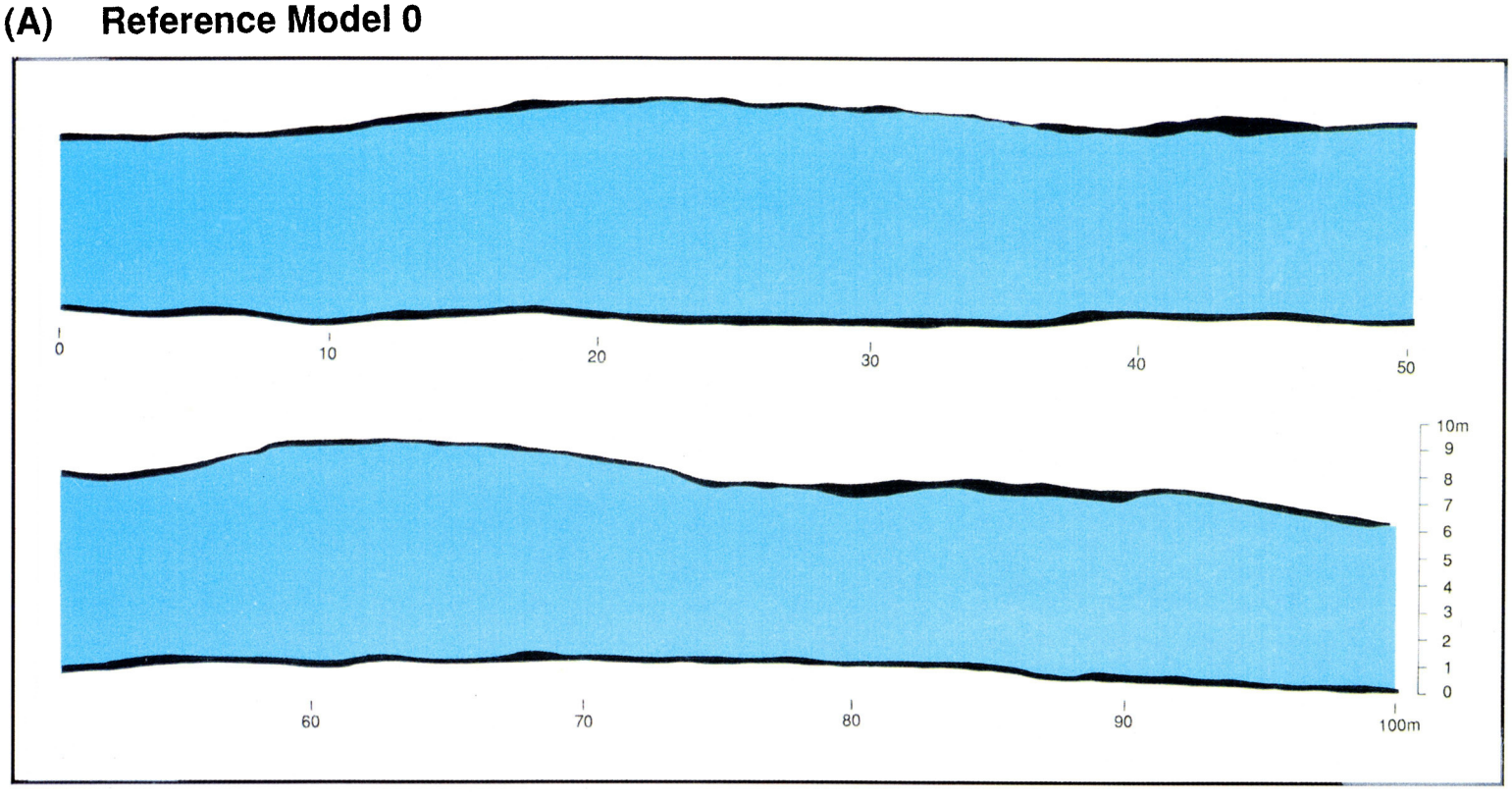

Fig. 9. Reference models used in simulation study. **(A)** Homogeneous reference model 0 with horizontal permeability of 420 mD corresponding to the mean arithmetic permeability of the nine permeability classes in Fig. 5; **(B)** Reference model 1 with horizontal permeability classes arranged in horizontal, parallel zones. In reference model 1, the permeability classes 8 and 9 of Figure 5 have been grouped together (1000–4000 mD).

(B) Reference Model 1

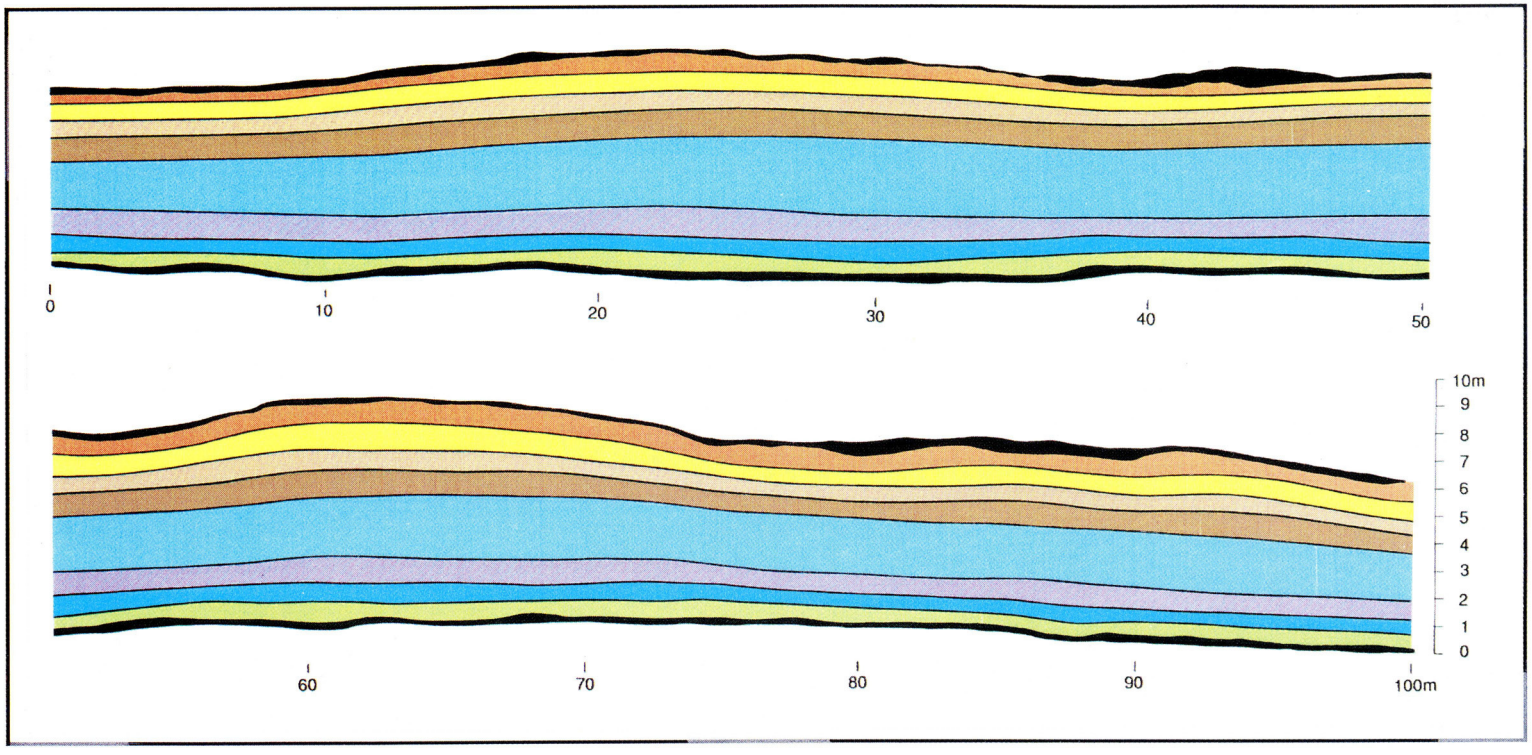

Horizontal Permeability (mD)

1000 - 4000	400 - 600	100 - 200	10 - 50
600 - 1000	200 - 400	50 - 100	1 - 10

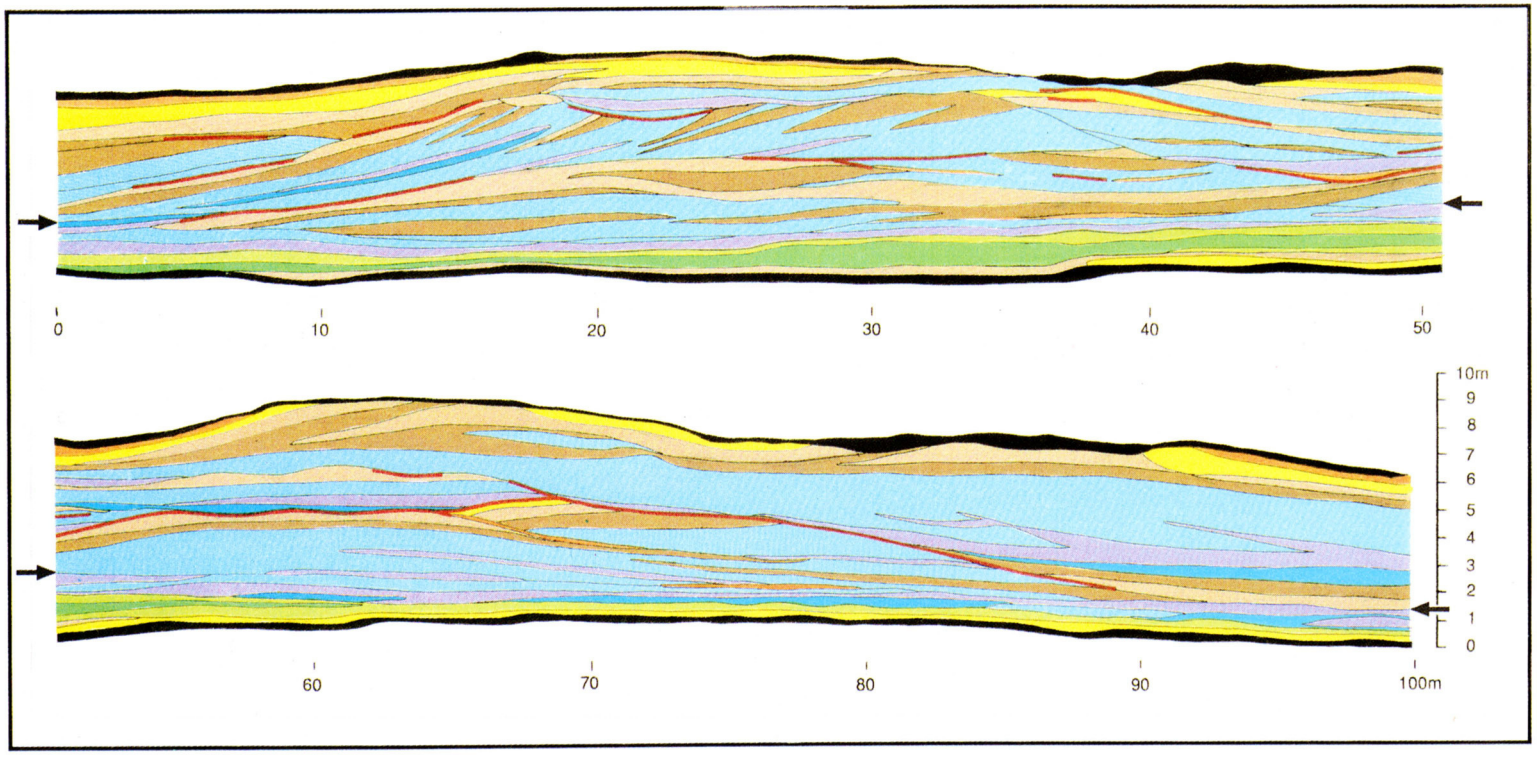

Fig. 10. Heterogeneous models used in simulation study. (**A**) Model 2 with shale drapes and continuous, high permeability basal zone (beneath level marked with arrows) overlying a thin, clast-rich conglomerate with lower permeability. (**B**) Model 4 with shale drapes and lensoid, discontinuous, high permeability basal zone (beneath level marked with arrows). Models 2 and 4 are similar above level marked with arrows. (Model 3 is similar to Model 2 except that the shale drapes have been removed). The colours correspond to colours used for horizontal permeability classes in Fig. 5.

(B) Heterogeneous Model 4

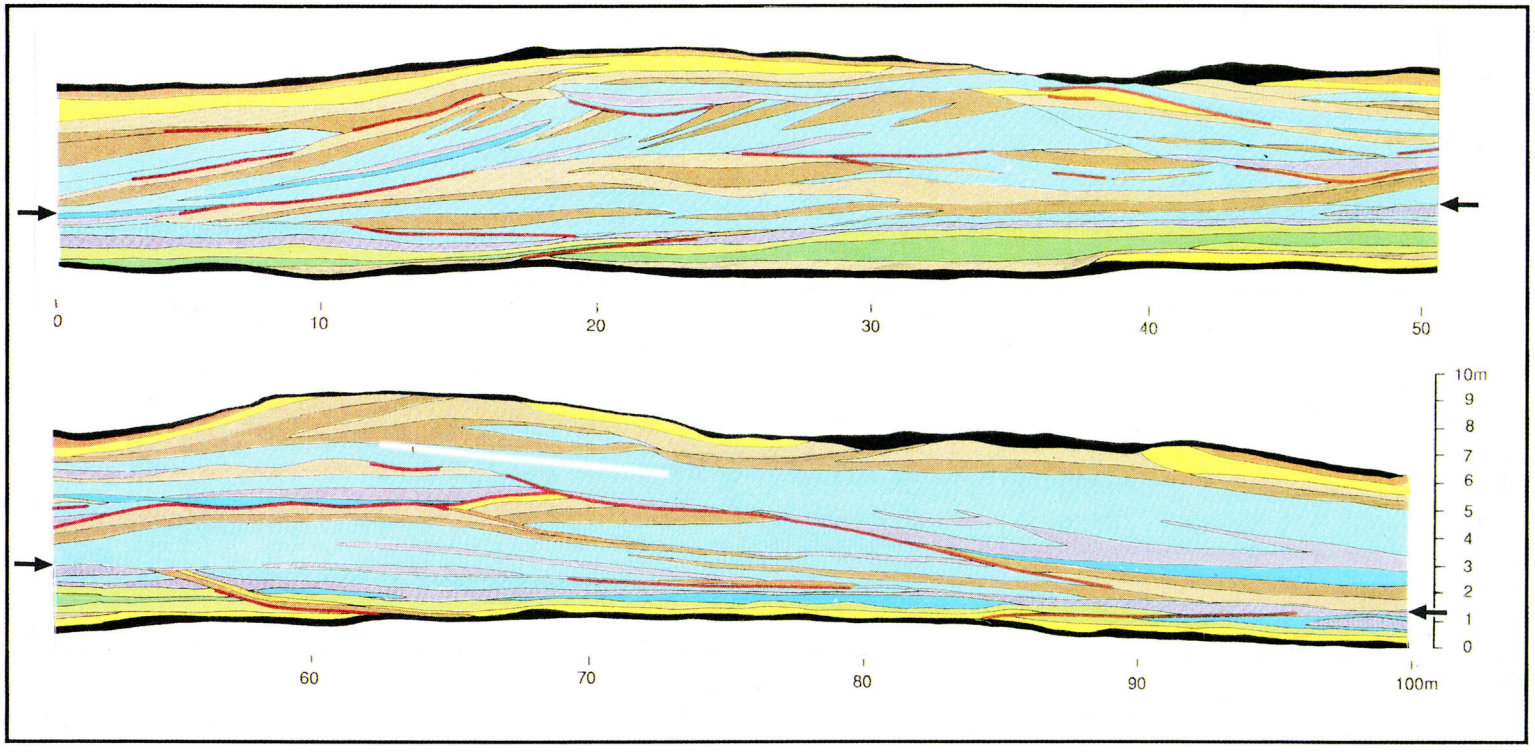

Horizontal Permeability (mD)

2000 - 4000	600 - 1000	200 - 400	50 - 100	1 - 10	
1000 - 2000	400 - 600	100 - 200	10 - 50		Impermeable Shale Drapes

channel and the type of the active-phase sandy infill (Dreyer *et al.* 1990). The lateral variation in permeability has, in our heterogeneous models 2, 3 and 4, been modelled according to lithofacies and grain size observed in the MSF sandbodies (Fig. 4), following the general principles of lateral permeability variations as recorded in uncemented sand beds (Pryor 1973).

The basal beds in model 2 are modelled as an 'open' high permeability zone, except for the lowermost bed which is inferred to have a reduced permeability due to shale clasts and a matrix enriched in clay and silt derived by the erosion of the underlying fine-grained floodplain deposits.

Model 3

Model 3 is similar to model 2 as regards internal geometry of the lens-shaped sandstones and horizontal permeability distribution, except that all the shale drapes are removed from this model. Model 3 retains the 'open' high permeability basal zone of model 2.

Model 4

In model 4 the basal beds are modelled as sandstone lenses separated by discontinuous shale drapes and thin zones of low permeability; thus the high permeability basal beds are assumed discontinuous and a more tortuous pathway for fluids is anticipated for this model than for models 2 and 3 (Fig. 10B).

Gridding, scaled-up versions and simulated waterflooding

The 2-D basic models, 0, 1, 2, 3 and 4, which are 104 m in length and 8.75 m in thickness (*yz*-plane), were divided into grid cells measuring 1 m × 0.25 m, resulting in 3640 cells in each model (Fig. 11A). The long side of the grid cells was orientated parallel with the structural dip of 8° in the MSF sandbody reservoir. This grid size is smaller than the grid cell of 2 ft × 50 ft × 20 ft which was advocated by Polasek & Hutchinson (1967) in order to reproduce permeability variations in a clean channel sandbody. With the small grid block size used in our simulation study, the internal heterogeneities were generally satisfactorily represented. However, the grid block size is still too large to test the impact of permeability variation on the scale of laminae; simulation studies by Kortekaas (1983) have shown that heterogeneity variations on this scale also affect recovery.

A structural dip of 8° was used in all simulations with an injector at the down-dip end and a producer at the up-dip end. The up-dip end was modelled to be open-ended. This orientation implies that the waterflood front was allowed to flow in the direction normal to the palaeo-drainage direction of the braided stream channel in accordance with the water injection programme on the MSF sandbodies. A constant permeability corresponding to the volume-weighted mean of the permeability classes present within individual grid blocks was assigned to each grid block. All erosional bounding surfaces were assumed to be zones of reduced permeability. Shale drapes were assumed to be complete barriers to flow. Other bounding surfaces were modelled as a reduction in transmissibility between the blocks on each side of the bounding surface. The reduction in transmissibility was set equivalent to that caused

by a 0.05 m thick zone that has a permeability equal to 1% of the permeability in the adjacent sandstone.

In order to test recovery efficiency and flow capacity over distances corresponding to the planned 900–1000 m injector–producer well spacing on the Snorre Field, three scaled-up versions were made (Fig. 11B). This is a simplified approach to test the effect of sandstone heterogeneity on the scale of well-to-well distance because the real heterogeneity variation will differ from a simple repetition of the short basic models. However, the scaled-up versions of the basic models have been run to test the effect of distance on the simulation results, rather than the effect of 'real' heterogeneities between wells.

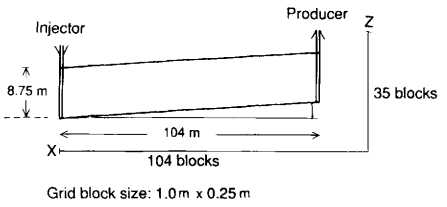

(A) Short basic models 0, 1, 2, 3, & 4

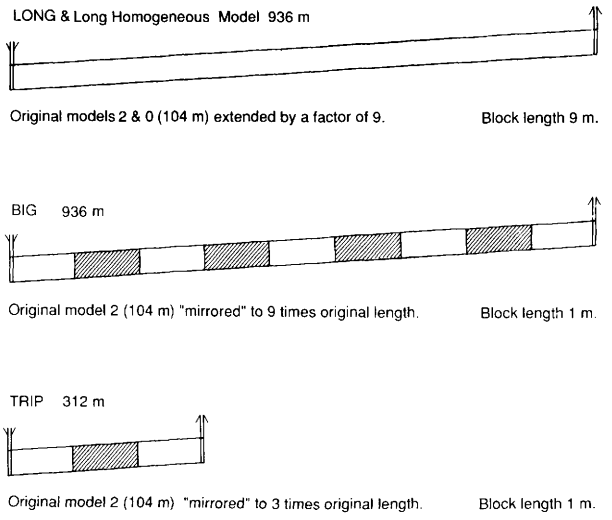

(B) Scaled-up versions of the short basic models

Fig. 11. Major geometrical features of the simulated models. (**A**) Structural dip, grid cell size, and position of injector and producer wells for the short basic models. (**B**) Scaled-up versions of models 0 and 2.

The scaled-up versions LONG and Long Homogeneous Model represent the basic heterogeneous model 2 and homogeneous model 0, respectively, extended by a factor of nine, giving a total length of 936 m. The original thickness of 8.75 m of the short basic models is retained. In this scaled-up model the grid cell measures 9 m × 0.25 m.

Version BIG is constructed by extending the basic model 2 (Fig. 10A) by repeating the 104 m × 8.75 m cross-section 9 times, mirroring the second, fourth, sixth and eighth sections relative to the original section (Fig. 11B). This gives a total length of 936 m. The thickness is retained at the original 8.75 m, and the grid cells thus still have the same size as in the original basic model, 1 m × 0.25 m. By scaling-up the basic model using this 'mirroring method', the original heterogeneous style is preserved and flow boundaries are not created between the linked sections.

Version TRIP is made from model 2 by the mirroring method but to a total length of only 312 m.

Dynamic modelling using the ECLIPSE reservoir simulator was established by opening injection connections at the downdip end blocks and production connections at the updip end. The velocity of injected water was in most runs approximately 0.6 m per day which is close to the estimated fluid flow velocity during water flooding for the middle Statfjord reservoir on the Snorre Field. However, in order to test the effect of flow rate on recovery efficiency, simulations were also run with model 2 by changing the model rate relative to the estimated mean fluid velocity of 0.6 m per day.

The significance of capillary pressure was tested by simulating models 2, LONG and TRIP both with and without capillary pressure implemented in the models.

Flow capacity was measured as mean effective permeability, calculated from a simple application of Darcy's law:

$$\frac{Q}{A} = \frac{k}{\mu}\left(\frac{\Delta\rho}{\Delta L} - \rho g \sin\alpha\right) \qquad \text{(Eq. 1)}$$

which gives

$$\frac{1}{K_{\text{eff}}} \sim \quad (\Delta\rho - \rho g L \sin\alpha) \qquad \text{(Eq. 2)}$$

where

k = permeability
K_{eff} = effective permeability
Q = model rate
A = model cross-section area
$\Delta\rho$ = pressure differential
L = length of model
ρ = fluid density
μ = fluid viscosity
α = model dip angle (8°)
$\rho g L \sin\alpha$ = hydrostatic pressure differential,

i.e. for a constant rate the effective permeability of a model is inversely proportional to the potential differential over the model. Thus, the effective mean permeability of the simulated fluvial sandstone models was found by comparing the potential loss in the models with that in the homogeneous reference model 0, which has the same external geometry and a constant permeability equal to the mean permeability of the heterogeneous models.

Results

The results of the simulation runs are shown in diagrams with recovery efficiency plotted against water cut (Figs 12–14).

The homogeneous model 0 has a high recovery efficiency at the time of water breakthrough (Fig. 12). The steep gradient of the curve indicates a steep, regular water front encountering the producing well at water breakthrough.

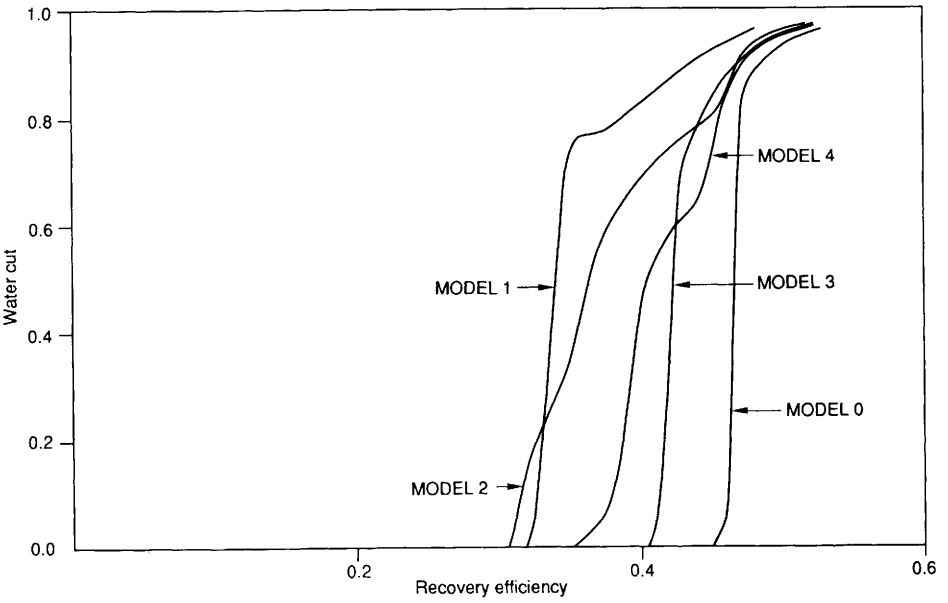

Fig. 12. Production profiles for models 0, 1, 2, 3 and 4. All runs have been performed with capillary pressure.

The other reference model, model 1, with permeability variation arranged in parallel layers and with a general upward-decreasing permeability gives a much lower recovery efficiency at water breakthrough than the homogeneous model. The production profile is very similar to that of model 0, except for higher water cuts. The moderate slope of the curve at high water cuts is interpreted as being related to the effect of water imbibition from the more permeable lower zones into the low permeability upper zones (see discussion below).

Model 2 has an even lower recovery efficiency than model 1 at water breakthrough. This is due to the higher permeability in the basal zone of model 2 where permeability classes 8 and 9 are modelled separately; in model 1 the permeability classes 8 and 9 have been combined, resulting in a lower mean permeability for the basal grid cells of this model. The recovery efficiency of the heterogeneous model 2 is lower than for the homogeneous model 0, but higher than for the layered model 1 except at the time of water breakthrough. The permeability barriers within this channel sandstone model tend to force the flooding water down to the highly permeable basal beds, giving rise to increased water-fingering and thus an early water breakthrough. On the other hand, the irregular permeability distribution in this sandstone has resulted in drainage of low permeability beds over a longer interval after water breakthrough compared to the homogeneous and layered models.

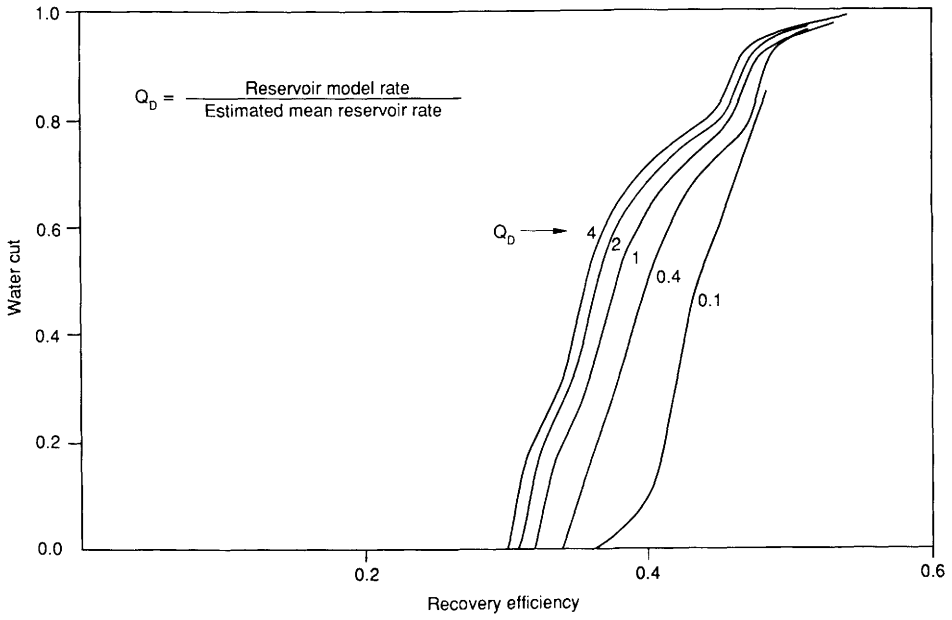

Fig. 13. Recovery efficiency as a function of flow rate; runs with model 2.

Model 3, which has an open basal zone and no shale drapes, reveals a production profile very similar to the homogeneous reference model 0, but with a lower recovery efficiency. At water cuts between about 0.6 and 0.9, model 3 has a lower recovery efficiency than the more heterogeneous model 4.

In model 4 all of the heterogeneous properties of model 2 have been preserved, and in addition the basal zone has been modelled as a discontinuous open zone dominated by high permeabilities (Fig. 10B). This model gives a higher recovery efficiency at water breakthrough than model 2 but lower than for model 3 and for the homogeneous model 0. The higher degree of heterogeneity in the basal zone of model 4 compared to model 2 has prevented water fingering and an early water breakthrough. Compared with model 2, shale drapes and the irregular permeability distribution in the lower part of the model 4 sandbody have reduced the flow capacity in the basal zone but have led to a better sweep in the middle and upper part of the sandbody.

The heterogeneous models 2, 3 and 4 have production profiles that nearly coincide at very high water cuts (Fig. 12). At a water cut of 90% these heterogeneous channel sandstones still have a higher recovery efficiency than a stratified sandstone with permeability varying with depth (model 1) but lower than the homogeneous sandstone with the same mean effective permeability (model 0). Simulation runs on model 2 with varying relative model rates demonstrate that for this heterogeneous sandbody the recovery efficiency increases markedly with decreasing flow rate (Fig. 13).

Of the scaled-up versions the Long Homogeneous Model, derived from the short homogeneous model 0, gives the best recovery efficiency (Fig. 14). Reservoir simulation of the scaled-up versions LONG, BIG and TRIP results in higher recovery efficiency than for model 2 from which they have been derived (Fig. 14).

Model BIG contains all the heterogeneities of model 2, and in the same proportions, and this model gives a higher recovery efficiency than model LONG which is of the same length. In model LONG, the lensoid permeability cells within subchannels and braid bar sandbodies have been extended 9 times relative to model 2; hence, the internal heterogeneity of model LONG approaches that of model 1 in which the permeability classes are organized in parallel layers. This type of heterogeneity is unfavourable for recovery efficiency. The extended permeability zones in the direction of waterflooding cause the water to flow preferentially through the highly permeable parts of the sandbody, causing less efficient drainage of the zones of lower permeability.

In model BIG, the smaller-scale heterogeneity causes a better dispersion of the water through the sandbody, resulting in a higher recovery efficiency for this model. Model TRIP has the same type of heterogeneity as BIG but gives a lower recovery efficiency. This feature must be a function of the change in the relative importance of viscous, capillary and gravity forces.

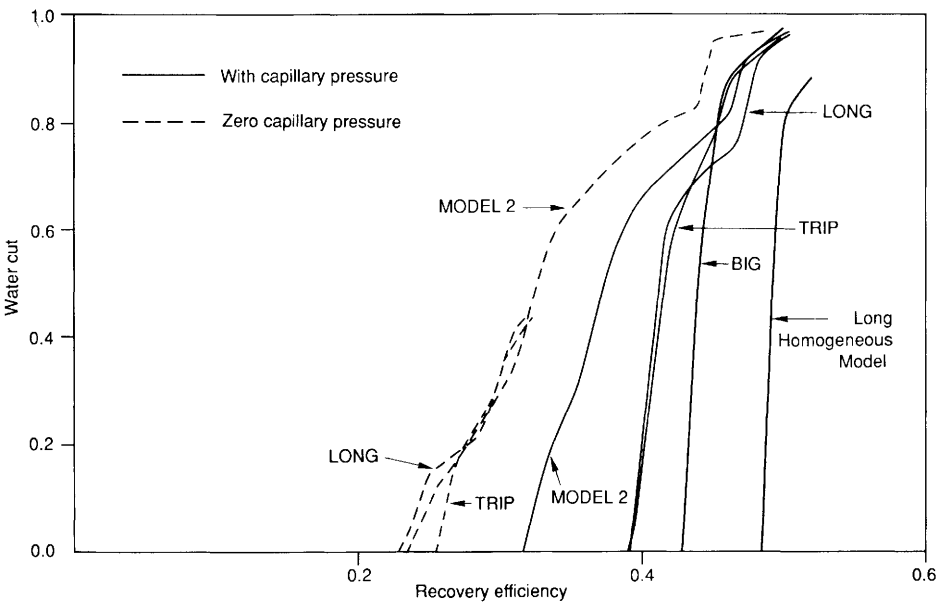

Fig. 14. Production profiles for the scaled-up versions, Long Homogeneous Model, LONG, BIG and TRIP, compared with the short basic model 2; simulation runs have been performed with and without capillary pressure.

The recovery efficiency obtained in simulations without capillary pressure is markedly reduced compared with runs with capillary pressure (Fig. 14). The curves showing recovery efficiency relative to water cut are very similar for the short heterogeneous model 2 and its scaled-up versions LONG and TRIP when simulated without using capillary pressure. However, when simulated *with* capillary pressure, there is a marked difference between the short model 2 on the one side and the two scaled-up versions on the other.

Table 4. *Results of simulations*

Model	Recovery efficiency of heterogeneous models 2–4 and reference models 0 and 1		Mean effective permeability (flow capacity) of heterogeneous models compared with reference model 0	
	Recovery efficiency at water breakthrough	Recovery efficiency at 90% water cut	Mean effective permeability	Reduction relative to model 0
0	0.450	0.484	420 mD	
1	0.314	0.436		
2	0.302	0.469	323 mD	23%
3	0.402	0.469	383 mD	9%
4	0.343	0.471	241 mD	42%
LONG			360 mD	14%

Table 4 shows estimated mean effective permeabilities (calculated from Eq. 2) and recorded recovery efficiency for the reference models and the basic short models of the heterogeneous channel sandbody.

Discussion

The results show that significant differences in simulated oil recovery occur as a response to variations in internal reservoir sandbody heterogeneity. The markedly higher recovery efficiency in simulations run with capillary pressure compared to runs without demonstrates the importance of capillary pressure in the sweeping process during waterflooding, as emphasized by Hamon & Vidal (1986). The effect of capillary pressure, together with viscous forces, can also explain most of the differences recorded in fluid flow behaviour between the heterogeneous sandbody models. The reduction of mean effective permeability relative to the homogeneous reference model is highest for the sandbody models with the highest frequency of shale barriers. This result is in accordance with the conclusions of Desbarats (1987) and shows the importance of quantifying shale barriers in reservoir simulation on a genetic scale.

As anticipated, an 'open' highly permeable basal zone combined with high internal heterogeneity with shale barriers in the major volume of the sandbody (models 2 and 4) results in water fingering, early water breakthrough and a reduced recovery efficiency compared to a homogeneous model. Gravity forces also tend to force the water down into the highly permeable zones located in the lower part of the reservoir body. Simulation studies of waterflooding on the same scale by Lasseter *et al.* (1986) show this to be an important mechanism. The rapid flow through the highly permeable zones decreases the time available, before breakthrough, for water to flush into the less permeable rocks in the reservoir. This is clearly demonstrated by model 4 relative to model 2. A retarded flow along the basal zone in the model 4 sandstone has reduced the mean effective permeability of this zone, and also increased the time available before water breakthrough to enhance intrusion of water into the less permeable upper parts of the sandbody. Similarly, in the heterogeneous model 3, which has an irregular permeability distribution but without internal

permeability barriers, the effective permeability of the upper parts is increased and the water intrusion here enhanced. However, the internal heterogeneity has caused a reduction in mean effective permeability for the sandbody as a whole relative to the homogeneous model with the same volume-weighted average arithmetic permeability (Table 4). Viscous forces are thought to be more important than capillary forces in simulation of fluid flow in the short basic models 2, 3 and 4.

The higher recovery efficiency of the scaled-up models compared to the short models can best be explained by the influence of capillary pressure. In these models, the waterflooding will occur during a longer time span than in the short models, and this will give rise to a better sweep due to imbibition of low permeability zones affected by capillary forces. These low permeability zones are in the type of fluvial channel sandbody modelled and simulated here dominating in the upper part. This should have the effect of increasing the gradient of the advancing waterfront. Additionally, in the scaled-up models, gravity forces probably contribute more effectively to reduce, relative to the model size, the basal tongue of the water front, compared to the short models.

The rate of waterflooding obviously has an impact on the recovery efficiency. At relatively low rates, there is more time, before water breakthrough, for the water to imbibe into the less permeable zones than at higher rates where the major water volume will tend to flow through the most highly permeable zones. High flow rates will increase the possibilities for oil being bypassed in pockets enveloped by discontinuous shale drapes. However, over time, capillary water invasion will result in very similar ultimate recovery obtained at very high water cuts, irrespective of flooding rates.

Conclusions

(1) The present 2-D simulation study has shown that the variation in pattern and degree of internal heterogeneity in a channel sandbody of braided stream origin has a significant impact on recovery efficiency. Relative to a homogeneous reference model, three heterogeneous sandstone models reveal reductions in recovery efficiency, at the time of water breakthrough, from between 11 and 33%, depending on the type and degree of internal heterogeneity. Flow capacity (mean effective permeability) is reduced from between 9 and 42% with increasing internal complexity of the sandstone heterogeneity.

(2) Simulation runs using capillary pressure data on individual permeability zones give about 25% higher recovery efficiency at water breakthrough than simulations performed without capillary pressure.

(3) Capillary pressure enhances imbibition of low permeability rocks during water flooding. This process explains higher recovery efficiency in simulations run on scaled-up model versions compared to the short basic models, and higher recovery efficiency obtained in runs with low flow rate compared to runs with high flow rate.

(4) 2-D reservoir simulations on genetic sandbody models constructed by combining reservoir data with heterogeneity information from exposed analogue units provide a simple and practical method for evaluating the impact of variations in geological reservoir characteristics on oil recovery during waterflooding.

(5) In heterogeneous fluvial reservoirs, similar studies on the effect of internal

heterogeneities in genetic sandbodies should be performed on various arrangements of internal heterogeneities and preferentially on models covering complete representations on well-to-well distances. 2- and 3-D simulations on this scale of 'true' natural heterogeneity representations recorded from outcrop studies will give information that can be used as correction factors to conventional 3-D element or full-field simulations. This scale of reservoir simulation makes strong demands on the effectiveness of procedures and methods of homogenization and pseudoization. Such use of data from outcrop studies on analogue sandbodies also presupposes a better understanding of the relationships between lithofacies, porosity and permeability. In addition to improving the significance of reservoir simulations, this type of reservoir modelling integrates the geological and engineering aspects of reservoir characterization, which is the fundamental issue of enhanced hydrocarbon recovery.

The authors are grateful to the PL 057 and 089 partnerships for giving permission to publish this presentation. We thank T. Blaker, K. Jorde and A. C. MacDonald for critical comments and suggestions for improvements to a previous draft of the paper and to J. Alexander and T. Corrigan for constructive referee work and to the Editor M. Ashton for all suggestions for making improvements to the paper. We also thank W. Jonassen, L. Ravdal, G. B. Røed and J. Slettebø for preparing the figures and D. Worsley for correcting the English.

References

ALEXANDER, J. & LEEDER, M. 1987. Active tectonic control on alluvial architecture. *In:* ETHRIDGE, F. C., FLORES, R. M. & HARVEY, M. D. (eds) *Recent Developments in Fluvial Sedimentology*. Society of Economic Paleontologists and Mineralogists Special Publication, **39**, 243–252.

ALLEN, J. R. L. 1978. Studies in fluviatile sedimentation: an exploratory quantitative model for the architecture of avulsion controlled alluvial suites. *Sedimentary Geology*, **21**, 129–147.

—— 1983. Studies in fluviatile sedimentation: bars, bar-complexes and sandstone sheets (low-sinuosity braided streams) in the Brownstones (L. Devonian), Welsh Borders. *Sedimentary Geology*, **33**, 237–293.

AUGEDAL, H. O., STANLEY, K. O. & OMRE, H. 1986. SISABOSA, a program for stochastic modelling and evaluation of reservoir geology. *Conference on Reservoir Description and Simulation with Emphasis on EOR*, Oslo, September 1986. Institute for Energy Technology, Kjeller, Norway.

BARTLESON, B. L. 1972. Permo-Pennsylvanian stratigraphy and history of the Crested Butte-Aspen Region. *Colorado School of Mines Quaterly*, **67**, 187–248.

BRIDGE, J. S. 1985. Paleochannel patterns inferred from alluvial deposits: a critical evaluation. *Journal of Sedimentary Petrology*, **55**, 579–589.

—— & LEEDER, M. R. 1979. A simulation model of alluvial stratigraphy. *Sedimentology*, **26**, 617–644.

CANT, J. D. 1978. Development of a facies model for sandy braided river sedimentation: comparision of the South Saskatchewan River and the Battery Point Formation. *In:* MIALL, A. D. (ed.) *Fluvial Sedimentology*. Canadian Society of Petroleum Geologists Memoir, **5**, 627–639.

CHAUVIN, A. L. & VALACHI, L. Z. 1980. Sedimentology of the Brent and Statfjord Formations of Statfjord Field. *In: The Sedimentation of the North Sea Reservoir Rocks*. Norsk Petroleumsforening, Oslo, Article XVI, 1–17.

CLEMETSEN, R., OMRE, H., HURST, A. & KNARUD, R. 1990. A computer program for evaluation of fluvial reservoirs. *In:* BULLER, A. T. *ET AL.* (eds) *North Sea Oil and Gas Reservoirs II*. Graham & Trotman, London, 373–385.

DEEGAN, C. E. & SCULL, B. J. (compilers) 1977. *A standard lithostratigraphic nomenclature for the Central and Northern North Sea*. Report, Institute of Geological Sciences London, **77/25**; and Norwegian Petroleum Directorate Bulletin, **1**.

DESBARATS, A. J. 1987. Numerical estimation of effective permeability in sand-shale formations. *Water Resources Research*, **23**, 273–286.

DREYER, T., SCHEIE, Å. & WALDERHAUG, O. 1990. Minipermeameter-based study of permeability trends in channel sand bodies. *The American Association of Petroleum Geologists Bulletin*, **74**, 359–374.

EVANS, R. C. 1987. An investigation into the influence of common sedimentary structures and diagenesis on permeability heterogeneity and anisotropy in selected sands and sandstones. *Society of Petroleum Engineers, Unconsolidated paper, SPE-17130* (Nov. 1987).

FRIEND, P. F., SLATER, M. J. & WILLIAMS, R. C. 1979. Vertical and lateral building of river sandstone bodies, Ebro Basin, Spain. *Journal of Geological Society, London,* **136**, 39–46.

GARDINER, S., THOMAS, D. V., BOWERING, E. D. & MCMINN, L. S. 1990. A braided fluvial reservoir, Peco Field, Alberta, Canada. *In:* HARWIS, J. H., MCPHERSON, J. G. & STUDLICK, J. R. J. (eds) *Sandstone Petroleum Reservoirs*. Springer-Verlag, New York, 31–56.

GUNDESØ, R. & EGELAND, O. 1990. SESIMIRA—a new geological tool for 3D modelling of heterogeneous reservoirs. *In:* BULLER, A. T. *ET AL.* (eds) *North Sea Oil and Gas Reservoirs II*. Graham & Trotman, London, 363–371.

HALDORSEN, H. H. & Chang, D. M. 1986. Notes on stochastic shales; from outcrop to simulation model. *In:* LAKE, L. W. & CARROLL, H. B. (eds) *Reservoir Characterization*. Academic Press, Inc, Orlando, Florida, 445–485.

HAMON, G. & VIDAL, J. 1986. Scaling-up the capillary imbibition from laboratory experiments on homogeneous and heterogeneous samples. *Society of Petroleum Engineers, SPE 15852*. (SPE European petroleum Conference, London, England, 20–22 October 1986).

HOLLANDER, N. B. 1987. Snorre. *In:* SPENCER, A. M. *ET AL.* (eds) *Geology of the Norwegian Oil and Gas Fields*. Graham & Trotman, London, 307–318.

JOHNSON, H. D. & KROL, D. E. 1984. Geological modeling of a heterogeneous sandstone reservoir: Lower Jurassic Statfjord Formation, Brent Field. *Society of Petroleum Engineers, SPE 13050* (59th Annual Technical Conference and Exhibition, Dallas, 16–19 September 1984).

JOHNSON, S. Y. 1987. Sedimentology and paleogeographic significance of six fluvial sandstone bodies in the Maroon Formation, Eagle Basin, Northwest Colorado. *US Geological Survey Bulletin*, **1787**, 1–17.

—— 1989. Significance of loessite in the Maroon Formation (Middle Pennsylvanian to Lower Permian), Eagle Basin, Northwest Colorado. *Journal of Sedimentary Petrology*, **59**, 782–791.

KIRK, R. H. 1980. Statfjord Field—a North Sea giant. *In:* HALBOURY, M. T. (ed.) *Giant Oil- and Gasfields of the Decade 1968–1978*. American Association of Petroleum Geologists Memoir, **30**, 95–117.

KORTEKAAS, T. F. M. 1983 Water/oil displacement characteristics in cross-bedded reservoir zones. *Society of Petroleum Engineers, SPE 12112* (58th Annual SPE of AIME Technical Conference, San Francisco, 5–10 October 1983).

LASSETER, T. J., WAGGONER, J. R. & LAKE, L. W. 1986. Reservoir heterogeneities and their influence on ultimate recovery. *In:* LAKE, L. W. & CARROLL, H. B. (eds) *Reservoir Characterization*. Academic Press, Inc, Orlando, Florida, 545–559.

LIEN, S. K. & NYSETVOLD, I. 1988. Snorre Field relative permeability and capillary pressure determination in the evaluation phase of field development. *Symposium Petroleum Well Log Analysts*. (11th Annual European Formation Evaluation Symposium 14–16 September 1988, Oslo, Transaction, Paper A).

MALLORY, W. W. 1972. Regional synthesis of the Pennsylvanian System. *In:* MALLORY, W. W. (ed.) *Geological Atlas of the Rocky Mountain Region*. Rocky Mountain Association of Geologists, 11–127.

MARTIN, J. H., EVANS, A. J. & RAPER, J. K. 1988. Reservoir modeling of low-sinuosity channel sands: a network approach. *Society of Petroleum Engineers, SPE 18364*. (European Petroleum Conference, London, England, 16–19 October 1988, Proc. Paper 259–271).

MAZZULLO, L. J. & MAZZULLO, J. M. 1985. Geology and clay mineralogy of the Morrow Formation, southeastern New Mexico. *Society of Petroleum Engineers/U.S. Department of Energy, SPE/DOE 13849* (SPE/DOE Conference on Low Permeability Gas Reservoir, Denver, 19–22 May, 1985).

MIALL, A. D. 1977. A review of the braided river depositional environment. *Earth Science Reviews*, **13**, 1–62.

—— 1978. Lithofacies types and vertical profile models in braided river deposits: a summary. *In:* MIALL, A. D. (ed.) *Fluvial Sedimentology*. Canadian Society of Petroleum Geologists Memoir, **5**, 597–604.

—— 1985. Architectural-element analysis: A new method of facies analysis, applied to fluvial deposits. *Earth Science Reviews*, **22**, 261–308.

—— 1988. Reservoir heterogeneities in fluvial sandstones: Lessons from outcrop studies. *American Association of Petroleum Geologists Bulletin*, **72**, 682–697.

NYBRÅTEN, G., SKOLEM, E. & ØSTBY, K. 1990. Reservoir simulation of the Snorre Field. *In:* BULLER, A. T. *ET AL.* (eds) *North Sea Oil and Gas Reservoirs—II*. Graham & Trotman, London, 103–114.

NYSTUEN, J. P., KNARUD, R., JORDE, K. & STANLEY, K. O. 1989. Correlation of Triassic to Lower Jurassic sequences, Snorre Field and adjacent areas, northern North Sea. *In:* COLLINSON, J. D. (ed.) *Correlation in Hydrocarbon Exploration*. Norwegian Petroleum Society, Graham & Trotman, London, 273–289.

POLASEK, T. L. & HUTCHINSON, C. A. 1967. Characterization of non-uniformities within a sandstone reservoir from a fluid mechanics standpoint. *Proceedings of 7th World Petroleum Congress 1967*, **(2)**, 397–407.

PRYOR, W. A. 1973. Permeability-porosity patterns and variations in some Holocene sand bodies. *American Association of Petroleum Geologists Bulletin*, **57**, 162–189.

QIU, Y., XUE, P. & XIAO, 1987. Fluvial sandstone bodies as hydrocarbon reservoirs in lake basins. *In:* ETHRIDGE, F. G., FLORES, R. M. & HARVEY, M. D. (eds) *Recent Developments in Fluvial Sedimentology*. Society of Economic Paleontologists and Mineralogists Special Publication, **39**, 329–342.

RAVENNE, C. & BEUCHER, H. 1988. Recent development in description of sedimentary bodies in a fluviodeltaic reservoir and their 3D conditional simulations. *Society of Petroleum Engineers, SPE 18310* (63rd Annual Technical Conference, Houston, 2–5 October 1988, Proc. Paper, 463–476).

RICHARDSON, J. G., HARRIS, D. G., ROSSEN, R. H. & VAN HEE, G. 1978. The effect of small, discontinuous shales on oil recovery. *Journal of Petroleum Technology*, **20**, 1531–1537.

RØE, S.-L. & STEEL, R. 1985. Sedimentation, sea-level rise and tectonics at the Triassic–Jurassic boundary (Statfjord Formation), Tampen Spur, northern North Sea. *Journal of Petroleum Geology*, **8**, 103–186.

RUST, B. R. 1978. Depositional model for braided alluvium. *In:* MIALL, A. D. (ed.) *Fluvial Sedimentology*. Canadian Society of Petroleum Geologists Memoir, **5**, 605–625.

STANLEY, K. O., JORDE, K., RAESTAD, N. & STOCKBRIDGE, C. P. 1990. Stochastic modelling of reservoir sand bodies for input to reservoir simulation, Snorre Field, northern North Sea, Norway. *In:* BULLER, A. T. *ET AL.* (eds) *North Sea Oil and Gas Reservoirs II*. Graham & Trotman, London, 91–101.

STEEL, R. & RYSETH, A. 1990. The Triassic-early Jurassic succession in the northern North Sea: meagasequence stratigraphy and intra-Triassic tectonics. *In:* HARDMAN, R. F. P. & BROOKS, J. (eds) *Tectonic Events Responsible for Britain's Oil and Gas Reserves*. Geological Society Special Publication, **55**, 139–168.

VAN DE GRAAFF, W. J. E. & EALEY, P. J. 1989. Geological modeling for simulation studies. *American Association of Petroleum Geologists Bulletin*, **73**, 1436–1444.

VOLLSET, J. & DORÉ, A. G. (compilers) 1984. A revised Triassic and Jurassic lithostratigraphic nomenclature for the Norwegian North Sea. *Norwegian Petroleum Directorate Bulletin*, **3**, 53 pp.

WALKER, T. R. 1972. Bioherm in the Minturn Formation (Des Moines age), Vail-Minturn area, Eagle County, Colorado. *Colorado School of Mines Quarterly*, **67**, 249–278.

WALTON, A. W., BOUQUET, D. J., EVENSON, R. A., ROFHEART, D. H. & WOODY, M. D. 1986. Characterization of sandstone reservoirs in the Cherokee Group (Pennsylvanian, Desmoinesian) of southeastern Kansas. *In:* LAKE, L. W. & CARROLL, H. B. Jr. (eds) *Reservoir Characterization*. Academic Press, Inc, Orlando, Florida, 39–62.

WEBER, K. J. 1986. How heterogeneity affects oil recovery. *In:* LAKE, L. W. & CARROLL, H. B. (eds) *Reservoir Characterization*. Academic Press, Inc, Orlando, Florida, 487–544.

From ASHTON, M. (ed.), 1993, *Advances in Reservoir Geology*,
Geological Society Special Publication No. 69, pp. 135–174.

Geometry and facies of large-scale flow units in fluvial-dominated fan-delta-front sequences

TOM DREYER

Norsk Hydro Research Centre, Sandsliveien 90, 5020, Bergen, Norway

Abstract: In heterogeneous reservoirs, an optimal number of large-scale flow-units (here termed building blocks) must be defined prior to detailed geological modelling. For the fluvial-dominated fan-deltaic parts of the Tilje Formation, Mid-Norwegian shelf, four fan-delta-front building blocks have been defined. Quantifications with regard to the geometry and spatial arrangement of these building blocks have been made based on outcrop studies of similar sediments in the Ridge Basin, California. The four building blocks are composite delta-front units (CDF), mouth-bar sandstones (MS), mouth-bar-related mudstones and carbonate-cemented zones (MMC), and distal delta-front mudstones (D). The main reservoir units in the Tilje Formation are the composite delta-front units. These have large lateral extents (tens of kilometres), and occur in three intervals separated by impermeable zones of building block D. Within the CDF units, the main heterogeneity is the alternation between permeable mouth-bar sandstones of building block MS and impermeable zones of building block MMC. The mouth-bar sandbodies have width (W)/thickness (T) ratios of 220–525, and constitute a considerably larger percentage of the reservoir volume than the less widespread MMC flow-barriers. Hence, the internal communication within the CDF units is believed to be generally good.

Accurate modelling of reservoir behaviour requires a geological framework in which the main features affecting hydrocarbon flow are represented. At the same time, the need for cost-efficient reservoir simulations means that the geological framework has to be set up within a limited number of large grid cells. In heterogeneous reservoirs, this integration between computer capacity and geological complexity is a painful process. In the past, simulation of complex reservoirs has often been performed with oversimplified and rather naive geological models. As a consequence, grid cells in such a simplified model have usually encompassed a range of lithologies and facies with large variations in lateral extent, water saturation, permeability etc. (e.g. Haldorsen 1986; Lasseter *et al.* 1986). The averaged reservoir parameters assigned to such 'heterogeneous' grid cells fail to reflect features like the true effective vertical and horizontal permeabilities in complex reservoirs.

To overcome this problem, it has been necessary to revise the simulation strategy for heterogeneous reservoirs (Gundesø & Egeland 1990; Wadsley *et al.* 1990). Rather than sacrificing important aspects of the geological model to make it fit into large grid cells, the grid cells are now distributed in such a way that they highlight large-scale geological flow units or *building blocks* (Galloway 1986). These building blocks are represented in the models as units with specified sets of dimensional and petrophysical values. Moreover, the building blocks are emplaced in the computer model according to rules which govern their spatial arrangement. The reasonable level of geological complexity which can be displayed by this particular simulation procedure gives a better approximation to the 'true' communication relationships in the reservoir.

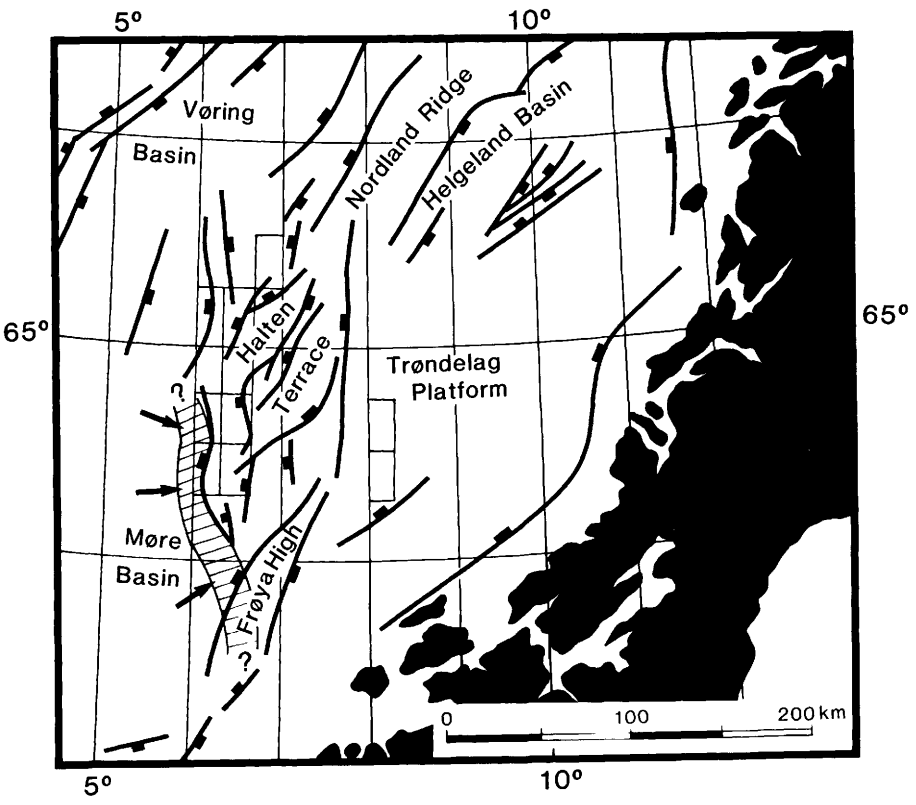

Fig. 1. Map of the Halten Terrace and surrounding areas, showing major structural elements. Arrows denote direction of sediment dispersal from the postulated main southwestern source area (cross-hatched).

The modelling procedure briefly outlined above is currently being applied to the Lower Jurassic Tilje Formation, one of the main reservoir units in the Halten Terrace, mid-Norwegian Shelf (Fig. 1). This very heterogeneous sequence, previously termed the Upper Aldra Formation, was deposited in marine to marginal marine, mostly tidal- to fluvial-dominated sedimentary environments (Fig. 2; Gjelberg *et al.* 1987). It is the aim of this paper to show that the lower parts of the Tilje Formation in the southwestern parts of the Halten Terrace were formed in a fan-deltaic setting, and subsequently to provide data on the geometries of and spatial relationships between *fan-delta-front* building blocks. As input to the reservoir modelling of the Tilje Formation, relevant geometry data have been collected from well-exposed fan-delta-front sediments of the Miocene Ridge Route Formation in the Ridge Basin, USA (Crowell & Link 1982). The Ridge Route Formation was selected as a study object because of its degree of analogy with the Tilje Formation (see below). Regardless of one's faith in the analogue approach, the data presented here are important in their own right since no previous numerical data-sets on the geometry of fan-delta-front deposits are present in the literature.

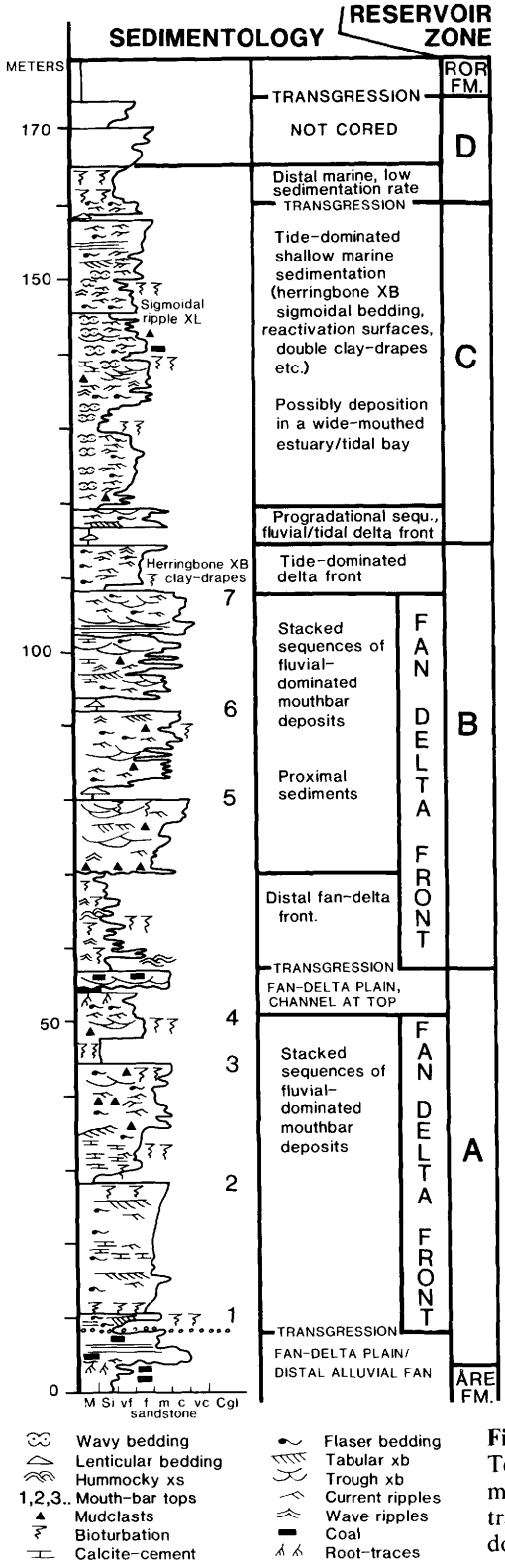

Fig. 2. Sedimentary core log from a Halten Terrace well containing a proximal development of the Tilje Formation. Note the vertical transition from fan-deltaic sediments to tide-dominated shallow marine deposits.

Depositional setting of the Tilje Formation

In general, the Lower Jurassic Tilje Formation on the Halten Terrace reflects deposition in a N–S-trending seaway influenced by sediment influx both from the east and west (Gjelberg *et al.* 1987). In several fields in this region, the Tilje Formation may be subdivided into four main reservoir zones (A to D on Fig. 2). The boundaries between the reservoir zones represent transgressive events, and tend to be characterized by a rapid deterioration in reservoir quality (sandstone to mudstone).

On a regional scale, most cored Tilje sequences have been interpreted as tidal-influenced deltaic, estuarine or shelf deposits (Gjelberg *et al.* 1987). Locally, however, fluvial processes may overprint the tidal influence. This overprinting primarily seems to be a function of proximity to the western source area. In those areas where the fluvial overprinting is especially pronounced, the Tilje Formation is believed to reflect deposition in *fluvial-dominated fan-delta complexes* (zone A and most of zones B and D, Figs 2 and 3). Stratigraphically upwards, these fan-deltaic deposits tend to be transitional to deposits formed in a regionally important *tide-dominated seaway* (most of zone C, Fig. 2). A detailed facies description and interpretation is given in the Appendix. The Tilje Formation overlies (fan)-delta plain deposits of the Åre Formation. The boundary between the two formations is usually marked by a transgressive lag. Another transgressive event separates the Tilje Formation from the overlying distal marine Ror Formation (Gjelberg *et al.* 1987).

Several factors indicate that parts of the Tilje/Åre sequence in the southwestern Halten Terrace were deposited in a fan-deltaic setting (Fig. 3). First, the very immature mineralogy and texture of the sandstones of the Åre Formation and lower part of Tilje Formation suggest proximity to the source area. The Åre Formation sandstones are interpreted as channel sandstones based on their erosive bases, general fining-upwards tendencies, extensive high-angle cross-bedding, absence of bioturbation, interbedding with mudstones and coals of coastal plain origin, and the high amount of mudstone intraclasts. The channel sandstone bodies are multistorey and up to 35 m thick, and have been interpreted as braided stream deposits. Seismic and dipmeter data suggest that the braided streams spread in a radial pattern (northeast to southeast) from a source area near the western margin of the Halten Terrace (Fig. 1). The braided streams are thus thought to represent distributaries on an alluvial fan system. In early Pliensbachian times, a major transgressive event caused backstepping of the alluvial fan, creating widespread shallow marine conditions (the Tilje Formation). The conformable boundary between the Åre and Tilje Formations, and the occurrence in the Tilje Formation of 5–15 m thick intervals of alluvial deposits intermixed with the marine deposits, suggest that the shallow marine and alluvial fan deposits were parts of a fan-deltaic system (Fig. 3).

Facies analysis (see Appendix) suggests that the fan-deltaic parts of the Tilje Formation were fluvial dominated. This can be inferred from the limited evidence for tide- and wave-generated processes, and the dominance of 2–12 cm thick beds of normally graded to ungraded, massive or horizontally laminated sandstone. The grain-size in these beds varies from fine to coarse grained, and ripples may occur in the upper part of the finer-grained beds. Thin (1 mm–2 cm) mudstone beds rarely separate the sandbeds. These sharp-based beds are thought to have been deposited by density currents at the delta-front (e.g. Wright 1977). They may represent hyperpycnal flows generated as sediment-laden fluvial discharge entered the basin, or

mass-flows in the relatively high gradient setting typical of fluvial-dominated fan-delta-fronts (e.g. Nemec 1990).

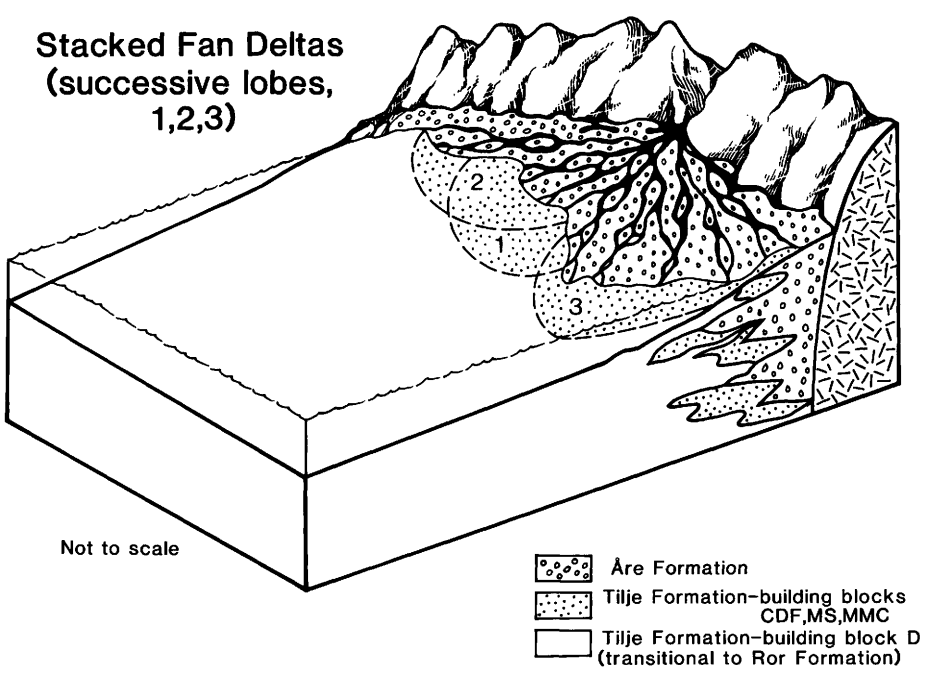

Fig. 3. Generalized Lower Jurassic palaeogeography for the proximal parts of Tilje/Åre fan-delta complex developed on the Halten Terrace.

Degree of analogy between the Tilje and Ridge Route formations

The Ridge Route Formation in the Ridge Basin, California (Fig. 4), was selected as an appropriate analogue to the fan-deltaic parts of the Tilje Formation on the Halten Terrace. In Miocene time, the Ridge Basin was subjected to strike-slip faulting (Crowell & Link 1982), and an almost 13 km thick sedimentary package formed. The Ridge Route Formation is part of the late-stage basin fill, and consists of alluvial fan and lacustrine fan-deltaic deposits that prograded mainly to the west-southwest toward the San Gabriel Fault (Fig. 4; Link & Osborne 1982).

The Ridge Route Formation contains five fan-deltaic sequences (Wood & Link 1987). Field studies indicated that the sedimentary characteristics of three of these (the Marple Canyon, Frenchman Flat and Apple Canyon Members) were in several respects analogous to those in the fan-deltaic parts of the Tilje Formation.

(1) The fan-deltaic deposits of the two formations are fluvial-dominated, and have the same levels of facies-related heterogeneity. However, fine-grained sandstones deposited in a distal to intermediate environment are less common in the Ridge Route Formation than in the Tilje Formation.

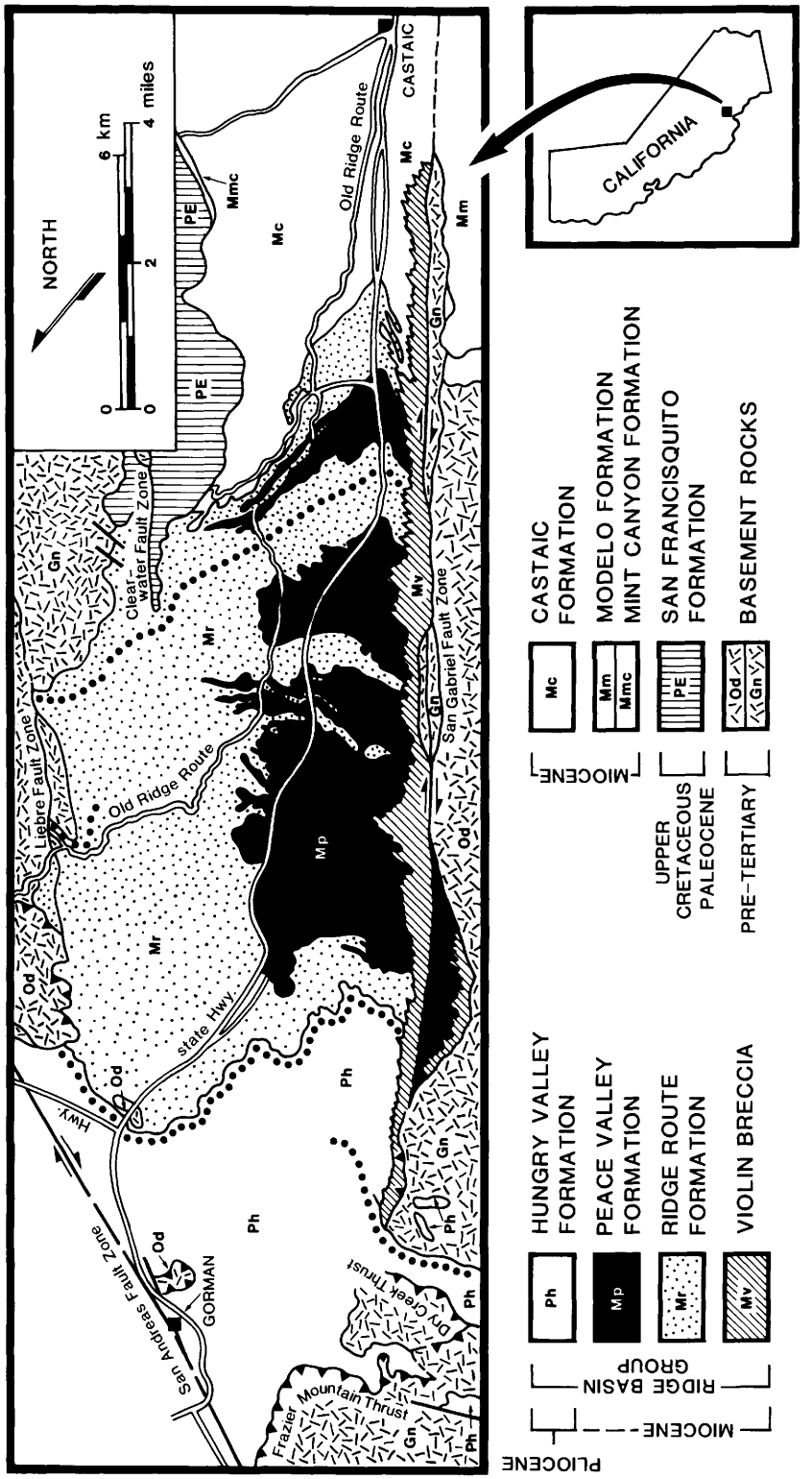

Fig. 4. Location and simplified geological map of the Ridge Basin, California, USA (after Crowell 1975).

(2) The Ridge Route Formation contains numerous laterally extensive and mappable mudstone-dominated sequences which seem to correspond to the 'transgressive' distal marine/delta-front deposits of Tilje (building block D).
(3) The degree of diagenesis in the Ridge Route Formation is varied. Most notably, the extent of carbonate-cementation changes from member to member, and sometimes also laterally within members. In those parts of the formation with a limited degree of carbonate cementation, the permeability ranges are comparable to those in the Tilje Formation.
(4) Various mouth-bar deposits seem to be the dominant building blocks in the fan-delta-front parts of both formations. These depositional elements tend to form composite delta-front units which on a large scale contain a mixture of mouth-bar sandstones and mouth-bar-related fine-grained sediments.
(5) The sand/shale ratios in the Tilje Formation and the studied parts of the Ridge Route Formation are similar.
(6) The distance from source area to depositional sites seems to have been only a few kilometres in both cases.
(7) The fan-deltaic sediments of the two areas accumulated in narrow basins where the distance between the bounding faults was 15–40 km (Link & Osborne 1982; Gjelberg *et al.* 1987). Moreover, rapid proximal to distal facies transitions can be documented in both cases.
(8) Both the Ridge Route Formation and the Tilje Formation have been subjected to syn-sedimentary tectonic activity which may have affected sediment dispersal trends, sedimentary thicknesses etc. Both normal faulting and strike-slip faulting are believed to have taken place in the Ridge Basin and the Halten Terrace (Crowell & Link 1982; Bukovics *et al.* 1984; Brekke & Riis 1987).

Although the sedimentary features of the Tilje and Ridge Route Formations are similar in many ways, the two units are definitely not 'perfect analogues' (if such a thing exists). Notable differences between the two formations include subsidence relationships and basin type. Subsidence rates were highest in the Ridge Basin, where it can also be demonstrated that an asymmetric subsidence pattern existed (Crowell & Link 1982). Moreover, although both basins were narrow, the Ridge Basin had the smaller width, and its length was small compared to that of the Halten Basin. These differences are primarily caused by the contrasting basin types; the Ridge Basin being a laterally restricted strike-slip basin whereas the Halten Basin is a sub-basin in a rift-complex that existed between Norway and Greenland in Mesozoic times (e.g. Larsen 1984; Brekke & Riis 1987). The effects of these differences on depositional geometries and sandbody stacking patterns are hard to quantify, but suffice it to say conversion procedures had to be established before data from the Ridge Route Formation were used in the modelling of the Tilje reservoir (see below).

Building blocks and depositional geometries in the Ridge Route and Tilje formations

Scales of reservoir heterogeneities

In complex reservoir sequences, heterogeneities exist at several scales (Fig. 5). At the most detailed scale, variations at the pore level are vital for the fluid flow properties

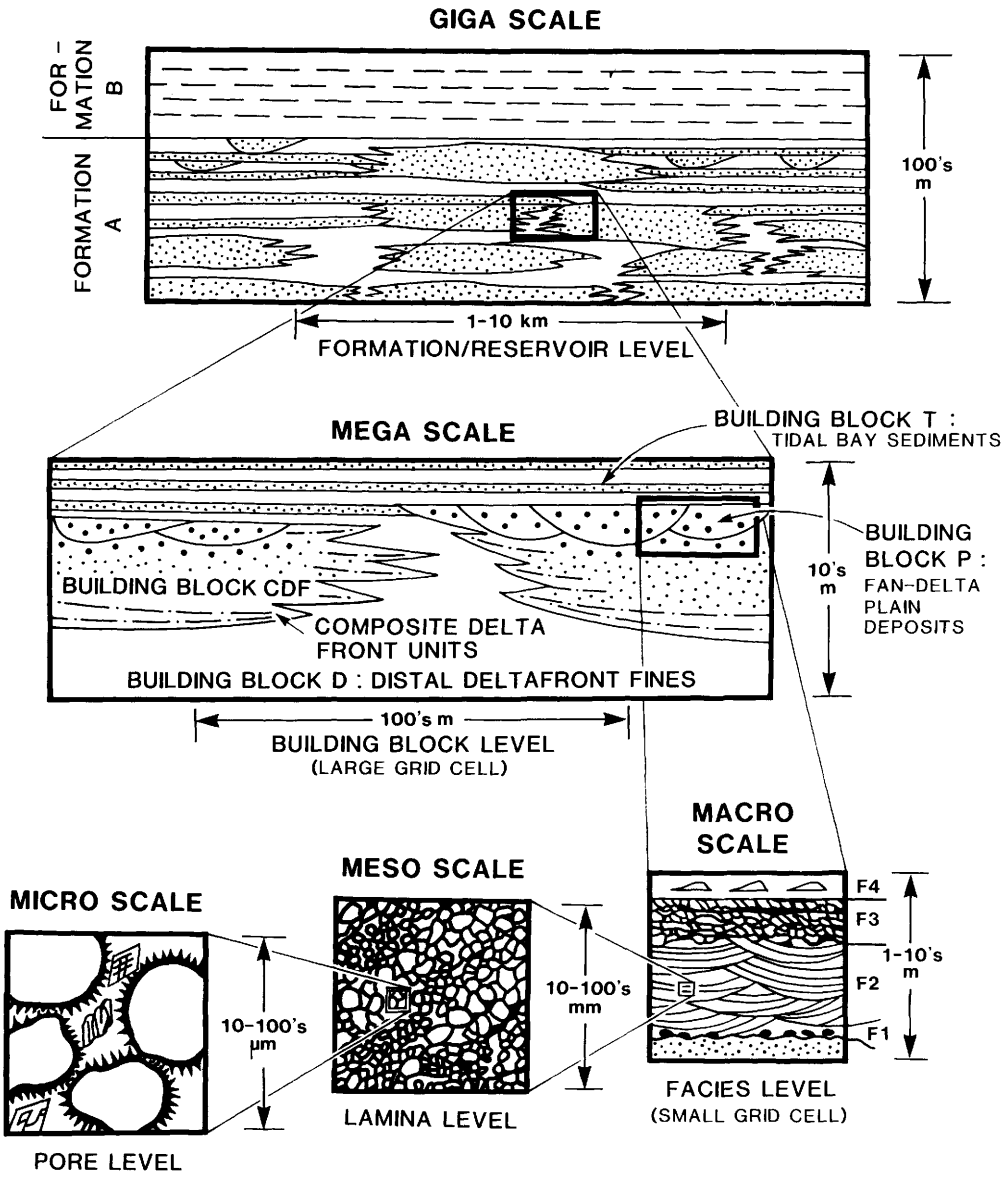

Fig. 5. Levels of heterogeneity in fluvial/tide-dominated shallow marine sediments (e.g. Tilje Formation). The four fan-delta-front building blocks discussed in this paper are schematically illustrated at the megascale. Here, building block CDF encompasses both building blocks MS and MMC (see text).

of the rock. In the Tilje Formation, the most critical factors include the effects of varying degrees of grain packing, clay content and carbonate cementation on pore throat size, and hence permeability. Differences in grain size and degree of cementation between adjacent sandstone laminae generate significant permeability contrasts at the mesoscale. At the facies level, it can be documented that variations in

permeability/porosity in the Tilje Fomation are related to changes in facies types (Appendix). For instance, the cross-bedded coarse-grained sandstones of facies F2 (Fig. 5) have significantly higher permeabilities than the fine-grained flaser-bedded to rippled sandstones of facies F3. This has led to the establishment of facies-related flow units which are used in the modelling of the Tilje reservoir. On the larger megascale, these flow-units can be combined into reservoir building blocks. At the building block scale, the most significant heterogeneities are related to the geometrical properties of these large-scale reservoir units. It is also important to understand the spatial relationships between the building blocks. Fault-patterns and extents of sandstone- and mudstone-dominated zones are critical heterogeneities at the gigascale. This paper is concerned with the patterns of heterogeneity present at the mega- and gigascales of Fig. 5.

Below, a brief presentation of the four fan-delta-front building blocks of the Tilje Formation will be given. Subsequently, the corresponding building blocks of the Ridge Route Formation will be discussed, with emphasis on their geometrical aspects.

Fan-delta front building blocks in the Tilje Formation

In the fan-deltaic parts of the Tilje Formation (Fig. 2), approximately 80% of the sediments are interpreted to have formed subaqueously. These fan-delta-front deposits can be subdivided into four building blocks:

Building block MS: mouth-bar sandstones. These deposits consist of fine to very coarse-grained sandstones with less than 15% mudstone interbeds. The mudstone interbeds are between 1 mm and 5 cm thick, whereas the entire MS-units vary in thickness from 8 to 22 m. A limited suite of marine trace fossils occur, with *Diplocraterion parallellum, Skolithos and Asterozoma* as the most common traces. The sandstones are moderately sorted, and usually show coarsening-upwards or coarsening- then fining-upwards grain size trends. In two thirds of the cases, MS units are amalgamated. Otherwise, they tend to be separated by the fine-grained deposits of building block MMC. Low-angle cross-bedded to horizontally bedded intervals and current rippled zones are common. The density current bed-type described above dominates in most intervals. Building block MS is interpreted to represent proximal to medial fan-delta front deposits in which fluvial-dominated mouth-bars are the most common sandbody type.

Permeabilities normally range from 50–2000 mD, with a mean value of 750 mD.

Building block MMC: mouth-bar-related mudstones and carbonate-cemented zones. Such rocks occur as 0.1–7 m thick, impermeable reservoir zones. The mudstone-dominated intervals contain 10–50% very fine- to fine-grained sandstones as thin beds or lenses, and moderate abundances of *Diplocraterion parallellum* and *Planolites* trace fossils are found. Current ripples, rarely with well-developed herringbone cross-lamination and mud-draped foresets, are common in the sandbeds. The mudstone-dominated intervals occur interbedded with the sandstones of building block MS, and are interpreted as low-energy deposits formed in the proximal to medial delta-front. They reflect periods of sand-starvation, possibly related to temporary abandonment of mouth-bar lobes. Additionally, a number of the mudstone-intervals

probably formed in interlobe areas (Fig. 6). The carbonate-cemented zones occur in both mudstone- and sandstone-dominated lithologies, and petrographical studies indicate that most of the carbonate formed early in the diagenetic history. Calcite is the most common type of carbonate cement, but sideritic varieties also occur. On average, the spacing between carbonate-cemented zones is 7 m, and their thicknesses range from 0.1–4 m, with an average of 0.35 m. The relations, if any, between sedimentary facies and occurrence of carbonate-cemented zones are, as yet, not understood.

Building block CDF: composite delta-front units. These units are represented by 7–55 m thick sections composed of alternating intervals of building blocks MS and MMC. Essentially, they correspond to reservoir zones A, B and D of Fig. 2. The CDF units were assigned building block status because they form gigascale (Fig. 5) sand-dominated intervals separated by laterally extensive mudstones of building block D. As such, the individual CDF zones might represent isolated reservoir compartments for which information about geometry and internal arrangement of permeable and tight intervals is needed. 60–80% of the CDF bodies consists of building block MS, and about two thirds of the individual MS sandbodies are amalgamated. These amalgamations tend to juxtapose high-permeability zones at the top of one MS unit against zones with at least an order of magnitude lower permeabilities at the base of another MS unit. The permeability contrast becomes even more pronounced in the cases where MMC deposits separate the sandbodies. Because these permeability contrasts significantly influence the degree of internal communication in the CDF bodies, emphasis was put on studies of the lateral developments of MS–MS and MS–MMC transitions in the Ridge Basin. The depositional environment of building block CDF can be inferred by combining information about the sedimentary settings of the component building blocks. This implies that the CDF units are sand-dominated fan-delta-front complexes composed of mouth-bar deposits and intervening mudstone-dominated interlobe abandonment sediments (Fig. 6).

Building block D: distal delta-front mudstones. Such mudstones occur as 2–30 m thick, impermeable intervals between the CDF units. These fine-grained sediments usually contain less than 35% sandstone, and host a number of trace fossils, the most common being *Asterozoma*, *Siphonites* and *Scalarituba*. Non-bioturbated intervals display lenticular bedding, parallel lamination or contain no visible stratification. The fine- to very fine-grained sandbeds are sharp-based, containing small clay intraclasts, hummocky cross-stratification, and wave ripples. They are less than 20 cm thick, ungraded to normal-graded, and were probably deposited as a result of storm-events. Building block D is interpreted as distal fan-delta front deposits, formed basinwards of the mouth-bar bodies described above. The transitions from building block CDF to building block D reflect transgressive events. They can be separated from the mudstones of building block MMC by their trace fossil assemblage and the higher degree of bioturbation, their greater thicknesses, and by the transgressive nature of the CDF–MMC boundaries.

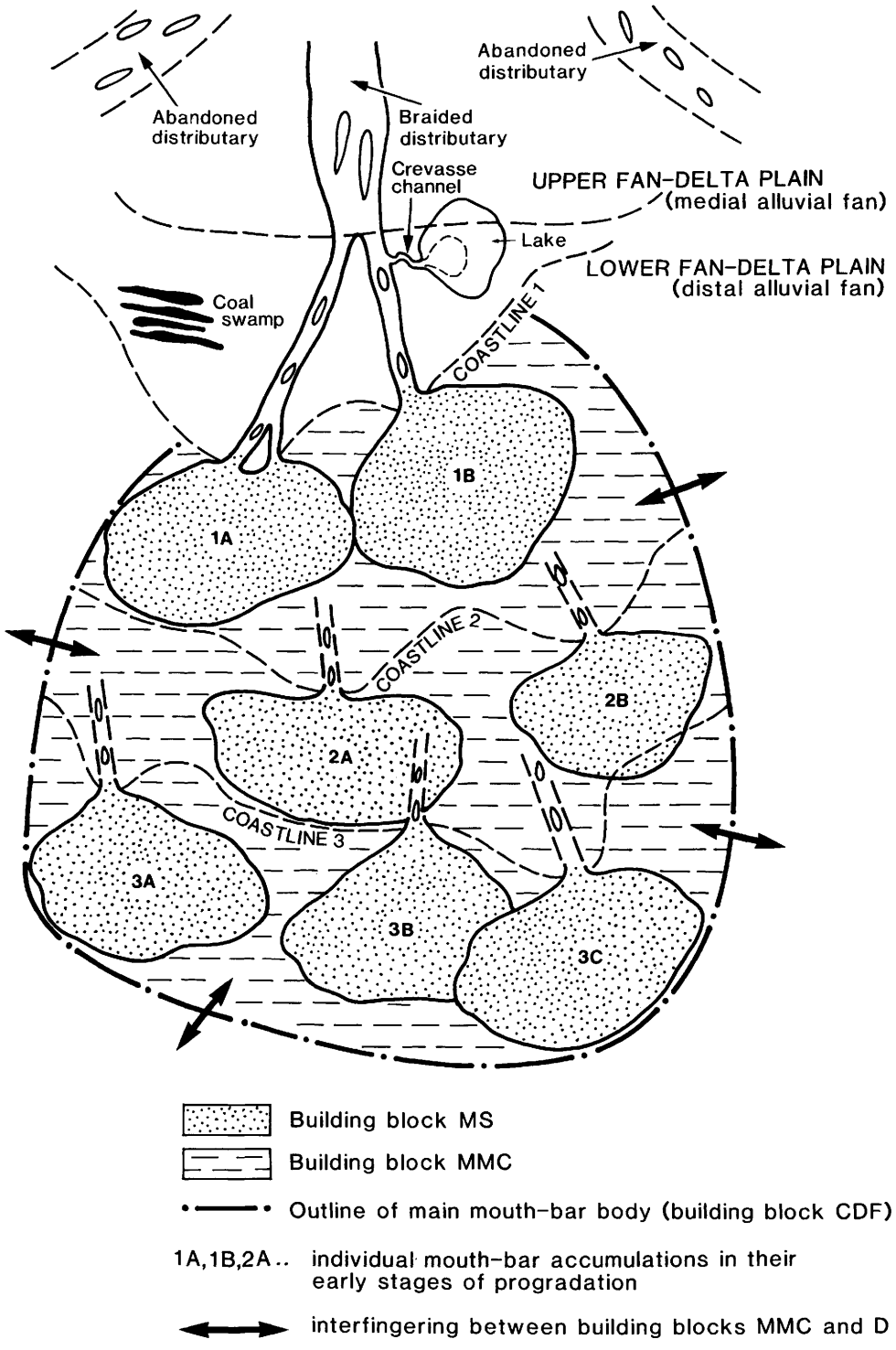

Fig. 6. Relationships between, and development of, building blocks CDF, MS and MMC. Note that since the mouth-bar bodies are drawn in their early stages of progradation, this illustration overestimates the preserved percentage of MMC mudstones in the CDF bodies.

Fan-deltaic building blocks in the Ridge Route Formation

The Ridge Route Formation contains five prograding braid- to fan-deltaic units (Wood & Link 1987). Field studies indicate that the sedimentary characteristics in three of these (the Marple Canyon, Frenchman Flat and Apple Canyon Members; Link & Osborne 1982) are similar to those of the fan-deltaic parts of the Tilje Formation. The four fan-delta-front building blocks recognized in the Tilje Formation were also found in the Ridge Basin (Fig. 7). Since their facies characteristics were found to be quite similar, the environmental interpretations given for the Tilje Formation are considered to be valid also for the Ridge Route Formation. Hence, to avoid repetition, only limited amounts of facies information will be given in the sections below.

Building block CDF. As in the Tilje Formation, this composite building block is thought to consist of one or more sandy mouth-bar deposits (building block MS) which are amalgamated, or separated by mudstone-dominated or carbonate-cemented intervals (building block MMC). Vertical sequences and architectural features of building block CDF are shown in Figs 8, 9, 10 and 14. The thickness of the CDF units is more variable than the Tilje, ranging from 5 to 77 m with a mean value of about 25 m. The inferred fan-deltaic depositional setting in which the CDF bodies accumulated is illustrated in Figs 3 and 6. In Fig. 6, a number of individual mouth-bars overlap due to accumulation in front of adjacent distributary mouths. The overlaps might have been caused by local, basinward-stepping lobe-shifts of a single stabilized distributary, or by simultaneous mouth-bar-sedimentation in front of several nearby distributaries.

The degree of internal communication in building block CDF depends on the spatial distribution of building blocks MS (sandbodies) and MMC (flow-barriers). Since building block MMC usually constitutes less than 25% of the CDF units, the ratio between the lateral extents of these two building blocks ought to give a good estimate of the MMC units' effectiveness as flow-barriers. Ratios of MMC/CDF lateral extents close to unity would imply that the MMC units were developed as flow-barriers within large parts of the CDF bodies. Low ratios (0.1–0.5) would mean that individual sandbodies in the CDF units were in good communication. A comparison of the dimensional data for building blocks CDF and MMC (below) indicate that the average ratio of MMC/CDF lateral extents is approximately 0.25. Hence, it may be assumed that the internal communication in the CDF units is generally good (Fig. 11).

The geometry of building block CDF was investigated by a combination of lateral tracing and correlation of closely spaced vertical profiles. Normal to depositional strike (length-dimension), 11 CDF bodies were measured in the Apple Canyon Member, while 18 bodies from the Marple Canyon and Frenchman Flat Members were measured in the width-dimension. Reconstructions of the varying basin configurations were based on data from Smale (1978), Wood & Link (1987), Wood & Osborne (1982) and Hollywood & Osborne (1982). Figure 12 shows L/T- and cumulative length-plots for building block CDF, while W/T- and cumulative width-plots are shown in Fig. 13. The 'best-fit' lines of these plots indicate that the Ridge Basin composite mouth-bars have W/T- and L/T-ratios of roughly similar values.

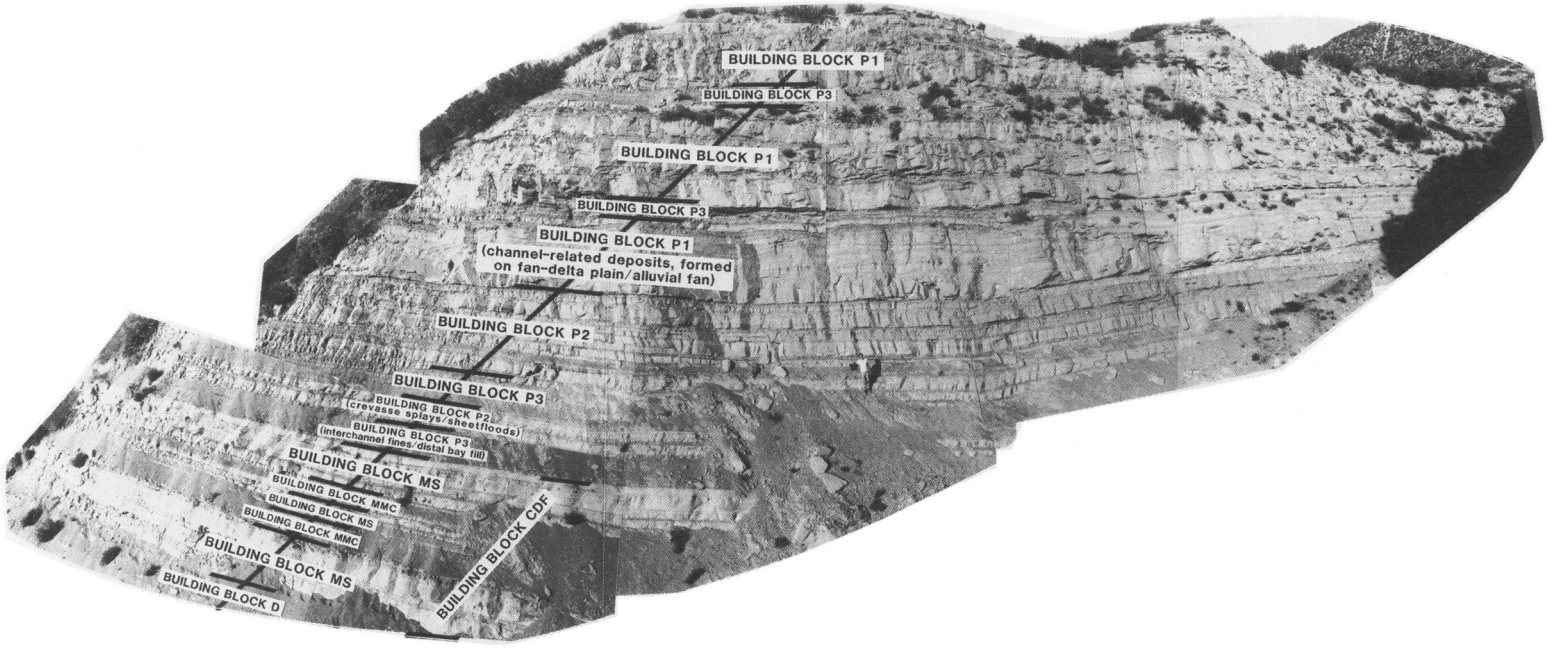

Fig. 7. Photographic overview of a progradational fan-deltaic section in the Frenchman Flat Member of the Ridge Route Formation. The exposure is located along Old Ridge Route. It is orientated normal to palaeocurrent, and the lower part contains the fan-delta-front building blocks discussed in this paper. Building blocks P1, P2 and P3 in the middle to upper parts of the exposure are interpreted to be fan-delta-plain deposits. Note the pronounced vertical heterogeneity, the mostly sheet-like beds, and the coarsening- and thickening-upwards of beds.

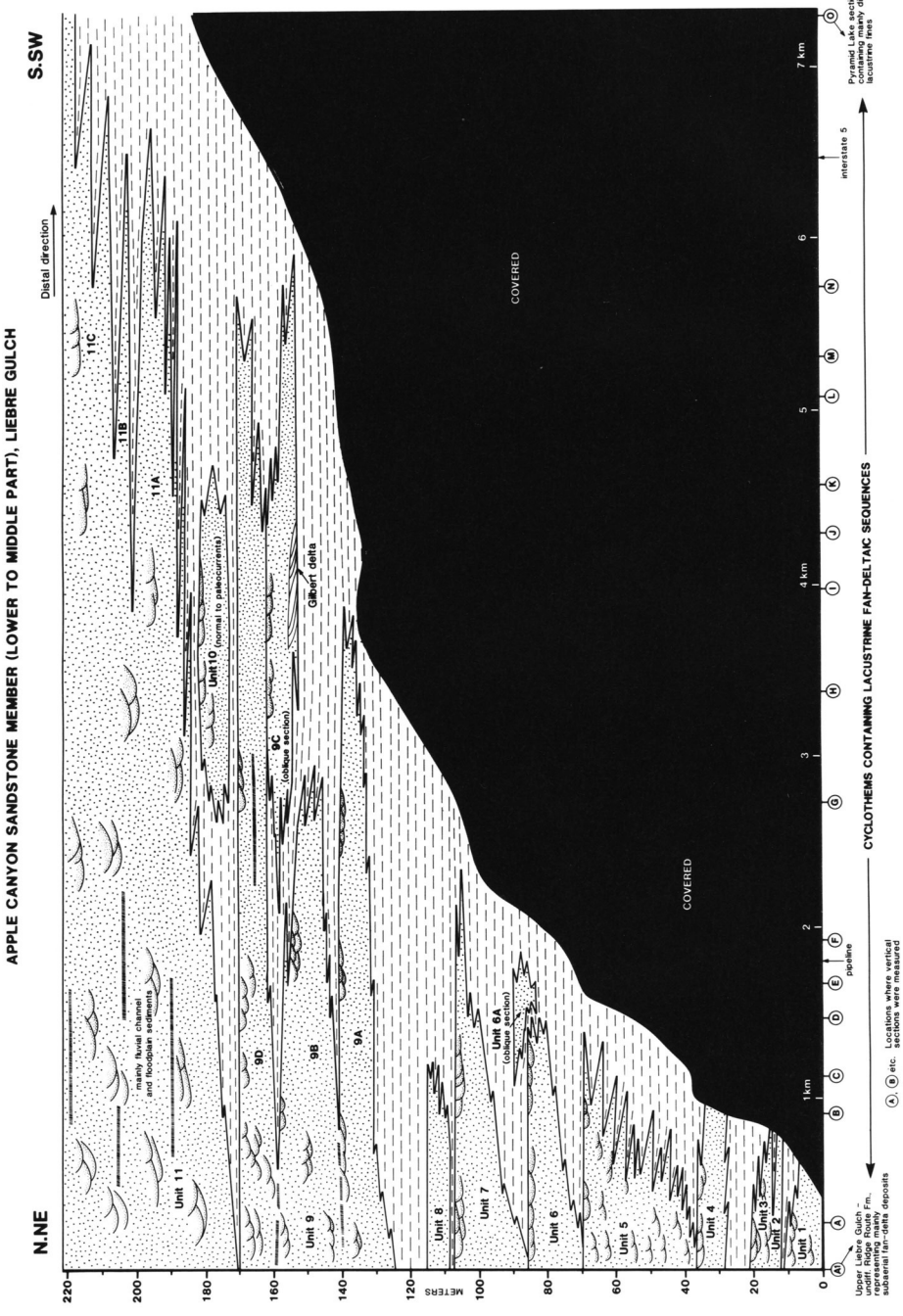

Fig. 8. Large-scale facies architecture in the Apple Canyon Member, Liebre Gulch, Ridge Basin. The dotted pattern represents individual fan-delta-front units (building block CDF), while the dashed pattern symbolizes distal lacustrine fines (building block D, tongues of the Alamos Canyon Siltstone Member). The exposure is nearly parallel to the main direction of deltaic outbuilding. Effects of structural disturbances have been removed, and the tectonic dip has been flattened. Note the tendency towards increasing lateral extent of the fan-deltaic units stratigraphically upwards. This change from dominantly vertical to dominantly lateral outbuilding may have been caused by an increase in the ratio of sediment supply to accommodation space.

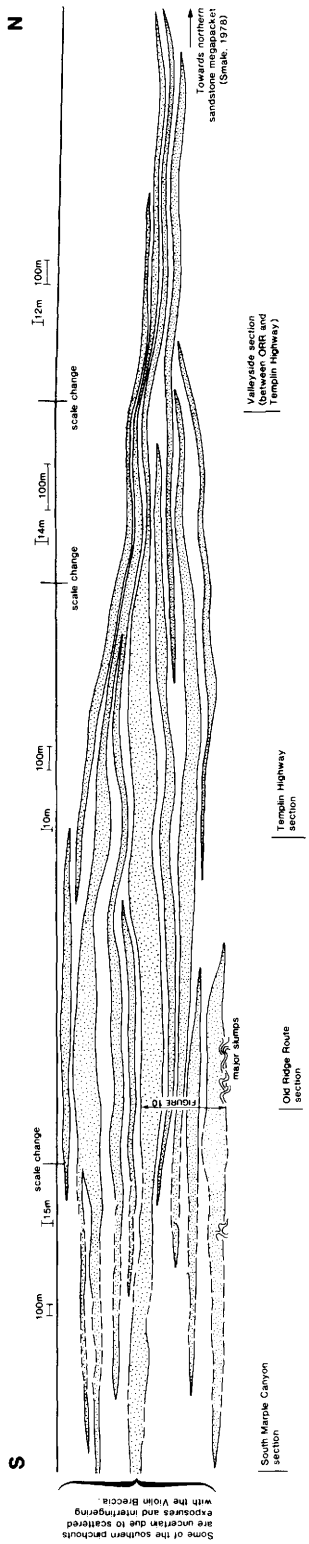

Fig. 9. Cross-section of the Marple Canyon Member in the south-western part of the Ridge Basin. The section is interpreted to be orientated mostly normal to palaeocurrent (cf. Smale 1978). Fan-delta-front sandbodies of building block CDF are stippled, and their internal heterogeneities are not shown. Note the variable but generally large lateral extents of the CDF-bodies. The sediments between the CDF-units are mudstone-dominated deposits formed in a distal lacustrine setting (building block D).

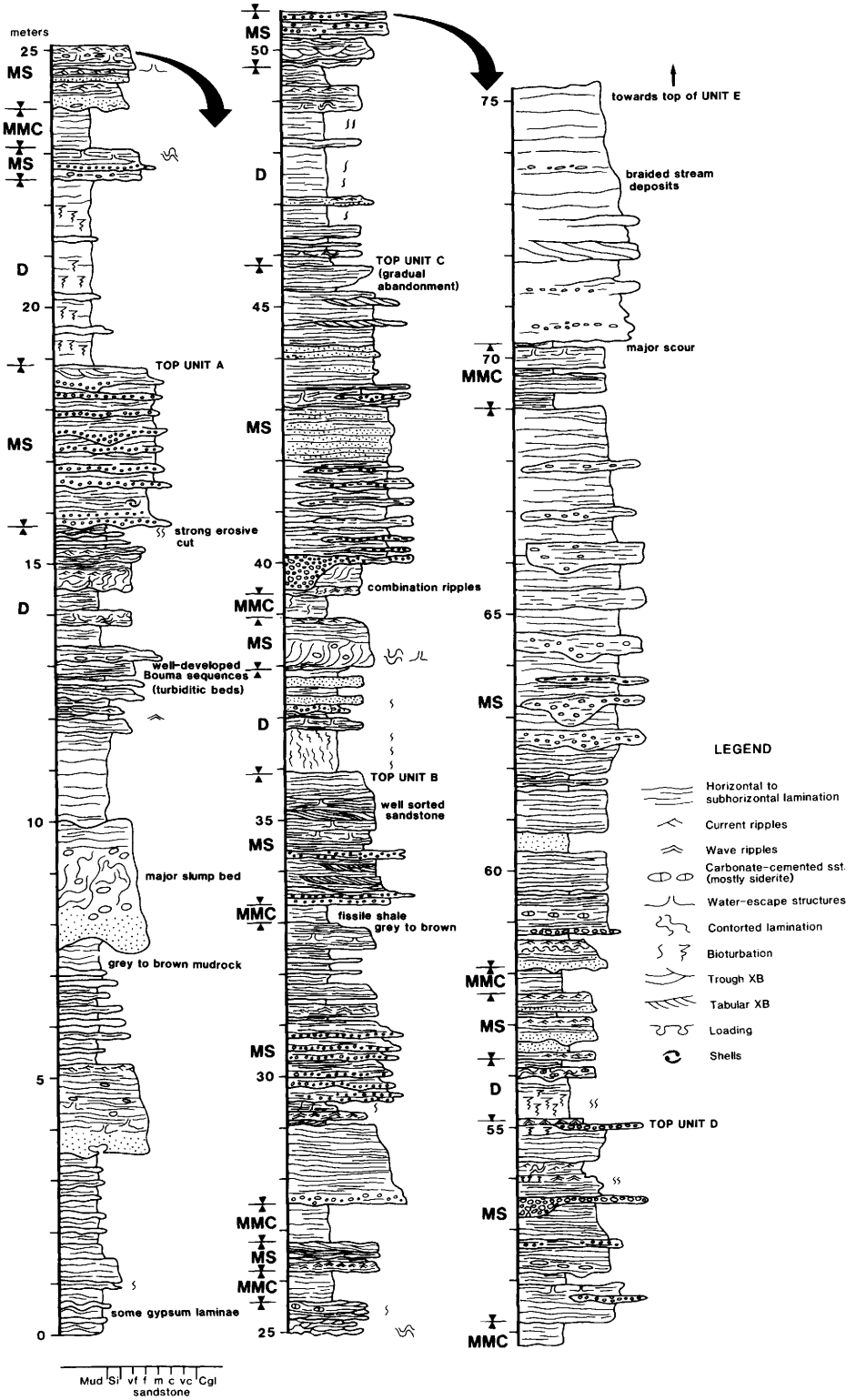

Note, however, that a change from W/T < L/T to W/T > L/T takes place as the thickness of the CDF bodies increases. This probably reflects the tendency towards more frequent lateral linkings of mouth-bars (Fig. 6) as the CDF bodies become increasingly complex.

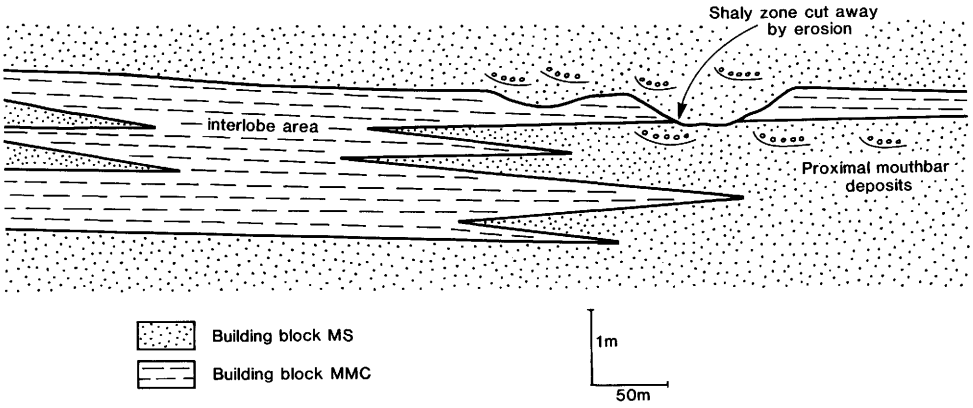

Fig. 11. Details of the lateral variations along the boundary between building blocks MS and MMC. Note the area where two MS units are in communication.

Building block MS. This building block contains the sand-dominated portions of the larger CDF bodies (Figs 10, 14, 15). As in the Tilje Formation, fine to coarse-grained, moderately sorted sandstone is most abundant, with grain-size variations from mud to conglomerate. Mudstone (often sideritic) occurs as rip-up clasts, armoured mudballs, or as thin and discontinuous beds or drapes on foresets/bedforms (Fig. 15), and constitutes 3–10% of the clastic material. Conglomeratic clasts make up 5–10% of the MS units, and are mostly found in scour pockets (Fig. 16), as basal lags in normal graded beds, or as thin and laterally persistent pebbly zones within thick and well-stratified sandbeds (Fig. 10). The sandstones occur in five main bedtypes (Table 1) which usually form broad (10–100 m wide, 0.1–2 m thick), interfingering lenses. Horizontal stratification and massive bedding are most common, with subordinate amounts of wave/current ripples and low-angle cross-bedding. Bioturbation occurs infrequently, mainly in the form of *Paleophycus* and ?*Chondrites* (Smith *et al.* 1982).

40% of the MS units display coarsening-upwards grain size trends, and have gradual lower contacts to mudstone-dominated sequences of building blocks MMC and D. In 30% of the cases, the MS units are developed as sharp-based sandbodies in which the grain size is roughly similar throughout the unit (ungraded type, Fig. 17).

Fig. 10. Vertical log from the Marple Canyon Sandstone Member (upper lithofacies and transition to the middle/lower lithofacies of Smale 1978). The log is from the intersection between Old Ridge Route and Templin Highway. Note the five main fan-deltaic shallowing upwards units (A–E), and the complex alternation between building blocks MS, MMC and D. The tops of units A–D represent correlatable flooding surfaces.

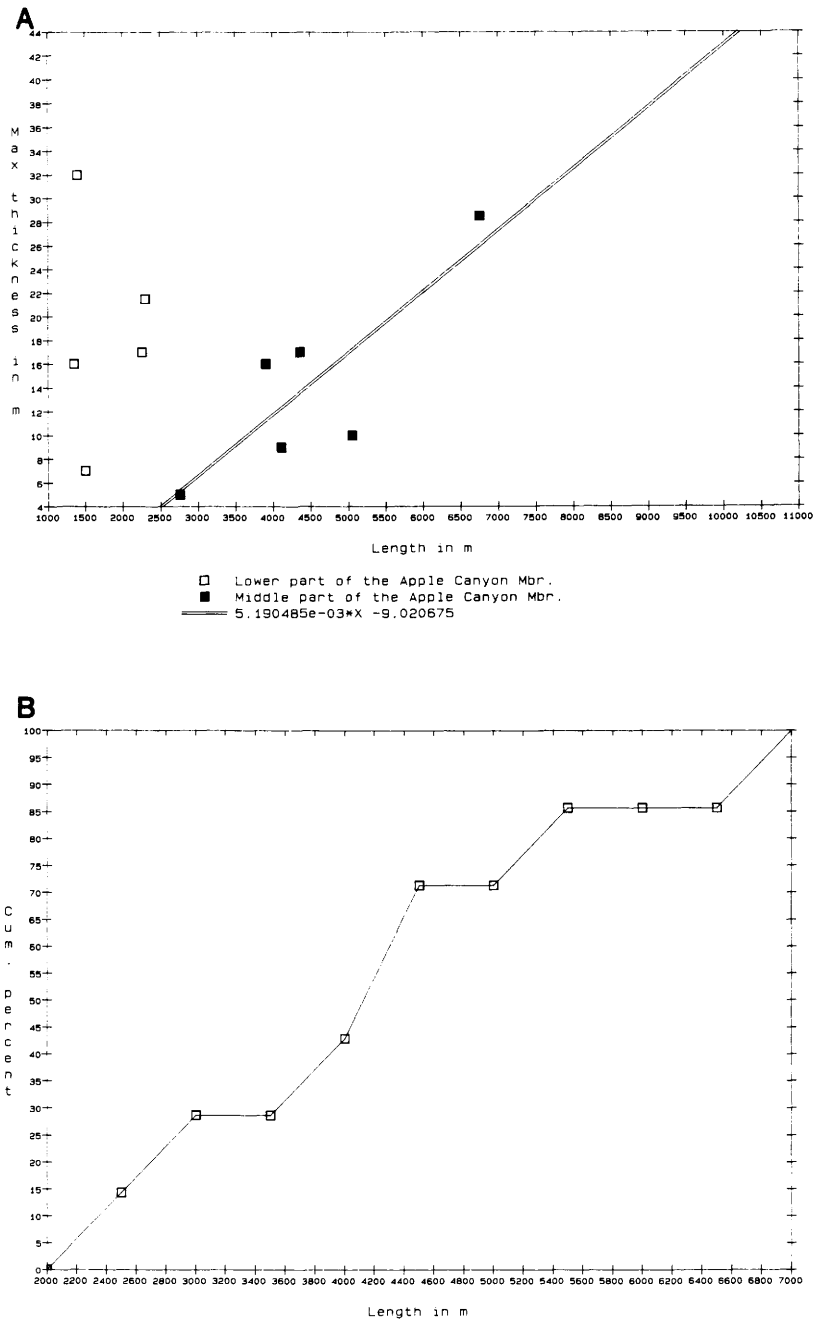

Fig. 12. (**A**) Relationship between length and thickness in building block CDF, Ridge Route Formation. The L/T line is based only on the data from the middle part of the Apple Canyon Member, and has a correlation coefficient (r) of 0.70. (**B**) Cumulative curve for the length of building block CDF, Ridge Basin.

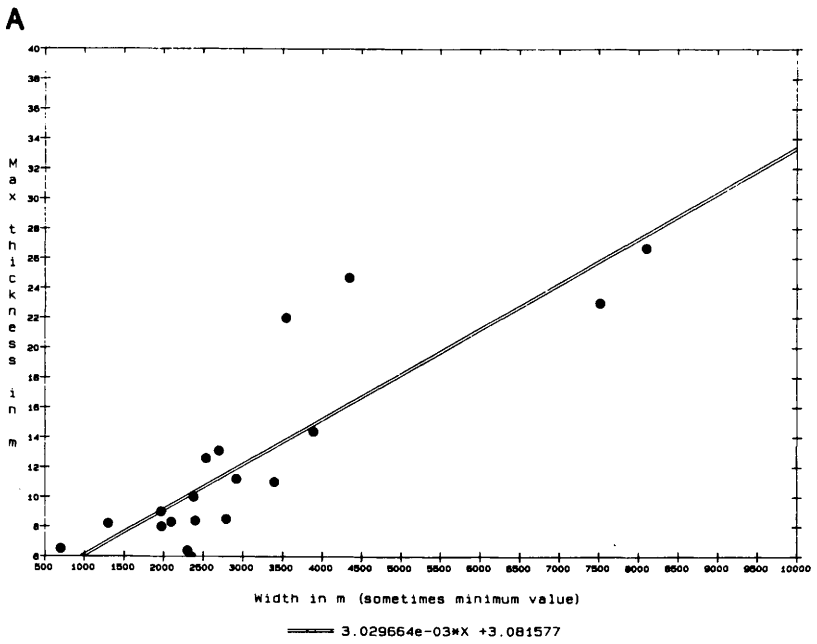

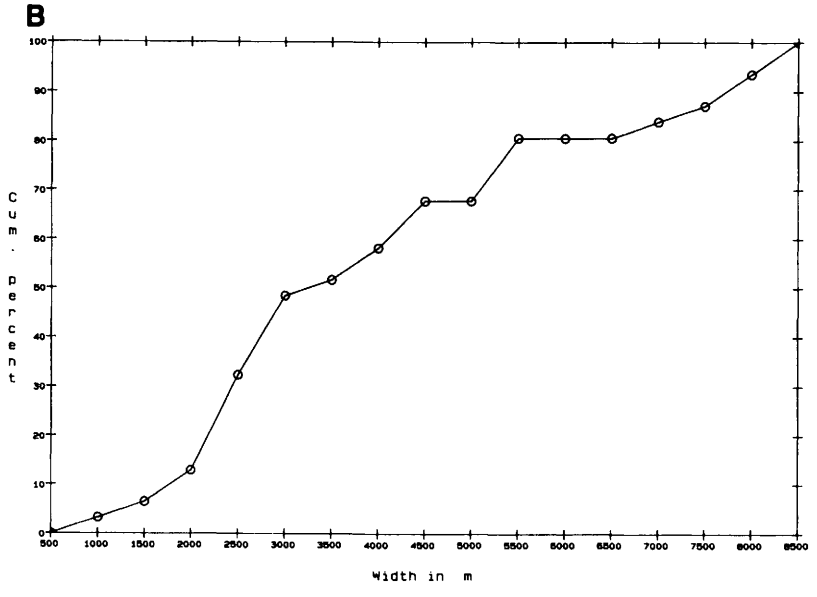

Fig. 13. (A) Relationship between width and thickness in building block CDF, Ridge Route Formation. The W/T line has a correlation coefficient (r) of 0.73. (**B**) Cumulative curve for the width of building block CDF, Ridge Basin.

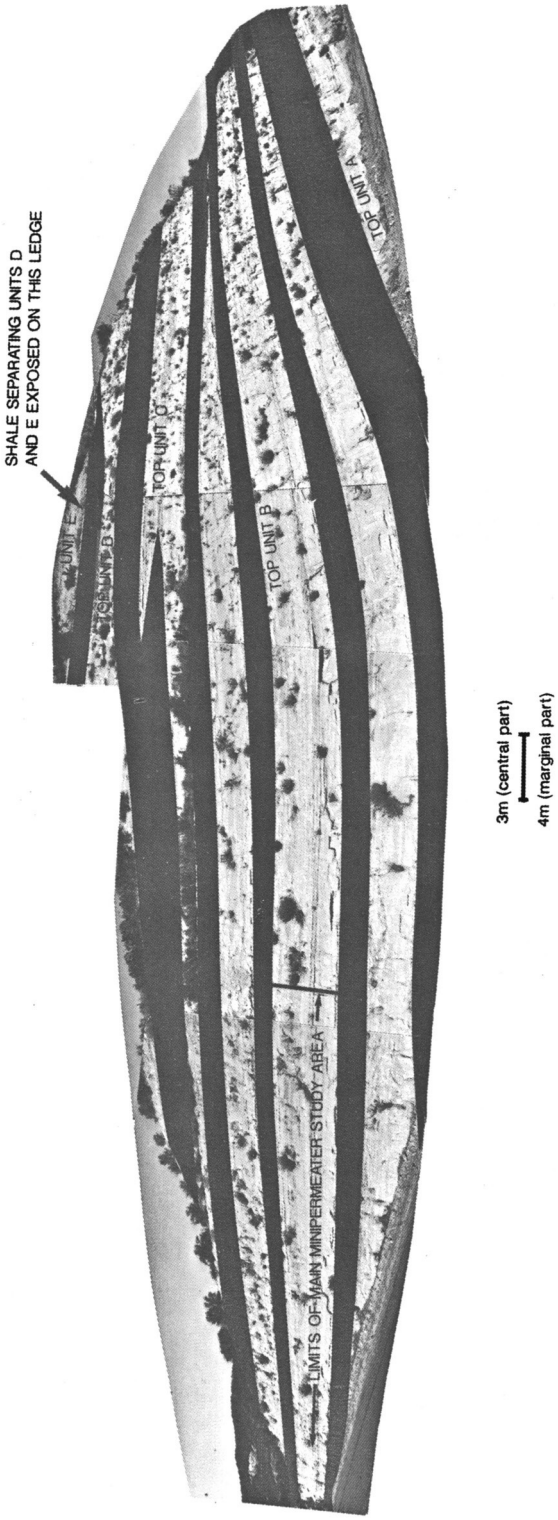

Fig. 14. Alternations between building block CDF (units A to E) and mudstones of building block D along Templin Highway, Ridge Basin. Mudstones are coloured black for contrast. The contacts between D and CDF units are interpreted as flooding surfaces. The mudstones occurring *within* units B and C belong to building block MMC (intra-mouth-bar fines).

Fig. 15. Lateral and vertical relationships between the Gilbert delta type of building block MS and overlying fan-delta-plain channels. The smaller photo shows details from the postulated density-underflow beds which form the toesets of the Gilbert delta unit.

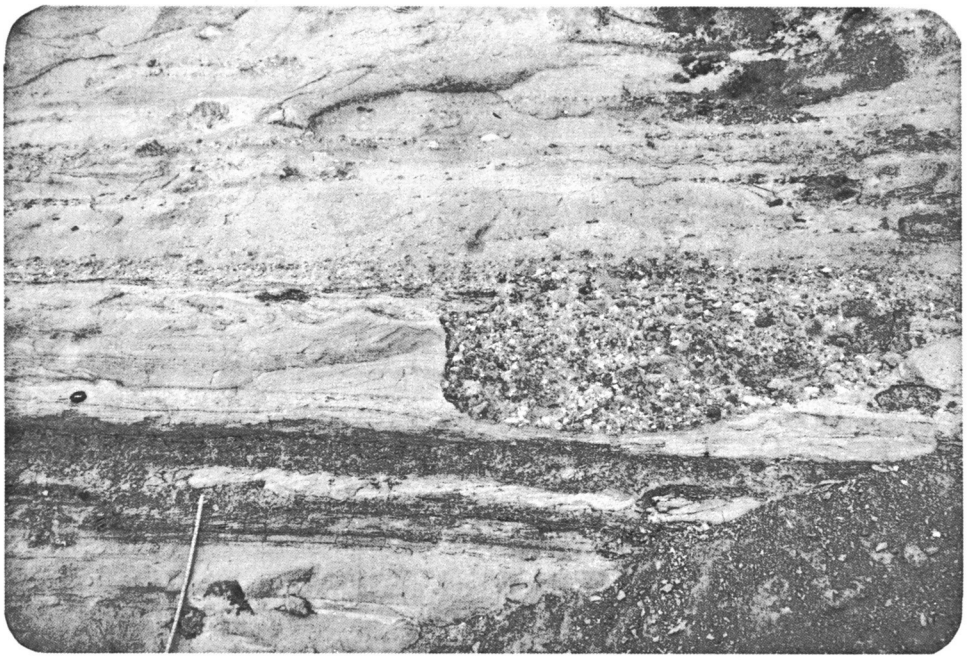

Fig. 16. Varying lithologies in building block MS. A zone of fine-grained sandstone (facies SSR) and grey, discontinuous mudbeds is overlain by medium- to coarse-grained sandstone with abundant soft-sediment deformation near its base (facies SSM and SSH). Subhorizontally laminated beds of gravelly sandstone are interbedded with the cleaner sandstone, and a major gravel-filled scour pocket cuts into the sandy sequence. The succession belongs to the proximal part of a mouth-bar sequence, and the scour pocket probably reflects rapid dumping of the coarsest bedload in the subaqueous continuation of a distributary channel. From the Marple Canyon Member, Old Ridge Route.

These primarily occur in proximal exposures, and in upper parts of CDF units. About 20% of the MS units showed fining-upwards grain size trends. This sandbody type is sharp-based, 2–10 m thick, and tends to occupy the lower portions of CDF units. The remaining 10% of the MS units may be referred to as Gilbert-delta units because of their dominant feature; large-scale tangential cross-beds accentuated by alternating beds of mudstone and facies SSM (Fig. 15, Table 1). The thickness of building block MS ranges from 2–23 m with a mean value of 9 m. As in the Tilje Formation, this building block is interpreted as mouth-bar deposits formed in a fluvial-dominated fan-deltaic setting. Clearly, the different types of MS units are a function of variations in sediment supply, location on the delta-front, delta-front gradients, etc. It is outside the scope of this paper, however, to discuss the spectrum of fan-delta-front morphologies and the factors controlling these.

The geometry of building block MS was investigated by lateral tracing in the field. The length-dimension was studied in the Apple Canyon Member (upper parts of the Libre Gulch, Fig. 8), while measurements of the width-dimension were made in the Marple Canyon Member (Fig. 9). A positive correlation between both length and maximum thickness and width and maximum thickness can be seen from Figs 18 and 19. Additionally, these figures show that the ranges of length and width for building

Table 1. *Sandstone facies types in building block MS, Ridge Route Formation*

Facies	Main characteristics	Depositional processes	Tilje Fm. equivalents*
SSM	Massive- to diffusely-laminated sandstones, medium- to very coarse-grained. Occasional water-escape structures. Beds are 5–150 cm thick, ungraded to normal-graded, and sharp-based.	Density-current deposits formed at the fan-delta front. May reflect re-sedimentation of mouth-bar sediments, or hyperpycnal flows generated as sediment-laden water entered the basin.	M2, M3, M6, M7
SSC	Crossbedded sandstone (Fig. 17), medium- to very coarse-grained. Lenticular beds, normally less than 10 m in lateral extent. Variable foreset migration directions (longshore, offshore-directed, landward-directed). Beds are sharp-based and 0.1–1.2 m thick. Mostly low foreset angles.	Migration of small- to medium-scale bedforms across the tops of the mouthbar bodies. The limited lateral extents, low foreset angles and variable (but not bipolar) dip directions suggest influence of wave-generated currents and fluvial discharge.	M14
SSH	Horizontally to subhorizontally bedded sandstone, medium to coarse grained, well sorted. Inverse-graded laminae. Occur in up to 5 m thick intervals. Laterally continuous bedsets. Some vertical burrows.	Deposits formed in shallow-water parts of the fan-delta front as a result of high-energy wave reworking. Some of these beds might also represent the proximal parts of density-current deposits (ref. facies SSM).	M12
SSR	Fine- to medium-grained sandstones displaying wave ripples and combined ripples. Contains some clay flasers. Bioturbation moderately common. Beds 5–35 cm thick.	Wave-reworked deposits formed during periods of lower basinal energy relative to the deposits of facies SSH.	M8, M11, M16
SSL	Lenticular erosively-based units of pebbly to coarse-grained sandstones. Mostly ungraded beds, massive to horizontally laminated and low-angle crossbedded. Moderately to poorly sorted, contains numerous outsize clasts. Beds 0.4–3.2 m thick, bedsets up to 7 m thick.	Deposits formed in partly channellized subaqueous segments of distributaries. Accumulated in proximal parts of the mouthbars. Individual beds may represent the traction load (main part of bed) and suspended load (fine-grained upper part of bed) of fluvial-derived underflows.	M13

* The Tilje Formation facies are listed in the Appendix.

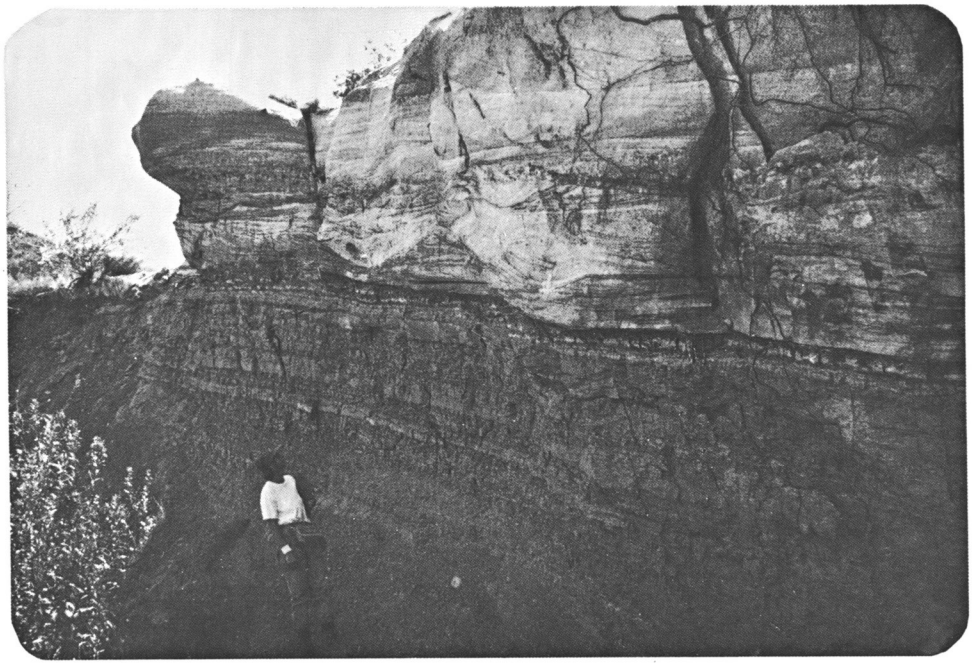

Fig. 17. Fine-grained deposits of building block D overlain by a thin CDF body consisting of only one sharp-based and ungraded MS unit. From the Apple Canyon Sandstone Member, upper part of Liebre Gulch.

block MS are approximately similar. There is a tendency, however, for the widths to cluster at lower values than the lengths. Figures 18 and 19 also indicate that for a given thickness, the length of a MS body tends to be similar to but somewhat larger than the corresponding width. This suggests that the individual mouth-bar bodies have a lobe-like shape with a slight elongation parallel to depositional dip. Compared to the dimensions of the CDF composite bodies (Figs 12 and 13), the MS mouth-bars tend to be 40–80% smaller. The size-reduction is largest in the length-dimension.

Building block MMC. The fine-grained and carbonate-cemented zones of this building block represent potential flow-barriers in the CDF units (Figs 7, 10, 11). The sedimentary characteristics of the MMC mudstones in the Ridge Route Formation are very similar to those of the Tilje Formation (above). Hence, these sediments are thought to have formed in a mouth-bar setting, both in areas between active lobes (Fig. 6) and in periods of temporary sand starvation. The carbonate-cemented zones in the Ridge Route Formation are more sideritic than those in Tilje. They only occur in sandstones, where they form, for the most part, seemingly randomly scattered concretions or beds. In some cases, however, carbonate-cemented zones are present on abandonment surfaces at the top of building block MS. These might have originated as incipient hardgrounds during transgressive periods when the rate of sediment supply was limited (Molenaar *et al.* 1988; Walderhaug *et al.* 1989).

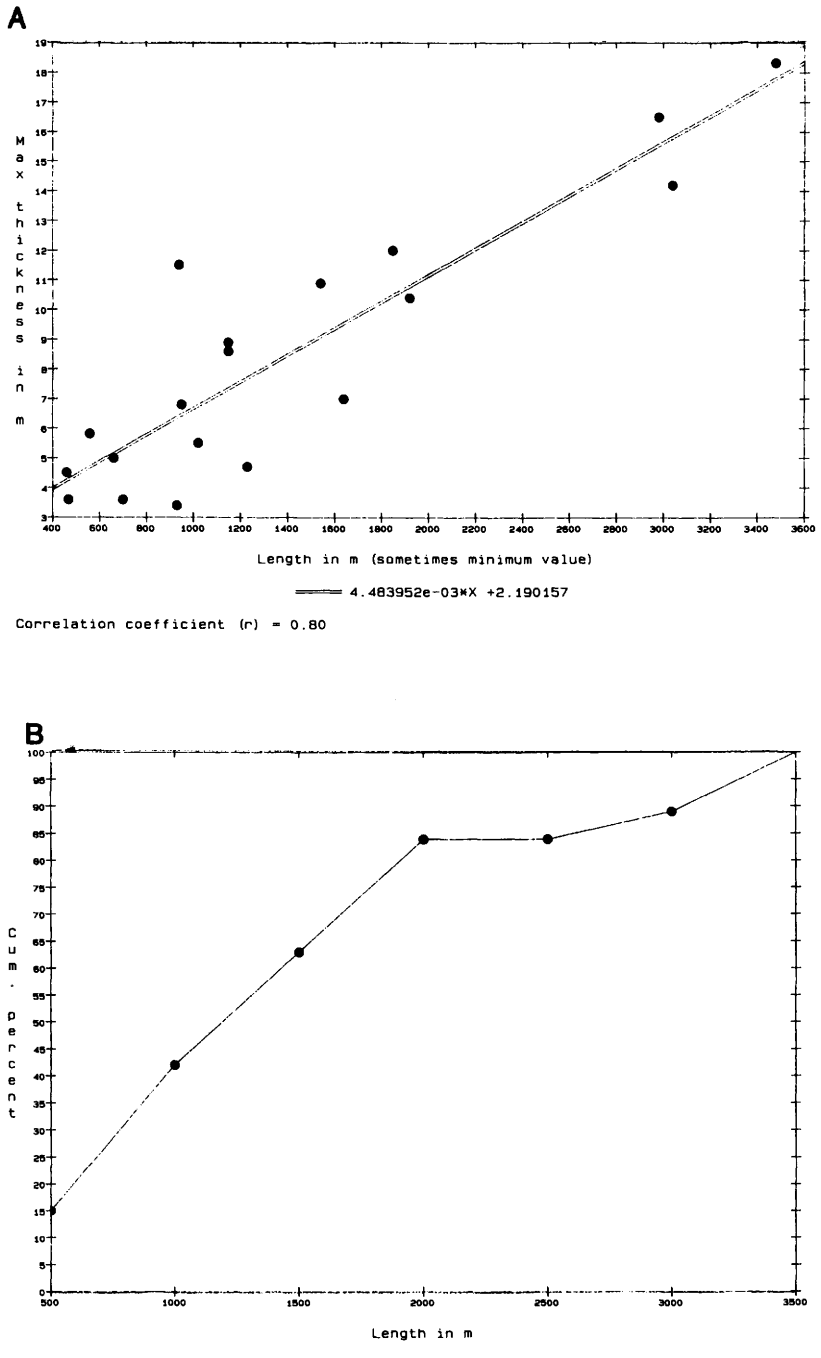

Fig. 18. (**A**) Relationship between length and thickness in building block MS, Ridge Route Formation. (**B**) Cumulative curve for the length of building block MS, Ridge Basin.

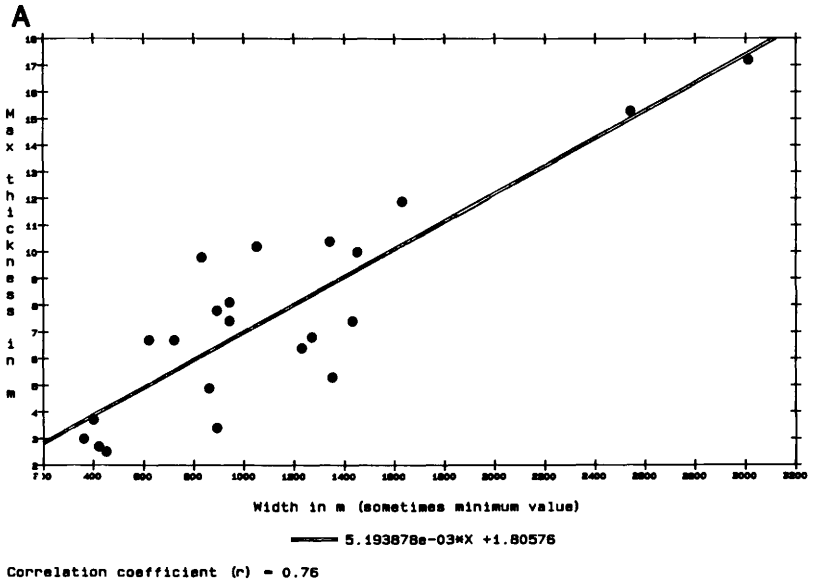

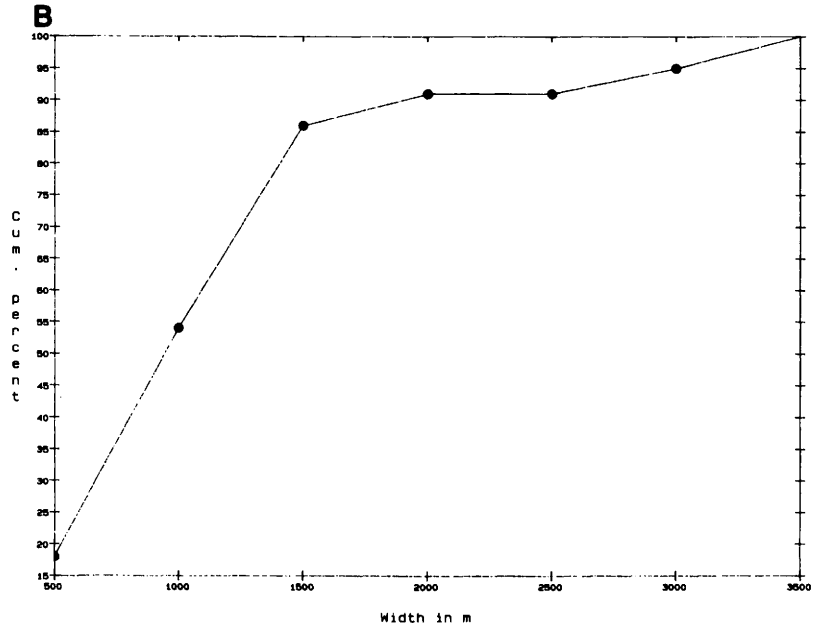

Fig. 19. (**A**) Relationship between width and thickness in building block MS, Ridge Route Formation. (**B**) Cumulative curve for the width of building block MS, Ridge Basin.

In the Ridge Basin, the geometry of the *mudstones* of building block MMC could only be observed in steep, cliff-like exposures where vegetation was scarce (e.g. Fig. 7). Since the lateral extent of most of these cliff-exposures usually was too small to observe both ends of the MMC mudstones, it was not possible to collect a statistically meaningful dataset on their geometries. However, some minimum values can be given. Regardless of thickness, *no* MMC mudstones had lateral extents of *less than 325 m*. Table 2 gives the results from the few reliable measurements in which both ends of building block MMC mudstones could be seen.

The data in Table 2 show no obvious correlation between thickness and lateral extent. It should be noted, however, that the thinnest mudstone zones have been subjected to erosion, thus making their true (unbroken) lateral extents smaller than indicated above (Fig. 11).

The lateral extents of some of the carbonate-cemented sandstones which make up the remainder of building block MMC were also recorded (72 measurements). In about 70% of the cases, these occurred as concretions no more than 5 m wide. In the cases where they formed continuous beds, their lateral extent was 10–1150 m, the most extensive ones being associated with the cabonate-cemented layers at the top of CDF units. Again, no obvious correlation was found between thickness and lateral extent of these beds.

Table 2. *Thickness and lateral extent of MMC mudstones*

Thickness	Lateral extent
Marple Canyon Member (lateral extent probably equal to width)	
1. 0.7 m	920 m
2. 1.15 m	770 m
Apple Canyon Member (lateral extent probably equal to length)	
3. 0.3 m	1645 m
4. 1.5 m	2270 m
5. 0.7 m	560 m
6. 0.4 m	780 m

Building block D. The mudstones of building block D form prominent zones of fine-grained material both in the Tilje and Ridge Route Formations (Figs 8 and 14). These fine-grained sequences probably represent the most distal deposits in the fan-deltaic system (prodelta), and are associated with transgressive events. A notable difference between the building block D developments in the two study objects is the character of the infrequent sharp-based sandbeds. The storm-generated sandbeds of the Tilje Formation are finer grained than those in the Ridge Route Formation, which frequently have medium-grained basal parts. In the Ridge Basin, the sandbeds occur as lenses or centimetre to decimetre thick normally graded to ungraded beds displaying load casts, sole marks, convolute lamination and massive bedding. The bases of the sandbeds may be strewn with mudstone intraclasts. These beds are thought to represent delta-front turbidites (Smith 1982*a*, *b*; Wood & Osborne 1982; Wood & Link 1987). Building block D also has more variable thicknesses in the

Ridge Basin, ranging from 1 m to several hundreds of metres. The small-scale parallel lamination in these mudrocks has been referred to as varve-like (e.g. Smith 1982*b*). Link & Osborne (1982), Smith (1982*a, b*), Smale (1978) and Wood & Osborne (1982) interpreted the sediments corresponding to building block D as lacustrine to brackish-water deposits which accumulated in moderately deep to deep water. This is in keeping with the prodelta interpretation given above.

The field studies indicated that building block D formed sheet-like intervals with very high W/T and L/T ratios. In fact, it was not possible to obtain a single complete (end-to-end) measurement of any bed belonging to this building block. This was due to the fact that beds of building block D had a lateral extent which surpassed the continuity of the exposures. However, by lateral tracing and correlations (Figs 8 and 9), a minimum horizontal extent of 3.3 km was recorded both in coast-normal and coast-parallel sections. In most cases, however, building block D appeared to have an almost basinwide extent, being present from the landward pinchout to the opposite basin margin in coast-normal sections (Fig. 8), and along large portions of the subaqueous parts of the basin in coast-parallel sections (Fig. 9). The widespread nature of these mudstones implies that they form important barriers to fluid flow in fan-delta-front reservoir sequences (see below).

Modelling of the fan-deltaic building blocks in the Tilje Formation

The quantitative sedimentological data, derived from the Ridge Route Formation, were used to calibrate the Tilje reservoir model. This was done by using conversion factors to transform the outcrop data to a format adjusted to the depositional conditions of the Tilje Formation. The conversion factors were arrived at by quantifying and comparing the influence of factors believed to control the sedimentary geometries in the two fan-deltaic settings. A representation of the calibrated geological model is illustrated in Fig. 20. Of the five wells shown here, V is the most proximal and Z the most distal. Details of this model and its implications for reservoir management will be discussed below.

The large-scale composite mouth-bar bodies of building block CDF occur in three zones (most of zone A, middle to upper parts of zone B, most of zone D). By combining the outcrop dimensions of this building block with its thickness and correlatability in the Tilje reservoir, W/T and L/T ratios ranging from 350:1 to 500:1 were calculated. Reservoir modellings incorporating these quantitative data predict that the lateral extent of the composite mouth-bar bodies is formidable. In reservoir zones A and B (Fig. 20), the CDF units were found to have lateral extents larger than 12 km, thus forming complex sand-dominated intervals with lateral dimensions mostly exceeding that of the hydrocarbon-trapping structure. This information is of considerable importance for field development planning, since it implies that sandstones with reservoir potential can be expected to occur in all as yet unexplored regions of fields like the one in Fig. 20.

Building block D occurs as sheet-like mudstones in the Ridge Route Formation and seems to be traceable over most of the basin. In the Tilje reservoir shown in Fig. 20, three zones containing this building block have been identified. By combining the converted outcrop dimensions with facies and correlatability observations from the wells, it was apparent that the lateral extent of the D mudstones by far surpassed the average well spacing. Hence, the three zones containing building block D could with

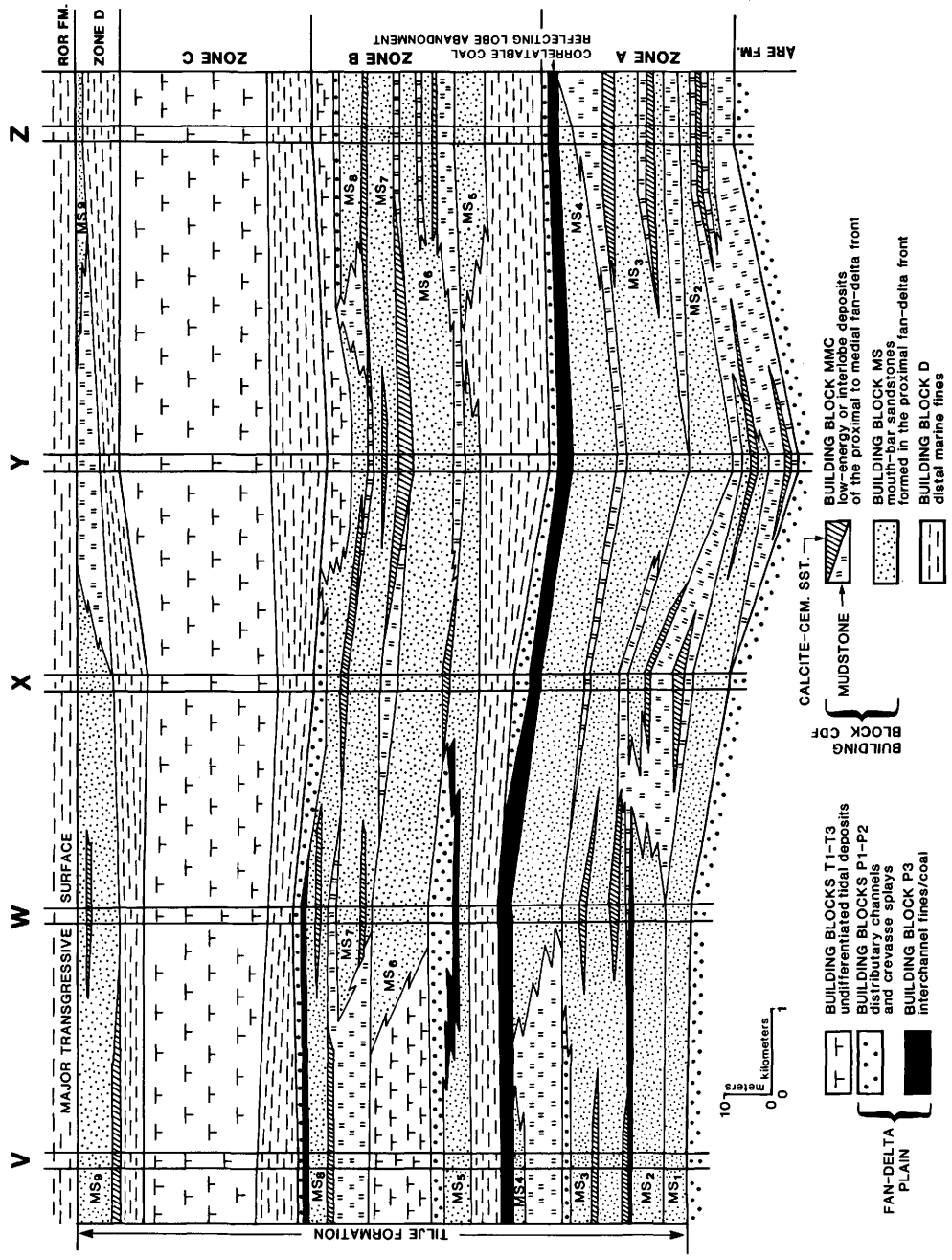

Fig. 20. Generalized reservoir-geological model of the Tilje Formation in an area where the formation is dominated by fan-deltaic sediments. The model is based on a combination of well data and the quantified geological data collected in the Ridge Basin, and illustrates the geometrical relationships of the four building blocks discussed in this paper. The scale bar is valid only for the inter-well areas.

confidence be correlated between wells in the reservoir section shown in Fig. 20. These mudstone-dominated units thus represent major flow-barriers which segment the Tilje Formation into three zones with no primary reservoir communication. This conclusion has several important implications for production planning. For instance, production wells need to be perforated in all three zones for optimal access to the hydrocarbons in the Tilje reservoir. Moreover, the successful performance of producer–injector well pairs demands that the two wells are located in the same CDF interval(s). Failure to do so would mean that the injected gases or fluids would be trapped in a reservoir compartment which was separated from the producing well by a building block D flow-barrier.

The large areal distribution of building blocks CDF and D reflects gigascale (Fig. 5) aspects of the Tilje reservoir architecture. Heterogeneity related to smaller-scale alternations between tight zones (building block MMC) and permeable zones (building block MS) is the main feature at the megascale. In Fig. 20, eight different generations of mouth-bar sandbodies (MS_1–MS_8) are illustrated. The lateral extent of these mouth-bars and their intervening fines have been derived from a calibrated version of the outcrop-derived geometry datasets presented above and in Figs 18 and 19. For the MS sandbodies, W/T and L/T ratios between 220 and 525 have been used in the modelling, thus creating sandbodies with variable but generally large lateral extents (2–8 km). It should be noted that the apparently higher lateral continuities of some of the MS sandbodies in Fig. 20 are due to amalgamation of adjacent mouth-bars. Due to the postulated low ratio of the MMC/CDF lateral extents (above), communication between the MS units is predicted to be moderate to good. This is substantiated by the fact that in the Tilje Formation, the volumetric ratio between building blocks MS and MMC is approximately 6:1. However, in distal areas (wells Y and Z, Fig. 20) and close to individual mouth-bar pinchouts, the frequency of building block MMC increases, making communication between neighbouring MS-units more problematic. The presumably good communication between MS-bodies means that even with a well spacing of one or a few kilometres, the recovery percentage is expected to be acceptable.

Conclusions

(1) The Tilje Formation displays several scales of heterogeneity. Large-scale heterogeneities, which are addressed in this study, can be quantified by subdividing the reservoir into an optimal number of large-scale flow-units or building blocks. In this paper, four building blocks are discussed. These were deposited in a fluvial-dominated fan-delta-front setting.

(2) In the fan-delta-front deposits, the main level of heterogeneity is associated with alternations between composite mouth-bar units (building block CDF) and prodelta fines (building block D). The considerable lateral extent of building block D segments the Tilje reservoir into zones with limited communication.

(3) Within the CDF units, the most significant heterogeneity is the alternations between mouth-bar sandbodies (building block MS) and intra mouth-bar fines and carbonate-cemented sandstones (building block MMC). Building block MS usually constitutes 70–80% of the CDF units. This, together with the rather limited lateral extents postulated for the MMC intervals, indicates that communication within the CDF units is good.

(4) The Ridge Route Formation (Ridge Basin, USA) contains fluvial-dominated fan-delta-front sediments similar to those of the Tilje Formation. Geometry studies in the Ridge Basin indicate that both the CDF and MS bodies are sheet-like, with high W/T and L/T ratios. The thicker CDF bodies tend to have lateral extents of 4–10 km, whereas the MS bodies generally pinch out within a couple of kilometres. No relationship between thickness and lateral extent could be established for the mudstones and carbonate-cemented zones of building block MMC. The average lateral extent of the MMC mudstones was slightly less than a kilometre, whereas the carbonate-cemented sandstones mostly occur as concentrations. Where they form more continuous beds, their lateral extents were 10–1150 m, the most extensive ones being associated with siderite-layers at the top of CDF units. Building block D form sheet-like deposits of very high W/T and L/T ratios. A minimum lateral extent of several kilometres was recorded.

Thanks are due to K. Busby-Spera (UC Santa Barbara) and A. Ryseth, Å. Scheie and R. Gundesø (Norsk Hydro) for guiding and assistance during the fieldwork in the Ridge Basin. Constructive reviews by T. Elliott and M. Ashton are greatly appreciated.

Appendix. *Overview of the facies types in the Tilje Formation*

Code	Main characteristics	Depositional/diagenetic processes
M1	Centimetre-thick isolated beds of pebbly sandstone, poorly sorted, extraformational and intraformational clasts, some large coal fragments, crude normal grading, no imbrication or stratification, contains 'floating' well-rounded clasts, only present at the base of vertically aggrading or coarsening-up marine sequences (notably at base of Tilje 1).	Transgressive lag-deposit formed as surf zone processes rework fluvial and marginal marine sediments during a relative rise in sea-level.
M2	Centimetre- to decimetre-thick amalgamated beds, medium- to coarse-grained sandstone, parallel laminated or massive, pronounced normal grading, often thin silt partings between beds, moderate amounts of kaolinite cement, moderate sorting, sharp erosive bases with little relief, lower parts of beds have the best permeabilities due to normal grading, mainly occur near the base of the Tilje Formation.	Density underflows deposited close to the shoreline during the deepening phase of transgressive pulses. The underflows consist of channel-derived material. They formed as sediment-laden river outflow was transformed into density flows, or by the redeposition of mouthbar sands during floods/storms. Moderate to high delta-front slopes are implicated. The catastrophic mode of deposition prevented significant reworking by basinal processes, creating a clay-rich grain framework.
M3	Centimetre- to decimetre-thick isolated or amalgamated beds of pebbly sandstone, bimodal, normally graded, erosive bases, gradational tops, massive, sub-angular fragments, mostly extraformational clasts, grain-supported, variable amounts of kaolinite cement, occur intermixed with facies M1 near the base of the Tilje Formation, also present near top of Tilje 3.	Coarser versions of the facies M2 density underflows (probably deposited from more powerful currents).
M4	Parallel-laminated very fine-grained to silty sandstone, 5–10 cm thick beds, occur between and on top of beds of facies M2 and M3, ungraded, non-erosive bases, rare.	Lower flow-regime deposits formed as the current energy in the underflows (facies M2 and M3) decreased. Rarely preserved due to amalgamation of underflows.
M5	Bioturbated beds of mudstone and very fine-grained sandstone, often sideritic, beds 1–7 cm thick, irregular upper and lower boundaries, separate sandy beds of facies association M, occur in all parts of Tilje (but most commonly in lower parts of shallowing-up sequences).	Fallout of suspended load during quiet periods in the basin, followed by colonization of burrowers.

M6	Massive to faintly laminated fine-grained sandstone, dish structures, well sorted, some bioturbation, no grading, beds are usually stacked in units several metres thick, muddy material interspersed as sand-sized grains, present in lower parts of shallowing-upwards sequences.	The facies characteristics suggest some kind of sorting *prior to* emplacement in moderately deep water. These beds probably represent redeposited shoreline/mouthbar sands. They probably accumulated in a more distal position relative to the superficially similar beds of facies M2/M3. Strong component of vertical aggradation.
M7	Similar to facies M6 except that these beds are dominated by medium-grained sandstone, present above M5 beds in shallowing-upwards sequences, water-escape structures, most common in lower parts of Tilje.	As facies M6, but deposited in a slightly more proximal position.
M8	Rippled to massive fine-grained sandstone with thin clay-drapes on laminae, occasional evidence for variable cross-bed migration directions, interbedded with mudstones of facies M5, often bioturbated, occur in metre-thick sequences, individual beds often 10–30 cm thick, diffuse bed boundaries, contain small sideritic clay-flakes, massive and rippled intervals alternate on decimetre- to centimetre-scale, common in all of the Tilje Formation, moderate sorting.	Shallow-marine sandstones, deposited in a relatively distal position with respect to the distributary mouth (or in periods with limited coarse clastic influx), moderate to low current energies, changes in ripple migration-directions due to mixed influences of basinal currents (shoaling waves, longshore drift, tides) and offshore-directed discharge, probably accumulated in 'sheltered' parts of the upper shoreface (lack of high-energy indicators).
M9	Sand- and siltstones of facies association M that are strongly cemented by calcium carbonate; 5 cm to 2.2 m thick zones that tend to occur in association with storm-beds or sediments formed at top of individual marine bar-units.	A 'diagenetic facies' which primarily have formed by local (re)-precipitation of calcitic material (on abandonment surfaces and in zones enriched in shell debris). The higher frequency of such beds is due to lower subsidence rate (more time available for calcite to precipitate).
M10	Centimetre-thick beds of mudstone, usually sideritizised, sharp bases, gradational or sharp tops, occur between sandbeds of facies association M, no bioturbation, fragmentation common (cf, facies M15).	Fallout of fine-grained material during low-energy periods in the basin. Lack of bioturbation may be due to freshwater dilution. The shaly beds probably represent drapes generated between episodes of wave and tide agitation.
M11	Similar in appearance to facies M8, except for the coarser grain size (medium-grained sand), the slightly lower percentage of clay-drapes, and the occasional presence of microtrough-lamination, usually present above M8 in CU-sequences, may also alternate with M8.	This facies was probably deposited in a transitional zone between the 'sheltered' to relatively distal marine M8 beds and the high-energy proximal delta-front deposits like facies M12, M13 and M14. As such, it may reflect reworking of fluvially derived sands by basinal currents in a medial part of the mouthbar system.

Appendix (*continued*)

Code	Main characteristics	Depositional/diagenetic processes
M12	Well-sorted parallel laminated sandstone, medium-grained, occur in thin beds or metre-thick intervals high up in CU-sequences, relatively rare, ungraded, sharp bases/tops, very little clayey matrix, moderately high degree of quartz cementation.	Wave-reworked deposits formed in shallow water, most commonly at or near tops of mouthbar units. May also represent foreshore deposits in areas adjacent to distributary mouths.
M13	Mostly massive medium- to coarse-grained sandstone, some diffuse parallel lamination and low-angle cross-bedding, moderately sorted, beds between 0.1–0.8 m thick, usually stacked in decimetre- to metre-thick intervals, interbedded with facies M11, M4, M8, M12 and M14, most common in Tilje 2, sharp to gradational bed boundaries, contains some well-rounded small mudclasts and a few coal fragments, individual beds are usually normal graded (pulses), varying degree of kaolinite cementation.	The textural and structural characteristics of this facies suggest mixed fluvial and basinal influences. This, together with their position in the aggrading sequences, suggests that these sandbeds were deposited in the mouthbar parts of the delta-front system. As the fluvial discharge entered the standing water, size-segregation and sorting took place due to flow-expansion and some influences from basinal currents. The material present in facies M13 (and M14) represents the coarsest fraction of this discharge, and can be termed proximal fluvial-dominated mouthbar deposits.
M14	Cross-bedded (low to moderate angle) or parallel laminated sandstone, coarse to medium grained mostly grades into M13, moderately sorted, 0.2–0.7 m thick intervals, sets/laminae are normally graded, some coalbits and clayclasts, most common in Tilje 2, clay-poor framework except for some kaolinite-rich laminae.	Proximal mouthbar deposits, see facies M13. In the generation of this facies, fluvial processes apparently dominated over basinal processes. The centimetre-thick sets/laminae represent incremental settling of the coarsest parts of discharge-pulses which entered the basin. Note that the sets/laminae do not represent density-underflows (facies M2 and M3), as the percentage of primary clay is much lower in this facies. The cross-bedding suggests episodes of bedform migration along the bartop (shoaling waves or fluvial progradation).
M15	Massive ungraded beds with extremely poor sorting, grains range from medium sand to conglomeratic clasts 5 cm in diameter, strong dominance of intraclasts (siderite and grey mudstone), beds from 3–25 cm thick, angular to well-rounded clasts, some beds are obviously disrupted mudlayers, occur interbedded with facies M13/M14 in upper parts of shallowing upwards sequences.	In-situ fragmentation of mudlayers by high-energy basinal processes (e.g. storms), *and/or* (short) transportation of the coarsest fraction stirred up by storm surges or flood-pulses on inner parts of mouthbars. The mixture of clay clasts and sandy matrix causes large variations in mini-permeameter permeability.

M16	Similar to those of M13/M14, except that this facies is dominated by fine- to medium-grained sand. Parallel lamination and low-angle cross-bedding are the dominant structures.	Fluvial-dominated outer mouthbar deposits, subjected to quite continuous influx of the finer-grained fractions of the fluvial discharge. Limited degree of basinal reworking.
M17	Wavy to lenticular bedded intervals of sand–mud–silt, synaeresis cracks common at sand/mud boundaries, combined ripples common, moderate degree of bioturbation (small burrows), the sand is mainly very fine grained, loading common, dark grey mud, occurs in decimetre- to metre-thick intervals interbedded with the other M facies (vertical flow barriers).	This facies probably formed at the delta-front when fluvial influx to the basin was limited. It represents reworking of material by weak wave-generated currents. Low rate of sedimentation (abandonment phase). Facies M17 also includes distal delta-front/mouthbar deposits.
P1	Pedo/bioturbated very fine-grained sand–silt–mud, the root-traces consist of black carbonaceous material, irregular upper and lower boundaries, occurs in intervals 0.3–1.5 m thick, usually present at the top of shallowing-upwards sequences.	Deposits formed in shallow bays/lakes on the lower delta-plain.
P2	Pedoturbated very fine-grained sand–silt, larger roots than in facies P1, some horizons/glaebules very rich in kaolinite, gradually overlies facies P1, thin beds, dark colour due to high organic content, no preserved laminations.	Paleosol profiles formed on poorly drained floodplain/delta plain.
P3	Coal/coaly shale, occur in beds less than a metre thick, present at top of shallowing-upwards sequences, associated with pyrite.	Swamp deposits on the lower delta-plain, usually formed at the top of infilled bays.
P4	Coarse-grained sandstone, moderately sorted and rounded, massive/parallel laminated/trough cross-bedded, erosive bases, sharp tops with limited FU, no bioturbation, occurs in bedsets 1.5–3 m thick, interbedded with other P-facies or directly cutting into M facies, contain clay rip-up clasts and coal debris, individual beds are often crudely normal graded, passes up into facies P5.	Active phase infill sequences formed in distal parts of deltaic distributary channels, only high-energy deposits preserved, some of the bedsets may have originated as subaqueous continuations of subaerial channels (inner mouth-bar deposits).
P5	Dominantly fine-grained sandstone with mudstone partings/interbeds, coal fragments, root-traces common near top, sharply overlies facies P4 with a non-erosive base, fining upwards, convolute lamination, current ripples, parallel lamination, rich in mica, moderate sorting, very little bioturbation, beds 0.2–1.5 m thick.	Partly active/passive phase infill sequences formed distally in distributary channels, mixture of bedload and suspended load deposits, indicates abandonment of channels.

Appendix (*continued*)

Code	Main characteristics	Depositional/diagenetic processes
P6	Wavy bedded fine-grained sand–silt–mud, loading and minor erosion common along sand/mud boundaries, current/wave ripples very common, low degree of bioturbation, micaceous, muddy material dark grey or brownish (siderite), not common, occurs in thin intervals interbedded with the other P facies.	This facies probably formed in interdistributary bays characterized by intermediate salinities, influence from both waves and unidirectional currents.
P7	Medium- to coarse-grained sandstone, poorly sorted, beds 0.3–1.2 m thick, normally graded, rooted tops, clay rip-up clasts/coal fragments, frequently calcite-cemented (P7A), unburrowed, massive/high angle crossbedding, current ripples in upper part, erosive base, gradational top, interbedded with the other P facies.	Crevasse splay deposits formed on the lower delta-plain, commonly associated with the distributary channels (facies P4/P5).
P8	Grey mudstone with lenticular bedding (lenses of fine- to very fine-grained sand), the lenses mostly exhibit wave ripple formsets, some current ripples, low degree of bioturbation (small burrows), some siderite beds, many mudstone beds are normal graded (silt to clay), occurs in 5–20 m thick interval at base of Tilje 3, overlies P or M facies, gradually coarsens up into T or M facies.	Settling of suspended load in the outer part of a wave-influenced bay/estuary. Above fairweather wave base. The occurrence of this facies in intervals correlatable in all wells suggests a large bay/estuarine system. This facies represents a barrier to flow in the reservoir.
P9	Centimetre-thick beds of fine- to medium-grained sand, interbedded with P3 (coaly shale), coal fragments, clay drapes/flasers, current ripples, erosive bases, normal grading, no bioturbation.	Levee-deposits/distal crevasse splays, formed subaerially on the floodplain.
P10	Extensively kaolinite-cemented coarse- to very coarse-grained sandstone, some pebbly intervals, very poor sorting, angular grains, massive/cross-bedded/parallel laminated, coal fragments, erosive bases, individual beds are often 0.8–1.2 m thick and show fining upwards, most common at the base of Tilje 1 (transition to Åre Formation).	Proximal distributary channel deposits (compare with facies P4), high-energy processes strongly dominant during infilling. The high content of kaolinite is relatable to proximality (leaching of unstable feldspar grains, primary kaolinite as matrix). Genetically, this facies belongs to the Åre Formation.
D1	Strongly bioturbated silt/very fine-grained sand, marine burrows, siderite cementation common, traces of lamination occasionally	Lower shoreface deposits, low rate of sediment input. Distal parts of stormbeds (suspension fallout).

	visible, alternates with facies D2/D5, usually present near the base of facies association D intervals.	
D2	Very fine to fine-grained sandstones and mudstone, wavy bedding ('wave-knit lamination'), hummocky cross-stratification, flaser bedding, some marine bioturbation, escape burrows, interbedded with other D-facies, centimetre-thick normal graded beds, HCS to wave ripples from base up in beds, sharp bed boundaries, common in base of Tilje 2 and 3.	Distal stormbeds deposited in the lower shoreface.
D3	Moderately sorted beds of fine- to coarse-grained sand, hummocky cross-stratification, pebbles lining laminabases, escape burrows, normal grading, sharp bed boundaries, 5–15 cm thick beds, rare.	Proximal parts of stormbeds, probably reflecting rare and exceptionally large stormevents affecting the lower shoreface.
D4	Strongly bioturbated fine- to very fine-grained sand, marine burrows, high faunal diversity, remnants of lamination, numerous clay flasers/interbeds, occur in decimetre to metre-thick intervals high up in facies association D, gradual bed boundaries.	This facies probably originated as stormbeds in the upper/lower shoreface, but was subsequently reworked by organisms. Moderate to low rate of sedimentation implied.
D5	Dark grey mudstone, normal graded laminae (silt to clay), some lenses of very fine-grained sand (wave ripple formsets), moderate degree of bioturbation, marine deepwater burrows (e.g. *Chondrites*), present mainly at the base of Tilje 2 and 3, may be the dominant facies in intervals 2–15 m thick.	Fallout of suspended load in the offshore transition zone (below mean fairweather wave base), deposited after transgressive pulses, forms barriers in the reservoir.
T1	Subdivisible into three parts: lenticular bedded mudstone (T1A), wavy bedded mud/sandstone (T1B), and flaser bedded fine-grained sandstone (T1C). Occurs in thick intervals (3–30 m) in Tilje 3 and Tilje 2 (−7/3 only), total sand content about 50%, very heterolithic (especially in the vertical direction where individual beds of varying lithology are 1–35 cm thick), usually well sorted, clay drapes common in the sand (some doubledrapes), current ripples show opposed foreset directions, wave ripples and mixed ripples also common, some synaeresis cracks, low degree of bioturbation, sharp bed boundaries, interbedded with other T facies.	The three subfacies reflect mostly suspension fallout in distal (?central) parts of a *tidal* estuary. The widespread lateral (several wells) and vertical occurrence suggests that the estuarine systems covered large areas. The transition from 'fluvial mouthbar' to estuarine sedimentation upwards in the Tilje Formation may indicate gradually diminishing fluvial influence (as well as a possible change in basin configuration). The wave influence in parts of facies T1 suggests deposition on outer parts of estuaries (compare with facies T3). Sand was mainly supplied from channels entering the estuary (see facies T4), and then reworked by back-and-forth washing tidal currents/waves. The alternations T1A/B/C may be due to lateral migration.

Appendix (*continued*)

Code	Main characteristics	Depositional/diagenetic processes
T2	Medium- to fine-grained sandstone with numerous clay drapes/flasers, carbonaceous debris, herringbone cross-beds, opposed current ripples wavy/clay-draped foresets, mudclasts, 0.15–1.25 m thick beds, interbedded with facies T1/T5, most common in Tilje 3, well sorted, no bioturbation, sharp ungraded beds (sometimes amalgamated).	Tidal sandflat, probably closely associated with tidal channels (facies T5). Similar in many aspects to facies T1C, but the tidal sandflats of facies T2 probably reflect infilling of the estuaries. This facies probably has a high lateral extent.
T3	Well-sorted fine- to very fine-grained sandstone, some clay matrix, abundant clay drapes (several doubledrapes), herringbone cross-beds, occasional wave ripples and clay rip-up clasts, reactivation surfaces, occurs in decimetre/metre-thick intervals in Tilje 3, forms CU-sequences, individual beds are commonly normal graded, rare marine burrows, some subhorizontally laminated intervals, contain some calcite cemented zones (termed facies T3A) and some centimetre-thick mudbeds (facies T3B).	Tidal-dominated shallow marine deposits, limited influence by fluvial/wave processes. The basic units (normal graded beds) reflect fluctuating sand supply, possibly on the distal parts of mouthbars. Evidence for strong tidal activity can be found in the reactivation surfaces, the regular mud-drapes, and the herringbone crossbedding). The occasional presence of subhorizontally laminated intervals and wave ripples indicates periods of wave reworking. Facies T3 may represent sandridges or shoals associated with estuaries, or tide-dominated delta-front deposits (note CU-tendency).
T4	As facies T3, but coarser grain size (mostly medium sand) and less clayey matrix/muddrapes. Usually overlies facies T3 in CU sequences. Massive beds occur, and the normal grading tends to be more pronounced.	Tidal-dominated mouthbars/estuarine deposits. The coarser grain size, smaller amount of clay and more pronounced normal grading suggest a significant fluvial influence and a more proximal depositional setting than facies T3.
T5	Medium- to coarse-grained sandstone, moderately sorted, large assemblages of mudclasts common near base, some clay flasers, the bedsets show fining upwards, erosive base, gradual top, interbedded with facies T1/T2, only found in Tilje 3, bedsets 1.2–2 m thick, massive/parallel laminated/trough crossbedded, no bioturbation.	Channel deposits cutting the tidal flats, probably represent tidal creeks, dominance of high-energy flow made this T facies less heterogeneous than the others.

M, 'mouthbar' sediments (proximal delta-front and shoreline deposits); P, delta-plain sediments (including bay deposits); D, distal delta-front/marine sediments; T, tidal-influenced sediments (muddy, sandy, and mixed tidal flat/shallow subtidal).

References

BREKKE, H. & RIIS, F. 1987. Tectonics and basin evolution of the Norwegian shelf between 62 degrees N and 72 degrees N. *Norsk Geologisk Tidsskrift*, **67**, 295–322.

BUKOVICS, C., SHAW, N. D., CARTIER, E. G. & ZIEGLER, P. 1984. Structure and development of the Mid-Norway continental shelf. *In*: SPENCER, A. M. *et al.* (eds) *Petroleum Geology of the North European margin*. Graham & Trotman, London, 405–425.

CROWELL, J. C. 1975. The San Gabriel fault and Ridge Basin. *In*: CROWELL, J. C. (ed.) *San Andreas fault in Southern California*. California Division of Mines and Geology Special Report, **118**, 208–233.

—— & LINK, M. H. (eds) 1982. *Geologic history of Ridge Basin, Southern California*. Pacific Section, Society of Economic Paleontologists and Mineralogists.

GALLOWAY, W. E. 1986. Reservoir facies architecture of microtidal barrier systems. *American Association of Petroleum Geologists Bulletin*, **70**, 787–808.

GJELBERG, J., DREYER, T., HØIE, A., TJELLAND, T. & LILLENG, T. 1987. Late Triassic to Mid-Jurassic sandbody development on the Barents and Mid-Norwegian shelf. *In*: BROOKS, J. & GLENNIE, K. (eds) *Petroleum Geology of North West Europe*. Graham & Trotman, London, 1105–1129.

GUNDESØ, R. & EGELAND, O. 1990. SESIMIRA—a new geological tool for 3D modelling of heterogeneous reservoirs. *In*: BULLER, A. T. *et al. North Sea Oil and Gas Reservoirs, Vol. 2*. Graham & Trotman, London, 363–372.

HALDORSEN, H. H. 1986. Simulator parameter assignment and the problem of scale in reservoir engineering. *In*: LAKE, L. W. & CARROLL, H. B. jr. (eds) *Reservoir Characterization*. Academic Press, London, 293–340.

HOLLYWOOD, J. M. & OSBORNE, R. H. 1982. Sedimentology of the Frenchman Flat Sandstone Member of the Ridge Route Formation, Ridge Basin, Southern California. *In*: CROWELL, J. C. & LINK, M. H. (eds) *Geologic history of the Ridge Basin, Southern California*. Pacific Section, Society of Economic Paleontologists and Mineralogists, 115–126.

LARSEN, H. C. 1984. Geology of the East Greenland shelf. *In*: SPENCER, A. M. *et al.* (eds) *Petroleum Geology of the North European margin*. Graham & Trotman, London, 329–339.

LASSETER, T. J., WAGGONER, J. R. & LAKE, L. W. 1986. Reservoir heterogeneities and their influence on ultimate recovery. *In*: LAKE, L. W. & CARROLL, H. B. jr. (eds) *Reservoir Characterization*. Academic Press, London, 293–340.

LINK, M. H. & OSBORNE, R. H. 1982. Sedimentary facies of Ridge Basin, Southern California. *In*: CROWELL, J. C. & LINK, M. H. (eds) *Geologic history of the Ridge Basin, Southern California*. Pacific Section, Society of Economic Paleontologists and Mineralogists, 63–78.

MOLENAAR, N., VAN DE BILT, G. P., VAN DEN HOEK OSTENDE, E. R. & NIO, S. D. 1988. Early diagenetic alteration of shallow-marine mixed sandstones: an example from the Lower Eocene Roda Sandstone Member, Tremp-Graus Basin, Spain. *Sedimentary Geology*, **55**, 295–318.

NEMEC, W. 1990. Aspects of sediment movement on steep delta slopes. *In*: COLELLA, A. & PRIOR, D. B. (eds) Coarse-grained deltas, International Association of Sedimentologists, Special Publication. **10**, 29–73.

SMALE, T. G. 1978. *Soft-sediment deformation in southern Ridge Basin, central Transverse Ranges, California*. Masters thesis, Univ. California at Santa Barbara.

SMITH, P. R. 1982*a*. Paleolimnology of Miocene lakes in Ridge Basin, Southern California. *In*: CROWELL, J. C. & LINK, M. H. (eds) *Geologic history of the Ridge Basin, Southern California*. Pacific Section, Society of Economic Paleontologists and Mineralogists, 259–264.

—— 1982*b*. Sedimentology and diagenesis of the Miocene Peace Valley Formation, Ridge Basin, Southern California. *In*: CROWELL, J. C. & LINK, M. H. (eds) *Geologic history of the Ridge Basin, Southern California*. Pacific Section, Society of Economic Paleontologists and Mineralogists, 151–158.

——, HARPER, A. S. & WOOD, M. F. 1982. Nonmarine trace fossils in the Mio-Pliocene Ridge Basin Group, Southern California. *In*: CROWELL, J. C. & LINK, M. H. (eds) *Geologic history of the Ridge Basin, Southern California*. Pacific Section, Society of Economic Paleontologists and Mineralogists, 253–258.

WADSLEY, A. W., ERLANDSEN, S. & GOEMANS, H. W. 1990. HEX, a tool for integrated fluvial architecture modelling and numerical simulation of recovery processes. *In*: BULLER, A. T. *et al.* (eds) *North Sea Oil and Gas Reservoirs, Vol. 2*. Graham & Trotman, London, 387–398.

WALDERHAUG, O., BJØRKUM, P. A. & NORDGÅRD BOLÅS, H. M. 1989. Correlation of calcite-cemented layers in shallow marine sandstones. *In*: COLLINSON, J. D. (ed.) *Correlation in hydrocarbon exploration*. Norwegian Petroleum Society Special Publication, Graham & Trotman, London, 367–376.

WOOD, M. F. & LINK, M. H. 1987. The nonmarine late Miocene to Pliocene Ridge Route Formation and its depositional framework. *In*: LINK, M. H. (ed.) *Sedimentary facies, tectonic relations, and hydrocarbon significance in Ridge Basin, California*. Pacific Section, Society of Economic Paleontologists and Mineralogists, Book **51**, 5–20.

—— & OSBORNE, R. H. 1982. Sedimentology of the Mio-Pliocene Apple Canyon Sandstone Member, Ridge Basin, Southern California. *In*: CROWELL, J. C. & LINK, M. H. (eds) *Geologic history of the Ridge Basin, Southern California*. Pacific Section, Society of Economic Paleontologists and Mineralogists, 135–142.

WRIGHT, L. D. 1977. Sediment transport and deposition at river mouths: a synthesis. *Geological Society of America Bulletin*, **88**, 857–868.

From ASHTON, M. (ed.), 1993, *Advances in Reservoir Geology*,
Geological Society Special Publication No. 69, pp. 175–194.

A discussion on the use of analogues for reservoir geology

JAN ALEXANDER

Department of Geology, University of Wales College of Cardiff, PO Box 914, Cardiff CF1 3YE, UK

Abstract: Whilst it may be easy to describe and quantify a sedimentary succession from outcrop or core, using these data to predict sedimentary facies, diagentic features and fracture distribution in unsampled areas still requires considerable intuition. Frequently, at the current state of geological knowledge, reservoir datasets must be supplemented by consideration of analogues. The aim of this paper is to sound caution on the indiscriminate use of analogues in reservoir geology.

Analogues used in reservoir geology fall into three main categories: comparisons with modern depositional processes, experimental simulations, and rock record analogues. All analogues used for reservoir geology suffer from limitations due to the physical and temporal scales at which the comparisons are made. Difficulty in selecting appropriate analogues results from the amount of interpretation of the nature of the reservoir required before an analogue may be selected, the large number of degrees of freedom in the processes of formation of reservoir rocks, and the limited numbers of well-documented analogues which are easily available.

Geology relies heavily on analogues and comparisons for the simple reason that the development of rocks and structures can rarely be observed directly. Many early geological interpretations, which are now taken for granted, were based on comparisons and analogies that have since been forgotten or are ignored. Analogues should be used to construct models which are then rigorously tested using a scientific approach. The acquisition of new data should result in refinement, modification or rejection of the model. Unless this approach has been taken, a model should be treated with scepticism and no model should be 'set in tablets of stone'.

The primary aim of geological reservoir models is to estimate the amount of recoverable hydrocarbons by determining the volume, character and distribution of the reservoir rocks. In achieving this, attempts are made to identify and quantify those features of the reservoir which will affect hydrocarbon production. Sandstone reservoirs rarely have constant thickness, shape or internal characteristics over the area of a field. As a consequence, it is essential to estimate reservoir and constituent facies architecture and geometry in order to optimize volume estimations and to assess reservoir connectivity and flow path tortuosity. Sandbodies are not homogeneous with respect to porosity and permeability, but contain internal heterogeneities and discontinuities. These internal variations may result from the inherent sediment variability of depositional processes, subsequent localization of diagenetic effects, and deformation during burial. To appreciate the intricacies of fluid flow through sandbodies it is necessary to have an understanding of the scale, density, distribution, geometry and inter-relationships between the various heterogeneities, so that their relative importance to hydrocarbon accumulation, distribution and recov-

ery can be assessed. Well spacing (particularly in offshore developments such as the North Sea) is rarely sufficiently close to evaluate quantitatively these parameters in any given field. Whilst it may be easy to describe and quantify a sedimentary succession from outcrop or core, using these data to predict sedimentary facies, diagenetic features and fracture distribution in unsampled areas still requires considerable intuition.

To evaluate the need for simulations of reservoir behaviour and to produce realistic simulation models, it is necessary to provide quantitative reservoir descriptions, to use these data in the context of the interpretation of the depositional environment and geological history of the basin, and to extrapolate accurately between control data points into areas of the reservoir where there are little or no data available (Haldorsen 1986). Geological reservoir models frequently rely on empirical relationships and analogue studies to enhance the perception of basic geological relationships, to supplement limited datasets and enable stochastic or other modelling methods to be applied. One major limitation on realistic reservoir simulation is the lack of understanding of the relationship between geological features and permeability distribution (K_v and K_h) at different scales. It is often easier to quantify the relationships through examination of the distribution of facies, structure and diagenetic features in analogous outcrop (where they can be evaluated in three dimensions) than in the subsurface.

A reservoir simulation which gives reliable results may not necessarily be geologically correct, as the aim of reservoir simulation models is to estimate recoverable hydrocarbons and production characteristics, and is not to reproduce the geology. However, models which are more geologically realistic and closer to the 'truth' will, in general, give more reliable results. Frequently, at the current state of geological knowledge, reservoir datasets must be supplemented by consideration of analogues. The aim of this paper is to sound caution on the indiscriminate use of analogues in reservoir geology.

Analogues used in reservoir geology fall into three main categories; comparisons with modern depositional processes and environments, experimental simulations, and rock record analogues. The selection of the type of analogue to apply depends on the nature of the particular aspects of a reservoir which need to be explained or quantified. Analogues used for reservoir geology suffer from limitations due to the scale at which the comparisons are made and the comparability of duration and geological time periods. Many of the problems of using analogues are independent of size, while other problems result from application of large-scale analogues to small-scale reservoir features or vice versa; consequently illustrative examples in this paper are drawn from exploration (regional) to sandbody scale. Difficulty in selecting appropriate analogues results from the amount of interpretation of the nature of the reservoir which is required before an analogue may be selected, the large number of degrees of freedom in the processes of formation of reservoir rocks, and the limited numbers of well documented analogues which are easily available.

Types of analogues

Comparisons with modern depositional processes and environments

It is generally agreed that one of the first steps of reservoir characterization is to determine the processes that formed the rock (Geehan *et al.* 1986; Lasseter *et al.*

1986; Walton *et al.* 1986; Weber 1986 and many others). Conceptual models employed to determine the depositional environment of reservoir rocks are largely based on comparisons with analogous depositional environments and deposits (cf. Reading 1986; Reading & Orton 1991 and others). A consequence of this is that depositional analogues are applied, often almost subconsciously, to most reservoirs. In addition to the use of such conceptual facies models, individual modern analogues are frequently used to increase the understanding of the reservoir rocks and the processes operating during their deposition. The consideration of modern processes and their products as analogues for reservoir rocks assumes, sometimes incorrectly, that 'the present is the key to the past'.

Modern depositional analogues, made at a range of scales from lamination type to regional distribution patterns, are often used in a purely illustrative way to enhance the 'feel' of the reservoir geology. Little attempt has been made to provide quantitative data to suport the descriptions, however, such quantitative data are increasingly in demand for construction of theoretical and empirical models of facies distribution to supplement reservoir models.

The main advantages of using modern analogues over rock record ones are the greater ease with which it is possible to examine the deposits, to determine the processes operating during deposition, and to define the controls on those processes. Studies of modern systems allow construction of conceptual facies models and form the basis for many theoretical models. For example, observations on modern rivers and alluvial plains were of major importance to the development of sedimentary simulation models by Bridge & Leeder (1979), Mackey & Bridge (1991) and Willis (1989). Modern methods of data collection combining surface mapping, vibrocoring and ground penetrating radar or shallow seismic surveys (e.g. Gawthorpe *et al.* in press) are generating datasets in a form which may easily be compared with reservoir data.

Laboratory experimental analogues

Scaled laboratory analogues and mathematical or chemical models can provide a geological insight, especially where modern depositional analogues and processes responsible for post-depositional changes are not directly observable. For example, it is difficult to observe directly the sedimentary processes in operation in deep marine environments. The study of turbidites and submarine fan deposits has been greatly enhanced by the use of scaled laboratory experiments and mathematical simulations. Observations of gravity currents generated in a controlled laboratory environment may be used to explain features seen in reservoir sandstones of turbiditic origin.

Additionally models may be generated mathematically from consideration of the mechanics of the depositional system (e.g. Tetzlaff & Harbaugh 1989). However, these require input parameters such as sediment supply rate which are difficult to define for any reservoir rock. The experimental analogues may be used to define the limitations of the depositional analogues or directly to improve the understanding of reservoir rocks.

The major problems inherent in laboratory analogues are that they are simplifications of geological reality and are inevitably based on sweeping assumptions. If the assumptions on which the experiments are based are incorrect, then their use for interpreting reservoir geology must be questioned. The major advantages of experimental analogues is that they may be used to investigate the effects of different controls independently, and may also be used to investigate unobservable processes.

Rock record analogues

Rock record analogues are comparisons made with rocks or structures observed in other places (exposed or subsurface), or with published descriptions which appear to be similar. Direct comparison of reservoir data with a well exposed similar rock units can lead to major advances in the understanding of the reservoir characteristics. In particular, data from outcrop have been used to model facies geometry, size and distribution, in order to give an indication of facies and diagenetic controls on porosity and permeability and therefore model reservoir behaviour. Numerical experiments (simulations) may be applied to the analogue data to test how measured permeability heterogeneity at different scales affect recovery efficiency. This is an important approach as data (permeability, porosity etc.) cannot be collected at the reservoir scale. If reservoir facies geometries and dimensions are being considered, it may be as useful to employ rock record analogues (or analogue databases) for immediate results. However, in this context they are being employed as substitutes for depositional models (and depositional analogue databases) and generally it would be better to understand the controls on the geometries and dimensions by applying theoretical physical models, as these may be more reliable and potentially more accurate than models based on rock record databases.

The emphasis on the use of rock record analogues rather than modern depositional processes or experimental analogues of physical theories relates partly to the familiarity of reservoir geologists with geological literature (using familiar ideas, terminology and means of data presentation) and a preference for comparing rocks with rocks.

Some geological processes cannot be examined directly and, therefore, rock record comparisons may aid understanding. One good illustrative example of this is the interpretation of structural discontinuities in reservoir rocks. For example, in the North Sea Rotliegend sandstones the distribution and character of fractures and diagenetic alteration of reservoir rocks associated with fluid movement through the fractured strata cause major heterogeneities and in some cases reservoir compartmentalization. The scale and distribution of these features are difficult to interpret from subsurface data; however, Edwards *et al.* (1991) have greatly improved their understanding of the reservoir heterogeneities resulting from faulting and fracturing, by examining similar features in the Permo-Triassic Hopeman Sandstone cropping out around the Moray Firth. The field data give them a qualitative model of distribution patterns and inter-relationships which can be applied to explain the subsurface observations.

Quantitative analysis of sandstones in outcrop is being undertaken by a growing number of people, in an attempt to characterize permeability distribution in sedimentary units which may be analogies of reservoirs. Chandler *et al.* (1989) examined the aeolian Page Sandstone (Jurassic) of Northern Arizona at outcrop to determine general permeability patterns which would be typical of aeolian sandstones, enabling simple flow models to be generated at the reservoir scale. They found that the average permeability of each facies was significantly different from that of the other facies. Lewis & Rosvoll (in press) examined the Tensleep sandstone of Wyoming and illustrated considerable spatial anisotropy of permeability variation in outcrop. Lewis *et al.* (1990) and Lewis & Rosvoll (in press) stressed the value of analogue studies, as they found that the anisotropy could not be adequately described from

permeability statistics derived from individual vertical logs ('wells'). Other published studies of permeability distribution in reservoir analogues include Alexander & Gawthorpe (in press), Dreyer (1990), Jacobsen & Rendell (in press), Pryor (1972) and Stalkup (1986). For most of these outcrop studies, it is assumed that the permeability distribution patterns (though not the permeability magnitudes) are a function of the sedimentary facies and depositional process (Weber 1986), and consequently, that the permeability patterns are applicable to the subsurface despite the diagenetic differences between sandstones currently at the surface and those in the subsurface (discussed, for example, by Stalkup 1986).

Outcrop analogues on the sandbody scale have been used to supplement subsurface data, and to test reservoir simulation models of heterogeneity and shale discontinuity. Sedimentary facies distribution (including sedimentary structure, grain size and grain fabric variations) and diagenetic features are major controls on fluid flow through a sandbody (van de Graaf & Ealey 1989). Discontinuous, relatively impermeable, barriers, such as shale lenses, increase the tortuosity of fluid flow through the sandbody. Therefore, a quantitative description of facies (including sedimentary and diagenetic features of sandstone and shales) is important to make realistic predictions of reservoir performance. As these features cannot be measured away from the well, either the reservoir must be assumed to be homogeneous or follow a simple pattern of heterogeneity around the well, or supplementary data such as may be measured from rock record analogues must be obtained. Outcrop data of analogous rocks have been used to estimate flow and sweep efficiency. For example, Hoimyr *et al.* (this volume) have used outcrop data from the Permo-Triassic Maroon Formation of Colorado to model sweep efficiency in the middle Statfjord Formation of the Snorre Field. Success depends on selection of an appropriate analogue which requires a perceptive knowledge base and thorough appreciation of a reservoir's context and characteristics.

Very large volumes of data from the subsurface are now available. These data, if used with discretion, can form valuable reservoir analogues. For example, abundant permeability data have allowed studies of its statistical distribution (Jensen *et al.* 1987) that may be used to explain reservoir data.

The problems with analogues

There are many problems inherent in the use of analogues for reservoir geology. The main disadvantage of using a direct comparison to improve qualitative understanding of a reservoir is if the analogue is seriously inaccurate, incorrect, or if the comparison is uncritically stretched beyond the aspects of the system for which it was proposed. The problems can be subdivided into problems of interpretation, scale of comparison, duration and geological time period, degrees of freedom, and lack of documentation of suitable analogues and analogue databases for statistical or empirical reservoir models. It is necessary to remember that there is no such thing as a perfect analogue.

The problems of interpretation

The problems of interpretation fall into two categories: interpretation of the reservoir data and interpretation of the analogues. In order to identify a suitable analogue,

some interpretation of the reservoir rocks' depositional environment and post-depositional alterations must be carried out. Incorrect initial interpretation of the depositional environment of reservoirs or post-depositional alterations leads to the use of inappropriate analogues. This need for some initial interpretation of the nature of the reservoir can result in circular arguments.

Geologists frequently use rock record analogues where the original interpretation of that analogue (as well as the reservoir rocks) is based on knowledge of modern examples or other geological analogues. In some cases it would be more instructive, and perhaps more useful to non-geologists at the receiving end of the interpretations, to see the analogue drawn directly with the modern environment. Interpretations of outcrops are necessarily subjective and using the interpretation as reservoir analogues may introduce an unquantified uncertainty into a model.

The application of rock record analogues is subjective; different people will consider that the same analogue has different values and limitations. One striking example of variations in the interpretation and assessment of the applicability of a rock record analogue is the use of the Ravenscar Group (Middle Jurassic, Cleveland Basin, UK; Fig. 1) as an analogue, or partial analogue, for the Brent Group of the northern North Sea (Alexander 1986, 1989, 1992; Alexander & Gawthorpe in press; Dreyer 1990; Dreyer *et al.* 1990; Eschard *et al.* 1989; Hancock & Fisher 1981; Jacobsen & Rendell in press; Kantorowicz 1984; Mjøs & Walderhaug 1989; Mjøs *et al.* 1990; Ravenne *et al.* 1987). In this example, on a large (exploration) scale there is a difference in the interpretation of the depositional environment between a delta and coastal plain setting. This difference in the interpretation of the analogue leads to different models of sandstone distribution and character (Alexander 1989). There have been differences in the interpretation of the origin and history of individual sandbodies which would lead to differing models of formation and consequently interpretation of internal structure. Perhaps more disturbing to many reservoir geologists is the apparent differences in interpretations of variations in permeability measured on the same sandbodies (Alexander & Gawthorpe in press; Dreyer 1990; Jacobsen & Rendell in press). Some of the conclusions drawn by different authors from the same analogues are clearly contradictory.

One example where modern analogues are often incorrectly drawn is in the interpretation of channel size and channel belt size from vertical profiles through alluvial sandbodies. This problem results from the uncertainties in assessing the nature and size of channels from vertical profiles (discussed by Bridge 1985) and interpreting the nature and width of the channel belt from the interpretation of channel type and size. Incorrect interpretation of channel and channel belt size and type lead to errors in estimates of sandbody size and internal complexity. These problems are discussed at some length by Fielding and Crane (1987) and Lorenz *et al.* (1985).

Problems of scale

Reservoir heterogeneity is frequently regarded as being hierarchical in nature (Haldorsen & Lake 1984; Miall 1988; Pettijohn *et al.* 1973; van de Graaff & Ealey 1989; Weber 1986; and others) with heterogeneity occurring from the intergrain scale (Morrow 1971) to formation or basin scale (cf. Bridge & Leeder 1979). Ideally, reservoir characteristics should be understood on all scales from laminae and grain-

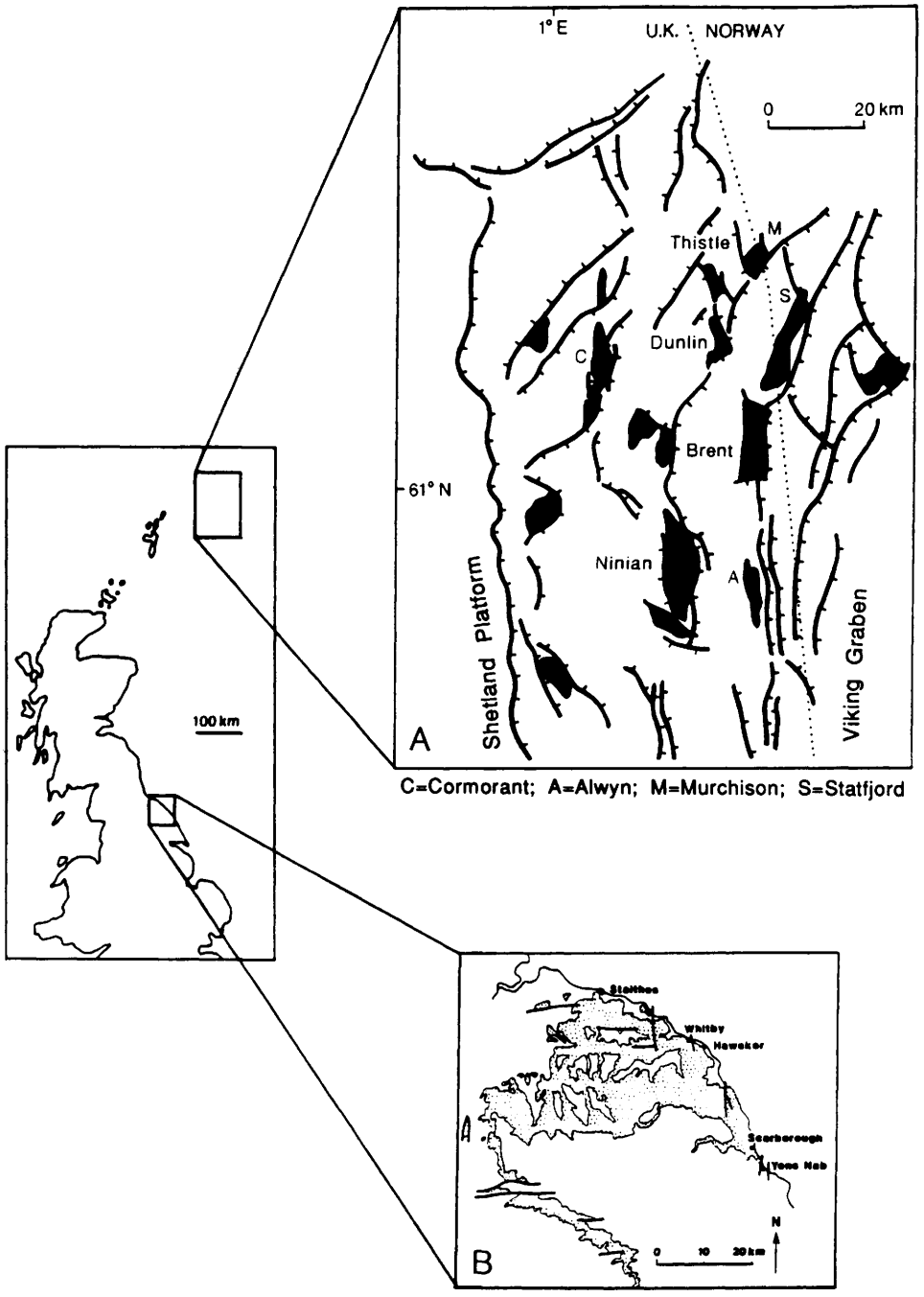

Fig. 1. A comparison of the scale of the Middle Jurassic Ravenscar Group outcrop of the Cleveland basin (**B**) and the Brent Group oilfields of the northern North Sea (**A**).

scale through bedform, storey or facies element, sandbody, to formation and basin scale. It is rare that any one analogue study considers heterogeneity at all these scales.

At an exploration stage, regional or basinal scale analogues may be used to predict reservoir rock distribution. At an early stage after discovery when limited bore-hole data are available, the analogues put forward typically consider formation scale and sandbody scale variations. The aims of such models will be, for example, to estimate inter-well continuity of reservoir facies. Problems may arise when the first analogues continue to be applied later in field development, when more data are available, without rigorous testing of the limitations of the analogy. Additional problems can arise where analogues introduced for comparability at a formation scale are used at a finer scale.

An important and rarely appreciated factor, is that depositional analogues are frequently inappropriately applied because of scale differences. This results largely from a lack of general, popular information on small and intermediate scale depositional systems, whereas large-scale systems are widely known (e.g. most British secondary school children probably know something about the Mississippi). For example, a large number of modern analogues have been used for the Brent Group of the northern North Sea including: the Grijalva (Budding & Inglin 1981), the Mississippi (Moiola *et al.* 1985), the Niger (Budding & Inglin 1981), the Nile (Fig. 2; after Johnson & Stewart, 1985), and the Rhone (Brown *et al.* 1987; Brown & Richards 1989) deltas. None of these is a very close analogue to the Brent Group as a whole, although, as discussed by Brown *et al.* (1987), parts of each analogue are similar to parts of the Brent Group. Consequently, when these large-scale analogues are applied to reservoir scale (or smaller) serious inconsistencies may be present. Although the area of the Jurassic Brent Group of the northern North Sea is comparable to that of the modern subaerial Nile Delta (Fig. 2; after Johnson & Stewart 1985) it is unlikely that any one reservoir will have the characteristics of any one part of the delta.

Depositional analogues selected on a reservoir scale are often difficult to apply on a well spacing scale. For example if a meander belt were selected to explain the nature of a reservoir, the distribution of facies and discontinuities within the reservoir could be very different to that of any one particular modern meander belt. The controls on meander belt sandbody internal heterogeneity resulting from meander growth and migration are poorly understood.

In contrast to depositional analogues, the problems of scales of comparison are frequently reversed when using rock record analogues as the data are often collected from relatively small exposures. In converting from outcrop studies to reservoir simulations on the scale of injection well to production well spacing, analogue models are frequently repeated or stretched (for example, Høimyr *et al.* this volume). In many cases scale factors are not realistically thought through, or their limitations not adequately stated. It may not be sensible to go from a simulation of one unit, for example a section 10×300 m, to a unit several times that size either by stretching the model or repeating the unit. Real systems will seldom, if ever, conform to a repeated building block model. For example, an alluvial channel sandbody of a given size will have been deposited under particular restricted conditions, a sandbody twice its width in the same setting may be produced by a channel of the same size which has migrated laterally, one or more channels of the same or different size eroding into an earlier sandbody or a larger channel; in any of these conditions the controls on the

channel facies will be different (different bank stability, discharge, etc) and the internal character of the sandstone may be considerably different.

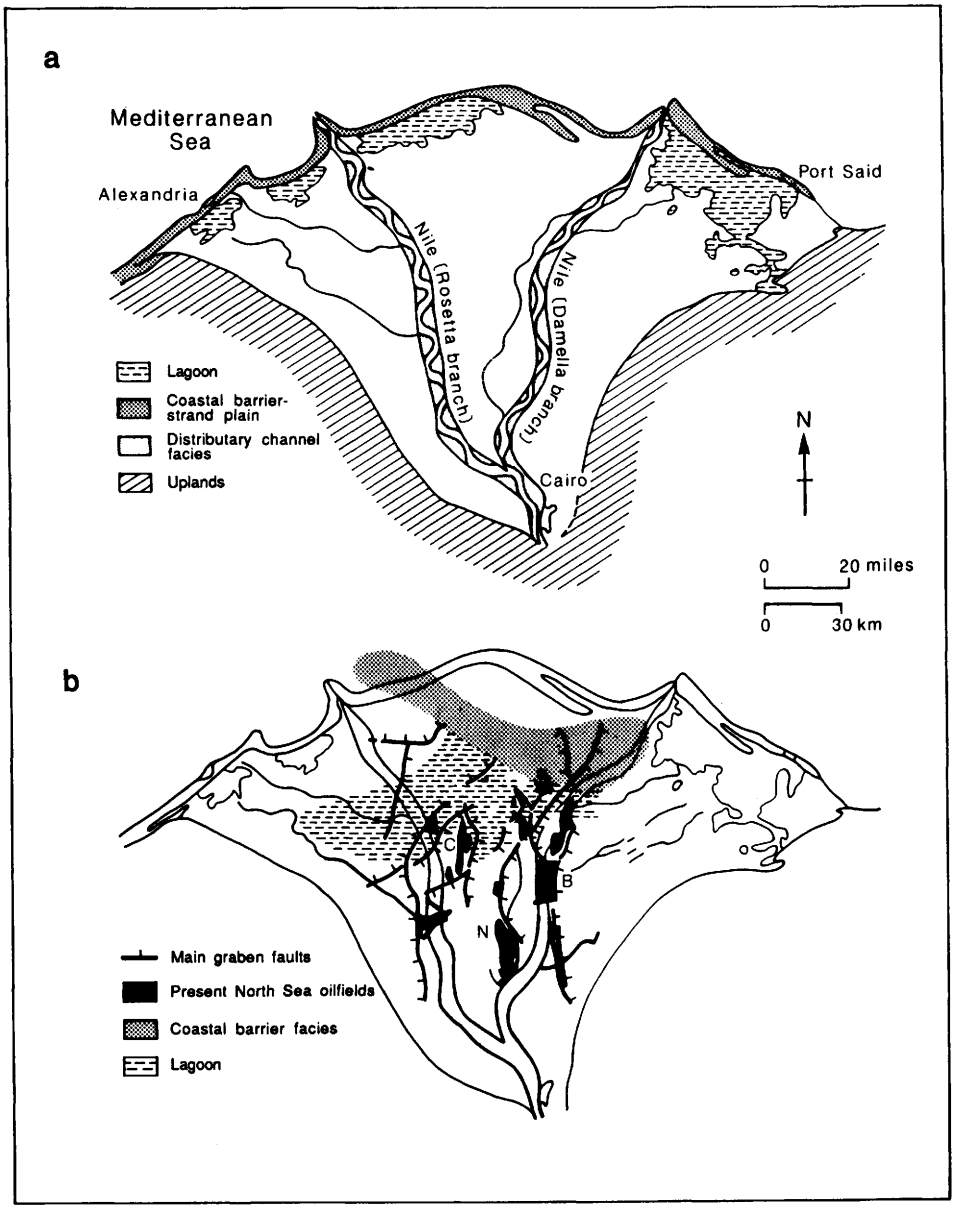

Fig. 2. The Nile Delta as an analogue for the Brent Group of the northern North Sea (after Johnson & Stewart 1885). (**a**) shows a highly simplified map of the delta, and in (**b**) the oil fields and observed facies distribution of a time-slice late in the period of deposition of the Brent Group are superimposed on a map of the Nile delta to allow comparisons of scale. B, Brent Field; N, Ninian Field; C, Cormorant Field.

An additional problem of comparing sandbodies of different sizes in the rock record is that resulting from selective diagenesis. In many cases the extent of dissolution or cementation is controlled by the fluid throughput during burial and as fluid flow is controlled by the size of the conduit, larger interconnected sandbodies may be more extensively altered. For example in the Jurassic alluvial sandbodies of Yorkshire permeability is controlled in part by feldspar dissolution, and the extent of dissolution appears to be correlated with the size and interconnection between channel sandbodies (cf. the difference in sandbody permeability recorded by Ravenne *et al.* 1987 in the Scalby Formation).

The problems of scale with experimental analogues is usually more complex than with either depositional or rock record analogues. For example to reproduce turbidity currents in a laboratory requires down scaling of a large number of factors including flow size, density contrast and sediment grain size. To assess the limitations in the applicability of the experimental models requires an understanding of the assumptions made during model design.

The problems comparing analogue duration and geological time periods

Given the prolonged period of time taken for the deposition of many reservoir rocks, a single analogue based on evidence from present day or historical time (a geologically instantaneous snap shot) may not be sufficient to explain the complex patterns in a reservoir. For example, the Brent Group of the northern North Sea is often compared to modern deltas (as discussed above), however, the deposits making up the Brent Group in any one field do not represent one delta but rather a prolonged period over which sedimentation occurred in a number of differing settings. Following the application of modern analogues, inconsistencies caused by variations in conditions through time, may become apparent and additional theoretical or rock analogue data may be employed successfully to improve the models.

With rock record analogues more complex problems result from the comparability of the duration of analogue and reservoir rock formation. As sedimentary and post-depositional processes are time dependent, rock record time periods should ideally be matched to that of the reservoir. Additionally, if the analogues are not drawn from the same geological time period then there could be additional, often unrecognized problems resulting from the evolution of environmental conditions through geological time (e.g. the influence of the evolution of vegetation on erosion, sediment dispersion and alluvial channel behaviour).

In experimental analogues there are inherent problems relating to time. Experimental analogues are rarely produced over geologically realistic time periods and, as with the problems of scaling size, the assumptions in the design of the experiments with regard to scaling time periods need to be understood before the limitations in the applicability of the analogue may be applied.

The problems resulting from degrees of freedom

The need for analogues for reservoir geology results from the very large number of factors which control the deposition and post-depositional alteration of reservoir rocks. The very large number of degrees of freedom in the reservoir forming process are as yet impossible to define, and consequently any analogue (or analogue dataset) can ony hope to represent partially the reservoir.

It is often problematic, when using depositional analogues to match the very large number of factors controlling the nature of the deposits between the analogue and the reservoir. To get an ideal analogue for the Brent Group at any site, for example, it would be necessary to consider: the source area character (size, exposed lithologies, topography, tectonic activity and climate), receiving basin character (size, depth, tidal activity, wave fetch, tectonic activity), the climate (and climatic change) of the depositional area, history of subsidence, and sea level change.

Additional difficulties are involved in assessing the limitations of depositional analogues for the investigation of reservoir rock. There is some difficulty in assessing the applicability of depositional analogue data due to uncertainties in the controls on sedimentary facies preservation. These problems may be solved by critical use of analogue data and should improve when current research on the preservation potential of sedimentary facies has been published. The most significant problems in evaluating data from modern depositional analogues, however, are caused by the changes which sediment undergoes as it is buried to reservoir depths. These changes, including compaction, diagenesis and tectonic deformation, are difficult to observe directly and must be assessed by consideration of experimental and rock record analogues.

In many cases a single formation (often of a different age and in a different sedimentary basin) is used as an analogue to supply quantitative data for reservoir models. Such comparisons are based on the assumption that if the deposits contain similar depositional facies, then the lithological geometry and continuity also will be similar (cf. Dreyer this volume; Geehan *et al.* 1986; Haldorsen & Chang 1986; Haldorsen *et al.* 1987; Høimyr *et al.* this volume; and others). It is not always reasonable to use one such rock record analogue, unless the depositional environment and burial history are accurately matched. Ideally, if only one analogue is to be presented, the controls on the deposition, diagenesis and tectonic history should be identical. Therefore, it would be better to present a range of possible alternatives. If a single analogous system is cited, it is essential to state in what ways the system is analogous and in what major ways it is different from the reservoir in question. For alluvial deposits, for example, it is important to consider matching climate of sediment source area and depositional area, source area size, channel load characteristics, base level fluctuations, tectonic setting of deposition and burial history. In the case of alluvial deposits, therefore, it makes little sense to use analogues based on a comparison of sandbody size as this leaves too many important factors unaccounted for. The internal facies architecture of a channel belt sandstone is *not* related to sandbody size but to the original channel and load characteristics, which are rarely easy to assess from the rock record.

Rather than attempt to find an analogue with matching controlling factors on facies architecture, most studies try to match the resulting facies distribution. Using this technique, a quantitative facies match may be attempted where the controlling factors are different, and therefore, a better understanding of the depositional system and physical controls of facies architecture will not be obtained.

The problems resulting from lack of documented analogues

In a few cases it may not be possible to find a depositional analogue for a reservoir rock. This difficulty may result from changes through geological time (for example changing river behaviour resulting from the evolution of land plants) or more

commonly insufficient data on modern systems. The lack of appropriate depositional analogues may lead to use of data where the limitations of similarity are not easily defined. For example, investigations of modern ocean floor sediment and features have increased the depositional analogue database on submarine fans and turbidites; however, there is some doubt as to the extent of similarity between turbidites in open oceanic settings from which most depositional analogues are obtained, and those deposited in confined basins (such as the North Sea) where many reservoir rocks were formed.

In many cases there is a significant problem in finding modern depositional analogues that are perceived to be as good or better than rock record comparisons. There is the added advantage of rocks that they are static and, therefore, may be easily measured whereas modern systems are constantly changing. However, assessment of parameters in a constantly changing system in many cases may be of greater use to an interpretation of reservoir rocks, as it dramatically illustrates the variability of the processes responsible for the formation of reservoir rocks and, therefore, the potential variations in reservoir character.

Dreyer (this volume) proposes the use of a conversion factor for transferring dimensional data from outcrop to subsurface datasets. He found this necessary because the match between his outcrop analogue (the Miocene Ridge Route Formation of California) and subsurface dataset (the Lower Jurassic Tilje Formation of the mid-Norway shelf) were not close enough to allow direct comparison and merging of datasets for reservoir modelling. The use of a conversion factor involved an attempt at quantifying the influence of a number of controlling factors on the facies dimensions of the analogue and reservoir rocks and using the resulting matrix to convert between the two datasets. Dreyer (this volume) considers the ratio between sediment supply and accommodation space, lobe-shift frequency, delta-front processes, configuration of the receiving basin, inflow characteristics and water composition to calculate conversion factors. The problem with this approach is that it is not realistically possible to quantify the effect and interdependence of controlling factors. If it were possible to quantify the controlling factors there would be no need of analogue studies as a physical model would already exist. Without a working physical model the conversion factors are based on a subjective comparison of two rock record examples and are then used to quantify that comparison. To overcome the circular problem Dreyer (this volume) proposes the use of Monte Carlo statistical techniques.

Analogue databases for statistical or empirical reservoir models

Increasingly analogue databases are being used to improve the understanding of geological processes, to assess the relationships between different reservoir features, and to quantify the distribution of reservoir rocks and reservoir characteristics. With the increase in the availability of data, the uses of databases are becoming increasingly sophisticated.

In recent years special attention has been paid to the empirical study of sandbody geometry and architecture, particularly in fluvial, deltaic and turbiditic systems (*e.g.* Fig. 3; Geehan *et al.* 1986). This has taken three main approaches:

(1) consideration of facies size in modern environments;

(2) combining data from modern environments and the rock record to construct empirical models;
(3) statistical datasets collected from outcrop.

A common approach to the problem of modelling size and distribution of facies (particularly of relatively impermeable material within a reservoir body) is to employ datasets from outcrops to constrain thickness and width distributions for use in probabilistic or empirical models. Examples of this approach to data collection and datasets have been presented by Dupuy & LeFebvre du Prey (1968), Gozalo & Martinius (in press), Kocurek (1981), Miall (1988), Ravenne *et al.* (1987), Weber (1982, 1987), and the application of analogue datasets to reservoir problems is exemplified by Clemetsen *et al.* (1990), Geehan *et al.* (1986), Haldorsen & Chang (1986), Luthi & Banavar (1988), Matheron *et al.* (1987) and others.

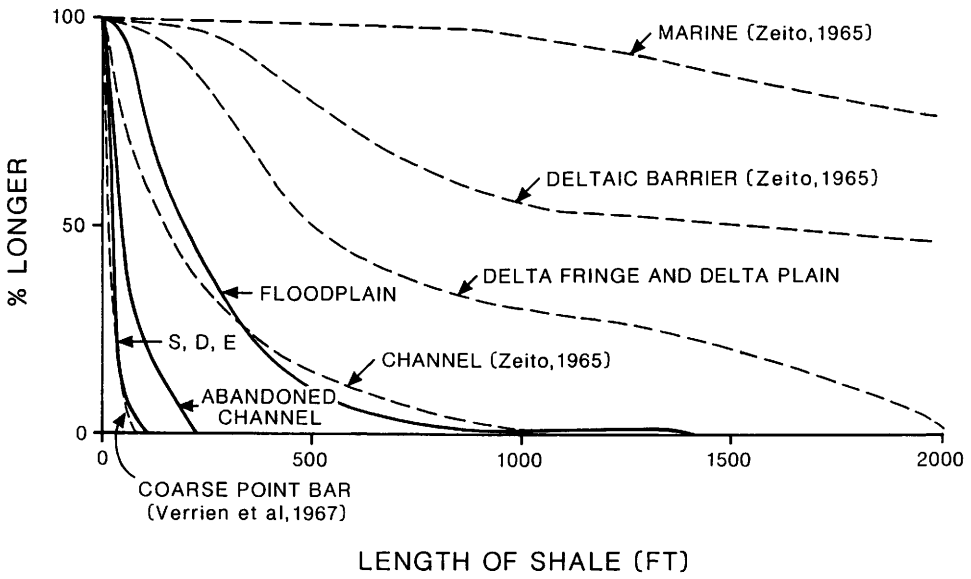

Fig. 3. Observed shale lengths as a function of depositional environment (after Geehan *et al.* 1986). Solid lines are from data collected by Geehan *et al.* (1986) from outcrops in Utah, and dashed lines are similar to data compiled by Weber (1982; S,D,E: slough/drape/eddy facies).

One application of analogue datasets has been to predict the lateral extent of alluvial channel-belt sandbodies and the likely continuity between proposed boreholes by applying models based on empirical relationships between channel parameters. Fielding & Crane (1987) used a combination of empirical relationships for channel dimensions calculated from limited numbers of modern channels (reviewed by Collinson 1978) combined with empirical data on the relationship between sandbody thickness and channel depth to derive a model for sandbody thickness to width relationship (Fig. 4). They emphasized some of the problems related to applying this model and stressed factors which had not been considered. The controls on sandbody size are complex and include: channel size, percentage of coarse grained sediment in the load, channel bank stability and erodability, avulsion periodicity, sea

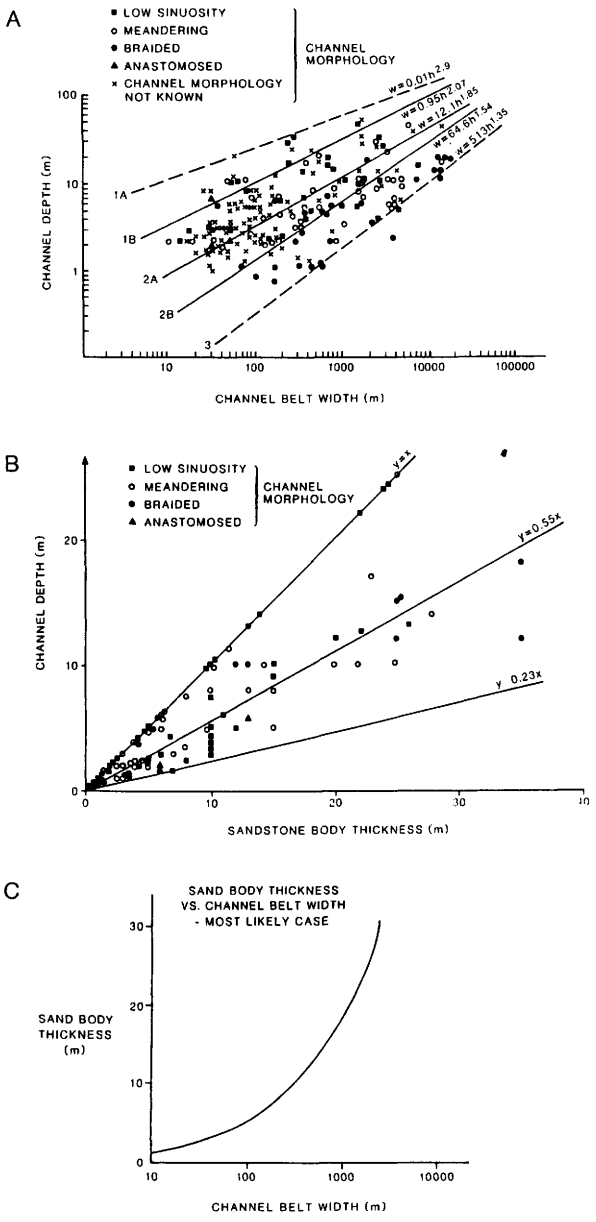

Fig. 4. Correlation diagrams after Fielding & Crane (1987).
(A) Channel depth v. channel belt width relationships for modern and ancient fluvial channel deposits. The correlation lines represent empirical relationships for channels under different conditions: 1A, incised, straight and non-migrating channels; 1B, non-migrating, non-incised channels; 2A, geometric mean of all channel types; 2B, channels with fully developed meandering profiles; 3, laterally unrestricted (braided) fluvial systems.
(B) Channel depth v. sandstone body thickness relationship. The two outer lines enclose the limited available data from published sources. The median line is taken by Fielding & Crane (1987) as a reasonable representation of the data.
(C) Sandstone body thickness v. channel belt width perpendicular to palaeocurrent for case 2A in (A).

level (or other base level) fluctuation, subsidence (accommodation space) and lateral variation in topography. Some of these factors are controlled by the interplay of climate, discharge and hinterland size. The significance of most of these factors is difficult to interpret from the rock record, and even where they are reasonably defined the relationships between them and the architecture of the deposits are not yet quantifiable. The disregard for controlling factors results in a very wide range of predicted size (Fig. 4).

It is often assumed that the width and thickness of shales or sandbodies is the same as the apparent width and thickness at outcrop. In the case of alluvial sandbodies, discussed above, attempts to overcome this problem consider the angle of the exposed faces relative to palaeoslope. However, this is not entirely satisfactory as in any alluvial system the orientation of a channel may vary greatly from the direction of the palaeoslope. Some (although considerably less) variation of the channel belt orientation may also occur, as discussed by Alexander (1986), Leeder & Alexander (1987) and Weston & Alexander (in press). In the case of shale discontinuities, any association shale elongation has to palaeoslope is unknown, but the assumption that the apparent width distribution will approach that of the true distribution is only reasonable if it is assumed that the shales have a circular shape (Wu *et al.* 1973). For example, an examination of 2D sections slightly oblique to the palaeoslope results in a dataset that does not record the full range of intra-channel and inter-channel, or intra-fan and inter-fan facies distributions, and lateral relationships between sandbodies. The width of the sandbody in cliff exposures is dependent on the width of the original channel, fan or sheet, its lateral migration, and the angle of the cliff to the palaeoflow direction. It may not represent the mean width of the sandbody, as for example in the case of channels, the width of the sandbody may be very variable as a result of meandering, braiding and down-channel changes in the extent of lateral migration. The orientation of the long axis of a sandbody is not always the same as the mean of palaeocurrent data measured in outcrop.

In most cases data collection of sandstone and shale size has been from selected, relatively small sampling sites (usually the most easily accessible). Small sampling areas within very large sediment tracts frequently introduce a sampling error which may be compounded by misinterpretation of the facies. If analogue datasets are unrepresentative of the analogue systems, their use to generate reservoir simulation models is wholly unreasonable, even where there is a close analogy between the outcrop example and hydrocarbon field example.

Producing a dataset for numerical simulations which is based on field data from a large number of rock record examples may initially seem more sensible than employing a single rock record analogue for reservoir models. However, in reality, databases drawing on a number of studies often introduce new problems. Firstly, the database will inevitably combine datasets from deposits formed under different conditions even where facies appear similar, and data averaging will occur. Also, the field data are invariably biased by outcrop availability and/or a limited amount of knowledge of the stratigraphical context such as aggradation rates, periods of erosion, sediment discharge and variations in those properties. Ultimately this approach is likely to produce a size frequency distribution for disconformities or sandbody size/shape representing a wide range of variations in controlling factors (*e.g.* Fig. 4; after Fielding & Crane 1987), but probably no more useful than a competent sedimentologist or geomorphologist could estimate from a consideration of modern processes.

It is not true to say that any dataset is better than no dataset. An unrepresentative dataset makes simulation models less rather than more realistic predictive tools. It may be more sensible to use a theoretical size distribution rather than an erroneous analogue dataset.

Conclusions

Geology depends on analogues, the use of comparisons and correspondence. The major problem of analogues is that no perfect analogue can be produced and inappropriate use of any analogue will result in erroneous conclusions. It is important, therefore, to know how far to take an analogue based on a reasoned and critical assessment of the problems and principal objectives involved, and the database available.

Modern depositional analogues are useful in the interpretation of facies variations, and the mechanisms and environments of deposition. Given the long time periods of deposition of most reservoirs, the explanation of formation-scale facies patterns requires an analogue study with a time-span allowing appropriate environmental changes. Some depositional processes cannot be observed directly and consequently rock record or experimental analogues must be used in place of modern depositional ones. Sediments undergo changes in reservoir characteristics after deposition due to diagenesis and deformation, consequently rock record and experimental analogues are needed to supplement depositional analogues.

Most analogues traditionally have been used in a qualitative or semi-quantitative way to improve qualitative understanding and prediction of characteristics of reservoir rocks. Increasingly, more quantitative studies of analogues are being used to build or enlarge datasets for statistical models, and more occasionally to produce empirical physical models or to test theoretical models. The main problems with producing geologically realistic mathematical models of the nature and distribution of reservoir characteristics result from a lack of quantitative data on fundamental controls and rates of sedimentation, compaction, diagenesis and fracture development.

Most published simulation studies present a non-rigorous approach, often testing only a few of the possible configurations of even the simplistic models they use. They do not estimate the statistical significance of any of the variations they model, or even discuss how they relate to geological reality. An analogue should ideally be tested rigorously, in a scientific manner.

Thanks to M. Ashton for asking me to write this discussion and forcing me to sharpen up my ideas. Thanks to A. Hartley, S. Leigh, two anonymous reviewers and especially to A.R. Hurst and T. Young for commenting on earlier versions. Thanks to M. Millen for help with the diagrams.

References

ALEXANDER, J. 1986. Idealised flow models to predict alluvial sandstone body distribution in the Middle Jurassic Yorkshire Basin. *Marine and Petroleum Geology*, **3**, 298–305.

—— 1989. Delta or Coastal plain? With an example of the controversy from the Middle Jurassic of Yorkshire. *In*: WHATELEY, M.K.G. & PICKERING, K.P. (eds) *Deltas: sites and traps for fossil fuels*. Geological Society, London, Special Publication, **41**, 11–19.

—— 1992. A discussion of alluvial sandstone body characteristics related to variations in marine influence, Middle Jurassic of the Cleveland Basin, UK, and the implications for analogous Brent Group strata in the North Sea Basin. *In*: MORTON, A.C. HASZELDINE, R.S., GILES, M.R. & BROWN, S. (eds). *Geology of the Brent Group*, Geological Society, London, Special Publication, **61**, 149–168.

—— & GAWTHORPE, G.L. In press. The complex nature of a multistorey alluvial sandstone body. *In*: NORTH, C.P. & PROSSER, J. (eds) *Characterization of fluvial and aeolian reservoirs*. Geological Society, London, Special Publication.

BRIDGE, J.S. 1985. Paleochannel patterns inferred from alluvial deposits: a critical evaluation. *Journal of Sedimentary Petrology*, **55**, 579–589.

—— & LEEDER, M.R. 1979. A simulation model of alluvial stratigraphy. *Sedimentology*, **26**, 617–644.

BROWN, S. & RICHARDS, P.C. 1989. Facies and development of the Middle Jurassic Brent delta near the northern limit of its progradation, UK North Sea. *In*: WHATELEY, M.K.G. & PICKERING, K.P. (eds) *Deltas: sites and traps for fossil fuels*. Geological Society, London, Special Publication, **41**, 253–267.

—— & THOMSON, A.R. 1987. Patterns in the deposition of the Brent Group (Middle Jurassic) UK North Sea. *In*: BROOKS, J. & GLENNIE, K. (eds) *Petroleum Geology of North West Europe*. Graham & Trotman, London, 899–913.

BUDDING, M.C. & INGLIN, H.F. 1981. A reservoir geological model of the Brent sands in Southern Cormorant. *In*: ILLING, L.V. & HOBSON, G.D. (eds). *Petroleum Geology of the Continental Shelf of North-West Europe*. Heyden, London, 326–334.

CHANDLER, M.A., KOCUREK, G., GOGGIN, D.J. & LAKE, L.W. 1989. Effects of stratigraphic heterogeneity on permeability in eolian sandstone sequence, Page Sandstone, Northern Arizona. *American Association of Petroleum Geologists Bulletin*, **73**, 658–668.

CLEMETSEN, R., HURST, A.R., KNARUD, R. & OMRE, H. 1990. A computer program for evaluation of fluvial reservoirs, *In: North Sea Oil and Gas Reservoirs — II*. The Norwegian Institute of Technology, Graham & Trotman, 373–385.

COLLINSON, J.D. 1978. Vertical sequences and sandbody shape in alluvial sequences. *In*: MIALL, A.D. (ed.) *Fluvial Sedimentology*. Canadian Society of Petroleum Geologists, Memoir **5**, 577–586.

DREYER, T. 1990. Sandbody dimensions and infill sequences of stable, humid-climate delta plain channels. *In*: BULLER, A.T. (ed.) *North Sea Oil and Gas Reservoirs — II*. The Norwegian Institute of Technology, Graham & Trotman, 334–351.

——, SCHEIE, A. & WALDERHAUG, O. 1990. Minipermeameter-based study of permeability trends in channel sand bodies. *American Association of Petroleum Geologists Bulletin*, **74**, 359–374.

DUPUY, M. & LEFEBVRE DU PREY, E. 1968. L'anisotropie d'ecoulement en milieu poreux presentant des intercalations horizontales discontinues. *Comunication No. 34 Troisieme Collogque de l'Association de Recherche sur les Techniques de Forage et de Production, Pau, France*.

EDWARDS, E., HOWELL, J. & BECKER, A. 1991 (abstract) Compartmentalisation of an aeolian sandstone reservoir by structural heterogeneities: Permo-Triassic Hopeman Sandstone, Moray Firth, Scotland. *In: Characterization of Fluvial and Aeolian Reservoirs*, abstract volume. Geological Society, London.

ESCHARD, R., HOUEL, P. & RUDKIEWICX, J-L. 1989. Three dimensional architecture and geostatic simulation of a fluvial to estuarine valley fill complex (Middle Jurassic, Cleveland Basin). *Abstract in The 4th International Conference on Fluvial Sedimentology*.

FIELDING, C.R. & CRANE, R.C. 1987. An application of statistical modelling to the prediction of hydrocarbon recovery factors in fluvial reservoir sequences. *In*: ETHRIDGE, F.G., FLORES, R.M. & HARVEY, M.D. (eds) *Recent Developments in fluvial sedimentology*. Society of Economic Paleontologists and Mineralogists, Special Publication **39**, 321–327.

GAWTHORPE, R.L., COLLIER, R.E.L., ALEXANDER, J., LEEDER, M.R. & BRIDGE, J.S. in press. Ground penetrating radar: application to sandbody geometry and heterogeneity studies. *In*: NORTH, C.J. & PROSSER, J. (eds). *Characterization of Fluvial and Aeolian Reservoirs*. Geological Society, London, Special Publication.

GEEHAN, G.W., LAWTON, T.F., SAKURAI, S., KLOB, H., CLIFTON, T.R., INMAN, K.F. & NITZBERG, K.E. 1986. Geological prediction of shale continuity Prudhoe Bay Field. *In*: LAKE, L.W. & CARROLL, H.B. Jr. (eds) *Reservoir Characterisation*. Academic Press, Orlando, 63–81.

GOZALO, C. & MARTINIUS, A.W. in press. Outcrop data-base for the geological characterisation of fluvial reservoirs. *In*: NORTH, C.J. & PROSSER, J. (eds) *Characterization of Fluvial and Aeolian Reservoirs*. Geological Society, London, Special Publication.

HALDORSEN, H.H. 1986. Simulator parameter assignment and the problem of scale in reservoir engineering. *In*: LAKE, L.W. & CARROLL, H.B. Jr. (eds) *Reservoir Characterisation*. Academic Press, Orlando, 293–340.

—— & CHANG, D.M. 1986. Notes on stochastic shales; from outcrop to simulation model. *In*: LAKE, L.W. & CARROLL, H.B. Jr. (eds). *Reservoir Characterisation*. Academic Press, Orlando, 445–485.

—— & LAKE, L.W. 1984. A new approach to shale management in field-scale models. *Society of Petroleum Engineers Journal*, **24**, 447–457.

——, CHANG, D.M. & BEGG, S.H. 1987. Discontinuous vertical permeability barriers: a challenge to engineers and geologists. *In*: KLEPPE, J., BERG, E. W., BULLER, A.T., HJELMELAND, O. & TORSAETER, O. (eds) *North Sea Oil and Gas Reservoirs*. The Norwegian Institute of Technology, Graham & Trotman, 127–151.

HANCOCK, N.J. & FISHER, M.J. 1981. Middle Jurassic North Sea deltas with particular reference to Yorkshire. *In*: ILLING, L.V. & HOBSON, G.D. (eds) *Petroleum Geology of the Continental Shelf of North-West Europe*. Heyden, London, 186–195.

JACOBSEN, T. & RENDELL, R. in press. Permeability patterns in some fluvial sandstones. An outcrop study from Yorkshire, North East England. *In*: LAKE, L. & CARROLL, H.B. Jr. (eds) *Reservoir Characterisation*. Academic Press, Orlando.

JENSEN, J.L., HICKLEY, D.V. & LAKE, L.W. 1987. A statistical study of reservoir permeability: distributions, correlations and averages. *Formation Evaluation*, **2**, 461–468.

JOHNSON, H.D. & STEWART, D.J. 1985. Role of clastic sedimentology in the exploration and production of oil and gas in the North Sea. *In*: BRENCHLEY, P.J. & WILLIAMS, B.P.J. (eds) *Sedimentology: Recent Developments and Applied Aspects*. Geological Society, London, Special Publication, **18**, 249–310.

KANTOROWICZ, J.D. 1984. The nature, origin and distribution of authigenic clay minerals from Middle Jurassic Ravenscar and Brent Group sandstones. *Clay Minerals*, **19**, 359–375.

KOCUREK, G. 1981. Significance of interdune deposits and bounding surfaces in eolian dune sands. *Sedimentology*, **28**, 753–780.

LASSETER, T.J., WAGGONER, J.R. & LAKE, L.W. 1986. Reservoir heterogeneities and their influence on ultimate recovery. *In*: LAKE, L.W. & CARROLL, H.B. Jr. (eds) *Reservoir Characterisation*. Academic Press, Orlando, 545–560.

LEEDER, M.R. & ALEXANDER, J. 1987. The origin and tectonic significance of asymmetrical meander belts. *Sedimentology*, **34**, 217–226.

LEWIS, J.J.M. & ROSVOLL, K.J. In press. Preliminary findings of an outcrop study of aeolian reservoir heterogeneity on the Tensleep Sandstone of Wyoming. *In*: NORTH, C.J. & PROSSER, J. (eds) *Characterization of Fluvial and Aeolian Reservoirs*. Geological Society, London, Special Publication.

——, LOWDEN, B. & HURST, A. 1990. *Permeability distribution and measurement of reservoir-scale sedimentary heterogeneities in sub-surface exposures of a shallow marine sandbody*. Fieldtrip A11 of the 13th International Sedimentological Congress, Nottingham, England.

LORENZ, J.C., HEINZE, D.M., CLARK, J.A. & SEARLS, C.A. 1985. Determination of widths of meander-belt sandstone reservoirs from vertical downhole data, Mesaverde Group, Piceance Creek Basin, Colorado. *American Association of Petroleum Geologists Bulletin*, **69**, 710–721.

LUTHI, S.M. & BANAVAR, J.R. 1988. Application of borehole images to three-dimensional geometric modeling of eolian sandstone reservoirs, Permian Rotliegendes, North Sea. *American Association of Petroleum Geologists Bulletin*, **72**, 1074–1089.

MACKEY, S.D. & BRIDGE, J.S. 1991. (abstract) Process-based alluvial stratigraphy models: a progress report. *In: Characterization of fluvial and aeolian reservoirs*, Geological Society, London, abstract volume.

MATHERON, G., BEUCHER, H., DE FOUQUET, C., GALLI, A., GUERILLOT, D. & RAVENNE, C. 1987. Conditional simulation of the geometry of fluvio-deltaic reservoirs. *Society of Petroleum Engineers, presented at the SPE Annual Technical Conference, Dallas, SPE paper*, 16753.

MIALL, A.D. 1988. Reservoir heterogeneities in fluvial sandstones: lessons from outcrop studies. *American Association of Petroleum Geologists Bulletin*, **72**, 682–697.

MJØS, R. & WALDERHAUG, O. 1989. Spatial organisation and geometries of channels and crevasse splay sandstones. Ravenscar Group, Yorkshire and Ness Formation, Oseberg Field. *In: 4th International conference on fluvial sedimentology, Abstract volume*, 186.

——, WALDERHAUG, O. & PRESTHOLM, E. 1990. Sandbody geometry and heterogeneity in the fluvio-deltaic Ravenscar Group of Yorkshire. *In: Advances in reservoir geology, Abstract volume*, The Geological Society, London.

MOIOLA, R.J., JONES, E.L. & SHANMUGAN, G. 1985. (abstract) Sedimentology and diagenesis of the Brent Group (Middle Jurassic, Statfjord field, Norway–United Kingdom. *In: Habitat of Hydrocarbons Norwegian Oil and Gas Finds*. NDF.

MORROW, N.R. 1971. Small-scale packing heterogeneity in porous sedimentary rocks. *American Association of Petroleum Geologists Bulletin*, **55**, 514–522.

PETTIJOHN, F.J., POTTER, P.E. & SIEVER, R. 1973. *Sand and sandstone*. Springer-Verlag, New York.

PRYOR, W.A. 1972. Reservoir inhomogeneities of some recent sand bodies. *Society of Petroleum Engineers Journal*, **12**, 229–245.

RAVENNE, C., ESCHARD, R., GALLI, A., MATHIEU, Y., MONTADERT, L. & RUDIEWCZ, J-L. 1987. Heterogeneities and geometry of sedimentary bodies in a fluvio-deltaic reservoir. *Society of Petroleum Engineers Journal*, 16752, 115–122.

READING, H.G. 1986 (ed.). *Sedimentary environments and facies*. Second edition, Blackwell Scientific Publications, Oxford.

—— & ORTON, G.J. 1991. Sediment calibre: a control on facies models with special reference to deep sea depositional systems. *In*: MULLER, D.W., MCKENZIE, J.A. & WEISSERT, H. (eds). *Controversies in Modern Geology*. Academic Press, London, 85–111.

STALKUP, F.I. 1986. Permeability variations observed at the faces of crossbedded sandstone outcrops. *In*: LAKE, L.W. & CARROLL, H.B. Jr. (eds) *Reservoir Characterisation*. Academic Press, Orlando, 141–175.

TETZLAFF, D.M. & HARBURGH, J.W. 1989. *Simulating Clastic Sedimentation*. Van Nostrand Rheinhold.

VAN DE GRAAFF, W.J.E. & EALEY, P.J. 1989. Geological modeling for simulation studies. *American Association of Petroleum Geologists Bulletin*, **73**, 1436–1444.

VERRIEN, J.P., COURNAD, G. & MONTADERT, L. 1967. Application of production geology methods to reservoir characteristics analysis from outcrop observations. *Proc. Seventh World Pet. Cong., Mexico*. 425–446.

WALTON, A.W., BOUQUET, D.J., EVENSON, R.A., ROFHEART, D.H. & WOODY, M.D. 1986. Characterisation of sandstone reservoirs in the Cherokee Group (Pennsylvanian, Desmoinesian) of Southeastern Kansas. *In*: LAKE, L.W. & CARROLL, H.B. Jr. (eds) *Reservoir Characterisation*. Academic Press, Orlando, 39–62.

WEBER, K.J. 1982. Influence of common sedimentary structures on fluid flow in reservoir models. *Journal of Petroleum Technology*, **34**, 665–672.

—— 1986. How heterogeneity affects oil recovery. *In*: LAKE, L.W. & CARROLL, H.B. Jr. (eds) *Reservoir Characterisation*. Academic Press, Orlando, 487–544.

—— 1987. Computation of initial well productivities in aeolian sandstone on the basis of geological model, Leman gas field, UK. *In*: TILLMAN, R.W. & WEBER, K.J. (eds) *Reservoir sedimentology*. Society of Economic Paleontologists and Mineralogists Special Publication, **40**, 333–354.

WESTON, P.J. & ALEXANDER, J. in press. Computer modelling of flow lines over deformed surfaces: the implications for prediction of alluvial facies distribution. *In*: MARZO, M. & PUIGDEFABREGAS, C. (eds) *Fluvial sedimentology*. International Association of Sedimentologists, Special Publication.

WILLIS, B. 1989. Palaeochannel reconstructions from point bar deposits: a three-dimensional perspective. *Sedimentology*, **36**, 757–766.

WU, T.H., VYAS, S.K. & CHANG, N.Y. 1973. Probabilistic analysis of seepage. *Journal of Soil Mechanics and Foundation Mechanics Division*, **99**, 323–340.
ZEITO, G.A. 1965. Interbedding of shale breaks and reservoir heterogeneities. *Journal of Petroluem Technology*, 1223–1228.

From ASHTON, M. (ed.), 1993, *Advances in Reservoir Geology*,
Geological Society Special Publication No. 69, pp. 195–217.

Analogue dipmeter logs through a prograding deltaic sandbody

GAVIN I. F. CAMERON,[1] JOHN D. COLLINSON,[2]
MALCOLM H. RIDER[1] & LI XU[3]

[1] *Rider–French Consulting Cambridge Ltd, Cambridge Science Park, Milton Road, Cambridge, CB4 4GG, UK*
[2] *Collinson Jones Consulting, 56 Shropshire Street, Market Drayton, Shropshire TF3 9DA, UK*
[3] *Department of Earth Sciences, Oxford University, Parks Road, Oxford OX1 3PR, UK*

Abstract: Detailed analogue dipmeter measurements have been made along a 430 m roadcut in the Upper Namurian Rough Rock at Elland in Yorkshire. A series of 21 vertical sections were measured with dip and azimuth (dip-log) readings taken every 0.2 m, which were calibrated to previously described sedimentological sections and recordings of surface natural gamma ray profiles.

The inter-relationship between the scale of sedimentary structures and dipmeter processing parameters is shown by dip-log measurements in medium scale, cross-bedded sedimentary structures. The analysis of grouped dip-log data is seen to give palaeocurrents very similar to those measured by traditional methods at outcrop. The relationship between sedimentological facies and 'dip-log facies' is applied to reservoir characterization, and statistical analysis of dip-log data is demonstrated to be an aid to inter-well comparisons.

Analysis techniques, mainly computer based and applicable in the subsurface, are applied to the outcrop data and the implications for subsurface dipmeter studies are stressed.

Sandbody orientation is one of the most sensitive factors in producing hydrocarbons from clastic reservoirs; it is also one of the most difficult to establish in the subsurface. Orientation occurs at all scales, from the megascale of the sandbody itself, to the mesoscale of bedforms, and to the microscale of laminae (van de Graaff & Ealey 1989). But significantly, the overall orientation of a sandbody can be indicated in the orientation of the smaller scale, constituent parts. This paper examines the study of the orientation of medium scale sedimentary structures and palaeocurrents in that they are indicators of overall sandbody orientation.

A practical way of assessing sedimentary structure orientation in the subsurface is by use of the dipmeter. Significant recent advances in dipmeter tool design have given the industry much improved subsurface dipmeter log data. In wells drilled with water-based muds the density and reliability of readings have improved dramatically. However, the use of dipmeter logs in the subsurface has long been hindered by poor methods of interpretation and a general lack of understanding of the relationship between dipmeter measurements and the geological recognition of dip as measured at outcrop. Despite the advances in dipmeter tool design, interpretation methods have still not changed. There is an unfortunate belief, extensively marketed because of its apparent simplicity, that the dipmeter can be related to sedimentary structures simply by identifying patterns of dip decreasing upwards, dip increasing upwards, and constant dip, the so-called red, blue and green patterns. There is no objective evidence to support this belief and no practical use for the idea.

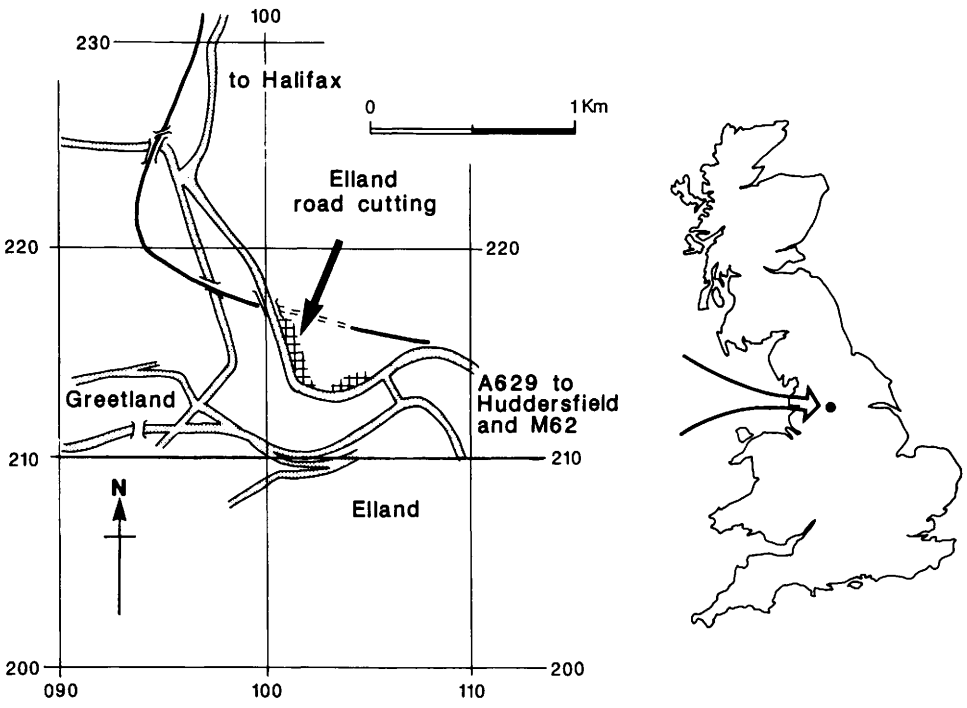

Fig. 1. Location of the Elland Roadcut, West Yorkshire, England.

As a pragmatic demonstration of dipmeter response and interpretation, a set of analogue dipmeter logs have been measured at outcrop over a well-studied and well-exposed sandstone sequence along a roadcut near Elland in West Yorkshire, England (Bristow & Myers 1989; Myers & Bristow 1989; Fig. 1). The logs have been hand measured in 21 vertical sections, spaced at 20 m intervals along the 430 m long road cut, which is some 25 m high. The section shows a coarsening-upwards sequence, interpreted to represent deltaic progradation, with the main sandstone interval, at the top of the section, deposited in large, braided distributary channels (Bristow & Myers 1989; Fig. 2). The rocks are from the Middle Carboniferous, uppermost Namurian (Yeadonian) Rough Rock Group, which is an oil producer in the West Midlands. Sedimentological logs have been published for 42 vertical sections at 10 m intervals along the outcrop (Bristow & Myers 1989), and at alternate vertical sections, surface natural gamma ray profiles have been measured (Myers & Bristow 1989). The same vertical sections chosen for the gamma ray profiles were used for the present analogue dipmeter (dip-log) measurements (Fig. 3).

The results are presented and discussed under the following headings:

dip-logs related to sedimentary structures
palaeocurrents from dip-logs
dip-logs related to facies
application to subsurface reservoir characterization
how representative is a single vertical profile?

First, the methodology of data acquisition is described since the dip-logs discussed are not true dipmeter logs, generated by a dipmeter tool, but analogue dipmeter log profiles measured at outcrop. The term 'dip-log' is used for 'analogue dipmeter logs', while 'dipmeter logs' always refers to results from a conventional, downhole dipmeter tool. This terminology is only for convenience and clarity in this paper and is not intended for wider usage.

Dipmeter tools, dipmeter data acquisition and data processing are described briefly in an appendix to the paper. It is suggested that the appendix is read before the main text by those unfamiliar with the dipmeter, since much of what is discussed in the text requires a basic understanding of all aspects of the subsurface dipmeter.

Data acquisition and manipulation

Nearly 1600 individual dip measurements have been made through 21 vertical sections across the Elland outcrop, in imitation of subsurface dipmeter readings. Ascending each vertical section (Figs 2 & 3) dip and azimuth measurements have been recorded every 0.2 m, the dip selected being that of the texturally best defined for that interval. This, therefore, gives a density of data corresponding to a subsurface dipmeter processed with a 0.2 m correlation interval. (For an explanation of the principles of subsurface dipmeter functioning see appendix.)

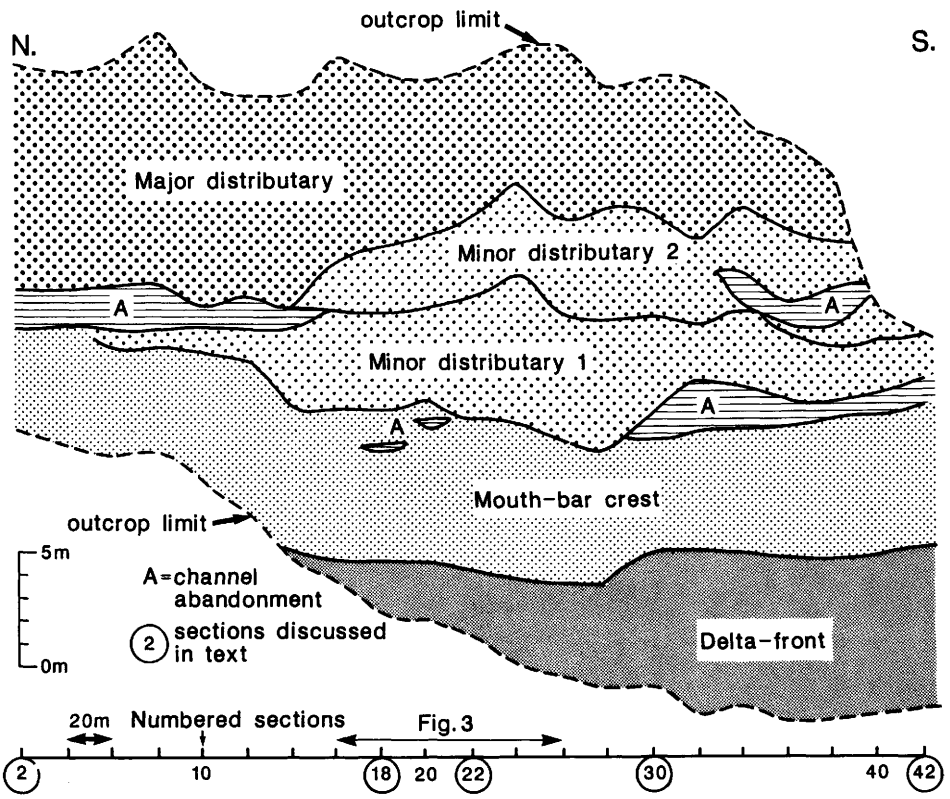

Fig. 2. Facies distribution in the Elland Roadcut. For location see Fig. 1. (after Bristow & Myers 1989).

In measuring dips, it has been assumed that visual textural contrasts at outcrop are essentially the same contrasts which would cause the electrical resistivity changes recorded on the micro-resistivity curves of the dipmeter tool. Moreover, the strength of visible contrast has been assumed also to correspond to the strength of micro-resistivity contrast. The theoretical basis for this is that F, the formation resistivity factor, is closely related to texture; changes in texture cause changes in F and hence also in measured resistivity. A practical demonstration of this can be found by comparing very detailed, expanded scale, dipmeter micro-resistivity curves with core. The correspondence of visually identified textural changes on the core to micro-resistivity changes on the dipmeter curves is excellent (Cameron 1986; Hocker *et al.* 1990). At the outcrop a dip quality scale, from A (excellent) to E (poor), has been noted, and this relates to visible textural contrasts. Where no textural contrast was visible over any 0.2 m interval, no dip was recorded.

Additionally, certain dips have been 'flagged' as corresponding to very high textural contrasts with the expectation that if a dipmeter were run over this section and processed with a large correlation interval this 'flagged' dip would dominate. For instance, at cross-bed set boundaries the textural contrast is often greater than that between constituent foreset laminae (Fig. 4). The set boundary would be 'flagged' while the foreset lamination would not. The flagged dip would give a large micro-resistivity peak on subsurface dipmeter records. This high peak would tend to dominate the statistical comparisons, used later in the computerized dipmeter processing, to correlate micro-resistivity curves and produce a calculated dip.

Throughout the dataset, each of the 0.2 m intervals with an outcrop dip and azimuth has been precisely recorded with the causal sedimentary structure, and tied to the previously logged sedimentary profile (Bristow & Myers 1989). The numbered sections are exactly those through which hand-held gamma ray spectrometry was recorded (Myers & Bristow 1989; Figs 2 & 3). The measured dips can therefore be tied precisely to a particular sedimentary structure, and positioned exactly in any section.

The field results were put into the computer both to produce a standard dipmeter output (Fig. 3) and to allow statistical manipulation using *DIPWORK.

Dip-logs related to sedimentary structures

Sedimentary structures are only fully described by their three-dimensional form. Although dip-logs give the true orientation of a measured plane, a vertical series of dip-log measurements through a sedimentary structure gives only a partial description of the complete three-dimensional shapes involved. To understand dipmeter logs in general and for this study in particular, it is important to examine the sedimentary surfaces measured when making the dip-logs and their possible or inferred relationships to three-dimensional forms.

Two types of surface are important for description of cross-bedding, the foreset surfaces and the set bounding surfaces. Foresets are either planar or concave upwards. Bounding surfaces are either essentially flat and parallel, or moderately dipping (although less than the foresets) and generally not parallel (Fig. 4). Tabular cross-bedding is defined as a set with essentially parallel bounding surfaces which

*Mark of Rider–French

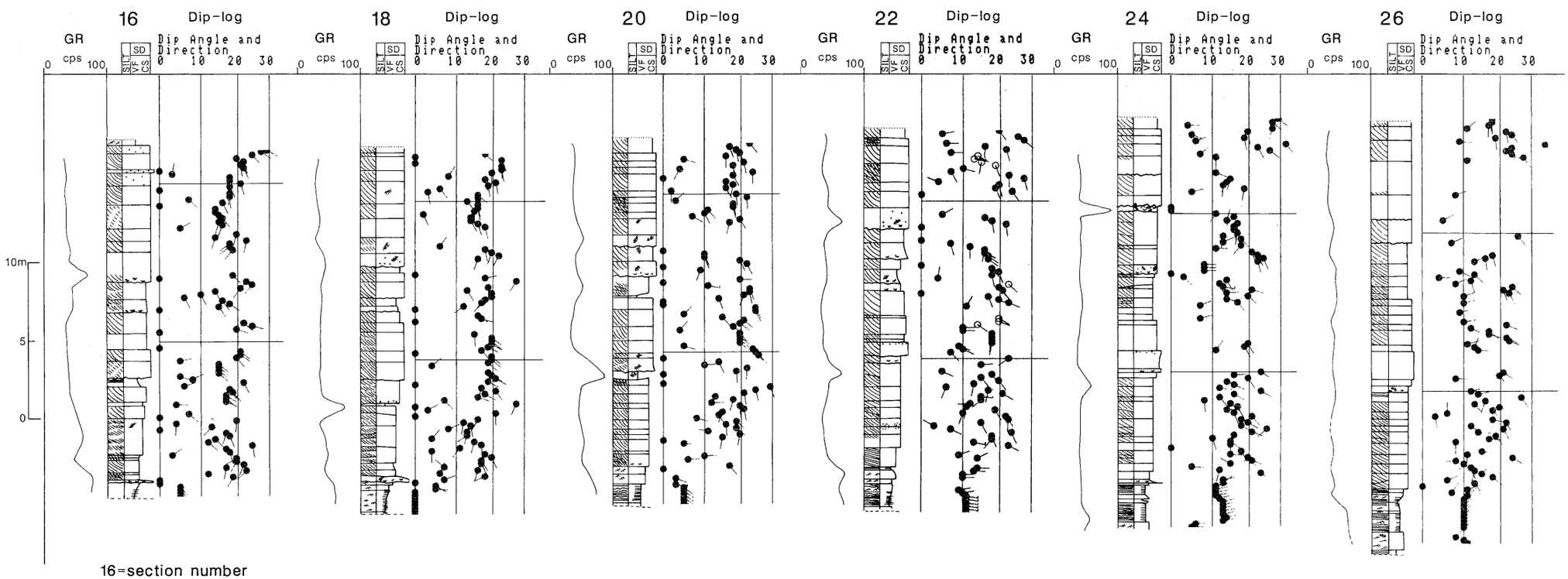

Fig. 3. Illustrative montage of dip-log plots, sedimentological sections, and natural gamma ray profiles for selected sections in the Elland Roadcut. For location see Fig. 2 (slightly modified after Bristow & Myers 1989, Myers & Bristow 1989).

have low dip. Foreset shapes within the parallel bounding surfaces may be either planar or concave upwards (Collinson & Thompson 1989). There is an inference that these sets are formed by bedforms which are straight crested in three dimensions (Fig. 4a; Harms *et al.* 1975). In contrast, set boundaries with variable but frequently moderately dipping set boundaries, are usually associated with trough sets which commonly have concave-upward foreset shapes. It is usually inferred that these are caused by bedforms which have curved crests in three-dimensions and create trough-shaped sets (Fig. 4b; Harms *et al.* 1975).

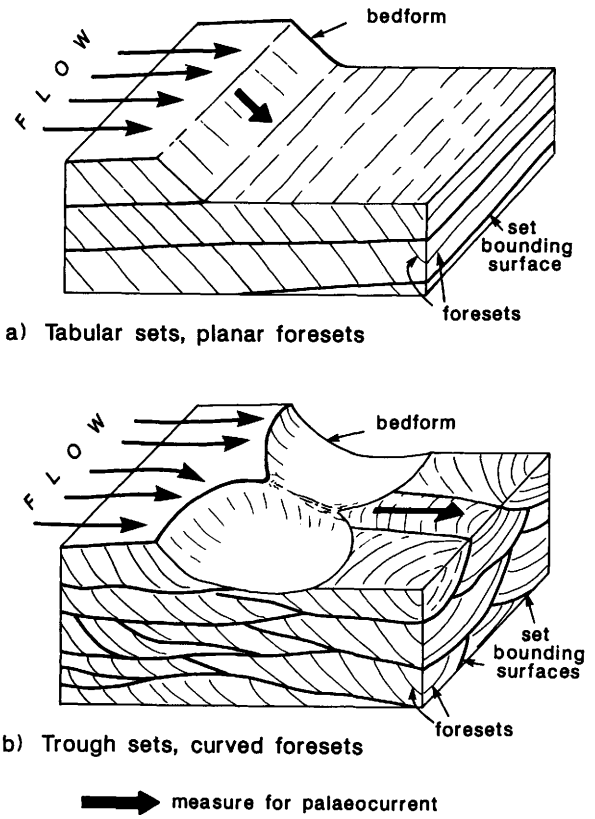

Fig. 4. Idealized sedimentary bedforms with foreset and set geometries.

In the studied outcrop, two medium-scale (less than 1 m in thickness) depositional sedimentary structures dominate and have been examined in detail: tabular cross-bedding and trough cross-bedding (Bristow & Myers 1989). Parallel lamination, wavy lamination and ripple cross-lamination are also present but have not been used in the study. Ripples are recorded on dipmeter only as irregular low-angle bedding since they are too small to be recorded individually. The interval of flat, planar laminated siltstones at the base of the section is used only as an indication of structural dip in the area (Fig. 3).

The scale of sedimentary structures has been documented in the study because of the influence it has both on interpretation and processing of subsurface dipmeter.

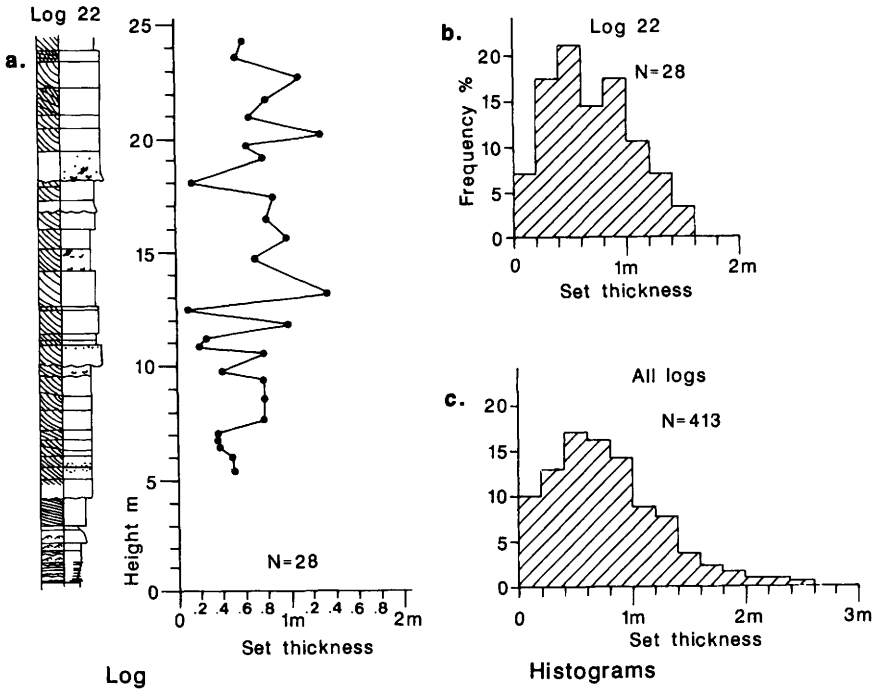

Fig. 5. Cross-bedding set thickness measurements: (**a**) illustrative vertical section (Log 22), (**b**) histogram from Log 22, (**c**) histogram of the entire dataset.

This is illustrated above and discussed later. The vertical thickness of cross-bedded sets, as sampled through each of the sections, ranges up to 2.5 m but nearly half (49% of 413 sets) are between 0.4 m and 1 m thick (Fig. 5c). Vertical sections show that sets tend to be thicker in the upper parts of the outcrop (Fig. 5a). Since dips have been measured every 0.2 m, the thickest sets give up to 12 individual dip readings per set while the thinnest give only 1. The most common set thicknesses give between 2 and 5 individual dip readings (Fig. 6).

Set bounding surfaces, when seen on the dip-logs, are essentially parallel and have either very low dips (below 5°) with very variable azimuths, or are not parallel and have dips typically between 5° and 10° (rarely to 15°) with azimuths tending to diverge from those of the associated foresets. The foresets themselves generally have dips between 10° and 30° with most between 14° and 22° (see below and Fig. 7a,c). In detail, two principal dip-log fabrics are seen within individual sets, especially the thicker ones with 3 or more dip-log readings per set. The first is of constant dip and azimuth within a single set which corresponds to planar foresets (Fig. 6a). The second is of moderate scatter, both in dip and azimuth equally within a single set which corresponds to curved foresets (Fig. 6b).

As indicated previously, the different profiles of the foresets and bounding surfaces are very incomplete descriptions of three-dimensional forms. Despite this, it is definitely possible, with the present data, to recognize two dominant, dip-log profiles: planar foresets with parallel, low-dipping set boundaries (Fig. 6a) and curved

foresets with more steeply dipping, non-parallel set bounding surfaces (Fig.6b). Two three-dimensional sedimentary structures are implied: tabular cross-beds and trough cross-beds (Fig. 4), although intermediate forms exist.

Regardless of the type of cross-bed profile, in the present data set the diagnostic dip-log characteristic of cross-bedded intervals is a grouping of dips in 'clumps' around foreset dip angles (Fig. 3). 'Clumps' with more-or-less the same azimuth and approximately the same dip correspond to one cross-bed set; curved foresets giving a less coherent 'clump' than planar foresets (Fig. 6a,b). Traditionally it is supposed that foresets can be identified by an upwards increasing pattern of dip (traditionally the blue pattern, Gilreath & Maricelli 1964). No such patterns exist in the present data even though the average set thickness and detail of dip measurement would make them visible. The characteristic is a series of 'clumps', not a systematic pattern (Cameron 1986).

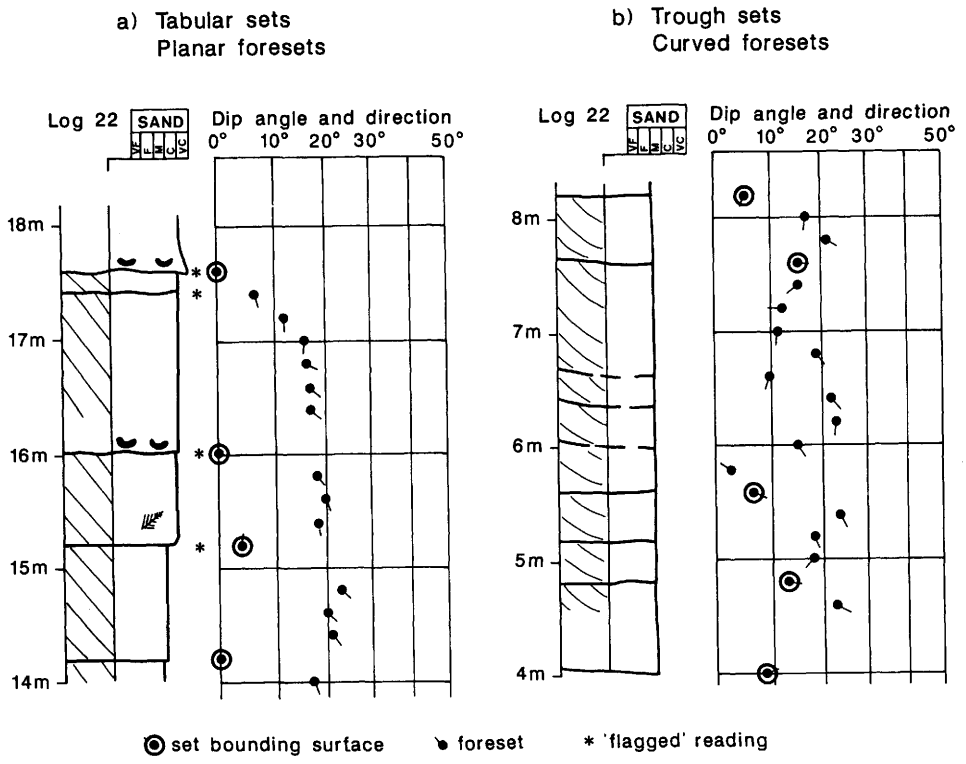

Fig. 6. Dip-log details of cross-bedding types: (**a**) tabular sets with planar foresets; (**b**) trough sets with curved foresets. Compare with Fig. 4.

If, in the studied data, dip magnitudes and dip azimuths are considered separately, they show very distinctive values and ranges. For this aspect of the study, the data from all the vertical profiles have been re-grouped according to their associated sedimentological facies (Fig. 2). Two facies are used for comparison, the mouth-bar crest and the major distributary (Fig. 7). Considering dips only, the histogram of dip-angles of the uppermost facies, the major distributary (Fig. 7a), shows dip values up to just over 30° but with two sub-populations, one above 10° and one below. The two

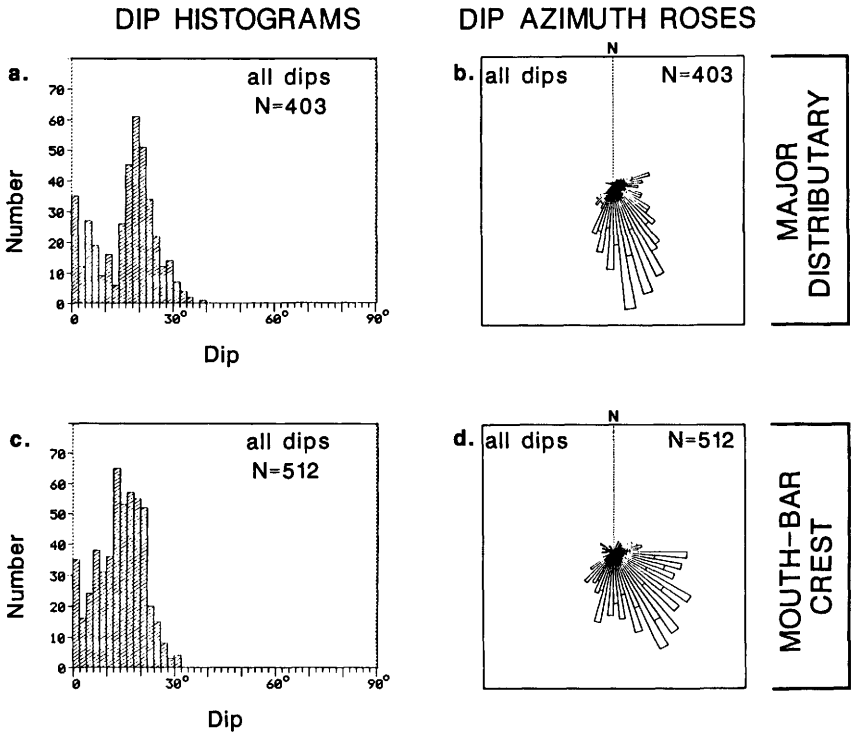

Fig. 7. Dip-log data grouped according to sedimentological facies: (**a**, **b**) major distributary facies, (**c**, **d**) mouth-bar crest facies.

sub-populations are separated by a marked trough. The sub-population of lower values, from the detailed acquisition records, can be identified as coming essentially from set bounding surfaces; the sub-population above 10° corresponds to the foresets themselves. The dip azimuths from the major distributary, when grouped, are relatively consistent (Fig. 7b). Records made during the measurement of the dip-logs, show that the interval is dominated by tabular sets and planar foresets.

The lowest facies interval, the mouth-bar crest, shows a dip histogram with no break at 10° and only one dip-angle population, albeit with a considerable number of dips with low angles (Fig. 7c). The separate low-angle sub-population of the major distributary facies is absent. Data records show that this interval has dipping, non-parallel set boundaries inferred to correspond essentially to trough cross-beds. The azimuth spread in this mouth-bar crest facies is greater than in the major distributary facies (cf. Fig. 7b,d). The difference is taken to be a result of the dominance of trough cross-beds in the mouth-bar crest.

In summary, in the studied dataset, when dips are measured every 0.2 m, the dip-logs of the cross-bedded intervals have the following characteristics.

Dip-logs typically show 'clumping' of 2–5 individual dips with relatively constant dip and azimuth which correspond to individual cross-bed sets typically between 0.4 m and 1 m thick. 'Clumps' with greater coherence tend to be associated with planar foresets, and those showing greater spread with curved foresets.

Set-bounding surfaces give either low dips with irregular azimuths, and are essentially parallel (implied tabular cross-beds), or have moderate dips with azimuths which diverge from the foreset dip azimuths (implied trough cross-beds).

Histograms of foreset dip magnitude show a peak around 18–20° but with the values up to 30° as expected. When tabular cross-bedding is dominant, the dip histograms show an indepenent sub-population below 10° which corresponds to set boundary dips. When trough cross-bedding is dominant, the distinct, separate peak below 10° is absent, set boundaries having low and moderate dips.

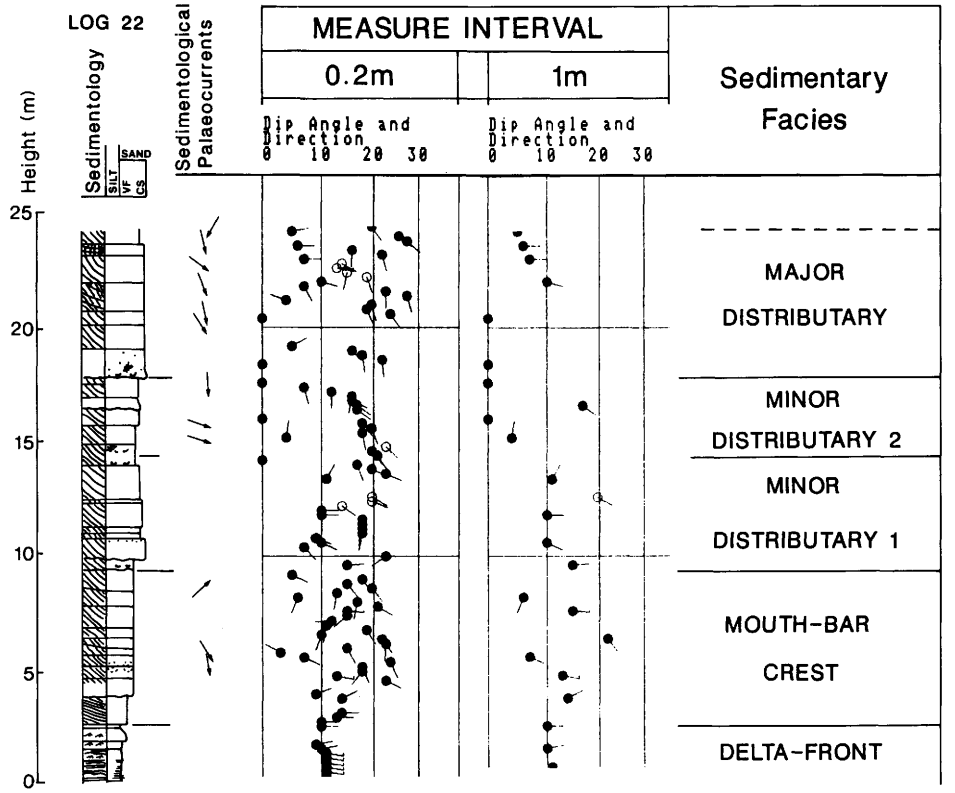

Fig. 8. Palaeocurrents from dip-logs. Comparison between the palaeocurrents measured during sedimentological studies, and dip and azimuth data from the dip-logs using a 0.2 m measurement interval and a 1 m measurement interval. Only the dip-log with a 0.2 m measurement interval shows dip directions parallel to the palaeocurrent. (Sedimentological data from Bristow & Myers 1989).

The dip-log characteristics listed above are a function of scale; scale of the sedimentary structures present, and scale of the dip-log measurements. In this case they result from taking a dip-log reading every 0.2 m in imitation of a dipmeter with a 0.2 m correlation interval. If a 1 m correlation interval is imitated the characteristics change dramatically. 72% of the cross-bed sets in the present data have thicknesses of less than 1 m (Fig. 5c). A dipmeter processed with a 1 m correlation interval would usually include two or more sets in any computer-generated curve correlation for a dip computation (refer to the appendix for the subsurface dipmeter processing

characteristics). The statistical method used by the computer in such cases will inevitably focus on any distinctive micro-resistivity peaks for curve correlation. In the present dataset, these peaks would correspond to the 'flagged' dip values referred to previously under the data acquisition and manipulation heading. These 'flagged' dips are generally the set boundaries (Fig. 6a,b) where textural contrast is greatest and, consequently, where the greatest micro-resistivity peaks would be expected (Rider 1978; Hocker *et al.* 1990). Log 22 is again used as illustration. The first column shows the 0.2 m Measure Interval display (Fig. 8). In the second column, only the 'flagged' dips have been plotted, repositioned in each metre interval in imitation of a subsurface dipmeter with a 1 m correlation interval (Fig. 8). In the second column foreset dips are essentially absent: set boundary dips dominate.

The interpretation of the 1 m correlation interval dip-log is obviously fundamentally different from that of the 0.2 m correlation interval dip-log. With a 0.2 m measurement interval cross-bedding can be recognized and analysed. With a 1 m measurement interval it is probable that cross-bedding would not be identified at all, and no analysis would be possible. The implications for subsurface dipmeter interpretation are clear: a correlation interval of 0.2 m allows cross-bedded structures of 0.4 m–1 m size to be identified while a 1 m correlation interval will contain no indications either of, or from, cross-beds of this size. Further implications are discussed under the heading 'palaeocurrents from dip-logs'.

Palaeocurrents from dip-logs

The original sedimentological analysis of the Elland outcrop was accompanied by measurements of palaeocurrent directions (Fig. 8). To this end 400 azimuth directions were recorded (Bristow & Myers 1989). This compares with over 1500 measurements in the dip-log profiles (Table 1). The contrast in data quantity has within it no notion of quality, it simply illustrates a basic difference in data acquisition.

A palaeocurrent measurement on an outcrop is typically made with a high degree of geological pre-selection. A site where a good measurement can be made is selected and the point of measurement chosen for its interpreted or implied relationship to palaeocurrent. For tabular cross-bedding with planar foresets (Fig. 4a) this will be a dip measurement on the face of one foreset, the azimuth of which will then be considered to represent the palaeocurrent direction for that set. Each set is selectively and separately measured. For trough cross-bedding (Fig. 4b) it is necessary to measure the axis of the trough as being representative of the palaeocurrent of that set, a dip may not be involved. Again, each set is measured separately. Thus, each selected measurement is an indication of palaeocurrent direction; it is not a dip and its azimuth. A palaeocurrent is an azimuth; a dip angle is not implied. The measurements made with the Elland sedimentological study therefore, as is generally typical, represent the best estimates of palaeocurrent direction at a number of selected and geologically pre-interpreted sites (Fig. 8).

The Elland dip-logs, on the other hand, have been acquired to imitate the dataset of a subsurface dipmeter log. In dipmeter processing, a dip and an azimuth are required for each (arbitrarily pre-selected) defined correlation interval and that is what the computer calculates consistently with the best statistical results possible. To make the dip-logs, a dip and azimuth have been measured for every 0.2 m interval

regardless, to imitate a 0.2 m correlation interval. There has been no geological preselection. In order to find palaeocurrent directions, it is necessary to interpret the dip-log dataset. The relationship between dip-log dip and azimuth and palaeocurrent is by no means as obvious as it would first appear.

Measurements for palaeocurrent directions made during the Elland sedimentological study have been based on three main sedimentary structures: tabular cross-bedding, trough cross-bedding and current ripples (Bristow & Myers 1989). Since ripple bedding is not seen as such on the dipmeter, discussion of palaeocurrent interpretation from the dip-logs is based only on cross-bedding.

Table 1. *The number of readings in the dip-log study compared to the number of palaeocurrent readings in the sedimentological study (sedimentological data from Bristow & Myers 1989)*

Facies	Number of readings	
	Outcrop palaeocurrent	Dip-logs
Major distributary	136	403
Minor distributary 2	44	174
Minor distributary 1	48	206
Mouth-bar crest	155	512
Delta-front	17	213*
Channel abandonment	0	99*
Totals	400	1607

*No palaeocurrent information in diplogs

The dip and azimuth of planar foresets in tabular cross-bedding sets is directly related to the palaeocurrent for that bedform (Fig. 4a). To interpret dip and azimuth measurements for a palaeocurrent azimuth it is necessary only to identify foreset dips which then indicate the palaeocurrent azimuth directly (Fig. 4a). To the contrary, in trough cross-bedding, an indication of palaeocurrent is given by the trough axis. Individual dip and azimuth points will describe the shape of the bedform but will not directly give the palaeocurrent. The azimuth directions, however, will be symmetrical about the trough axis. This is because a set is thicker at the axis and more likely to be recorded in a vertical set of dip measurements than the flanks (Fig. 4b). Thus, even though foreset dip measurement in trough cross-beds does not give the trough axis, a vertical section is weighted towards an azimuth spread which is relatively close to it. To interpret the palaeocurrent azimuth, it is first necessary to identify foreset dips in the trough cross-bedding and then to group them as a statistical population to calculate a vector mean. This is the best estimate of the trough axis and palaeocurrent direction.

Clearly, the possibility of identifying an individual dip as originating from planar or trough cross-bedding is effectively nil in the uncored subsurface. For any palaeocurrent interpretation, grouping of the data becomes obligatory; individual dipmeter points will be unreliable considered singly. The problem for interpretation then becomes one of how to group, what to group, and how to make the group significant. The following paragraph considers these aspects.

Previous sedimentological studies have shown that foresets have dips typically between 5° and 35° with a peak between 15° and 25° (Cameron 1986). In the present dataset, similar ranges are recorded, although the peak is between 14° and 24° (Fig. 7a,c). Over the cross-bedded intervals, as has been demonstrated, not only foresets are represented on the dip-logs but also set boundaries (Fig. 6). The set boundaries have dips typically up to 8° in tabular sets but generally up to 10° in trough sets (rarely to 15°). Consequently, eliminating all dips below 10° for palaeocurrent interpretation will largely eliminate readings from set boundaries and will lead to a more reliable azimuth. This simple filtering has been applied to the present dataset, using the facies divisions derived from the sedimentological study. The result is illustrated using the major distributary facies in Fig. 9.

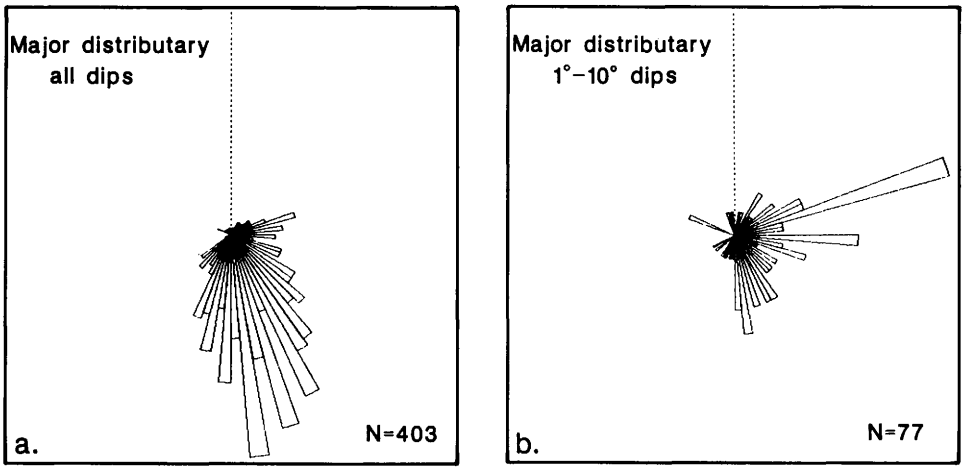

Fig. 9. Dip azimuth roses from the major distributary facies: (**a**) azimuth rose from all readings, (**b**) azimuth rose only from dips below 10°. The azimuth of dips below 10° does not parallel the major palaeocurrent trend.

Table 2. *Palaeocurrent directions from sedimentological studies (Bristow & Myers 1989) and vector mean azimuths from dip-log measurements, 0–90° and 10°–90° only*

	Sedimentological palaeocurrent	Dip-log, vector mean azimuth	
		0–90°	10–90°
Major distributary	163° (N=136)	155° (N=403)	162° (N=301)
Minor distributary 2	145° (N=44)	145° (N=174)	152° (N=137)
Minor distributary 1	138° (N=48)	122° (N=206)	128° (N=152)
Mouth-bar crest	171.5° (N=155)	146° (N=512)	153° (N=368)
Delta-front	189° (N=17)	* (N=213)	* (N=50)

* No palaeocurrent information in the dip-logs: structural significance only.

To pass from the azimuth rose to a palaeocurrent direction, it is necessary to analyse the rose statistically. This is accomplished by using the vector mean azimuth and Rayleigh test (Curray 1956). The latter is simply a statistical test of the vector mean, giving a figure for the probability that it is from a random population. For the three major facies the results are presented graphically against the sedimentologically derived palaeocurrents (Fig. 10) while Table 2 illustrates the comparable figures from all the facies. The effectiveness of the filtering is clear from the figures and shows that the azimuth roses encompass the palaeocurrent directions of the sedimentological set and can be statistically analysed to give vector mean directions very similar to those derived from sedimentological measurements at outcrop. The readings, it should be noted, are valid for a certain gross interval (sedimentological facies) and are not related to an exact level. Using each individual dip point for a single palaeocurrent indication will inevitably lead to errors; grouping the data gives a valid result, but for broad intervals.

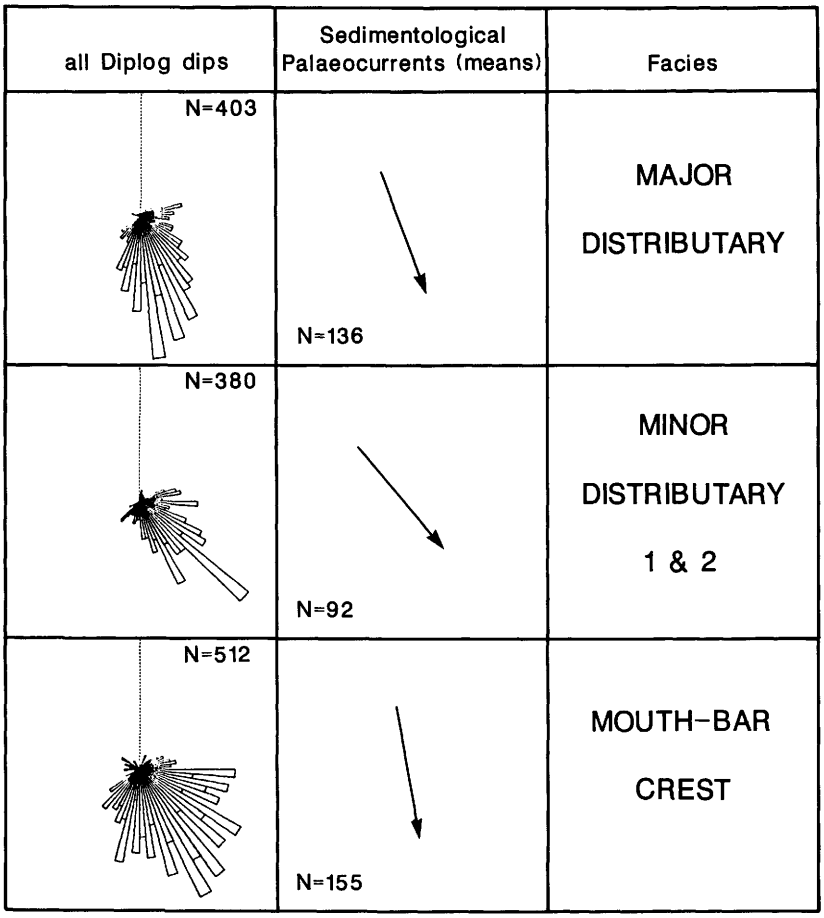

Fig. 10. Comparison between dip-log derived dip azimuth roses grouped by facies, and palaeocurrents from sedimentological studies, for the three principal sedimentological facies. (sedimentological palaeocurrents from Bristow & Myers 1989).

The foregoing, demonstrably effective analyses, are valid with dip-logs measured every 0.2 m. A dataset with measurements from each 1 m would not allow this type of analysis. The dip-log from section 22 (Fig. 8) shows that if a dip filter were applied at 10° very few dips would remain. Moreover, those remaining, especially in the mouth-bar crest facies are essentially from steeply dipping set boundaries which are nearly perpendicular to the trough axis, and hence, the palaeocurrent. The scale relationship between the sedimentary structures and the dip-log acquisition parameters, already stressed, is also important in palaeocurrent interpretation.

The Elland example shows that in the subsurface, the simple statistical analysis of dipmeter data which contains palaeocurrent indications can give directions which are comparable to those derived from traditional outcrop studies. The methodology involves grouping the data into recognizable facies, applying a dip filter to isolate palaeocurrents indicating foresets (in this case 10–30°, but will vary slightly with each bedform type), and then analysing for vector mean azimuth. This analysis presupposes that the dipmeter processing parameters, especially the correlation interval, have been correctly chosen for the size of sedimentary structure to be investigated. Palaeocurrents in the subsurface or at outcrop can only be derived from a correctly gathered dataset, correctly processed, and correctly analysed.

Dip-logs related to facies

Throughout this paper it is stressed that dipmeter data should be interpreted not data point by data point but by simple statistical analysis of grouped data. The grouping in this analogue example is based on five, previously defined sedimentological facies, major distributary, minor distributaries (minor distributaries 1 & 2 have been combined) mouth-bar crest, delta-front, and channel abandonment (Bristow & Myers 1989; Fig. 2). The grouping was initially applied in each vertical section but subsequently, in order to represent the entire outcrop, data were pooled for each facies from all the 21 sections. The results from the outcrop-wide pooling are presented in Table 3 and discussed below by facies, both from the qualitative and statistical view points.

Table 3. *Statistical characterization of the sedimentological facies using the dip-log measurements*

Facies	N	Azimuth			Dip	
		Vector mean azimuth	‡Vector magnitude	†Probability Rayleigh test	‡ Vector dip mean magnitude	‡ Vector magnitude
Major distributary	403	155°	73%	$P < 10E^{-15}$	15°	83%
Minor distributaries	380	132°	75%	$P < 10E^{-15}$	15°	87%
Mouth-bar crest	512	146°	64%	$P < 10E^{-15}$	13°	89%
Delta-front	213	73°*	84%	$P < 10E^{-15}$	4°	94%
Channel abandonment	99	59°*	52%	$P < 10E^{-15}$	3°	95%

*No palaeocurrent information in dip-logs: structural significance only.
†These values all indicate that the vector mean azimuth is statistically non-random.
‡Indicates the spread of data about the mean. 100% signifies zero spread.

Sedimentologically the delta-front and channel abandonment facies are distinct in being fine grained and essentially planar laminated. Regular lamination is quite visible on both the dip-logs themselves and in the statistics. A statistical analysis is hardly necessary to bring out the obvious visual aspect of the logs (Fig. 11).

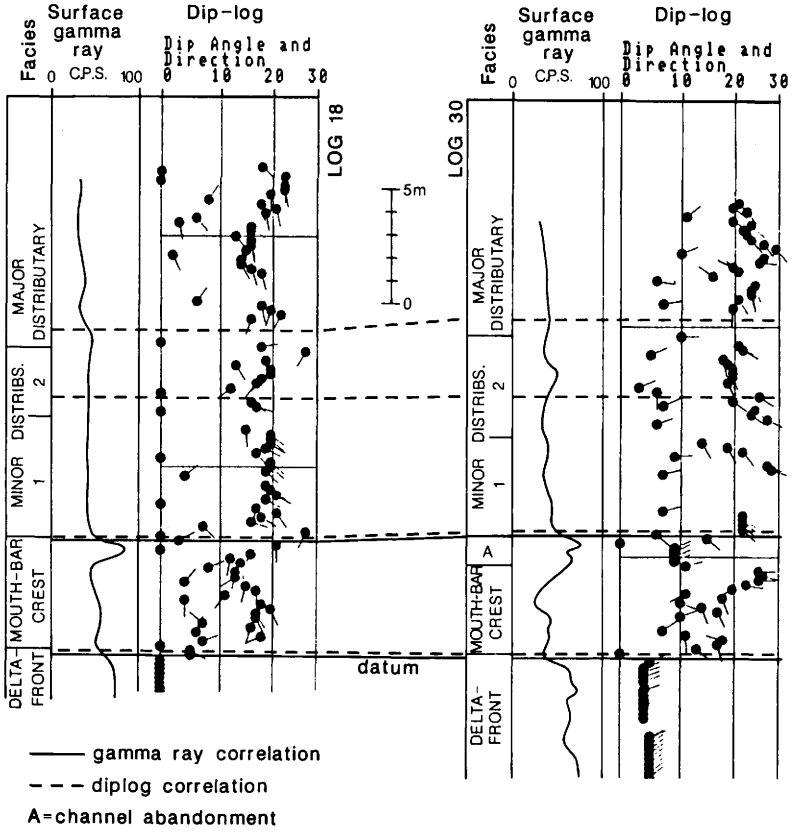

Fig. 11. Illustration of correlation based on (**a**) gamma ray profiles alone and (**b**) gamma ray combined with 'dip-log facies' (surface gamma ray profiles from Myers & Bristow 1989).

The major distributary and minor distributary facies consist of coarse to very coarse-grained sandstones and are dominated by cross-bedding, mainly tabular. Visually (qualitatively) the dip-logs of the two facies are similar (i.e. show similar dip range and spread), although an azimuth difference between them can possibly be identified (Fig. 11). The statistics show a dip population with a dip mean magnitude of 15° (vector magnitude of 83–87%), but a difference in vector mean azimuth between 155° and 132° respectively (vector magnitude 73–75%; Table 3). The influence of the tabular cross-bedding is presumed to be at the origin of the similarities in dip characteristics while the difference in azimuth is a real difference in the palaeocurrent direction.

The mouth-bar crest facies consists of medium-grained sandstones and is dominated by trough cross-bedding, contrasting sedimentologically with the major and minor distributary facies. This difference can be seen to some extent, qualitatively, on

the dip-log profiles but is clear when the dip histograms and azimuth roses are compared. Qualitatively, the mouth-bar crest shows a greater spread on the azimuth rose than either the major or minor distributaries and only a single dip peak on the dip histogram (cf. Fig. 7). The respective differences are expressed statistically in the lower vector mean magnitude (64% against 73% and 75%) and in the lower dip mean magnitude (13° against 15°; Table 3).

The preceding descriptions indicate that in this example sedimentologically defined facies show up qualitatively on the dip-log profiles. A particular sedimentological facies being expressed in a particular dip-log character which can be defined as a 'dip-log facies'. Reference to the outcrop data shows that 'dip-log facies' reflect the response to a particular set of sedimentary structures which also influence the sedimentological definition of the facies. The laminated delta-front facies is an extreme example of this. However, it is with statistical analysis that the response to the sedimentological grouping becomes evident. The grouped dip-log data from each facies give statistically coherent populations and significant differences exist between them (Table 3). Sedimentological grouping of the dip-log data, therefore, is statistically valid and has geological significance.

Application to subsurface reservoir characterization

The preceding sections attempt to show how dip-logs may be analysed, especially by grouping data. The grouping is seen to be valid when based on outcrop sedimentological information, but in the subsurface such detailed information is not always available. An illustration of a simulated subsurface situation is made below using the dip-log dataset in combination with the surface natural gamma ray profiles, both measured on the same vertical sections along the outcrop (Myers & Bristow 1989).

Two surface gamma ray profiles have been selected as examples from the outcrop and are shown with an empirical log correlation (Fig. 11). This is based principally on the basal zone of high radioactivity which corresponds to the silty, delta-front facies underneath the main sandstone interval. Within the sandstone section itself lateral correlation is made empirically using peaks of high radioactivity (Fig. 11). These peaks actually correspond to the clay-rich intervals of the channel abandonment facies which, when followed across the outcrop, are not physically continuous (Fig. 2). None-the-less they occur at approximately the same vertical position in relation to the surrounding facies and in the subsurface would probably be correlated (but hopefully not assumed to be continuous). Using just the gamma ray profiles this is the limit of correlation and subdivision possible. In terms of outcrop sedimentology, the delta-front facies (higher gamma ray values) is readily distinguished from the mouth-bar crest (low gamma ray values). The mouth-bar crest has been distinguished from the major and minor distributaries using the gamma ray peaks, but the minor and major distributary facies (low, featureless gamma ray values) cannot be separated or sub-divided.

When the dip-log set is combined with the gamma ray profiles, refinements are possible. Firstly, there is simply a confirmation of the correlations and subdivisions based on the gamma ray logs. The high gamma ray interval (delta-front facies) is quickly seen to have a distinct 'dip-log facies' indicating flat lamination, so the correlation is confirmed (Fig. 11). Correlation of the gamma ray peaks also appears to be valid as both underlying sections have a similar 'dip-log facies' (mouth-bar crest

facies). For the lower zones, the two datasets are complementary, the dip-logs adding the extra information of orientation.

Secondly, however, over the upper zones, the dip-logs allow basic subdivision and directional correlation which the gamma ray profiles alone are unable to supply. Three divisions can be identified in each section using 'dip-log facies' and each can be correlated on the basis of similarity of azimuth and dip 'clumps'. These correlations give categoric information on the dominant orientations in each of the divisions. Comparison with the outcrop shows that the dip-log based correlations follow sedimentological facies (major and minor distributaries), although the exact sedimentological divisions are not followed.

Clearly, combining the dip-log data and gamma ray profiles provides a degree of refinement in subdivision and correlation. However, this refinement is empirical and it is only when the underlying sedimentological information is used that there is actually understanding. In the subsurface, cores supply the fundamental sedimentological information and whenever available, must be examined in parallel with the dipmeter data and other well logs. But it is only from the dipmeter that orientation data can be obtained (unless the core is oriented or image logs are available).

How representative is a single vertical profile?

Describing a hydrocarbon reservoir requires that this fundamental question be addressed: 'How representative is a single well?' That is, to what lateral extent can the characteristics of one well be extrapolated and, when the dipmeter is being considered, in what direction? With the density of data collected at Elland it is possible to illustrate how typical one section is of the ensemble and how the interpretation of one section would lead to an overall interpretation. There are two ways of analysing the diplog data, qualitatively as a vicarious geological set, or quantitatively as statistical populations.

Qualitative comparison

The 430 m section at Elland represents a relatively consistent vertical sequence of laterally continuous (for the outcrop) facies which is essentially parallel to the palaeocurrent (Fig. 2). For example, through the sections 18 and 30, 120 m apart, there is a similar vertical set of sedimentological facies while the dip-logs show a broadly corresponding sequence of 'dip-log facies' (Fig. 11). When it is seen that the vertical sequence of 'dip-log facies' broadly parallels the sedimentary facies in these two sections, a superficial, qualitative judgement would be that both of the dip-log profiles are representative of the outcrop as a whole. A visual scan of all the other sections (cf. Fig. 3) would warrant this generalization, i.e. the four gross divisions seen at the outcrop (delta-front, mouth-bar crest, minor distributaries, major distributary) are paralleled by the 'dip-log facies'. However, such qualitative observations are not satisfactory, and a more rigorous approach is desirable.

Statistical comparison

It has been constantly demonstrated in this paper that grouping of the dip-log data is necessary for their proper interpretation. It has been discussed specifically in terms of

palaeocurrents and facies for the outcrop generally. However, data grouped by section can also be analysed individually and be considered as statistical populations to be used for quantitative comparisons between sections. The comparisons are difficult in that both the azimuth and dip data represent 'closed' datasets and variations in azimuth are independent from variations in dip. The methods used, therefore, take these factors into consideration but yet remain simple enough that the values of the original data can still be seen.

The illustrative results of comparisons are from dip-logs first divided into sedimentological facies before being subjected to comparison; the mouth-bar facies is used as an example. Comparisons are made on graphs with profiles in geographical order on the x axis. This gives an indication as to how far horizontally (essentially parallel to palaeocurrent) the characteristics of a particular profile may be considered as 'typical' (Fig. 12).

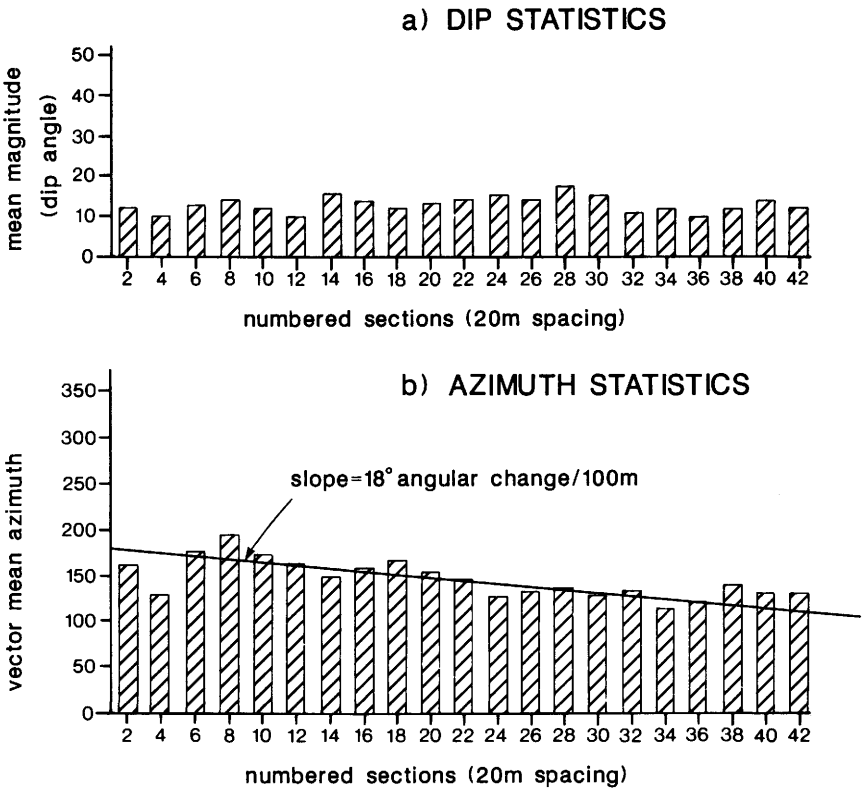

Fig. 12. Comparisons, using simple statistics, between measured sections of the mouth-bar facies. Sections are plotted geographically on the x-axis: (**a**) dip mean magnitudes, (**b**) vector mean azimuths (see also Table 4).

The comparative graph of dip mean magnitudes (Fig. 12a) shows that values from this facies are between a minimum of 10° and a maximum of 17° with an overall population mean of 13° (Table 3). The variation is essentially random as is to be expected from the type of sedimentary structure being measured. The variations in

azimuth, however (Fig. 12b), show a regular swing across the outcrop which is approximately 18° per 100 m (along the outcrop and essentially down palaeocurrent). Example sections 2, 22 and 42, each 200 m apart, in this facies have mean dips very close to the population mean of 13° (although the possible range is 10–17°) and azimuths well below the mean progressive change of 36° (Table 4). If the three sections represented three wells at 200 m spacings, their dip means would be close to the population dip mean but the azimuths would not indicate the full mean azimuth change.

Table 4. *Comparisons of the statistics of three illustrative sections 200 m apart along outcrop in the mouth-bar crest facies*

Section	A Mean dip (av. = 13°)	B* Mean azimuth (change) (var. 18°/100 m)
2	12°	161°
22	14°	149° (12°)
42	12°	133° (16°)

* See Fig. 12 for graphs.

Conclusions

The dip-log dataset measured from the Elland outcrop has been used to understand and test ways in which subsurface dipmeter data may be interpreted. Although the data were collected from a limited set of deltaic facies in a section approximately parallel to palaeocurrent, it shows basic elements common in the subsurface. The conclusions which follow contain principles which are valid for the outcrop and for the subsurface.

(1) The dipmeter will only measure foreset dips within a sedimentary bedform when the correlation interval is significantly smaller than the size of that bedform. In the present example, most bedforms are between 0.4 m and 1 m, and internal foresets are seen with a correlation interval of 0.2 m. With a 1 m correlation interval they are not seen at all.
(2) Foresets are typified by 'clumps' of dip points of roughly similar angle and azimuth which often represent a single cross-bedded set. 'Clump' character varies with cross-bed type. Set bounding surfaces are recorded, generally with dips below 10°. No red or blue patterns exist.
(3) Palaeocurrents can be effectively interpreted using dip and azimuth populations to which dip filters have been applied. The filter isolates foreset data points which have significance for palaeocurrent measurement. For the sedimentary structures at Elland, if only the dips in the range of 10°–30° are used, the vector mean azimuths from the dip-log populations are very similar to the mean palaeocurrents measured by traditional methods.
(4) Sedimentological facies should be used as a basis for grouping dip and azimuth data. To some extent dip-log character ('dip-log facies') reflects sedimento-

logical facies. However, it is with simple statistical analysis that the dip-log groupings are best described. Dip data are plotted in histograms and analysed statistically for the mean. Azimuth data are plotted as rose diagrams and statistically analysed for the vector mean qualified using the Rayleigh test.

(5) Dip and azimuth data can be used qualitatively in parallel with logs to refine correlations and enhance reservoir description. However, prior integration with sedimentological information (cores in the subsurface) is essential for a proper use of the dipmeter.

(6) Quantitative comparisons between dip and azimuth data in separate wells is possible using simple statistics. In the tested example mean dip was seen to vary randomly while vector mean azimuth showed a progressive change. Sample points 200 m apart were only partially representative of the entire outcrop population in this example.

This study shows that subsurface dipmeter interpretation must be based on a clear understanding of the relationship between log processing and the sedimentological features in the rocks. When statistical methods are applied to correctly grouped dip and azimuth data, valid quantitative directional information can be produced which has predictive possibilities. But dipmeter data must be correlated with sedimentological information (cores in the subsurface) for a proper understanding and interpretation.

It is hoped that this paper demonstrates how dipmeter interpretation can benefit from outcrop studies and it is also hoped that more dip orientated studies in different facies will be undertaken. The unthinking application of the red and blue pattern concept has for a long time hindered the proper use of the valuable dataset that the dipmeter represents.

Appendix

The dipmeter: a brief description of the dipmeter tool and a very summary explanation of dipmeter processing.

A typical dipmeter tool has four arms, all at right angles, each supporting a pad with very shallow, focused, microresistivity measuring electrodes (Fig. A1). The electrodes have a resolution of the order of millimetres (0.1 inch) and samples (values) are taken about every 5 mm (0.2 inches) or less. The tool contains navigational instruments so that its exact position, inclination and speed in the borehole are continuously and accurately recorded.

The raw data from the dipmeter tool consist of a series of microresistivity curves measured at each pad. These curves are compared to one another during dipmeter processing and correlations are made between identifiable curve features such as distinctive curve peaks or troughs (Fig. A1). These curve features are seen most frequently at bed boundaries where a contrast of lithology or rock texture occurs, and therefore the plane that passes through the correlated curves is a direct record of the dip of a bed boundary surface or other sedimentary surface crossing the borehole at that point (Fig. A1).

The most common method used to correlate microresistivity curve features in dipmeter processing is the fixed interval correlation technique. In this method, pairs of microresistivity curves are cross-multiplied with one another in all of the possible correlation positions to test for the best match. The results of the cross-multiplication for each curve pair can be represented graphically as in Fig. A2, such that the best curve match corresponds to the peak on the cross-correlation diagram (in this case at shift position 4). When all the curves have been matched with one another in this way, the shift positions are analysed and the best plane is fitted through the correlated curve positions. The dip magnitude and azimuth of this plane are then recorded as the dip result for that depth.

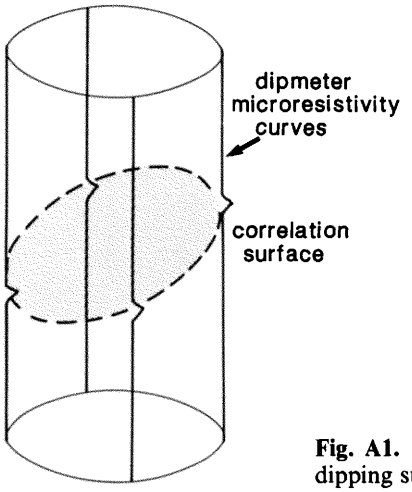

Fig. A1. Schematic diagram illustrating the correlation of a dipping surface from four dipmeter microresistivity curves.

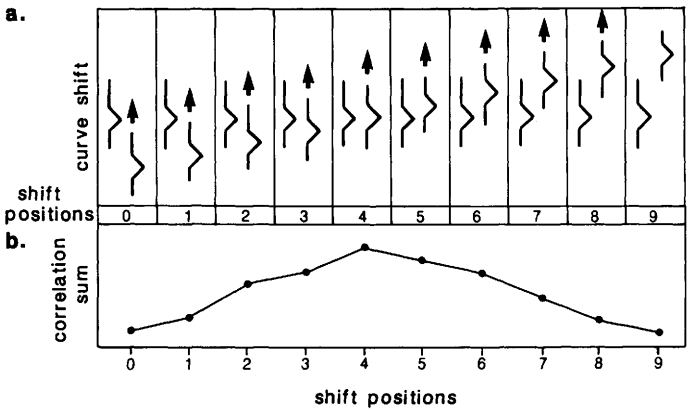

Fig. A2. Simplified illustration of the correlation of two microresistivity curves by cross-multiplication and the construction of a correlogram. Shift position 4 represents the statistically chosen correlation.

In order to implement the correlation process, three variables must be specified. These are the correlation length, the step distance and the search angle (Fig. A3).

The correlation length is the length of curve used in the curve pair comparisons during correlation. The longer the correlation length, the more the dip results will become dominated by bed boundary dips at the expense of other sedimentary surfaces such as foresets where the microresistivity contrasts are more subtle. Correlation lengths used typically vary from 10 cm (4 inches) to 1 m (3 ft) (Fig. A3).

The step distance is the distance allowed between successive correlation attempts in the microresistivity curves. This is generally chosen so as to allow for some overlap between each correlation round (Fig. A3).

The search angle is necessary because the process is attempting to correlate dipping events. The correlation programme opens a window around each length of curve being correlated to allow for the vertical displacement between curve features that will naturally result from dipping beds. The size of this window is controlled by the size of the search angle (Fig. A3).

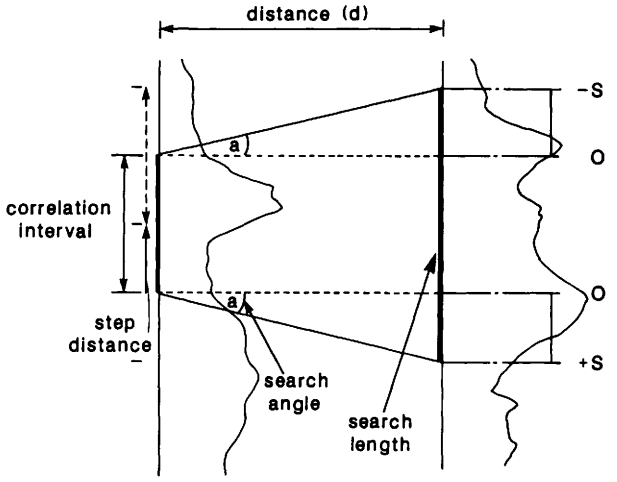

Fig. A3. Correlation Interval, Step Distance and Search Angle defined for the comparison of two curves. The correlation interval defines the length of the first curve to be used in comparisons. The search angle allows the search length of the second curve to be defined (maximum displacement $S = d \tan a$). The step distance defines the position of the succeeding correlation calculations.

The above description is necessarily much simplified. Dipmeter tools exist in various models such as with 6 independent arms or four interconnected arms but two electrodes on each pad. Each type of tool requires a different curve correlation programme. However, the basics described above still apply.

Correlation programmes do exist, however, which use curve likeness instead of the cross-multiplication method. These programmes do not use a correlation interval and actually allow peak to peak correlation. The notions of scale discussed in the paper do not apply to this kind of processing.

References

BRISTOW, C.S. & MYERS, K.J. 1989. Detailed sedimentology and gamma-ray log characteristics of a Namurian deltaic succession I: Sedimentology and facies analysis. *In*: WHATELEY, M.K.G. & PICKERING, K.T. (eds) *Deltas: Sites and Traps for Fossil Fuels*. Geological Society, London, Special Publication, **41**, 75–80.

CAMERON, G.I.F. 1986. Confidence and the identification of foresets in stratigraphic dipmeter surveys. *Transactions of the Tenth European Formation Evaluation Symposium*, paper O, pp. 1–17.

COLLINSON, J.D. & THOMPSON, D.B. 1989. *Sedimentary Structures*. Unwin Hyman, 2nd ed.

CURRAY, J.R. 1956. The analysis of two dimensional orientation data. *Journal of Geology*, **64**, 117–131.

GILREATH, J.A. & MARICELLI, J.J. 1964. Detailed stratigraphic control through dip computations. *American Association of Petroleum Geologists Bulletin*, **48**, 1902–1910.

HARMS, J.C., SOUTHARD, J.B., SPEARING, D.R. & WALKER, R.G. 1975. *Depositional environments as interpreted from primary sedimentary structures and stratification sequences*. Short Course Notes No. 2. Dallas S.E.P.M.

HOCKER, C., EASTWOOD, K.M., HERWEIJER, J.C. & ADAMS, J.T. 1990. Use of Dipmeter Data in Clastic Sedimentological Studies. *American Association of Petroleum Geologists Bulletin*, **74**, 105–118.

MYERS, K.J. & BRISTOW, C.S. 1989. Detailed sedimentology and gamma-ray log characteristics of a Namurian deltaic succession II: Gamma-ray logging. *In*: WHATELEY, M.K.G. & PICKERING, K.T. (eds) *Deltas: Sites and Traps for Fossil Fuels*. Geological Society, London, Special Publication, **41**, 81–88.

RIDER, M.H. 1978. Dipmeter Log Analysis: an Essay. *Transactions S.P.W.L.A. Nineteenth Annual Logging Symposium*, paper G, 1–18.

VAN DE GRAAFF, W.J.E. & EALEY, P.J. 1989. Geological Modeling for Simulation Studies. *American Association of Petroleum Geologists Bulletin*, **73**, 1436–1444.

From ASHTON, M. (ed.), 1993, *Advances in Reservoir Geology*,
Geological Society Special Publication No. 69, pp. 219–232.

Permeability images: a new technique for enhanced reservoir characterization

LAWRENCE T. BOURKE,[1] N. CORBIN,[2] STUART G. BUCK[1] & GAVIN HUDSON[3]

[1] *Schlumberger Log Services B.V., Woodlands Drive, Kirkhill Industrial Estate, Dyce, Aberdeen AB2 0ES, UK*
[2] *Schlumberger, 1 Kingsway, London WC2B 6XH, UK (Present address: Z & S Geology Ltd, Glover Pavilion, Balgownie Drive, Aberdeen AB22 8GW, UK)*
[3] *Department of Petroleum Geology, University of Aberdeen, Marischal College, Aberdeen AB9 1AS, UK (Present address: GAPS Geological Consultants, 13 Deodar Rd, Putney, London SW15 2NP, UK)*

Abstract: The small probe tip size of the nitrogen probe permeameter (typically 4 mm internal diameter) facilitates the investigation of small volumes of reservoir rock in core samples. The nitrogen probe permeameter measures gas flow rate at a known delivery pressure. This gas flow rate can in turn be calibrated to permeability. A closely spaced grid of such permeability measurements sampled every 4 mm in the x and y directions provides a basis for detailed sandstone permeability characterization. This paper presents permeability images, generated from such datasets, that reveal primary bedding fabric even where such features were not visually apparent in rock samples. A strong correlation is reported herein between images generated by probe permeametry from core samples and microresistivity images acquired from the borehole wall for the same reservoir interval. The similarity of features revealed by permeability and microresistivity images suggests a strong correspondence to rock properties measured by both techniques. Permeability images therefore offer considerable potential for the geological verification of microresistivity images where their direct interpretation is ambiguous. Furthermore, permeability and microresistivity images provide a mechanism for locating petrographical sampling points from which the controls on the permeability heterogeneities can be established.

The minipermeameter or probe permeameter, as defined by Eijpe and Weber (1971), has been used in the petroleum industry for detailed permeability profiling since its introduction over forty years ago (Dykstra & Parsons 1950). In recent years, interest in the probe permeameter has been renewed by both the petroleum industry and academic research for the detailed study of reservoir heterogeneity (Clelland 1984; Kortekas 1985; Daltaban *et al.* 1989; Adams *et al.* 1990; Halvorsen & Hurst 1990; Lewis *et al.* 1990; Robertson & McPhee 1990; Hurst & Rosvoll 1991). Our need to investigate such heterogeneity is governed by increasing demand for improved reserve evaluation and recovery efficiency.

In this paper the generation of permeability images is described. Images are derived using permeability data gathered by regular close-spaced sampling of core by probe permeametry. These permeability images provide a useful visual representation of the permeability heterogeneity in apparently homogeneous clastic reservoir rocks. Images of similar resolution are derived by wireline measurement from the borehole wall using the Formation MicroScanner (FMS*) tool. These microresistivity images

*Mark of Schlumberger

are being increasingly utilized for reservoir characterization, especially in thinly-bedded sequences (Harker *et al.* 1990; Adams *et al.* 1990), and have an advantage in covering the entire reservoir interval compared to the often more restricted interval sampled by cores. In this paper we compare examples of permeability and microresistivity imaging from equivalent rock units, and discuss the relationship between these two techniques. First impressions indicate that similar related features are revealed by both methods, and this is supported by subsequent petrographical investigations. This work therefore adds confidence to the use of microresistivity images for investigation and characterization of permeability heterogeneity in reservoir sequences outwith cored intervals. An example is drawn from a North Sea reservoir to illustrate the permeability imaging technique and its relationship to microresistivity images.

The nitrogen probe permeameter

The nitrogen probe permeameter allows rapid, non-destructive, close-spaced permeability measurements to be made on reasonably flat rock surfaces. The equipment used is that described by Clelland (1984), which is a modified design of the equipment designed and described by Eijpe & Weber (1971). The probe tip is sealed against the rock surface with a clamping force. The flow of nitrogen gas into the rock surface is measured via a flow meter at a known regulated gas pressure (Fig. 1). The measured nitrogen flow rate is directly related to the pressure of the gas supply and to the permeability of the sample (Eijpe & Weber 1971).

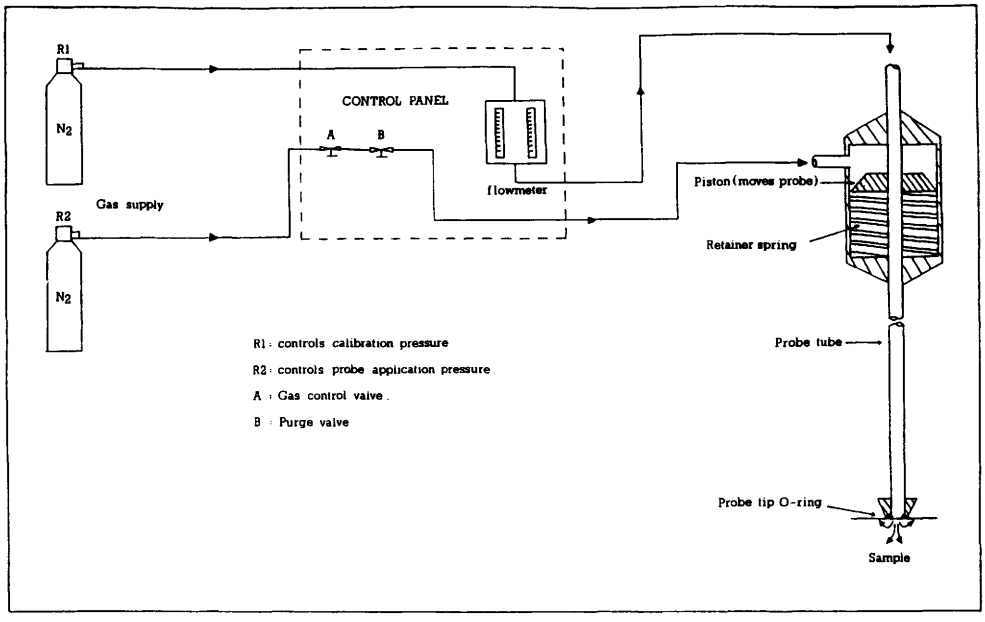

Fig. 1. Simplified schematic diagram of the nitrogen probe permeameter.

The seal between the probe permeameter probe tip and the rock surface is provided by a 4 mm ID (internal diameter) rubber 'O' ring. Clelland (1984) added a modification to the basic design to improve seal efficiency by incorporating a pressure-

driven minicylinder to engage the probe against the sample surface at a known clamping force. Once the probe tip is engaged on the sample surface by the minicylinder, the 'O' ring deforms to provide a seal. Tests of the sealing efficiency in relation to clamping pressure are described by Clelland (1984) and Halvorsen & Hurst (1990). Flow into the sample is hemispherical below the probe tip, and flow penetration is generally less than 1 cm (Goggin *et al.* 1988; Chandler *et al.* 1989; Halvorsen & Hurst 1990). The probe permeameter provides nitrogen flow rate measurement in cubic centimetres per minute. Repeatability of measured values is excellent (Clelland 1984; Hudson 1989). Measurement precision with the currently used equipment is good, with an error range of 2–4%. Similar accuracy and precision of measurements have been noted by Halvorsen and Hurst (1990) and Hurst & Rosvoll (1991).

Slabbed core is positioned below the probe on a fine-screw driven sample rack which enables measurement sites to be positioned accurately in x and y directions by vernier scaled guides. Probe permeameter flow rate measurements were made every 4 mm following a regular grid pattern across the sample surface.

Probe permeameter calibration

The calibration of probe permeameter measured flow rate to permeability has been made using conventional core plugs cut from whole core samples. An analytical solution for direct calculation of permeability from flow rate was derived by Goggin *et al.* (1988), and tested by Halvorsen & Hurst (1990). Alternatively, an empirical conversion of probe permeameter flow rate to permeability can be derived from the linear relationship of probe permeameter flow rate and conventional core plug gas permeability. Clelland (1984), Halvorsen & Hurst (1990) and Robertson & McPhee (1990), describe in detail the methodology for empirical calibration of minipermeameter flow rate to core plug permeability, and this methodology has been strictly applied during our investigation. Selected conventional core plugs (2.5 cm in diameter) of uniform lithology and texture have been used in this calibration. The permeability derived by probe permeametry is not absolute permeability (K) but an effective permeability (K_e) and is subject to the effects of residual saturation, differences in sample volume, and the quality of the probe tip seal.

Probe permeameter analysis was performed, where possible, using cleaned core slabs. However, effective cleaning of oil saturated, low permeability, large whole core samples is not always possible. Residual hydrocarbons and drilling fluid residues can constrict pore throats resulting in lower permeability values from uncleaned or incompletely cleaned core relative to those from cleaned core. The core slabbing process is also known to cause some degree of surface alteration. Consequently the interpreter should be aware that in low permeability oil-bearing sands it may not be possible to remove completely all residues from pore space and hence measured values may be under-estimated. Clelland (1984) measured permeabilities before and after cleaning and reported a slight increase in permeability after cleaning. This clean-up increase was proportional to the measurement made before cleaning, thus the presence of pore residues does not in general mask relative changes in permeability across the sample surface. Permeability images therefore provide a means to characterize permeability variation at a fine sampling scale.

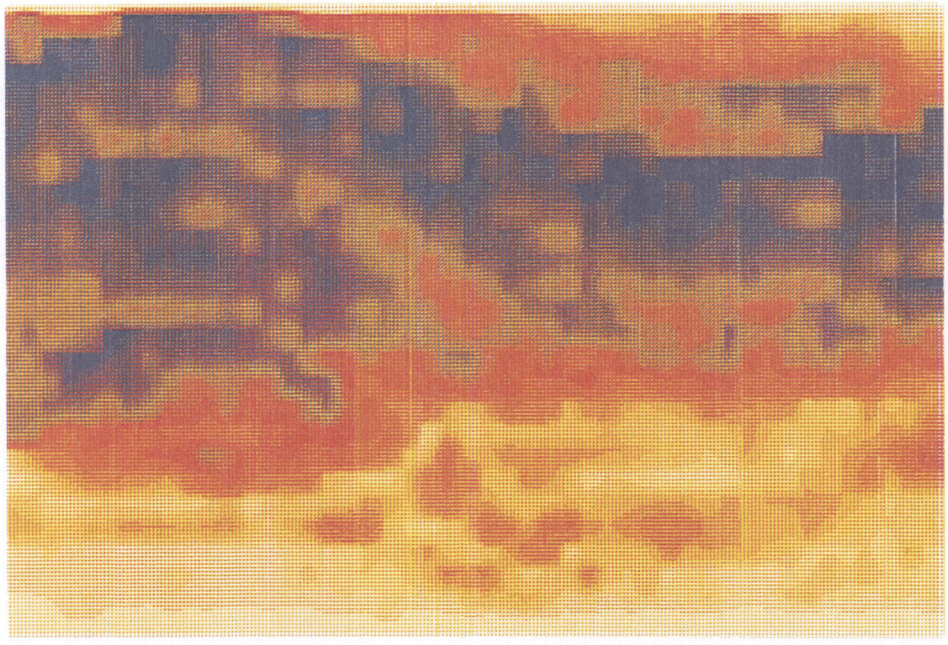

(b)

(a)

Fig. 2. Core cut from an outcrop sample from the Triassic Burghead Beds, Burghhead, north-east Scotland. The cross-bedding in the core sample (**a**) is also clearly visible on the unwrapped permeability image derived by 4 mm grid sampling on the outer surface of the core cylinder (**b**).

Permeability image generation

Two-dimensional probe permeameter sampling grids involved traversing a 4 mm spaced regular grid pattern across the surface of slabbed core samples. These probe permeameter sampling surveys were constrained by the sample size of slabbed conventional cores, and covered areas measuring 6–8 cm by 15–20 cm, depending on

the number of core breaks and conventional core plug sampling points. The resulting large arrays of flow rate measurements were converted to permeability using the calibration technique described above. A bit map image processing technique was used with interpolation between the data points to achieve image smoothing, and the results are output as a bit map to a 200 dpi colour printer or colour monitor. The false-colour images produced have a yellow-brown colour spectrum with which the measurement range is subdivided into 43 colour classes. Such images give the interpreter greater perception of permeability variation than can be achieved with black and white images where only 17 levels of grey shade can be recognized by the eye. Figure 2 shows a cross-bedded sandstone in a 3.5 inch (8.8 cm) diameter core cut from a fluviatile sequence in the Triassic Burghead Beds, Scotland, together with the corresponding permeability image sampled from the outer surface of this sample. The primary depositional fabric is faithfully reproduced on permeability images.

Formation MicroScanner tool and microresistivity imaging

The Formation MicroScanner tool is a hybrid dipmeter tool comprising a dense array of closely spaced electrodes providing microresistivity data from 2 or 4 pads depending on tool configuration (Fig. 3). Microresistivity data on these pads is sampled vertically and laterally every tenth of an inch (2.5 mm). Oriented grey scale or colour images of microresistivity variations are generated after restoration of acquisition data for tool speed variations, irregular electrode response, and correction for focusing voltage. The tool principles and image generation are discussed in Ekstrom *et al.* (1986) and the processing steps for image generation are summarized in Table 1. Images generated from acquisition data are presented as oriented strips of resistivity image from the borehole wall, each 6 cm wide.

Table 1. *Summary of Formation MicroScanner image processing steps after Harker* et al. *(1990)*

Objective: to represent formation conductivity changes as changes in grey-scale or colour shades.

1. Data restoration: speed correction to correct for variations in tool speed during logging.
   —Correction for variation of 'EMEX' focusing current.
   —Equalization of curves to the same gain and offset.
2. Image generation: each datapoint assigned to one of 127 grey-levels or one of 256 colour shades.
   Light = resistive; Dark = conductive.
3. Image enhancement
   —Static normalization: normalization of grey-scales over a large interval (400–500 ft). Shows gross resistivity variations.
   —Dynamic normalization: normalization of grey-scale within a short (1–3 ft) sliding window. Enhances small resistivity variations.
   —Dynamic histogram normalization: normalization of the full histogram of the data in a sliding window. Provides more detailed enhancement of resistivity variations.

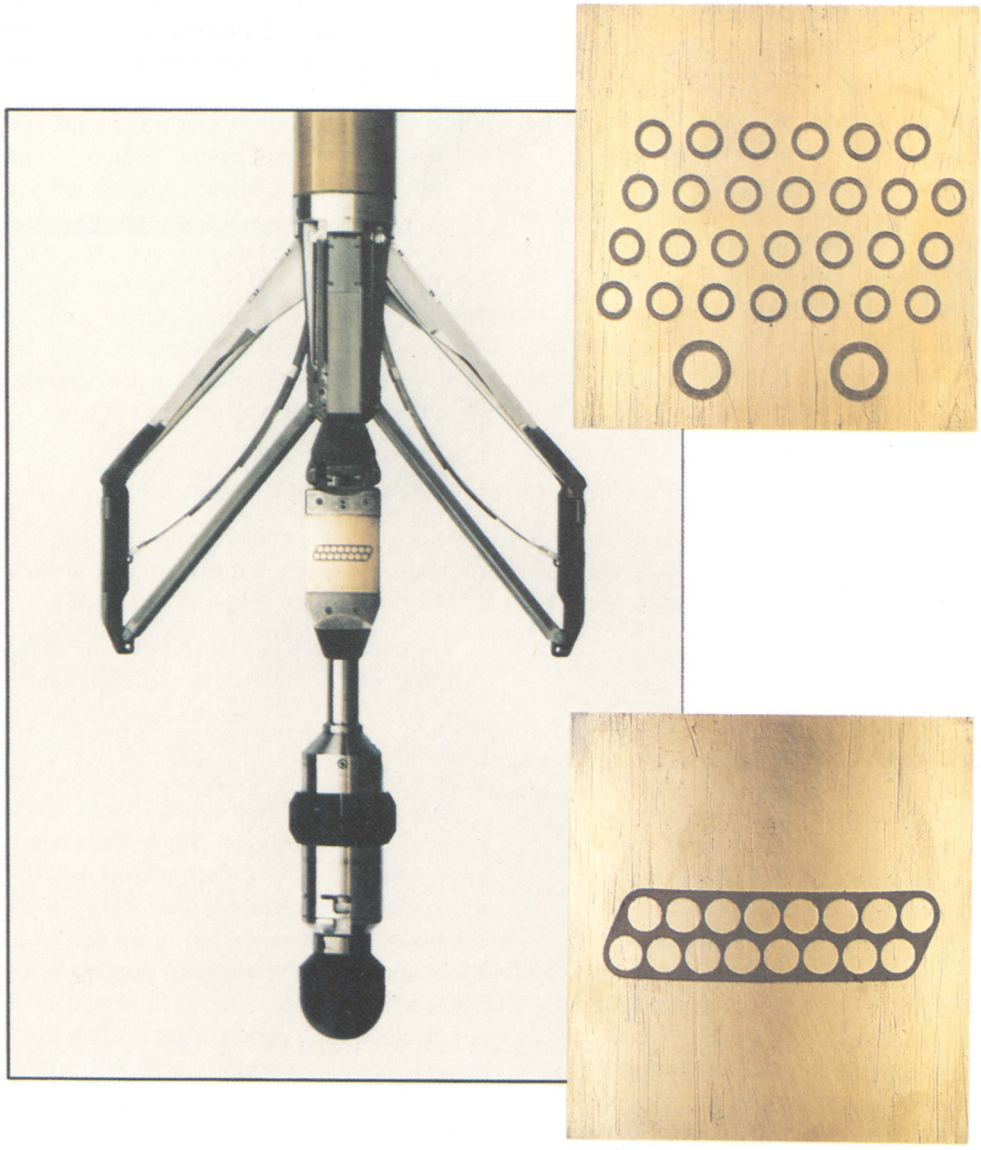

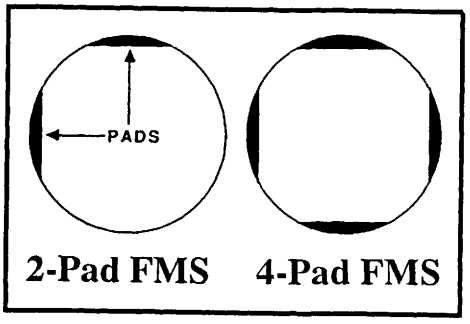

Fig. 3. The Formation MicroScanner Tool is pictured in the main panel (above) with the 2-pad version shown in the upper inset and more recent 4-pad version in the lower inset. Both pads measure 8 cm across. Borehole wall coverage achieved by these tools is illustrated (left).

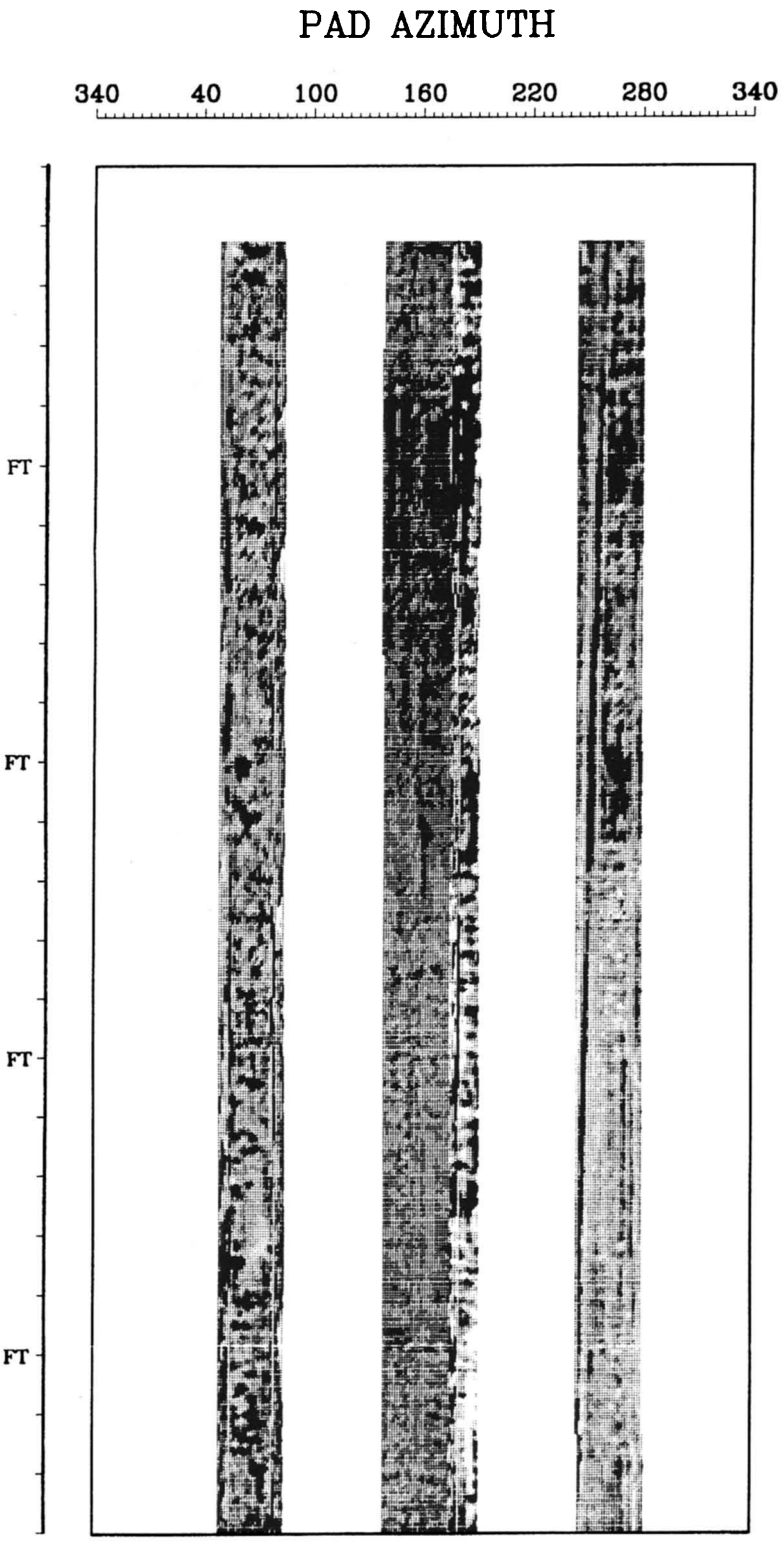

Fig. 4. Mottled microresistivity image in an apparently massive sandstone succession.

Borehole wall microresistivity images are commonly acquired for the study of sedimentary features, fracture analysis, and thin bed evaluation (Serra 1989; Bourke *et al.* 1989; Harker *et al.* 1990; Luthi & Banavar 1988). FMS images can be presented as continuous paper plots but are most easily studied using interactive workstations (Boyeldieu & Jeffreys 1988; Adams *et al.* 1990).

North Sea Example

The example described herein is from a North Sea reservoir sequence consisting of sand-rich submarine gravity-flow deposits. The cored sandstones of this succession are apparently structureless, and organized as decimetre to metre thick beds with sparsely interbedded thin claystones (centimetre- to millimetre-thick beds). The lack of apparent structure in such sandstones is commonly ascribed to rapid sedimentation from high concentration sediment gravity flows in which there was insufficient time for particle sorting to generate a sedimentary fabric. Conventional core analysis results show that horizontal gas permeability ranges from 20 to 1300 millidarcies, and helium porosity ranges between 6% and 24% of the rock volume.

Microresistivity images

Borehole wall microresistivity images from these sands show that many of the apparently massive sandstones display mottling features of a few centimetres in diameter. These features, which are present in sandstones from both the oil zone and the aquifer, were initially interpreted as mudcake artifacts on the borehole wall (Fig. 4) because of the apparently structureless nature of the core.

Rigorous quality control of FMS images has been discussed by Bourke (1989) and Harker *et al.* (1990). These works have identified three grades of images ranging from geological features which can be recognized directly from FMS images (obvious), to images which require some local geological knowlege to maintain interpretation confidence, and finally to images which are ambiguous. The latter group largely comprise artifact images, which have been comprehensively described, and their diagnosis discussed, in Bourke (1989). When artifact images have been systematically recognized and separated from geological features by careful log quality control, confident geological and diagenetic feature recognition from FMS images can then be extrapolated with considerable confidence into uncored intervals.

Permeability images

Closely-spaced probe permeameter sampling along the length of a 'massive' sandstone core from this formation revealed variation of the flow rate consistent in dimensions to the mottle-features shown by FMS microresistivity images described above (Fig. 5). Such probe permeametry profiling on core was the basis of the classification of these FMS image mottles as 'derived images' in Bourke (1989). Derived images are defined as 'images of actual geological features which differ from core appearance due to borehole geometry, the nature of FMS tool measurement, and mud filtrate invasion profile'. Such sedimentary and diagenetic features could be considered to be subtle (permeability and microresistivity visible) and therefore visually difficult to reconcile with core observations.

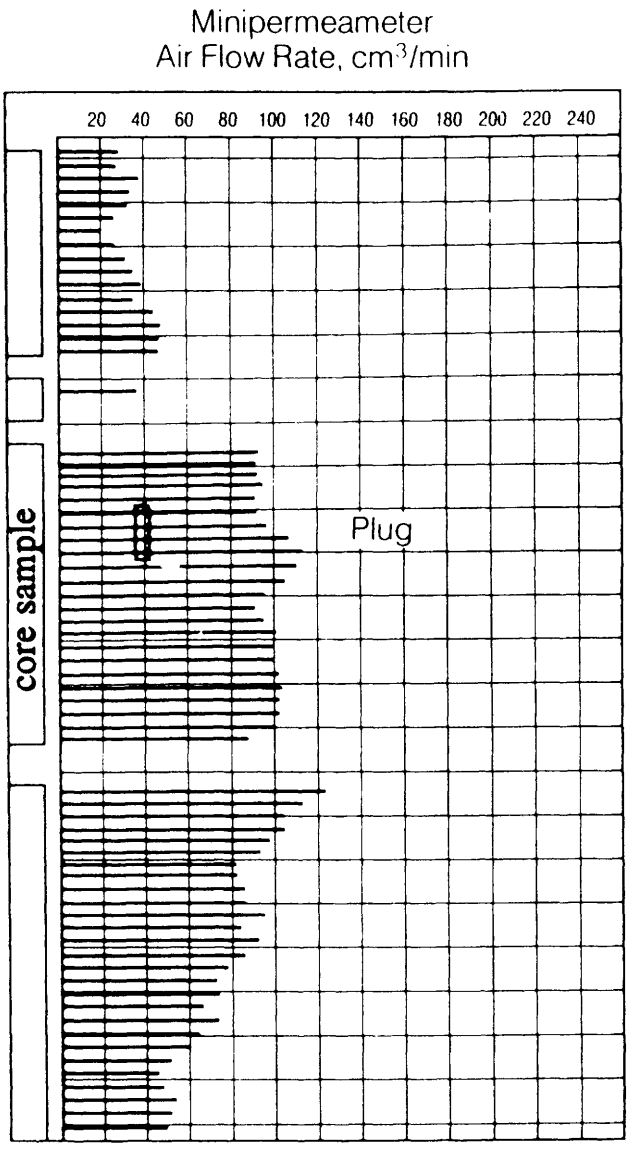

Fig. 5. Graph of probe permeameter flow rate (cm^3/minute) versus depth, sampled every 4 mm down the long axis of a 'massive' sand core slab. Flow rate variations are at an equivalent scale to the mottle features seen on FMS images in these sandstones and illustrated in Fig. 4.

To investigate further the validity of the mottle-features apparent in micro-resistivity images, a detailed probe permeameter survey was undertaken to derive high resolution permeability images. The survey was carried out on slabbed cores corresponding to the intervals in which mottling had been recognized on the FMS images. The resulting permeability images are compared with the depths corresponding to the FMS images in Fig. 6. The permeability images show a mottled pattern and vague bed definition similar to the microresistivity images. Unfortunately, these microresistivity and permeability images do not sample the same rock surface, i.e. the

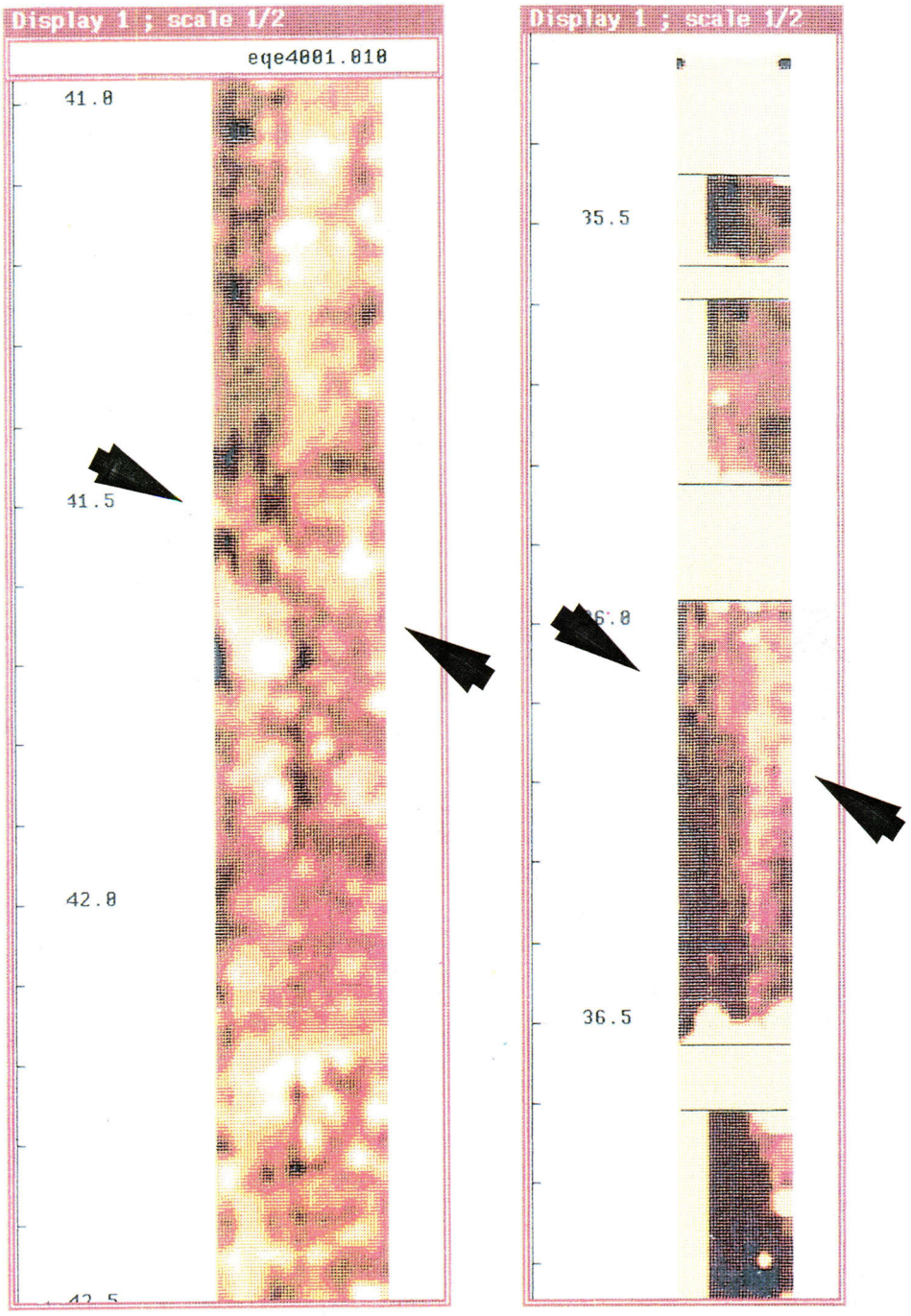

Fig. 6. On the left is a mottled FMS image in sandstones with massive appearance in core although vague high-angle bedding is arrowed. The right permeability image was generated by probe permeametry from slabbed core at the corresponding log depth, similar mottles and vague high-angle bedding are again reproduced (arrowed). Light shades are lower permeability.

permeability image represents a plane through the axis of the borehole, while the microresistivity image samples the borehole wall. However, sufficient similarity is shown between the two image types that we consider they reflect real small-scale variation in rock fabric affecting both the permeability and microresistivity.

Petrographical verification

A number of thin-sections were prepared from core to investigate the origin of the mottle-features indicated by both permeability and microresistivity images in what otherwise appeared as massive and structureless sandstones. The images were used to pinpoint the position in cores from which the thin-sections were to be prepared. Samples were selected to examine the junction between high and low permeability zones of the mottle-features. Large format thin-sections were produced and coloured, vacuum impregnated resin used to highlight pore space. These samples were examined for pore size variations using low magnification on a polarizing microscope.

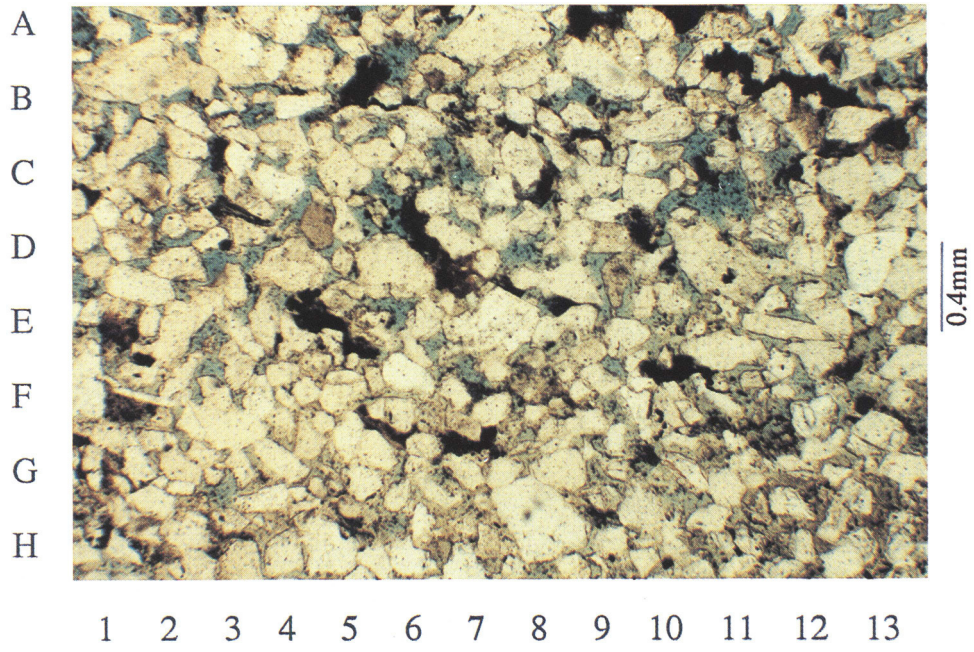

Fig. 7. Plane-polarized photomicrograph of the junction between a permeable and less permeable zone in these 'massive' sandstones. Above E/1-13, the sandstone is characterized by an open pore texture, some of the larger pores are secondary. Below E/1-13 pores are smaller and are extensively clay filled. Dark particles are organic fragments.

Correlation was found between zones of large, clean open pores apparent in thin-section and zones of higher permeability indicated by the permeability/FMS images (Fig. 7). Similarly, zones of lower permeability were found to contain significant amounts of detrital illite which block intergranular pores. Thus, the permeability variations seen on these core images are clearly reflected in the detrital fabric of the

rock. In the context of the known submarine gravity flow setting for these sands, the distribution of clays observed seem most likely to arise from sediment dewatering during deposition. The differentiation of detrital clays within and around these dewatering features are too subtle to be seen by visual inspection of cores, but are revealed by permeability images and microresistivity images. In addition, the dewatered zones cleaned of clays, locally become the sites for later cementation, which in turn provides further small-scale reservoir heterogeneity.

Discussion

This paper demonstrates that primary depositional fabric can be reproduced by generating images from fine grid probe permeameter sampling. The sensitivity of the technique is such that geological fabric too subtle to be visually apparent in core, but distinguishable on microscopic examination, is readily revealed by both permeability imaging and microresistivity imaging. Workstation based image analysis techniques provide a means to quantify these reservoir characteristics.

The similarity of features revealed by microresistivity images and permeability images suggests a strong correspondence of rock properties measured by both techniques. The FMS tool is actually measuring the conductivity of the borehole wall to a very shallow depth of investigation (14 mm). This microresistivity is the resistivity of the rock plus the fluids in the pore network. There will therefore be a strong correlation between the fluid saturation of the reservoir rock and the measured resistivity. Clearly there is also a strong correlation between the fluid saturation and the permeability of the rock. In a fine grained clastic rock there is likely to be a strong relationship between the primary depositional fabric and permeability distribution unless this has been overprinted by diagenesis.

Conclusions

(1) Permeability images generated by probe permeametry and microresistivity images derived from the Formation MicroScanner borehole logging tool both provide powerful visual techniques for the recognition and characterization of reservoir heterogeneities.

(2) Collection of large numbers of flow rate measurements to generate permeability images is a slow process and is best resolved using automated measuring techniques. However, even automated techniques are too slow to realistically consider routinely generating images from large cored intervals.

(3) The similarity of detail revealed by both permeability images and microresistivity images, is not unexpected as both techniques measure properties related to the tortuosity and connectivity of the pore system. This commonality therefore provides the unique opportunity to calibrate FMS images indirectly in terms of permeability and extrapolate these data into uncored well sections for detailed reservoir analysis.

(4) Where log quality control has indicated apparently 'derived images' as defined by Bourke (1989), permeability imaging offers a technique to assess their geological validity.

(5) The small-scale permeability heterogeneities indicated by probe permeameter imaging in apparently massive sandstones raises questions concerning the

conventional use of one foot sample core analysis data for some reservoir characterization. At present in the petroleum industry, the vertical profiling of permeability variations within cores, by probe permeametry, is commonly provided every tenth of a foot. Clearly the small permeability heterogeneities described herein, and defined by 4 mm sampling, would most probably not have been recognized in these sandstones by one foot sampling.

(6) Reservoir heterogeneities revealed by permeability and microresistivity images provide an indication of suitable locations for detailed petrographical analysis to establish the controls on reservoir quality.

Much of the data gathering to validate the theory and ideas presented in this paper was collected by G. N. Hudson as part of his MSc thesis at the University of Aberdeen.

References

ADAMS, J.T., BOURKE, L.T. & BUCK, S.G. 1990. Integrating Formation MicroScanner images and cores. *Oilfield Review*, **2**, 52–65.

BOURKE, L.T. 1989. Recognizing artifact images of the Formation MicroScanner Tool, *SPWLA Thirtieth Annual Logging Symposium, June 11–14th, Denver*. **2**, paper WW. 1–25.

——, DEFINER, P., FETT, T., GRACE, M., LUTHI, S., SERRA, O., STANDEN, E. & TROUILLER, J. C. 1989. Using Formation MicroScanner images. *The Technical Review*, **37**, 16–40.

BOYELDIEU, C. & JEFFREYS, P. 1988. Formation MicroScanner: New Developments, *SPWLA Eleventh European Evaluation Symposium, Oslo*, **1**, paper F.

CHANDLER, M. A., GOGGIN, D. J. & LAKE, L.W. 1989. A Mechanical Field Permeameter for making rapid, non destructive, permeability measurements. *Journal of Sedimentary Petrography*, **59**, 613–615.

CLELLAND, W. D. 1984. *Measurement and analysis of small scale permeability distribution in sandstones*. PhD thesis Heriot-Watt University, Department of Petroleum Engineering.

DALTABAN, T. S., LEWIS, J.J.M. & ARCHER, J.S. 1989. Field minipermeameter measurements—their collection and interpretation. *5th European Symposium on improved Oil Recovery, Budapest 25–27 April, 1989, Hungarian Hydrocarbon Institute*, 671–682.

DYKSTRA, H. & PARSONS, R. L. 1950. The prediction of oil recovery by waterflood. *In: Secondary recovery of oil in the United States, 2nd Edn.*, API, New York, 160–174.

EIJPE, R. & WEBER, K. J. 1971. Minipermeameters for consolidated rock and unconsolidated sand. *American Association of Petroleum Geologists Bulletin*, **55**, 307–309.

EKSTROM, M.P., CHEN, M.Y., ROSSI, D.N., LOCKE, S. & AARON, J. 1986. High resolution microelectrical borehole well imaging. *SPWLA Transactions of the Tenth European Formate Evaluation Symposium*.

GOGGIN, D.J., THRASHER, R. & LAKE, L.W. 1988. A theoretical and experimental analysis of minipermeameter response including gas slippage and high velocity flow effects. *In Situ*, **12**, 79–116.

HALVORSEN, C. & HURST, A. 1990. Principles, Practice and Applications of Laboratory Minipermeametry. *In*: WORTHINGTON, P.F. (ed.) *Advances in core evaluation accuracy and precision in reserves estimation*. Proceedings of the 1st Society of core analysts European core analysis symposium, London, 521–549.

HARKER, S.D., MCGANN, G.J., BOURKE, L.T. & ADAMS, J.T. 1990. Methodology of Formation MicroScanner Tool image interpretation in Claymore and Scapa Fields (North Sea). *In*: HURST, A., LOVELL, M.A. & MORTON, A.C. (eds) *Glological Applications of Wireline Logs*. Geological Society, London, Special Publication, **48**, 11–25.

HUDSON, G.N. 1989. *Title restricted*. MSc thesis. University of Aberdeen. Department of Petroleum Geology.

HURST, A. & ROSVOLL, K.J. 1991. Permeability variations in sandstones and their relationship to sedimentary structures. *In*: LAKE, L.W., CARROLL, H.B. (Jnr) & WESSON, T.C. (eds) *Reservoir Characterisation*. Academic Press, 166–196.

KORTEKAS, T.F.M. 1985. Water/oil displacement characteristics in crossbedded reservoir zones. *Society of Petroleum Engineers Journal*, **25**, 917–926.

LEWIS, J.J.M., HURST, A. & LOWDEN, B. 1990. Permeability distribution and measurements of reservoir scale heterogeneities in the Lochaline Sandstone (Cretaceous). *Field Guide, 13th International Sedimentological Congress, Nottingham*. 1990.

LUTHI, S.M. & BANAVAR, J.R. 1988. Application of borehole images to three-dimensional geometric modelling or eolian sandstone reservoirs, Permian Rotliegende, North Sea. *American Association of Petroleum Geologists*, **72**, 1074–1089.

ROBERTSON, G.M. & MCPHEE, C.A. 1990. High resolution Probe permeametry: an aid to reservoir description. *In*: WORTHINGTON, P.F. (ed.) *Advances in core evaluation accuracy and precision in revenues estimation*. Proceedings of the 1st Society of core analysts European core analysis symposium, London, 495–520.

SERRA, O. 1989. Formation MicroScanner Image Interpretation. *Schlumberger Educational Services Publication, Houston*, Publ. No. SMP-7028.

Index

Note. Italicized page references indicate figures. Emboldened page references indicate tables.

Advances in Reservoir Geology

edited by

Michael Ashton (Badley, Ashton & Associates, Horncastle, UK)

Owing to the maturity of exploration in the North Sea Basin, reservoir geology will increasingly focus on the exploitation of smaller and technically more demanding hydrocarbon accumulations and the need to maximize reserves from the established producing fields. More refined geological reservoir interpretation and modelling are therefore required.

This book details new methods, and the improved use of existing methods in such areas as sequence stratigraphy, petrography, sedimentology, inorganic geochemistry, production logging, quantitative image analysis of pore structure, the dipmeter tool and permeability imaging; and the integration of data from a variety of these sources, including outcrop-derived data.

- **240 pages**
- **140 illustrations**
- **15 pages of colour**
- **Index**

Also available:

Exploration Britain: Geological Insights for the Next Decade
Edited by R. F. P. Hardman
Hardback ISBN 0-903317-82-6, 312 pages

Geological Applications of Wireline Logs II
Edited by A. Hurst, C. M. Griffiths & P. F. Worthington
Hardback ISBN 0-903317-80-X, 404 pages

Geology of the Brent Group
Edited by A. C. Morton, R. S. Haszeldine, M. R. Giles & S. Brown
Hardback ISBN 0-903317-68-0, 506 pages

United Kingdom Oil and Gas Fields, 25 Years Commemorative Volume
Edited by I. L. Abbotts
Hardback ISBN 0-903317-62-1, 574 pages

Petroleum Migration
Edited by W. A. England & A. J. Fleet
Hardback ISBN 0-903317-66-4, 286 pages

ISBN 0-903317-84-2

9 780903 317849